

# **ASSESSING THE BEHAVIOUR OF REINFORCED CONCRETE COLUMNS UNDER BLAST LOADS**

**Margi Vilnay**

Submitted for the degree of Doctor of Philosophy

Heriot Watt University

School of Energy, Geoscience, Infrastructure and Society

January 2017

*The copyright in this thesis is owned by the author. Any quotation from the thesis or use of any of the information contained in it must acknowledge this thesis as the source of the quotation or information.*

## ABSTRACT

This Thesis is concerned with the numerical investigation of the structural response of reinforced concrete columns under blast loads, by means of dynamic nonlinear finite element analysis. This study provides an in depth understanding of the mechanics underlying reinforced concrete structural response under blast loading and studying the effect of certain important design parameters on the exhibited behaviour. The numerical investigation was carried out through the use of a well-established commercial finite element package (Abaqus) and employed a numerical model capable of accounting for the brittle nature of concrete. The latter model forms an extension to the '*brittle crack*' model (already available in Abaqus) and was developed in order to overcome the shortcomings of the existing concrete model in describing concrete material behaviour in compression. The verification of the validity of the numerical predictions is based on a comparative study with relevant experimental data. The validated models are then employed to investigate the effect of various parameters on the exhibited response and are used to identify the reasons that trigger the experimentally and numerically observed change in structural behaviour under high loading rates (compared to that established under static loading). On the basis of the predictions obtained from the FE analysis a new graphical method was developed, based on building complementary diagrams, for the effective derivation of Pressure-Impulse (P-I) diagrams. This method aims to overcome the problems associated with their inherent sensitivity to any change in the state of the analysed structural system. Through the combined use of the validated FE model and the proposed graphical method, P-I diagrams and the associated complementary diagrams are presented and the efficiency and applicability of the methodology is demonstrated.

## ACKNOWLEDGEMENTS

I would like to thank the Edinburgh Joint Research Institute for their generous scholarship which first enabled me to embark on this PhD. My sincere thanks also go to Dr Dimitri Val who presented me with the opportunity and explored the research themes with me. I also thank Prof. Yong Lu who generously gave his time to provide guidance.

I am deeply indebted to Dr Demetrios Cotsovos, without who this research would not have developed into what it is today. My deepest thanks to Dr Cotsovos for his guidance, motivation, and immense knowledge. I could not have imagined having a better advisor and mentor, not only for my PhD research but also in my academic career.

My warmest gratitude is also due to Dr Leon Chernin who helped shape the contents of this research and encouraged me to see the light in each of my failed attempts.

My sincere gratitude is also due to my two examiners – Dr Benny Suryanto and Dr Arash Fallah, not only for their valuable comments which have improved this work, but also for their insights into future research avenues.

I would also like to thank my ex-Atkins colleagues for their friendship and support, especially during the tougher times. My warmest thanks to Michelle Magee for being an exceptional friend, advisor and cheerleader. Thanks also to Kay Vickers, Gregg Hepburn, Matt Dickson, Thomas Aldhous, Craig Nicholson, Jonny Gill, Katy Primavesi, Matt Lira, Charlotte Hill and many more – we had some great times together. Also, for their continued support and insights into the intricacy of advanced numerical modelling, in no particular order; Drs Les Thomson, Ian Hunter, Mike Casey, Khaled El-Deeb, Crerar Christie and Mark Manzocchi – you truly are wizards!

Thanks to all my fantastic colleagues at Abertay for their patience and understanding whilst I completed this research and for celebrating the outcome with me. A special thanks to Professor David Blackwood for taking a chance on me and believing I would finish my PhD, Eddie Simpson for mentoring me through the challenges of my new role and Dr Cony Doerich-Stavridis for her encouragement, friendship and support.

Finally, I would like to thank my family. My deep and sincere gratitude to my mum and dad for their continuous love, help and support. To my beautiful sister for always believing in me. A particularly heartfelt thanks to my husband, Leon, for his patience, support and love. And for my two children, Jonny and Michelle, who inspire me to be the best that I can – yes, it's finally time to play!

ACADEMIC REGISTRY  
**Research Thesis Submission**



Name:	Margi Vilnay		
School/PGI:	School of Energy, Geoscience, Infrastructure and Society		
Version: <i>(i.e. First, Resubmission, Final)</i>	Final	Degree Sought (Award <b>and</b> Subject area)	PhD Civil Engineering

**Declaration**

In accordance with the appropriate regulations I hereby submit my thesis and I declare that:

- 1) the thesis embodies the results of my own work and has been composed by myself
- 2) where appropriate, I have made acknowledgement of the work of others and have made reference to work carried out in collaboration with other persons
- 3) the thesis is the correct version of the thesis for submission and is the same version as any electronic versions submitted\*.
- 4) my thesis for the award referred to, deposited in the Heriot-Watt University Library, should be made available for loan or photocopying and be available via the Institutional Repository, subject to such conditions as the Librarian may require
- 5) I understand that as a student of the University I am required to abide by the Regulations of the University and to conform to its discipline.

\* Please note that it is the responsibility of the candidate to ensure that the correct version of the thesis is submitted.

Signature of Candidate:		Date:	
-------------------------	--	-------	--

**Submission**

Submitted By <i>(name in capitals)</i> :	MARGI VILNAY
Signature of Individual Submitting:	
Date Submitted:	

**For Completion in the Student Service Centre (SSC)**

Received in the SSC by <i>(name in capitals)</i> :			
<i>Method of Submission</i> <i>(Handed in to SSC; posted through internal/external mail):</i>			
<i>E-thesis Submitted (mandatory for final theses)</i>			
Signature:		Date:	

Please note this form should bound into the submitted thesis.

Updated February 2008, November 2008, February 2009, January 2011

# Table of Contents

<b>List of Tables .....</b>	<b>v</b>
<b>List of Figures.....</b>	<b>vii</b>
<b>Chapter 1: Introduction.....</b>	<b>1</b>
1.1. Background .....	1
1.2. Research Aim and Objectives .....	2
1.3. Innovative aspects of this research.....	4
1.4. Contents of the Thesis .....	5
<b>Chapter 2 : Reinforced Concrete (RC) Structural Response under Blast Loads .....</b>	<b>7</b>
2.1. Introduction .....	7
2.2. Blast Loads .....	7
2.2.1. Blast Phenomena.....	11
2.2.2. Blast Load Modelling .....	12
2.3. Concrete Material Behaviour .....	17
2.3.1. Effect of Loading Rate on Concrete Material Behaviour .....	22
2.3.2. Material Models Describing Concrete Behaviour under High Loading Rates ..	30
2.4. Steel Material Behaviour.....	33
2.4.1. Effect of Loading Rate on Steel Material Behaviour.....	34
2.5. Methods for Assessing RC Structural Response under Blast .....	35
2.5.1. Experimental Methods .....	36
2.5.2. Nonlinear Finite Element Analysis .....	41
2.5.3. Methods Employed in Practice .....	49
2.6. Limitations of Existing Assessment Methods.....	53
2.7. Concluding Remarks Concerning RC Structural Response under Blast.....	55
References.....	56
<b>Chapter 3: Pressure Impulse Diagrams .....</b>	<b>66</b>
3.1. Introduction .....	66
3.2. Literature Review .....	66
3.3. Derivation of P-I diagrams.....	71
3.3.1. Methods of investigating structural response .....	71
3.3.2. Search Algorithms .....	74

3.4.	Classification of P-I diagrams .....	78
3.4.1.	Closed-form formulation .....	78
3.4.2.	Open-form consistent formulation.....	89
3.4.3.	Open-form mixed formulation.....	92
3.5.	Sensitivity to load time history .....	95
3.5.1.	Analytical model.....	95
3.5.2.	Derivation of P-I diagrams and Discussion .....	97
3.5.3.	P-I diagram for finite load rise time history.....	103
3.6.	Sensitivity to axial loads .....	105
3.7.	Conclusions .....	107
	References.....	108
<b>Chapter 4</b>	<b>: Graphical Method for the Derivation of P-I Diagrams.....</b>	<b>115</b>
4.1.	Introduction .....	115
4.2.	New Graphical Method .....	115
4.3.	Dimensional method .....	119
4.4.	Normalised method .....	120
4.5.	Case study: axially preloaded beam under blast load .....	122
4.5.1.	P-I diagram.....	124
4.5.2.	N-I diagram.....	125
4.5.3.	N-P diagram.....	127
4.5.4.	Dimensional graphical method .....	129
4.5.5.	Normalised graphical method.....	130
4.6.	Conclusions .....	133
	References.....	134
<b>Chapter 5</b>	<b>: Finite Element Modelling of Reinforced Concrete Structures.....</b>	<b>137</b>
5.1.	Introduction .....	137
5.2.	Reinforced concrete models in Abaqus.....	138
5.2.1.	Available models .....	138
5.2.2.	Verification Studies .....	147
5.2.3.	Strain Rate.....	153
5.2.4.	Conclusions.....	160
5.3.	Modelling RC structural response.....	162
5.3.1.	Modelling of reinforcement .....	162

5.3.2.	Modelling Blast Loads .....	162
5.3.3.	Nonlinear solution strategy .....	162
5.3.4.	Mesh Size and Time Increment .....	164
5.4.	Verification studies .....	166
5.4.1.	Three-point bending static test.....	166
5.4.2.	Predicting Brittle RC Failure .....	169
5.4.3.	Predicting Ductile RC Failure.....	175
5.4.4.	RC column under blast.....	180
5.5.	Discussion and conclusions.....	200
	References.....	201
<b>Chapter 6: Assessing Reinforced Concrete Structural Response under Blast Loads and Pressure-Impulse Diagram Investigation.....</b>		<b>203</b>
6.1.	Introduction .....	203
6.2.	Parametric investigation.....	203
6.2.1.	Blast intensity.....	203
6.2.2.	Axial Force.....	206
6.2.3.	Longitudinal reinforcement .....	212
6.2.4.	Transverse reinforcement.....	216
6.2.5.	Boundary conditions .....	220
6.2.6.	Static, Dynamic and Impulsive Reactions .....	225
6.2.7.	Reaction Time.....	230
6.2.8.	Reinforcement Element Definition .....	234
6.2.9.	Conclusions.....	237
6.3.	Pressure-Impulse Diagram Investigation .....	239
6.3.1.	Description of column used in investigation .....	239
6.3.2.	Building of P-I and complementary diagrams for different structural/loading parameters .....	242
6.3.3.	Response mechanisms in different loading regimes .....	250
6.3.4.	Implementation of the graphical method .....	252
6.3.5.	Conclusions.....	256
	References.....	258
<b>Chapter 7: Summary, Conclusions and Future Work.....</b>		<b>259</b>
7.1	Summary and Conclusions .....	259
7.2	Future Work.....	263

<b>Appendix A</b> .....	<b>265</b>
A.1. Introduction .....	265
A.2. Axially preloaded elastic beam subjected to blast loads .....	265
A.2.1. Pinned-pinned supports .....	269
A.2.2. Forced vibration phase: $t \leq t_0$ .....	269
A.2.3. Free vibration phase: $t > t_0$ .....	271
A.2.4. Time of maximum deflection .....	271
A.2.5. Mode contribution .....	272
References .....	274
<b>Appendix B</b> .....	<b>277</b>
Brittle Crack Compression Subroutine .....	277



## List of Tables

Table 2.1. Types of load time history used for modelling of blast loads.....	13
Table 2.2. Computer programs that are currently being used for modelling blast effects on structures [23].....	42
Table 3.1. Coefficients $n_1$ and $n_2$ for the normalised P-I diagram [33] .....	81
Table 3.2. Coefficients $\beta$ and $\gamma_v$ for the P-I diagrams for the bending and shear failure of beams, Eqs. (3.19) and (3.20).....	84
Table 3.3. Values of $P_{cr}$ , $I_{cr}$ , $C$ and $D$ for the P-I diagram for RC columns subjected to a blast with a triangular time history, Eq. (3.28). .....	87
Table 3.4. Fitted values of constants in P-I curve formulas.....	103
Table 5.1. General concrete properties .....	148
Table 5.2. Damaged Plasticity concrete properties.....	148
Table 5.3. Extended brittle crack concrete properties for user subroutine .....	149
Table 5.4. Notched beam- concrete properties .....	168
Table 5.5. Bresler and Scordelis beam components' geometry.....	169
Table 5.6. Bresler and Scordelis beam- concrete properties.....	170
Table 5.7. Bresler and Scordelis beam- steel material properties.....	170
Table 5.8. Hughes and Speirs beam components' geometry .....	175
Table 5.9. Hughes and Speirs beam- concrete properties .....	175
Table 5.10. Hughes and Speirs beam- steel material properties .....	176
Table 5.11. Mid beam displacement for experiment and simulation.....	178
Table 5.12. Column components' geometry.....	182
Table 5.13. Steel Material Properties.....	183
Table 5.14. Concrete Material Properties .....	183
Table 5.15. Column components' geometry.....	188
Table 5.16. Steel Material Properties.....	188
Table 5.17. Concrete Material Properties .....	188
Table 5.18. Test 7 – column response.....	194
Table 5.19. Test 7 – numerical analysis response.....	195
Table 5.20. Test 8 – column response.....	197
Table 5.21. Test 8 – numerical analysis response.....	199
Table 6.1. Levels of blast intensity investigated.....	204
Table 6.2. Levels of axial force investigated .....	207
Table 6.3. Column response under varying axial load.....	211
Table 6.4. Levels of longitudinal reinforcement areas investigated .....	212
Table 6.5. Column response under varying longitudinal reinforcement .....	216
Table 6.6. Diameter of transverse reinforcement investigated .....	216
Table 6.7. Column response under varying transverse reinforcement.....	220
Table 6.8. Boundary conditions examined .....	221
Table 6.9. Column response under the different boundary conditions .....	225
Table 6.10. Levels of blast pressures, durations and equivalent force investigated .....	225
Table 6.11. Levels of blast pressures, durations and equivalent force investigated .....	230

Table 6.12. Column components' geometry .....	239
Table 6.13. Steel Material Properties .....	240
Table 6.14. Concrete Material Properties .....	240
Table 6.15. Parameters for P-I equations .....	246
Table 6.16. Pressure and impulse values used for different loading regimes.....	250
Table 6.17. New Parameters for P-I equations .....	253
Table A.1: Modal participation factors $\Gamma_i$ for different spatial load distributions for pinned-pinned beams.....	270

## List of Figures

Figure 2.1. Ronan Point after the domestic gas explosion 1968 [6] .....	8
Figure 2.2. The Murrah Building after the explosion 1995 [9] .....	8
Figure 2.3. The Oppau Explosion 1921 [15] .....	9
Figure 2.4. The Piper Alpha disaster 1988 [18].....	10
Figure 2.5. Fukushima Daiichi nuclear disaster in Japan in 2011 [18].....	10
Figure 2.6. Characteristic forms of blast waves: (a) shock wave and (b) pressure wave .....	11
Figure 2.7. Simplified shapes for modelling of blast loads: (a) rectangular, (b) triangular, (c) triangular with finite rise time, (d) bilinear-triangular, (e) bilinear-rectangular, (f) concave, (g) exponential and (h) sinusoidal.....	12
Figure 2.8. Reflection of blast wave at the earth’s surface in an air blast; $t_1$ to $t_4$ represent successive times [26] .....	14
Figure 2.9. Typical compressive stress-strain curves for normal density concrete.[59].....	17
Figure 2.10. Concrete behaviour in tension[61] .....	18
Figure 2.11. Relationship between splitting tensile strengths and compression strengths [60] .....	19
Figure 2.12. Strength and modes of failure on biaxially loaded concrete[60].....	20
Figure 2.13. Triaxial compression tests on cylinders (a) stress paths used (b) typical stress-strain relationships [64].....	21
Figure 2.14. Stress-strain curves in compression at various strain rates [66].....	22
Figure 2.15. Schematic representation of the SHPB test in compression [69] .....	23
Figure 2.16. SHPB test setup, and specimens [69] .....	23
Figure 2.17. Stress–strain curves of 40 MPa concrete solid specimen, as shown in Figure 2.16 [69].....	24
Figure 2.18. Yan et al testing system [71] .....	25
Figure 2.19. Failure surface of concrete beams at different strain rates (a) $10^{-6}/s$ , (b) $10^{-5}/s$ , (c) $10^{-4}/s$ and (d) $10^{-3}/s$ [72].....	25
Figure 2.20. Schematic test setup [74].....	26
Figure 2.21. Changes of tensile strength for wet and dry micro-concrete as a function of critical time to failure [74] .....	26

Figure 2.22. Experimental device (projectile, input bar, specimen) and instrumentation (light sources, photo-diodes, strain gauges, accelerometer, and laser extensometer) [75]	27
Figure 2.23. Variation of load-carrying capacity with strain rate for concrete in uniaxial compression (maxPd=dynamic load carrying capacity, maxPs=load carrying capacity under static loading) [78]	28
Figure 2.24. Variation of load-carrying capacity with strain rate for concrete in uniaxial tension (maxPd=load carrying capacity, maxPs=load carrying capacity under static loading) [79]	28
Figure 2.25. Stress-strain diagram of structural steel [100]	33
Figure 2.26. Reinforcing bars under different rates of loading [104]	35
Figure 2.27. Cendón et al [89] experimental set up	38
Figure 2.28. Kakogiannis et al [93] experimental setup	39
Figure 2.29. Zhang et al [97] experimental setup	39
Figure 2.31. Stud wall and masonry in the Blast Simulator[119]	40
Figure 2.32. Hydraulic actuators at the Protective Engineering Laboratory in Nanyang Technological University, Singapore [120]	41
Figure 2.33. Finite element slab (a) geometry and (b) damage for a 10 kg charge at a 0.5m distance [125]	43
Figure 2.34. Geometry of the RC beam [121]	44
Figure 2.35. Damage comparisons between the experiment and simulation [121]	44
Figure 2.36. Finite element model of RC two storey frame with masonry infill [128]	45
Figure 2.37. Numerical model of a six-storey building [129]	46
Figure 2.38. Displacements of the (a) two storey and (b) 8 storey buildings at at 1sec after explosion at scaled distance $0.5\text{m/kg}^{1/3}$ [130]	47
Figure 2.39. Finite element model of the AMIA building [107]	48
Figure 2.40. Simple SDOF system [133]	49
Figure 2.41. Pressure-Impulse diagram	50
Figure 2.42. Truss modelling function of an RC beam at its ultimate limit state [140]	50
Figure 2.43. Pipers Row Car Park, Wolverhampton Partial Collapse, March 1997[143]	51
Figure 2.44. RC beam exhibiting type II behaviour	52
Figure 2.45. Internal actions developing in a RC beam exhibiting (a) type III and (b) type IV behaviour	53
Figure 3.1. Normalised P-I diagram	69

Figure 3.2. Load-response regimes: (a) impulsive, (b) quasi-static and (c) dynamic.....	71
Figure 3.3. Numerical derivation of P-I diagrams .....	75
Figure 3.4. Search algorithms for the derivation of P-I diagrams: (a) Pressure-controlled, (b) impulse-controlled and (c) mixed search algorithms .....	76
Figure 3.5. Case study beam: geometry, loading and boundary conditions .....	95
Figure 3.6. Derivation of P-I diagram for the case study beam.....	98
Figure 3.7. P-I diagrams for the pressure load with different time history shapes .....	98
Figure 3.8. Comparison of P-I diagrams for rectangular time history.....	100
Figure 3.9. Comparison of P-I diagrams for triangular time history .....	101
Figure 3.10. Comparison of P-I diagrams for concave time history.....	101
Figure 3.11. Comparison of P-I diagrams for exponential time history .....	102
Figure 3.12. Comparison of P-I diagrams for sinusoidal time history.....	102
Figure 3.13. P-I diagrams for the axially preloaded simply supported beam subjected to uniformly distributed transverse blast loading with a rectangular time history..	106
Figure 4.1. P-I Diagram .....	116
Figure 4.2. Graphical method .....	118
Figure 4.3. (a) Basic and (b) extended F-I (F-P) diagrams.....	119
Figure 4.4. (a) Beam-column model and (b) load time history .....	122
Figure 4.5. P-I diagrams.....	124
Figure 4.6. Normalised N-I diagram.....	125
Figure 4.7. Extended normalised N-I diagram.....	126
Figure 4.8. Normalised N-P diagram.....	128
Figure 4.9. Dimensional graphical method.....	130
Figure 4.10. Normalised graphical method.....	131
Figure 5.1. Response of concrete to uniaxial loading in tension (a) and compression (b)[6]	140
Figure 5.2. Uniaxial load cycle (tension-compression-tension) assuming default values for the stiffness recovery factors: $w_t = 0$ and $w_c = 1$ . [6].....	141
Figure 5.3. Postfailure stress-displacement curve [6].....	142
Figure 5.4. Principle of shear friction in concrete crack with unbroken aggregates [17].....	143
Figure 5.5. Power law form of the shear retention model [6].....	144
Figure 5.6. Schematic representation of the stress-crack opening relation for uniaxial tension [17].....	145
Figure 5.7. The $\sigma_c - \varepsilon_c$ and $E_c - \varepsilon_c$ curves describing Eqs. (5.5) and (5.6).....	146

Figure 5.8. The single element concrete cube with tensile loading .....	148
Figure 5.9. Comparison between Elastic moduli for the concrete models .....	150
Figure 5.10. The single element concrete cube results for tensile loading .....	151
Figure 5.11. The single element concrete cube results for compressive loading .....	152
Figure 5.12. Finite element model of concrete prism .....	153
Figure 5.13. Strain rate results in tension .....	154
Figure 5.14. Strain rate results for tension compared to experimental results [7].....	155
Figure 5.15. Displacement in tension for displacement rate of 10 mm/sec at t= 0, 25%, 50%, 75% and 100% of time to maximum observed stress .....	155
Figure 5.16. Displacement in tension for displacement rate of 100 mm/sec at t= 0, 25%, 50%, 75% and 100% of time to maximum observed stress .....	156
Figure 5.17. Displacement in tension for displacement rate of 1,000 mm/sec at t= 0, 25%, 50%, 75% and 100% of time to maximum observed stress.....	156
Figure 5.18. Displacement in tension for displacement rate of 2,000 mm/sec at t= 0, 25%, 50%, 75% and 100% of time to maximum observed stress.....	156
Figure 5.19. Displacement in tension for displacement rate of 10,000 mm/sec at t= 0, 25%, 50%, 75% and 100% of time to maximum observed stress.....	156
Figure 5.20. Displacement in tension for displacement rate of 20,000 mm/sec at t= 0, 25%, 50%, 75% and 100% of time to maximum observed stress.....	157
Figure 5.21. Strain rate results in compression.....	157
Figure 5.22. Strain rate results for compression compared to experimental results [8] .....	158
Figure 5.23. Displacement in compression for loading rate of 10,000 MPa/sec at t= 0, 50%, 75% and 100% of time to maximum observed stress .....	159
Figure 5.24. Displacement in compression for loading rate of 100,000 MPa/sec at t= 0, 50%, 75% and 100% of time to maximum observed stress .....	159
Figure 5.25. Displacement in compression for loading rate of 200,000 MPa/sec at t= 0, 50%, 75% and 100% of time to maximum observed stress .....	159
Figure 5.26. Displacement in compression for loading rate of 400,000 MPa/sec at t= 0, 50%, 75% and 100% of time to maximum observed stress .....	160
Figure 5.27. Displacement in compression for loading rate of 2,000,000 MPa/sec at t= 0, 50%, 75% and 100% of time to maximum observed stress.....	160
Figure 5.28. Displacement in compression for loading rate of 4,000,000 MPa/sec at t= 0 50%, 75% and 100% of time to maximum observed stress .....	160
Figure 5.29. Mid column displacement for the meshes examined .....	165

Figure 5.30. Damage patterns for the (a) 40mm (b) 50mm and (c) 100mm meshes.....	165
Figure 5.31. Mid column displacement for the 50mm mesh with varying time increment...	166
Figure 5.32. Notched beam[6] .....	167
Figure 5.33. Notched beam- finite element model .....	167
Figure 5.34. Notched beam- analysis results .....	169
Figure 5.35. Beam cross section .....	170
Figure 5.36. Loading arrangement and instrumentation [10] .....	171
Figure 5.37. View of the finite element model of the Bresler and Scordelis beam .....	171
Figure 5.38. Concrete material properties in tension.....	172
Figure 5.39. Concrete material properties in compression .....	172
Figure 5.40. Typical crack pattern for shear-compression failure [10] .....	173
Figure 5.41. Observed crack patterns in numerical model .....	174
Figure 5.42. Load- Deflection curves for Bresler and Scordelis beam- experimental and numerical results .....	174
Figure 5.43. Details of test beams.....	175
Figure 5.44. Loading arrangement and instrumentation [22] .....	176
Figure 5.45. View of the finite element model of the Hughes and Speirs beam .....	176
Figure 5.46. Concrete material properties in tension.....	177
Figure 5.47. Concrete material properties in compression .....	177
Figure 5.48. Amplitude used to simulate the impact case in experiment C-2 .....	178
Figure 5.49. Crack development for numerical simulation of Hughes and Speirs C-2 experiment.....	179
Figure 5.50. Final observed crack pattern in Hughes and Speirs C-2 experiment.....	179
Figure 5.51. Hughes and Speirs experimental results alongside numerical results .....	180
Figure 5.52: Reinforced Concrete Column Model [23].....	181
Figure 5.53. Reinforced Concrete Column Model.....	181
Figure 5.54. Column experiment reading placements .....	182
Figure 5.55. Damaged Plasticity Results (a) Maximum residual strains (b) Results for mid column displacement.....	184
Figure 5.56. Concrete material properties in tension.....	185
Figure 5.57. Concrete material properties in compression .....	185
Figure 5.58. Extended Brittle Crack Results (a) Maximum residual strains (b) Results for mid column displacement.....	186
Figure 5.59. Overview of Explosive Loading Laboratory Facility with Test Setup [12].....	187

Figure 5.60. Concrete material properties in (a) compression and (b) tension.....	189
Figure 5.61. Link system [12].....	189
Figure 5.62. Numerical heading constraints .....	190
Figure 5.63. Hydraulic jacks for vertical load [12].....	190
Figure 5.64. Finite element model of full scale column .....	191
Figure 5.65. Equivalent Pressure - Test 7[12] .....	192
Figure 5.66. Test 7 experimental responses at (a) 6.7 (b) 41.7 (c) 84.3 and (d) 558 msec[12] .....	193
Figure 5.67. Test 7 post-test damage at (a) top and (b) bottom of the column [12] .....	193
Figure 5.68. Test 7 - numerical response at 4, 10, and 150 msec .....	194
Figure 5.69. Test 7 - crack pattern at 10 msec .....	195
Figure 5.70. Equivalent Pressure - Test 8[17] .....	196
Figure 5.71. Axial load simulation - Test 8 .....	196
Figure 5.72. Test 8- post-test, removed from fixture [17] .....	197
Figure 5.73. Test 8 - numerical response at 4, 10, and 150 msec .....	198
Figure 5.74. Test 8 - crack pattern .....	198
Figure 6.1. Blast loads investigated .....	204
Figure 6.2. Comparison of damage patterns at 5 msec function of the user-defined variable .....	205
Figure 6.3. Comparison of damage patterns at 150 msec function of the user-defined variable .....	205
Figure 6.4. Mid column displacements for varying ratios of blast intensity .....	206
Figure 6.5. Progression of damage in case A1 (at 0, 5, 10, 15, 30 and 100 msec) .....	208
Figure 6.6. Progression of damage in case A2 (at 0, 5, 10, 15, 30 and 100 msec) .....	208
Figure 6.7. Progression of damage in case A3 (at 0, 5, 10, 15, 30 and 100 msec) .....	209
Figure 6.8. Progression of damage in case A4 (at 0, 5, 10, 15 and 30 msec) .....	209
Figure 6.9. Progression of damage in case A5 (at 0, 5, 10, 15 and 30 msec) .....	210
Figure 6.10. Comparison of crack pattern between cases (a) A2 and (b) A5 at 5 msec, function of the user-defined variable .....	211
Figure 6.11. Progression of damage in case L1 (at 0, 5, 10, 15. 30 and 100 msec) .....	213
Figure 6.12. Progression of damage in case L2 (at 0, 5, 10, 15. 30 and 100 msec) .....	213
Figure 6.13. Progression of damage in case L3 (at 0, 5, 10, 15. 30 and 100 msec) .....	214
Figure 6.14. Progression of damage in case L4 (at 0, 5, 10, 15. 30 and 100 msec) .....	214



Figure 6.15. Damage pattern in cases (a) L1, (b) L2, (c) L3 and (d) L4 at 3 msec, function of the user-defined variable .....	215
Figure 6.16. Mid-column displacements for varying ratios of longitudinal reinforcement...	215
Figure 6.17. Progression of damage in case T1 (at 0, 5, 10, 15, 30 and 100 msec after the application of the blast load) .....	217
Figure 6.18. Progression of damage in case T2 (at 0, 5, 10, 15 and 25 msec after the application of the blast load) .....	217
Figure 6.19. Progression of damage in case T3 (at 0, 5, 10, 15, 30 and 100 msec after the application of the blast load) .....	218
Figure 6.20. Progression of damage in case T4 (at 0, 5, 10, 15, 30 and 100 msec after the application of the blast load) .....	218
Figure 6.21. Damage pattern in cases (a) T1, (b) T2, (c) T3 and (d) T4 at 3 msec after the application of the blast load, function of the user-defined variable .....	219
Figure 6.22. Damage pattern in cases (a) T1 and (b) T4 at 150 msec after the application of the blast load, function of the user-defined variable .....	219
Figure 6.23. Mid column displacements for varying ratios of transverse reinforcement .....	220
Figure 6.24. Progression of damage in case BC1 (at 0, 5, 10, 15, 30 and 100 msec after the application of the blast load) .....	222
Figure 6.25. Progression of damage in case BC2 (at 0, 5, 10, 15, 30 and 100 msec after the application of the blast load) .....	222
Figure 6.26. Progression of damage in case BC3 (at 0, 5, 10, 15, 30 and 100 msec after the application of the blast load) .....	223
Figure 6.27. Damage pattern in cases (a) BC1, (b) BC2, (c) BC3 at 5 msec after the application of the blast load, function of the user-defined variable .....	224
Figure 6.28. Damage pattern in cases (a) BC1, (b) BC2, (c) BC3 at 15 msec after the application of the blast load, function of the user-defined variable .....	224
Figure 6.29. Mid-column displacements under the different boundary conditions .....	225
Figure 6.30. Load profiles used for static, dynamic and impulsive cases .....	226
Figure 6.31. (a) Applied load vs. reaction force and (b) damage pattern at time of max reaction for static case .....	226
Figure 6.32. (a) Applied load vs. reaction force and (b) damage pattern at time peak load for dynamic case .....	227
Figure 6.33. (a) Applied load vs. reaction force and (b) damage pattern at time of peak load for impulsive case .....	228

Figure 6.34. Total internal energy in the static and impulsive cases .....	228
Figure 6.35. Damage pattern in (a) Static, (b) Dynamic and (c) Impulsive cases at 5 msec, function of the user-defined variable .....	229
Figure 6.36. Damage pattern in (a) Static, (b) Dynamic and (c) Impulsive cases at 250 msec, function of the user-defined variable .....	229
Figure 6.37. Comparison of damage patterns at 5 msec, function of the user-defined variable .....	230
Figure 6.38. Comparison of damage patterns at 150 msec, function of the user-defined variable.....	231
Figure 6.39. (a) Applied load vs. damage dissipation energy and (b) damage pattern at time of max reaction for case RT1 .....	232
Figure 6.40. (a) Applied load vs. damage dissipation energy and (b) damage pattern at time of max reaction for case RT2 .....	232
Figure 6.41. (a) Applied load vs. damage dissipation energy and (b) damage pattern at time of max reaction for case RT3 .....	233
Figure 6.42. (a) Applied load vs. damage dissipation energy and (b) damage pattern at time of max reaction for case RT4 .....	233
Figure 6.43. comparison of the damage dissipation energy in all four cases .....	234
Figure 6.44. Comparison of damage patterns at 5 msec for column with (a) beam element reinforcement and (b) truss element reinforcement, function of the user-defined variable.....	235
Figure 6.45. Comparison of damage patterns at 150 msec for column with (a) beam element reinforcement and (b) truss element reinforcement, function of the user-defined variable.....	235
Figure 6.46. Mid column displacements for different reinforcement element definitions ....	236
Figure 6.47. Reinforced concrete column (a) Finite element view and (b) cross section.....	239
Figure 6.48. Concrete material properties in (a) compression and (b) tension.....	241
Figure 6.49. Blast load time history .....	242
Figure 6.50. (a) Loading steps and (b) flowchart describing derivation.....	243
Figure 6.51. Points derived for the P-I diagram.....	245
Figure 6.52. P-I Diagram fitted curves .....	246
Figure 6.53. Points derived for the N-I diagram.....	247
Figure 6.54. N-I Diagram fitted curves.....	248
Figure 6.55. Points derived for the N-P diagram .....	249

Figure 6.56. N-P Diagram fitted curves .....	250
Figure 6.57. Analysis points in each regime .....	251
Figure 6.58. Structural response in (a) impulsive (b) dynamic and (c) quasi-static loading regimes .....	251
Figure 6.59. New P-I diagram derived for the axial force of 1229.1 kN .....	254
Figure 6.60. New PI curves and FE analyses results .....	255
Figure 6.61. Comparison of P-I curves derived with and without axial force .....	256

# Chapter 1: Introduction

## 1.1. Background

The work described in this Thesis aims at investigating numerically (via dynamic nonlinear finite element analysis) the structural response of reinforced concrete (RC) columns under blast loads. Concrete is one of the most widely used construction materials. High-rise buildings, tunnels, bridges, slab-tracks for high-speed railways, off-shore and marine structures, storage and industrial facilities as well as nuclear power-plants are fully or partially constructed from RC. As these structures are often integrated into large networks any structural integrity and performance issues can lead to disruptions across the whole network with potentially detrimental implications for economy and safety. Considering the higher construction costs associated with such structures (compared to those of more "conventional" ones) and their importance to local and national economy, it is essential that they achieve the intended level of resilience in order to sustain the action of loads (such as, for example, those generated due to collisions or explosions, natural disasters or even acts of terrorism) induced at rates significantly higher than those of the dynamic loads considered by current design codes (e.g. earthquakes, loads generated by moving vehicles or trains, wind loads).

In research, the in-depth study of RC structural response under high loading rates, often associated with blast problems, relies on the use of complex numerical or experimental methods producing data characterised by a high degree of variability and uncertainty. On the other hand, in practice resort is usually made to simplified approaches which, however, do not accurately account for important characteristics of the problem at hand thus, raising questions concerning the validity and effectiveness of the proposed design solutions. As a result, it is becoming increasingly necessary for practical structural analysis to accurately account for the effect of such loads on RC structural response in order to facilitate the development of efficient design solutions (both in terms of both safety and economy) capable of safeguarding structural integrity, resilience and performance requirements. To achieve this it is essential that a better understanding of the mechanics underlying RC structural response under blast loading is achieved and to identify (qualitatively and quantitatively) the effect of certain important design parameters (e.g. the amount and arrangement of the reinforcement,

the geometry of the specimen, the boundary conditions imposed, the level of axial loading applied) on the exhibited behaviour.

## 1.2. Research Aim and Objectives

Considering that the dynamic response of RC structural elements exhibits significant departures from that established under static loading, as certain thresholds of applied loading-rate are surpassed, the proposed work will set out to identify the main reasons that trigger these changes. The work in this thesis will numerically investigate the response of RC columns when subjected to blast loads, through the use of detailed dynamic nonlinear finite analysis (NLFEA), in order to provide insight into the mechanisms underlying RC structural response. The numerical investigation will be carried out through the use of a well-established commercial finite element package (ABAQUS) which is capable of realistically accounting for the brittleness characterising concrete material behaviour and the nature of the problem at hand: a wave propagation problem within a highly nonlinear material medium.

Specifically, the aim of this research is to further understanding of structural response of RC structures under blast loads. In particular, to develop a method for the reliable prediction of structural response and assessment of post blast structural integrity.

This will be achieved via the main objectives of this research, which are as follows:

- To overcome the shortcomings of the brittle crack model available in ABAQUS.

The brittle crack model is purpose-built for describing the behaviour of brittle materials dominated by tensile cracking. This is largely true in the case of RC flexural structural elements where cracks form within the concrete medium in the tensile region of the elements considered. Such cracks gradually extend (into the compressive region) with increasing levels of applied loading, ultimately leading to structural failure. The extended model will overcome the shortcomings of the existing model which assumes that material behaviour in compression is essentially linear elastic. Using the extended '*brittle crack model*', the behaviour of plain concrete prismatic specimens under uniaxial compression and tension will be numerically investigated in order to determine the underlying causes that trigger the experimentally observed shift in their behaviour with increasing loading rates.

- ❑ To develop finite element models of RC structural elements capable of predicting the behaviour exhibited under blast loading.

The developed numerical models, based on the finite element method, will be capable of realistically representing the RC structural configurations considered herein (beams, columns) and providing accurate predictions of the behaviour exhibited under blast loading. The numerical model will be able to realistically account for the brittle behaviour characterising concrete material behaviour and the nature of the problem at hand: a wave propagation problem with a highly nonlinear medium. The subject models will provide insight into the mechanism underlying RC structural response under blast loads.

- ❑ To employ the validated models for the assessment of the effects of specific parameters on structural response under blast loading.

The validated finite element models will be used to conduct parametric investigations in order to assess the effect of specific parameters (boundary conditions, level of axial loading, amount and arrangement of the available reinforcement) on certain important aspects of the exhibited structural response under blast loading. Such aspects include the deformation and cracking profiles exhibited throughout the loading process, the reaction force and displacement time histories, the distribution of stresses and strains at different stages of the loading process, the exhibited mode of failure, the residual stiffness and load-bearing capacity.

- ❑ To develop a method for more efficient derivation of P-I diagrams, based on building complementary diagrams.

To this end, a new graphical method for more efficient derivation of P-I diagrams, based on building complementary diagrams will be developed. This method is based on the use of validated numerical models and will account for the effect of multiple parameters. The obtained P-I diagrams will be capable of providing accurate predictions of certain important aspects of RC structural response exhibited under blast loads. The validity and practicality of the proposed methodology will be demonstrated through the comparison of its predictions with its numerically and experimentally established counterparts for a number of case studies

### **1.3. Innovative aspects of this research**

The first key innovative aspect of this work is the use of a concrete material model capable accounting for the brittle nature of concrete behaviour. The predictions of the subject model are validated for a number of problems investigating the behaviour of plain and reinforced concrete structural forms under static and high rate loading associated with impact and blast problems. An additional advantage of this extended material model is that it is defined by a small number of parameters and does not require any recalibration when used for predicting the behaviour of different structural configurations under static or dynamic loading conditions.

The second key innovative aspect is the development of a new graphical method as an efficient means for derivation of P-I diagrams accounting for the effect of up to two parameters on structural response. P-I diagrams can form the basis of a practical tool for the assessment of RC structural forms under blast loads, however, they are sensitive to any change in the state of the analysed structural system (stemming from the variation of the initial load conditions, design parameters, boundary conditions). Each time a change occurs a new P-I diagram has to be built. In this work a novel graphical method is introduced as a means to enhance the efficiency of P-I diagrams. This method is based on derivation of complementary loading/structural parameter vs. impulse and loading/structural parameter vs. pressure diagrams and allows for the derivation of new P-I diagrams from an existing one, capable of accounting for the effect of the variation of multiple parameters on certain important aspects of structural response.

The importance of this work is in furthering our understanding of the response of RC structures exhibited under blast loads. The research will provide insight into the mechanics governing the response of RC structures that will allow a deeper understanding of the influence of localised phenomena on the overall global structural response. Various parameters affecting the structural behaviour, including reinforcement ratio, boundary conditions and different reinforcement modelling approaches, will further contribute to the investigation. This will lead to more efficient blast resistant design of RC structures as well as to more reliable assessment of their safety in the aftermath of an explosive event. The graphical method developed in this work represents a powerful tool for preliminary design as well as quick assessment of multiple typical structures or structural elements exposed to extreme loads generated by explosions. An additional strength of this method is that it

provides immediate graphical information about the influence of various parameters on the response of a structure to the blast load, which is especially valuable in engineering practice. It can be easily incorporated into relevant standards and design codes and also can be suggested for educational purposes.

#### **1.4. Contents of the Thesis**

The body of the work is divided into the following chapters:

Chapter 2 provides an extensive literature review. Blast loads, the physical phenomena as well as some notable events are discussed in detail. The assumptions typically made in the blast resistant design of various types of structures are presented. Data describing the material behaviour of concrete and steel under static and high rate loading conditions are presented and discussed. The observed effects of strain-rate in different experimental setups, the results and the theories explaining the observed material behaviour are discussed. The available (experimental and numerical) methods employed for investigating the response exhibited by reinforced concrete structural configurations under blast loads, such as shock tube and drop-weight testing, nonlinear finite element analysis and alternative simplified methods employed in practice are examined alongside their limitations. The chapter concludes with the description of the structural response of reinforced concrete members under blast loads established experimentally or numerically.

Chapter 3 includes a comprehensive discussion of the P-I diagram method, a review of the existing approaches for derivation of P-I diagrams and an extensive state-of-the-art review of existing P-I curve formulae. P-I diagrams are then derived using an analytical model of an elastic beam subjected to a transverse load. Different spatial load distributions and time histories typically used in modelling of extreme and accidental loading events such as blast and impact loads are presented and discussed. The accuracy of several existing P-I curve formulae is then critically assessed using the derived P-I diagrams.

Chapter 4 focuses on the development of a new graphical method for the efficient derivation of P-I diagrams. This method is based on building complementary *loading/structural parameter vs. impulse* and *loading/structural parameter vs. pressure* graphs. An elastic beam-column subjected to a transverse pressure load and axial force is used to illustrate and benchmark the method. The derived complementary diagrams are used to demonstrate the advantages and efficiency of the proposed graphical method in both its forms.



Chapter 5 focuses on the development of finite element reinforced concrete models. The existing material models available in Abaqus and their limitations are discussed. An extension of the existing 'brittle crack material model' by use of a user defined subroutine is presented. The predictions of the proposed material model are then validated against their experimental counterparts obtained from tests conducted on plain concrete prismatic specimens subjected to uniaxial compression or tension under increasing loading rates. The latter studies provides insight into the reasons that trigger the experimentally observed change in plain concrete specimen behaviour (from that exhibited under static loading) once certain thresholds of loading rate are surpassed. The advantages of the proposed model compared to other existing concrete models built-in in Abaqus are outlined. The proposed material is then used to develop finite element models capable of realistically representing RC structural configurations and providing accurate predictions concerning the response exhibited under static and blast loading. The predictions obtained are validated against their experimental counterparts obtained from static, impact or blast tests. The results show that the extended brittle crack model is suitable for applications in a wide range of loading scenarios.

Chapter 6 utilises the findings of Chapter 5 and analyses one of the experiments validated under different conditions. The different conditions are used to gain insight into the effects of different parameters on the structural behaviour of a column under blast loads. The different parameters investigated include blast intensity, initial axial force, ratio of longitudinal and transverse reinforcement and boundary conditions. In each case the numerical analyses are presented and the results discussed. Following this, the derivation of P-I diagrams using the finite element method with the extended brittle crack material model for concrete are presented. Complementary diagrams are also built for axial force. The P-I and complementary diagrams are then used to demonstrate the new graphical method. The advantages of this method are demonstrated and discussed.

Chapter 7: This chapter discusses the main conclusions and observations drawn from this work. Topics for further research in the subject are presented and discussed.

## **Chapter 2 : Reinforced Concrete (RC) Structural Response under Blast Loads**

### **2.1. Introduction**

In this chapter an overview is presented concerning blast loads, how they are generated and their effect on RC structures accompanied by some notable cases of explosions on structures. The typical assumptions adopted by researchers and engineers when modelling blast loads are also discussed. This is followed by a detailed discussion on the effect of loading rate on the material behaviour of concrete and steel reinforcement in an attempt to elucidate the main reasons that trigger the experimentally and numerically observed shift in specimen behaviour. An overview of the methods employed in research and practice for assessing RC structural response under high loading rates are discussed and their limitations identified. On the basis of the available experimental and numerical data, this discussion is then extended to include the effect of high loading rates, often associated with blast problems, on certain important aspects of RC structural response.

### **2.2. Blast Loads**

Explosives were initially used in China during the mid-ninth century when alchemists invented gunpowder during an attempt to create an immortality potion [1]. The Chinese used gunpowder for fireworks and later on for producing rockets, guns, cannons and bombs. Following the Mongol conquest of China in the 13<sup>th</sup> century the knowledge of gunpowder was spread throughout the world. In Early Modern Europe gunpowder was used in many military and industrial applications including mining and construction of canals and tunnels. Nowadays, many different types of solid, liquid and gaseous explosives have been produced (e.g., mercury fulminate, lead azide, nitroglycerine, dynamite, TNT, RDX, ANFO, etc. [2,3]), and industry widely uses explosive energy for different applications, such as sheet-metal forming, fast coupling of composites, producing electricity, etc [2].

Although explosive devices have been used for hundreds of years, it was only during and after World War II (WWII) that comprehensive research into the effects of blast loads on structures and their mitigation began. During WWII a vast amount of data and observations were compiled, leading to tens of thousands of reports [4]. Further experience and insightful observations as to modes of failure in buildings due to explosions were gained during the

Irish Republican Army attacks [4]. The Ronan Point building collapse in London 1968 (see Figure 2.1), where a domestic gas explosion demolished a load-bearing wall causing the collapse of one entire corner of the building, led to a government commissioned enquiry and to major changes in building regulations [5].



*Figure 2.1. Ronan Point after the domestic gas explosion 1968 [6]*

Many other occurrences have been well documented and investigated such as the 1995 FBI Murrah building in Oklahoma [7] (see Figure 2.2) and the World Trade Centre in 1993 [8].



*Figure 2.2. The Murrah Building after the explosion 1995 [9]*

Industrial explosions can cause devastation on a very large scale. The most common facilities to suffer explosions are those associated with the defence, energy, food, manufacturing and mining industries [10]. Some notable cases include the 1906 Courrières mine disaster in France which is still the worst mining accident in Europe [11], the Oppau explosion in Germany 1921 (see Figure 2.3) in which a tower silo storing 4500 tonnes of ammonium nitrate fertilizer and ammonium sulfate exploded at a BASF plant [12], the Ojhri camp disaster in Pakistan in 1988 when a military storage center exploded [10] and the Seest fireworks disaster in Denmark 2004 in which a fireworks factory exploded [13]. Dust explosions, such as the 1979 German Roland Mill flour dust explosion [10] and the 2008 Georgia sugar refinery explosion in the US [14], are the most common source of explosion in the food industry.



*Figure 2.3. The Oppau Explosion 1921 [15]*

Due to its nature, the energy industry suffers a large amount of explosion disasters. These include the 1988 Piper Alpha disaster in an explosion and resulting fire on a North Sea oil production platform (see Figure 2.4) caused the world's worst offshore oil disaster [16], the Hertfordshire Oil Storage fire in 2005 in which a series of explosions at the Buncefield oil storage depot devastated the terminal and many surrounding properties [10] and the Lac-Mégantic derailment in Canada 2013 when a derailment of an oil shipment train subsequently caught fire and exploded [17].



*Figure 2.4. The Piper Alpha disaster 1988 [18]*

Additionally, in recent times there have been some explosions of nuclear facilities. The most notable and documented being the Chernobyl 1986 accident in Ukraine [19] and the Fukushima Daiichi nuclear disaster in Japan, following the Tōhoku earthquake in 2011 [19]. Apart from the immediate devastation they cause nuclear explosions still cause damage decades later due to the release of radioactive materials to the environment.



*Figure 2.5. Fukushima Daiichi nuclear disaster in Japan in 2011 [18]*

Apart from the disasters, mentioned above, a number of natural explosions have also been recorded. Most of these arise from various volcanic processes [10]. Explosions also occur as a result of impact events and in phenomena such as hydrothermal explosions also associated with volcanic processes [10].

Given the impact that explosions have on human lives and the financial implications, whether deliberate or accidental, there is a need to improve our understanding of the structural response exhibited under blast loads in order to develop innovative techniques capable of safeguarding certain required structural performance criteria for new structures and the retrofitting existing facilities.

### 2.2.1. Blast Phenomena

An explosion is characterised by a sudden release of large amounts of energy during the detonation process into a space limited to a charge size [2,3,20–24]. The detonation is a very rapid and stable chemical reaction proceeding through the explosive material with supersonic speed. As a result, the explosive material is converted into a very hot and dense high-pressure gas, which expands outwards in all directions from the explosion source with a velocity of between  $10^3$ - $10^4$  m/s creating a high intensity blast wave. The range of pressure immediately behind the shock front varies between 10-40 GPa [25]. The form (shape and intensity) of the blast wave depends on the type of explosive used and the distance from the explosion epicentre. As the blast wave propagates from the epicentre it gradually attenuates. There are two types of blast waves [20]: shock and pressure waves shown in Figure 2.6. Both types of blast waves have two distinct pressure phases: a positive phase (or overpressure) and a negative phase [26]. The positive phase is also called “compression”, while the negative phase “suction”. The characteristic feature of the shock wave is that the positive phase starts with an almost instantaneous rise in pressure to its peak value, followed by a gradual return to the ambient pressure level (see Figure 2.6a). On the other hand, the positive phase of the pressure wave has a gradual rise in pressure to the peak followed by a gradual decay (see Figure 2.6b). The shock wave is usually the result of condensed phase detonations (i.e., solid or liquid explosives) or extremely energetic vapour cloud explosions. The pressure wave is the result of vapour cloud deflagrations (subsonic explosions with slower burning process) or confined dust explosions [20–22]. Extensive data on the high energy condensed phase explosives can be found in [25], while vapour cloud explosions are discussed in [21,22,27].

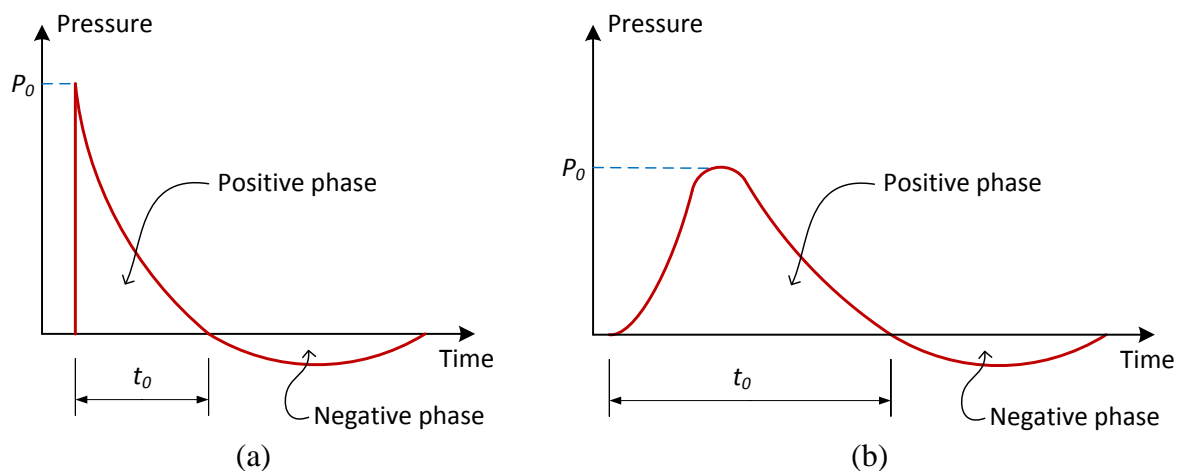


Figure 2.6. Characteristic forms of blast waves: (a) shock wave and (b) pressure wave

### 2.2.2. Blast Load Modelling

It is usual in civil engineering practice to rely on simplifying assumptions when modelling complex loading conditions. Therefore, the positive phase of the blast wave is often approximated using linear (Figure 2.7a, b), bilinear (Figure 2.7c, d, e), concave (Figure 2.7f), exponential (Figure 2.7g) or sinusoidal (Figure 2.7h) curves (e.g [20–25,25–42]).

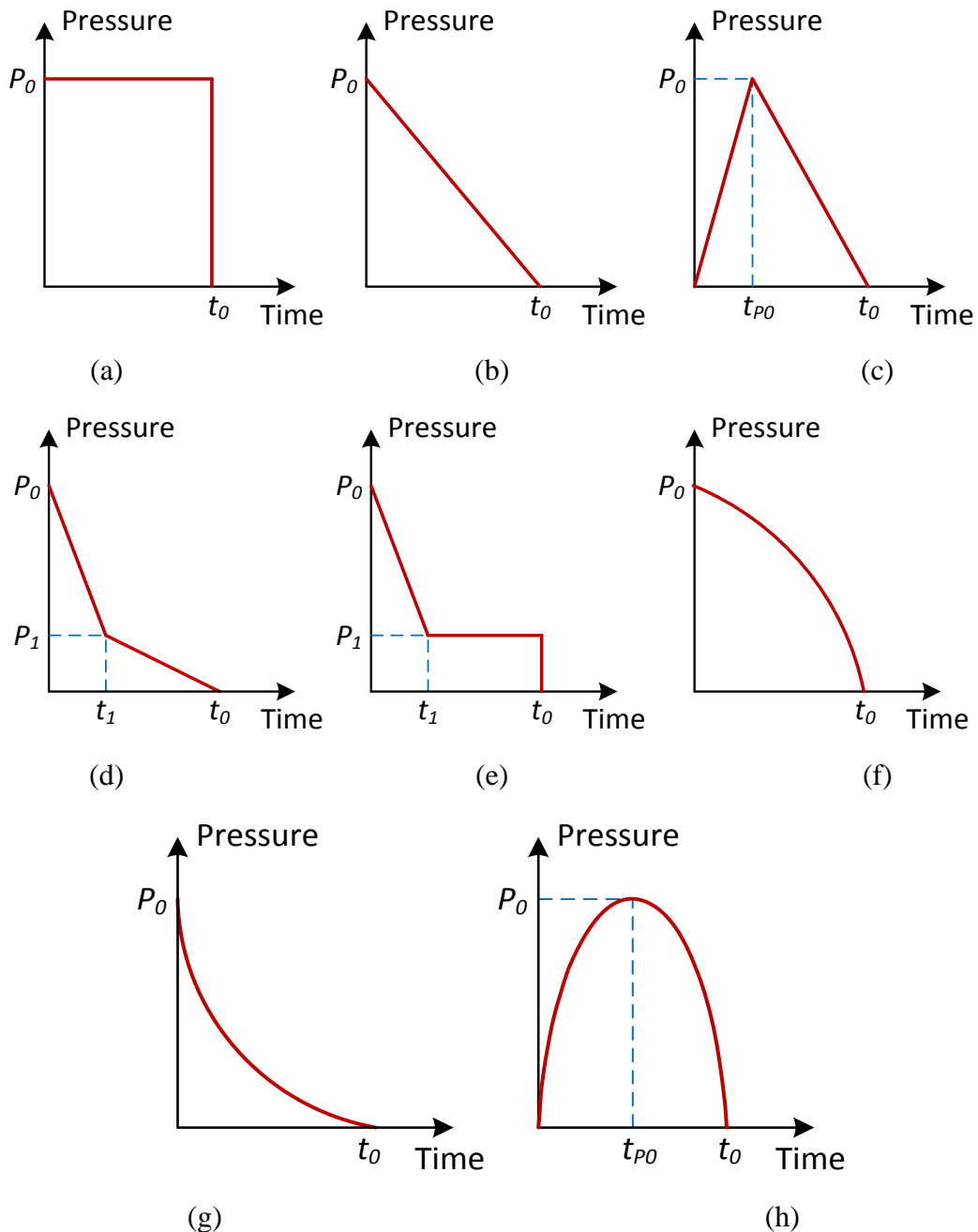


Figure 2.7. Simplified shapes for modelling of blast loads: (a) rectangular, (b) triangular, (c) triangular with finite rise time, (d) bilinear-triangular, (e) bilinear-rectangular, (f) concave, (g) exponential and (h) sinusoidal

A number of simplified shapes of the pressure time history  $P(t)$  commonly used for the modelling of extreme loads are presented in Table 2.1 [2,3,24–28,30,32–52].

Load time history	$P(t)/P(0)$
Rectangular (Fig. 2a)	$\begin{cases} 1 & 0 \leq t \leq t_0 \\ 0 & t > t_0 \end{cases}$
Triangular (Fig. 2b)	$\begin{cases} (t_0 - t)/t_0 & 0 \leq t \leq t_0 \\ 0 & t > t_0 \end{cases}$
Triangular with finite rise time $t_{p0}$ (Fig. 2c)	$\begin{cases} t/t_{p0} & 0 \leq t \leq t_{p0} \\ (t_0 - t)/(t_0 - t_{p0}) & t_{p0} \leq t \leq t_0 \\ 0 & t > t_0 \end{cases}$
Bilinear-triangular with the curve break at $t_1$ (Fig. 2d) $C_r$ is the load reduction factor	$\begin{cases} ((C_r - 1)t + t_1)/t_1 & 0 \leq t \leq t_1 \\ C_r(t_0 - t)/(t_0 - t_1) & t_1 \leq t \leq t_0 \\ 0 & t > t_0 \end{cases}$
Bilinear-rectangular with the curve break at $t_1$ (Fig. 2e) $C_r$ is the load reduction factor	$\begin{cases} ((C_r - 1)t + t_1)/t_1 & 0 \leq t \leq t_1 \\ C_r & t_1 \leq t \leq t_0 \\ 0 & t > t_0 \end{cases}$
Concave (Fig. 2f) $C_n$ is the load fitting constant	$\begin{cases} \exp[C_n t/t_0] (t_0 - t)/t_0 & 0 \leq t \leq t_0 \\ 0 & t > t_0 \end{cases}$
Exponential (Fig. 2g) $C_x$ is the load fitting constant	$\begin{cases} \exp[-C_x t/t_0] (t_0 - t)/t_0 & 0 \leq t \leq t_0 \\ 0 & t > t_0 \end{cases}$
Sinusoidal (Fig. 2h)	$\begin{cases} \sin(\pi t/t_0) & 0 \leq t \leq t_0 \\ 0 & t > t_0 \end{cases}$

Table 2.1. Types of load time history used for modelling of blast loads

An appropriate choice of  $P(t)$  depends on the type of the event. For example, the triangular shape with zero rise time (Figure 2.6b) is recommended for modelling shock waves [20], while the triangular shape with a finite rise time (Figure 2.6c) for modelling pressure waves. According to UFC 3-340-02 [25] and Dragos et al [52–55], the bilinear-triangular and bilinear-rectangular shapes (Figure 2.6d and Figure 2.6e) are suitable for modelling confined explosions that may occur in tunnels, subway stations and car parks, inside bunkers and buildings with strong walls, etc. In particular, the bilinear-triangular shape is suitable for modelling confined explosions in vented spaces, whereas the bilinear-rectangular shape in unvented spaces. Technical manuals for blast resistant design [25–27,43] recommend use of a bilinear shape with zero rise time (Figure 2.6d) for modelling external blast loads on the walls



facing the explosion source, while the triangular shape with finite rise time (Figure 2.6c) for modelling blast loads on the side and rear walls and roofs. The negative phase of the blast wave is usually neglected in the analysis and design of blast resistant structural elements since it is much weaker and more gradual. Detailed guidelines for the characterisation and treatment of the negative phase of the blast wave are given in [25], mainly that the effects of the negative phase parameters are usually not important for the design of the more rigid type structures such as reinforced concrete.

The primary parameters describing the form of the blast wave are the peak pressure  $P_0$ , impulse  $I$  and duration  $t_0$ , as presented in Figure 2.6a. In addition, there are also a number of secondary parameters, which can be determined based on the primary ones, such as the peak reflected pressure  $P_{0R}$ , peak dynamic (or blast wind) pressure  $P_{0W}$ , shock/pressure front velocity  $U_{S/P}$  and blast wave length  $L_{BW}$  [2,3,20–22,24,25,54].

When a blast wave generated by an air explosion reaches a surface it is reflected amplifying the incident blast wave, see Figure 2.8.

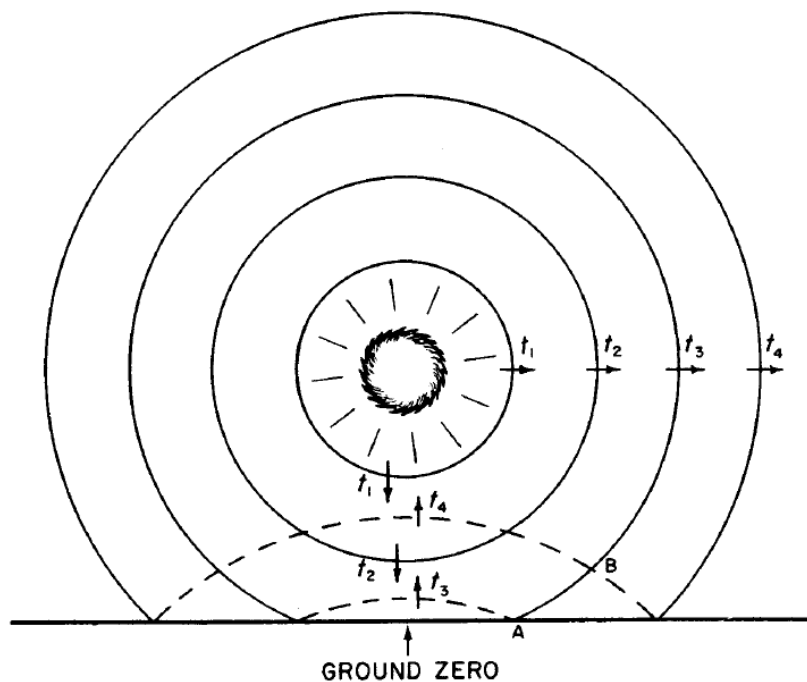


Figure 2.8. Reflection of blast wave at the earth's surface in an air blast;  $t_1$  to  $t_4$  represent successive times [26]

The magnitude of  $P_{0R}$  is determined as:

$$P_{0R} = C_R P_0 \quad (2.1)$$

where  $C_R$  is the reflection coefficient depending on the pressure  $P_0$ , the type of blast wave and the angle of incidence of the blast wave front relative to the surface [54]. When multiple reflections occur, as in the case of a confined explosion, the peak pressure of the blast wave may grow extremely high [25] and secondary peaks corresponding to the number of reflections develop in the pressure time history [21,22].

A propagating blast wave generates strong wind, especially in the positive phase [26]. This wind exerts dynamic drag pressure on the structure. The peak drag pressure  $P_{0D}$  is evaluated as [20,24,25,54].

$$P_{0D} = C_D P_{0W} \quad (2.2)$$

where  $C_D$  is the drag coefficient depending on the Mach number (or Reynold's number at low incident pressures) and the relative geometry of the structure.  $C_D$  for the roof and walls is in the range of 0.2-0.4 depending on  $P_{0W}$  [24]. For open frame civil and industrial structures including masts, pylons, lattice towers, truss bridges, etc. the dynamic pressure represents the dominant blast effect.

The reduction factor  $C_r$  incorporated in the bilinear relationships in Table 2.1 defines the initial amplification of the pressure due to its reflection during a confined explosion [52,53,56,57]. In this case  $C_r$  can be found as

$$C_r = P_g/P_{0R} \quad (2.3)$$

where  $P_g$  ( $\equiv P_1$  in Figure 2.6d and Figure 2.6e) and  $P_{0R}$  ( $\equiv P_0$ ) are the peak gas and reflected pressure, respectively. When the bilinear curve with zero rise time (Figure 2.6d) is used for modelling the blast loading on the front walls in a reflected region [20,24,25],  $C_r$  can be found as

$$C_r = (P_{0E}/P_{0R})(t_0 - t_1)/t_0 \quad (2.4)$$

where  $P_{0E}$  ( $= P_0 + P_{0D}$ ) is the effective non-reflected peak pressure, and  $t_1$  represents the duration of the reflected pressure.  $t_1$  is formulated in [25] depending on the structural geometry (width and height) and the velocity of sound. The side and rear walls and the roof will experience smaller blast pressure due to lack of reflected pressure and a larger distance from the explosion epicentre [20,24,25].

The effective peak pressure  $P_{0E}$  on the side/rear walls and roof can be found as

$$P_{0E} = C_E P_0 + P_D \quad (2.5)$$

where  $C_E$  is the effective reduction factor depending on the ratio between the blast wave length and the length of the structural element in the direction of the traveling blast wave [25]. Since the rear wall load is opposite in its direction to the front wall load, it is used only for evaluation of the net overall loading on a structure and often ignored in the analysis [20].

The concave and exponential relationships given in Table 2.1 include the constants  $C_n$  and  $C_x$ , respectively. These constants allow further fitting of the shapes of the modelled load time histories to the recorded data, which leads to the increase in the accuracy of the analysis. In a number of research studies the following values of the constants were used:  $C_n = 1$  in [48] and  $C_x = 2.8$  in [39,40,48].

As the blast wave propagates in the air with supersonic velocities the evaluation of the shock/pressure front velocity  $U_{S/P}$  and the blast wave length  $L_{BW}$  is extremely complicated. Therefore, there are only limited data describing  $U_{S/P}$  available in the technical literature. The technical manual, TM 5-1300 [25], for instance, provides plots of the shock front velocity  $U_S$  vs. scaled distance for high energy TNT explosives only. Other manuals (e.g., [20]) recommend to conservatively assume that the pressure front velocity  $U_P \approx U_S$ . According to [54],  $U_{S/P}$  (in m/s) can be approximately found for a low pressure air explosion in normal atmospheric conditions as

$$U_{S/P} = 345(1 + 0.0083P_0)^{0.5} \quad (2.6)$$

In similar conditions, TM 5-1300 [25] recommends to approximate  $L_{BW}$  as

$$L_{BW} = U_{S/P} t_0 \quad (2.7)$$

It is important to note that there is much more certainty in correct evaluation of the parameters of blast loads generated by standardised types of explosives (e.g., TNT, RDX or ANFO). The parameters of accidental industrial explosions, which are most often vapour cloud explosions, will strongly depend on the potentially explosive materials handled and the manufacturing processes applied [20]. The wide variety of the industrial materials and processes combined with the shortage of codes and industrial standards seriously complicate the situation.

### 2.3. Concrete Material Behaviour

Concrete is one of the most widely used construction materials and is commonly used for the construction of buildings, highways, bridges, bunkers and nuclear reactors. Concrete is a composite material consisting of aggregates (sand and stone) and rehydrated cement. Its major advantages are that it is durable, economical and can easily be cast into any shape. The primary advantage of concrete is in its compressive strength, however, despite having relatively high compressive strength, concrete's tensile strength is significantly lower (about 10% of its compressive strength). The practical implication of this is that concrete elements subjected to tensile stresses must be reinforced with materials that are strong in tension, such as steel or fibre reinforced polymers (FRP). Additionally, concrete is essentially a brittle material, and has a low strength-to-weight ratio. Actual concrete properties can vary widely depending on the choice of materials used, their proportion and manufacturing process adopted [58].

Structural behaviour under different loads highly depends on the stress-strain relationship expressing the material behaviour and the type of load the structure is subjected to. Under static loading such curves are obtained by measuring strain in cylinder tests under increasing levels of loading [59]. Although the constituents of concrete (namely aggregates and cement) are brittle elastic materials, the stress-strain curve describing the behaviour of concrete in compression is nonlinear [60]. This is attributed to internal microcracks that form and extend within the concrete medium and the ensuing. Figure 2.9 shows typical compressive stress-strain curves for concrete with different peak compressive stresses.

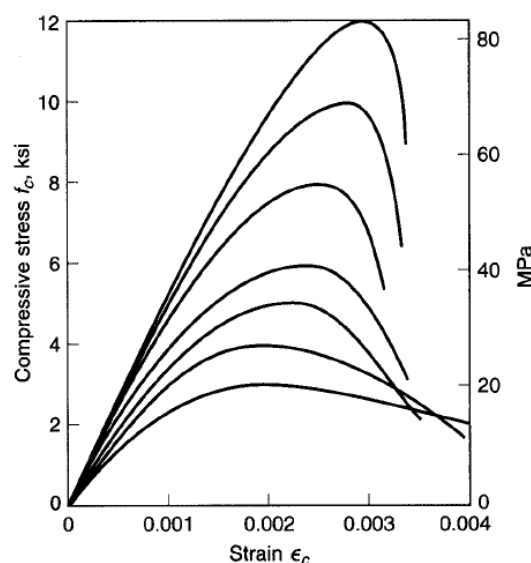
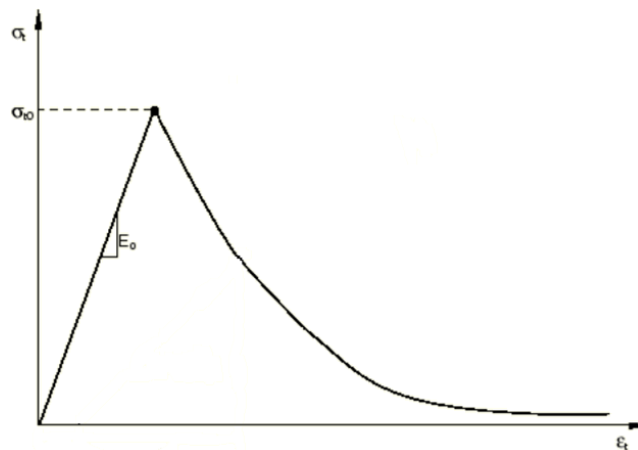


Figure 2.9. Typical compressive stress-strain curves for normal density concrete.[59]

All the curves are comprised of an initial elastic part for values of stress approximately equal to 40% of the maximum peak compressive stress followed by a nonlinear portion up to the maximum peak stress (compressive strength) at strains between 0.002 and 0.003 followed by a descending branch. It is important to note that the characteristics of the descending curve are highly dependent on the test procedure and on specimen boundary conditions [59]. The experimental results may, therefore, express the interaction between the specimen and the setup rather than the material properties.

The direct tensile strength of concrete is only about 7 to 15 percent of its compressive strength. The behaviour of concrete in tension is described by the stress-strain curve is presented in Figure 2.10. Concrete tensile strength increases with an increase in compressive strength. However, as shown in Figure 2.11, the ratio of tensile to compressive strength decreases with the increase in compressive strength [60].



*Figure 2.10. Concrete behaviour in tension[61]*

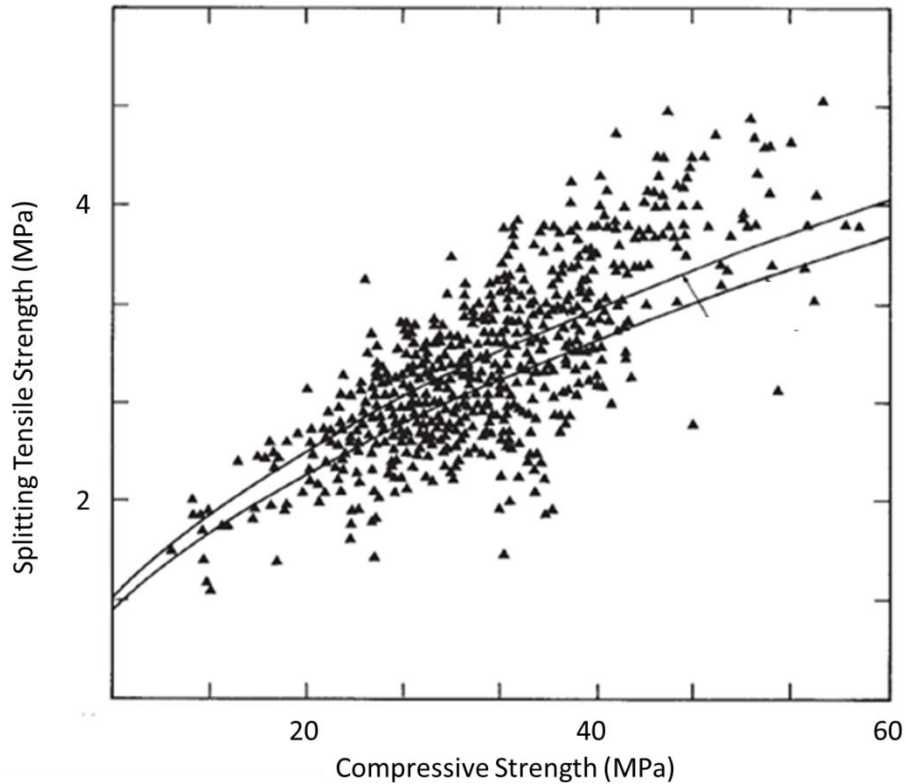


Figure 2.11. Relationship between splitting tensile strengths and compression strengths [60]

Under biaxial loading conditions the strength and failure mode in concrete varies as a function of the combination of the loading stresses, as shown in Figure 2.12. The curve in Figure 2.12a describes the behaviour of concrete under biaxial stresses  $\sigma_1$  and  $\sigma_2$ .  $A$  and  $A'$  are the uniaxial compressive strength, whereas  $B$  and  $B'$  represent the uniaxial tensile strength. If concrete is subjected to biaxial tension (zone 1) the strength is close to the uniaxial tension stress and failure is due to tensile fracture perpendicular to the maximum principle tensile stress as shown in Figure 2.12b. When one of the loading stresses is in compression and the other in tension then the concrete cracks at a lower stress than either of the uniaxial stresses (zone 2). In this case failure occurs due to tensile fracture on planes that are perpendicular to the principle tensile stresses. The lower strengths suggest that failure is governed by limiting tensile strain [60]. In uniaxial compression (zone 3) the failure is due to tensile cracks on the planes of maximum principle tensile strain, which are parallel to the maximum compressive stresses. In biaxial compression (zone 4) the failure pattern changes to parallel fracture surfaces parallel to the unloaded side of the member, as shown in Figure 2.12d. In this case the concrete ductility increases and the concrete compressive strength increases past the uniaxial compressive strength.

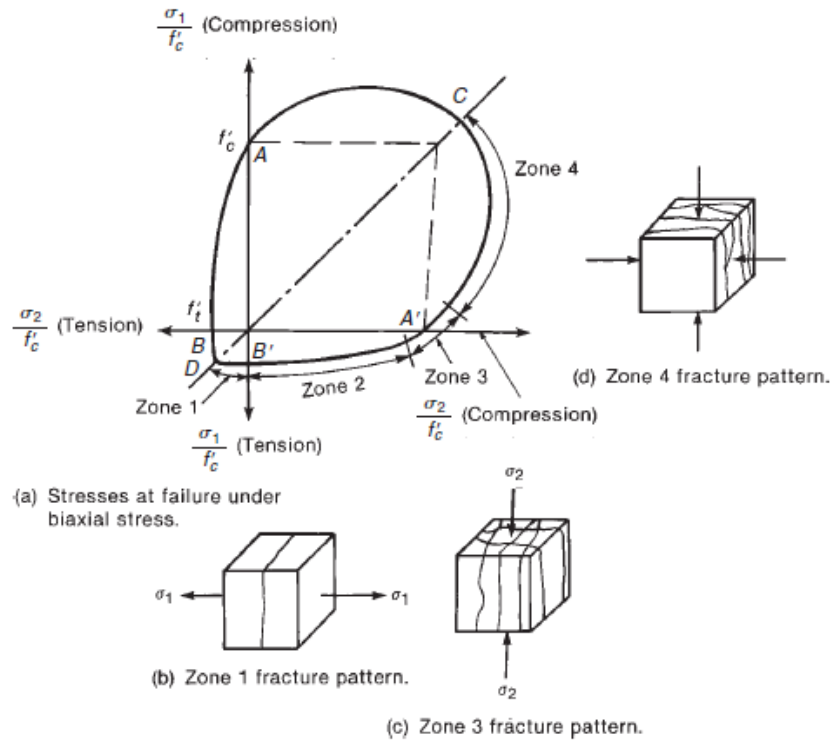


Figure 2.12. Strength and modes of failure on biaxially loaded concrete[60]

Generally, however, concrete in a structure will be subjected to a multi axial stress state. The type of failure under these conditions has been studied using confined concrete cylinders subjected to axial compression  $\sigma_a$  [62,63]. The experiments were conducted so as to achieve stress states of triaxial compression by increasing the axial compression ( $\sigma_a > \sigma_c$  where  $\sigma_c$  is the lateral confining pressure) or triaxial extension by decreasing the axial compression ( $0 < \sigma_a < \sigma_c$ ). The stress-strain relationships obtained, Figure 2.13, indicate that under triaxial compression concrete exhibits gradual reduction in load carrying capacity post the ultimate stress whilst the triaxial tension models suffered an immediate loss of load carrying capacity. These findings [64] suggest that an unrestrained concrete component under compressive stress conditions would suffer a complete loss of load-carrying capacity on reaching its maximum strength. Therefore, it can be assumed that brittle failure is a characteristic of concrete behaviour at a material level under any state of three-dimensional compression.

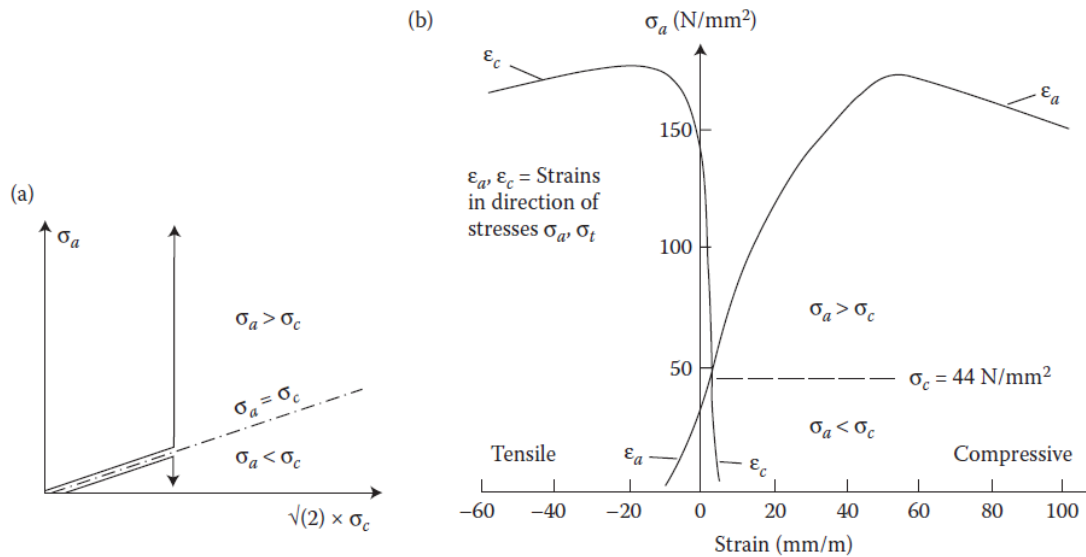


Figure 2.13. Triaxial compression tests on cylinders (a) stress paths used (b) typical stress-strain relationships [64]

The cause of nonlinear behaviour exhibited by concrete up to fracture and failure is generally deemed to be attributed to pre-existing flaws in the concrete material [64]. These are mainly attributed to discontinuities in the cement paste matrix, pores caused by shrinkage or thermal movements due to incompatibility between the properties of the various phases present in concrete, discontinuities at the boundary between the aggregate particles and voids present as a result of incomplete compaction. Due to the nature of these flaws they can be assumed to be randomly distributed and orientated.

When stress and strain are applied at the element boundary a strain field, dependant on the distribution of the different concrete components and flaws is generated [64]. Strain concentrations are intensified to far higher orders of magnitude due to the presence of flaws, particularly those with high aspect ratios and it is these flaws which are the potential sources of any load-induced cracking.

Due to its low tensile strength concrete is often reinforced with steel to form a composite material. The ACI Code requires that reinforcement be steel bars or steel wires [65].



### 2.3.1. Effect of Loading Rate on Concrete Material Behaviour

The effect of the speed of loading on concrete behaviour is very distinct on the stress-strain curves in compression. In Figure 2.14 the stress-strain curves of the same concrete loaded with different loading speeds are presented. It can be seen that the descending branch of the curves is more pronounced at the faster rates, indicating the further internal cracking [60]. It is also shown that the maximum compressive strengths recorded are higher at higher loading speeds.

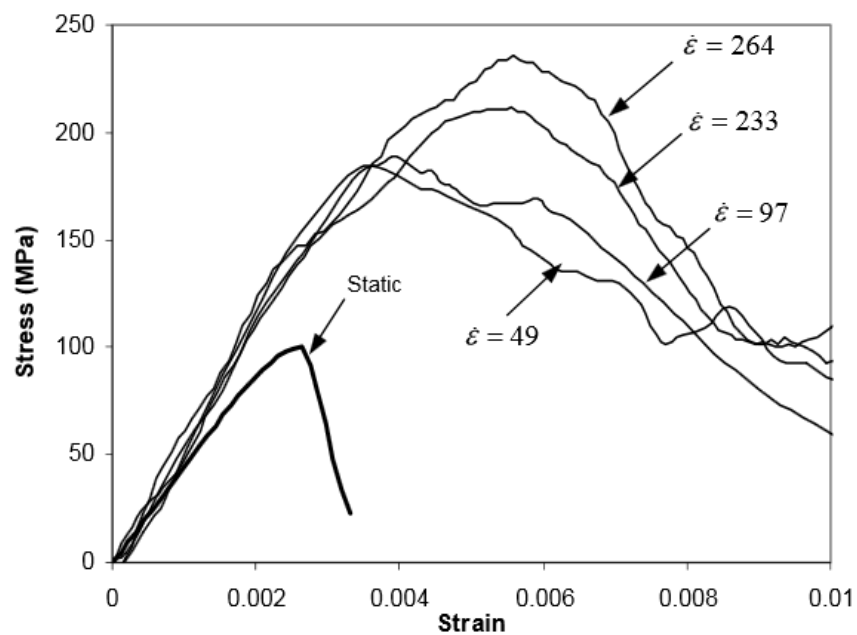


Figure 2.14. Stress-strain curves in compression at various strain rates [66]

This observed behaviour of concrete under high strain rates has been the subject of much interest. Abram was the first researcher to observe rate sensitivity in the compressive strength of concrete [67]. Since then, a large number of experiments dealing with the behaviour of cylindrical and prismatic concrete specimens have been carried out, the main objective being to investigate concrete behaviour under extreme loading conditions. Continuous improvements in experiments, equipment and techniques have led to the achievement of better results and understanding of the phenomena in recent decades.

The use of split Hopkinson pressure bars (SHPB), shown in Figure 2.15, to study dynamic behaviour of materials was utilised by Kolsky [68].

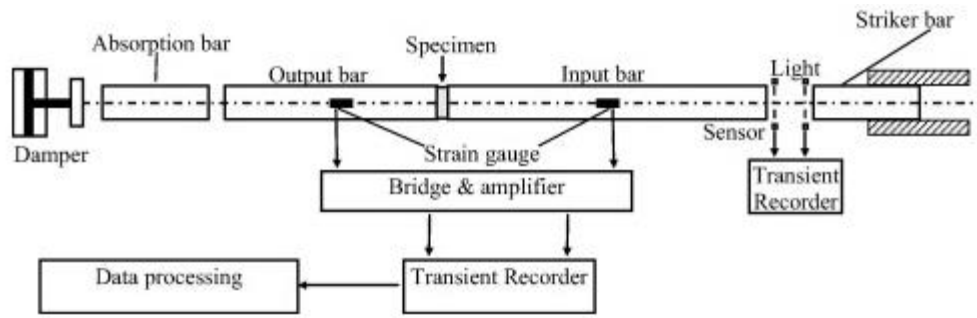


Figure 2.15. Schematic representation of the SHPB test in compression [69]

SHPB experiments studying the rate dependency of concrete behaviour were recently conducted by Al-Salloum et al [69]. They conducted a series of experiments of solid and annular cylindrical cement mortar specimens with different aspect ratios and quasi-static compressive strengths using the SHPB, as shown in Figure 2.16.



Figure 2.16. SHPB test setup, and specimens [69]

They found an obvious increase in the compressive stress of the concrete specimens when subjected to higher strain rates, as shown in Figure 2.17. The mode of failure of concrete observed was ductile failure at high strain-rates and brittle at low strain-rates.

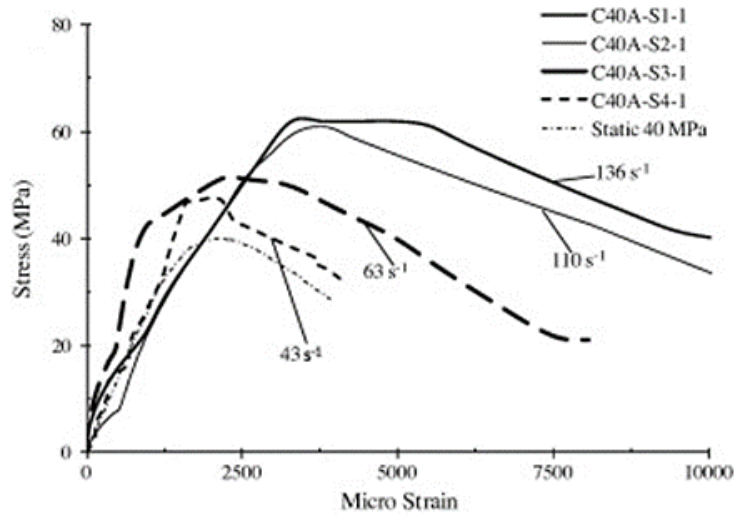


Figure 2.17. Stress–strain curves of 40 MPa concrete solid specimen, as shown in Figure 2.16 [69]

Hughes and Gregory [70] used drop weight tests to measure concrete compressive strength at high loading rates. Yan et al [71] studied the biaxial behaviour of plain concrete subjected to dynamic compression with constant lateral stress on a custom designed hydraulic controlled machine, shown in Figure 2.18. Their aim was to characterise the biaxial compressive behaviour of concrete under a rapidly applied axial load with constant confining pressure, and to validate existing strength prediction equations extrapolated from uniaxial test data. The importance of these experiments was that although a number of other studies dealing with the dynamic properties of concrete the majority of them were conducted in a uniaxial stress state. This does not represent the multi-axial stress condition of concrete in RC structures due to complex loadings and the confinement of transverse reinforcement. They analysed over 60 concrete cubes and found that the ultimate strength of concrete under axial and lateral loads increases with strain rate. Yan et al also found that the stress-strain curves at various strain rates were similar in shape, with a significant increase in tangent modulus in the non-linear range of the curves.

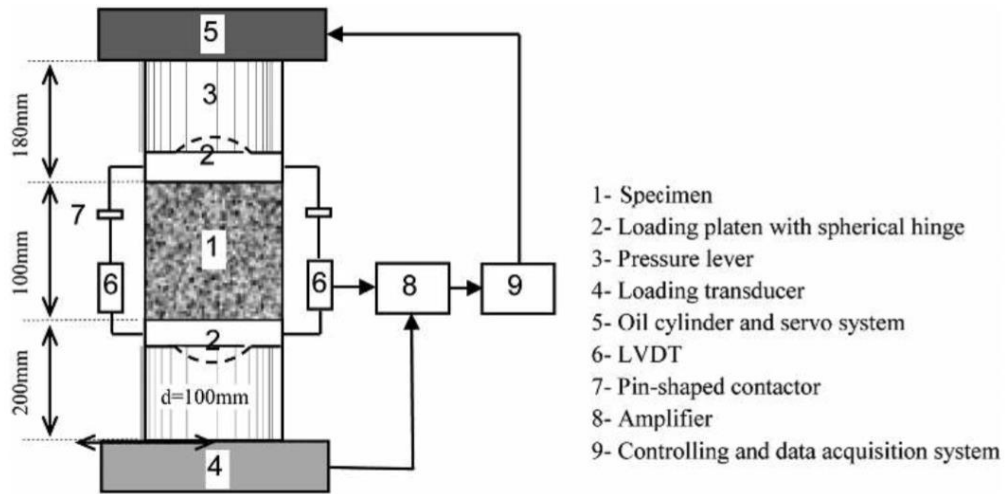


Figure 2.18. Yan et al testing system [71]

Chen et al [72] examined the flexural behaviour of large concrete specimens using the 4 point bending test under different strain rates. Their results show that the increase in strain rate led to the specimens having a more flattened fracture surfaces and more broken aggregates on the fractured surface, as shown in Figure 2.19. They correlated the elastic modulus and flexural strength of the concrete to the strain rate. In a different paper Chen et al [73] proceed to use the 4 point bending test and a direct tension test to examine the effect of testing method and strain rate on stress-strain behaviour of concrete. Their results confirm that the peak stresses increase with an increase in the strain rate. It is also observed that this effect is more pronounced in direct tensile specimens. In both testing methods under the same strain rate the fractured surfaces become more flattened with increasing strain rate.

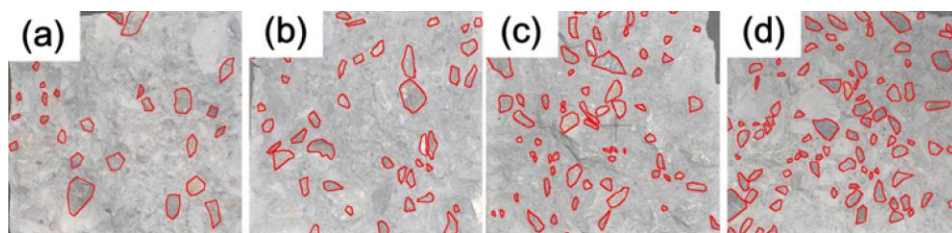


Figure 2.19. Failure surface of concrete beams at different strain rates (a)  $10^{-6}/s$ , (b)  $10^{-5}/s$ , (c)  $10^{-4}/s$  and (d)  $10^{-3}/s$  [72]

Brara and Klepaczkob conducted tensile tests on cylindrical concrete specimens at different strain rates from  $10 \text{ s}^{-1}$  to  $120 \text{ s}^{-1}$  [74]. The technique used in their experiments combines the principles of wave propagation in a Hopkinson bar and phenomenon of spalling, presented in Figure 2.20. The setup consists of the gas launcher, the striker, one Hopkinson bar and a cylindrical specimen. The striker impacts the Hopkinson bar and the incident compression

wave is directly transmitted into cylindrical specimen being in contact with the bar. The incident wave is reflected in the specimen as tensile wave triggering spall.

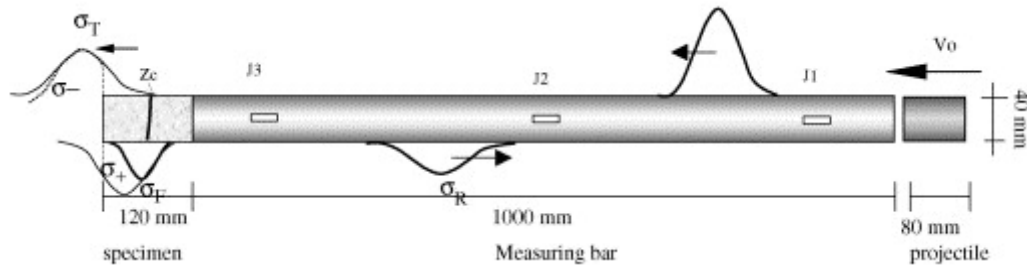


Figure 2.20. Schematic test setup [74]

The specimens used in the experiment were produced using micro-concrete MB50 with a very uniform distribution of aggregates resulting in very heterogeneous specimen in relation to its dimensions. The tests conducted for both wet and dry micro-concretes at high strain rates clearly demonstrate close relation between the critical time to failure and tensile strength, as shown in Figure 2.21. As shown, the shorter the loading time the higher the concrete strength.

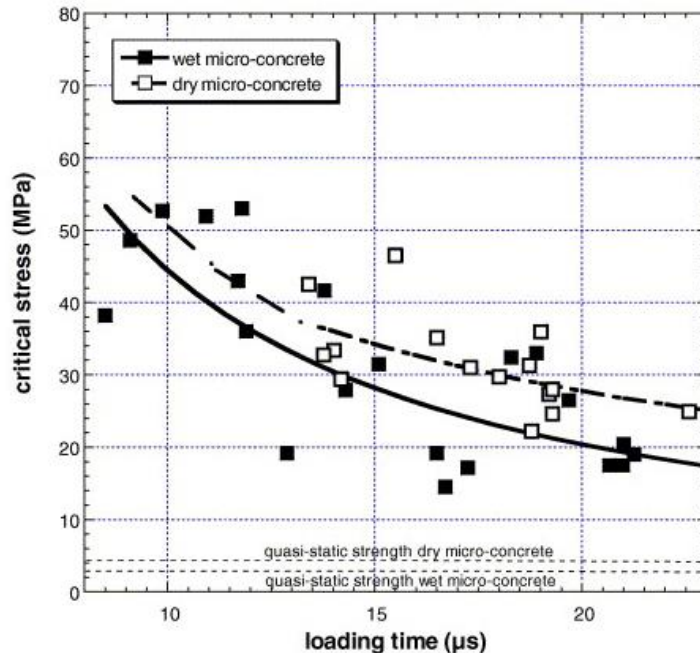


Figure 2.21. Changes of tensile strength for wet and dry micro-concrete as a function of critical time to failure [74]

Erzar and Forquin [75] investigated the dynamic tensile strength of concrete by means of spalling tests. The experimental device used for the present spalling tests, as shown in Figure

2.22. The setup consists of a projectile, a Hopkinson bar and a concrete specimen, similar to the previous experiment discussed. The observations revealed that an enhanced uniformity of the strain rate was obtained for positive stresses in the range of 10 to 20 MPa in which the dynamic strength is observed and that at high strain-rate failure is the consequence of numerous oriented cracks.

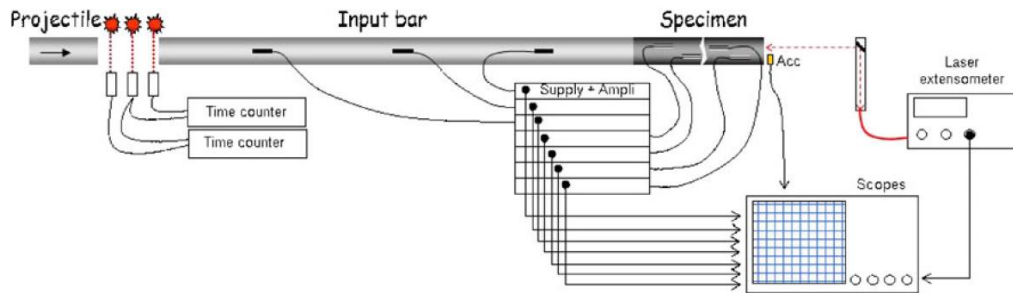


Figure 2.22. Experimental device (projectile, input bar, specimen) and instrumentation (light sources, photo-diodes, strain gauges, accelerometer, and laser extensometer) [75]

More recently, with the emergence of new non-destructive techniques such as acoustic emission (AE), new types of experimental studies have been carried out. Sagar and Rao [77] studied the effect of loading rate in tension on the fracture process in RC structures. They observed that the faster the loading rate the quicker cracks propagate. They also found that concrete behaviour is relatively more brittle at higher strain rates. The authors do point out, however, that AE released during fracture process in real scale components is a relatively new field and still needs refinement.

In conclusion the responses exhibited during dynamic tests have been shown to differ from those carried out with static conditions. The difference is mainly the increase of the specimens load carrying capability and maximum sustained axial strength. The difference becomes more apparent with the increase of the loading rate. However, apart from that qualitative statement it must be noted that the experimental data is characterised by considerable scatter, both in compression and in tension [78,79], as presented in Figure 2.23 and Figure 2.24. Additionally, many parameters vary between the different experiments, such as technique, shape, size, moisture content, type of concrete used. There is also a basic difficulty in interpreting experimental data from dynamic tests due to their short duration [78]. Therefore, the experimental data can only describe the qualitative behaviour of concrete under increased loading rates.

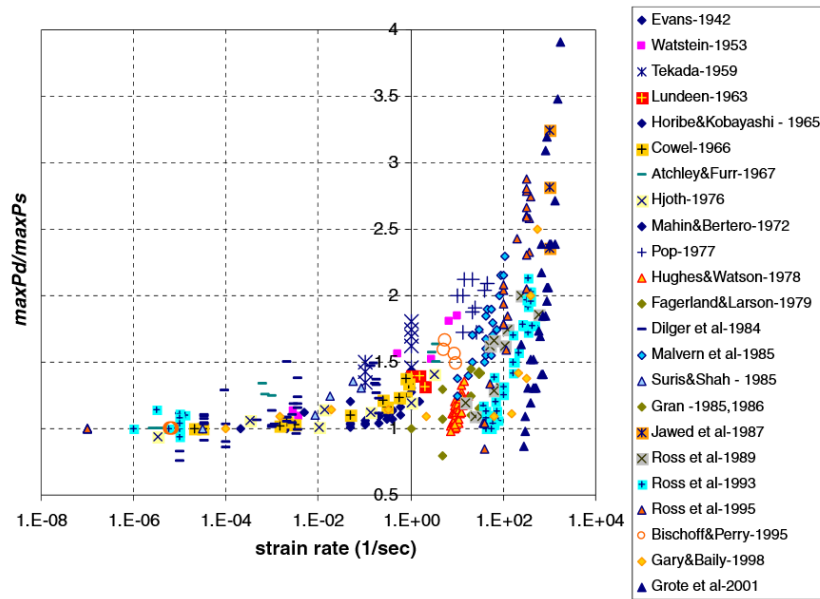


Figure 2.23. Variation of load-carrying capacity with strain rate for concrete in uniaxial compression ( $maxPd$ =dynamic load carrying capacity,  $maxPs$ =load carrying capacity under static loading) [78]

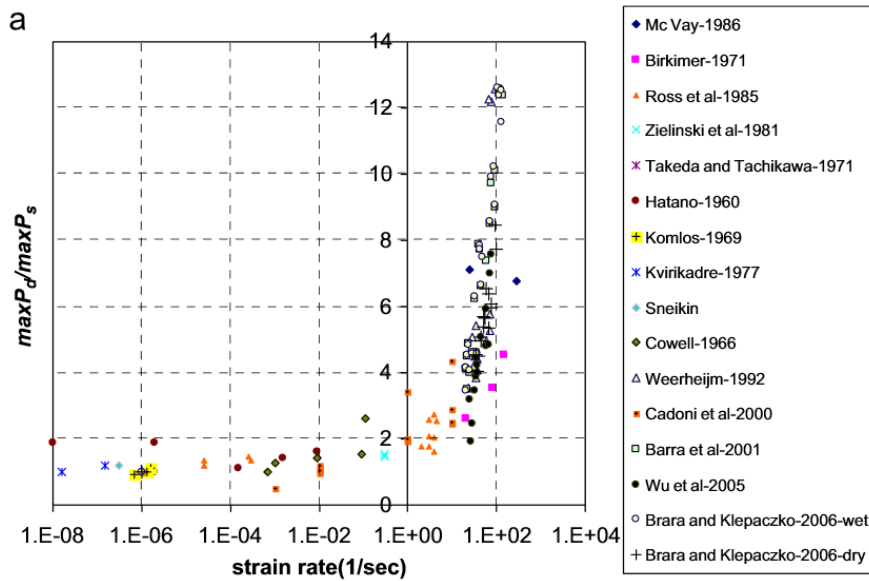


Figure 2.24. Variation of load-carrying capacity with strain rate for concrete in uniaxial tension ( $maxPd$ =load carrying capacity,  $maxPs$ =load carrying capacity under static loading) [79]

Although the qualitative observations, namely the increase of strength with the increase in the speed of loading, is generally accepted the explanations to the phenomena are not. The central questions are whether the strength enhancement of concrete with strain-rate is a

genuine material property and what the causes of this phenomenon are. Currently, only a few researchers have dealt with these questions [80].

Bischoff and Perry [81] argued that the observed rate enhancement of concrete in compression might be due to a number of factors. The results might be influenced by the testing procedure due to equipment, testing techniques, boundary effects and specimen size (which is relatively short) and lateral inertial effect. Additionally, the results could be influenced by the specimens' material makeup, specifically concrete static compressive strength, aggregate grade, curing and moisture condition and age. Ožbolt et al [82] further stress that capturing the uni-axial tensile behaviour of concrete experimentally is difficult even under static load. For that reason, under dynamic loads the problem is often studied through indirect tests such as SHPB. In the SHPB the measurement of concrete strength is based on the theory of uni-axial wave propagation through elastic media and measurements of strain and strain rates in the bar. Though this setup is widely used for determining the dynamic compressive and tensile strength for concrete, there are still uncertainties in the reliability of such test for concrete materials. Wu et al. [83] commented that the SHPB results are reliable only for ductile materials such as metals, whereas the results may contain significant errors when measurements are made using SHPB on concrete-like materials, mainly caused by the required high rigidity of experimental set up due to the low dynamic tensile strength of concrete. Additionally, they note that the brittle nature of concrete increases difficulty with data processing and experiment repetition and that there are problems ensuring good connections between the concrete specimen and the pressure bar. Ožbolt et al [82] point out that no rate sensitivity can be observed in linear elastic materials or within the linear elastic range, while significant influence is observed in materials that exhibit damage and fracture behaviour, such as concrete. They believe that this indicates that rate sensitivity is closely related to damage and softening of the material, i.e. more damage, the stronger will be the influence of loading rate on structural response and back this theory by experimental results that show concrete-like materials exhibit the highest rate sensitivity whereas brittle materials, such as glass, are much less sensitive to the strain rate.

Several researchers have claimed that under strain rates of  $1/s$  the strength enhancement of concrete is due to free water within the material, otherwise known as Stefan effect [84–86]. Rossi et al [84] argued that the presence of pore water in the concrete contributed to the strain rate effect. Others have claimed that at strain rates over  $10/s$  the observed enhancement is due to inertial effects in the loaded specimen [69,78,80,87,88]. When subjected to dynamic loads



the body is under dynamic equilibrium and the applied load is balanced by transmitted reactions and also by inertial forces [82]. Until a certain strain rate the inertial contribution is small and the loads are roughly equal to the reactions, though higher than the results of a static analysis. Once the critical strain rate threshold is passed the impact of the inertial forces becomes more prominent and the applied load becomes higher than the reaction. This effect, the influence of inertia, increases with the increase of loading rate and is not a material property [82]. Therefore, during a dynamic experiment the measured applied load does not provide the true strength of the material as there is an inherent inertial component. This conclusion was further stressed by Al-Salloum et al [69]. Their research of solid and annular cylindrical cement mortar specimens using SHPB concluded that the dynamic increase factor (DIF) of annular specimen was lower than the DIF of solid specimens at high strain-rates. This phenomenon further strengthens the view that the lateral inertia plays an important role in a rapid increase in the DIF at high strain rates. Li and Meng [87] also investigated the dynamic compressive strength of concrete and reported that beyond the strain rate of 100/s the apparent dynamic strength enhancement is strongly influenced by the hydrostatic stress effect due to the lateral inertia confinement in an SHPB test. They warned that the dynamic strength enhancement, incorrectly interpreted as strain rate effect, had been adopted in dynamic structural design in concrete, leading to over prediction of the dynamic strength of concrete. They strongly recommended further experimental and numerical research in order to fully understand the effects of strain rate.

### **2.3.2. Material Models Describing Concrete Behaviour under High Loading Rates**

It should be noted that in the case of blast loads strain rates are typically in the range of  $10^2$  to  $10^4 \text{ s}^{-1}$  [23]. In existing codes (such as [25,89]) strain rate is modelled by multiplying the stresses using a single DIF. However research has shown that this approach can predict unrealistic results resulting in a structure that is stronger than observed structural behaviour [90].

Recent years have seen great advancement in computational capabilities. It is possible to perform numerical simulations of concrete structures under severe shock and impact loads [91]. Simulations can further enhance experiments by reducing experimental costs and can provide additional insight regarding the material response [80]. However, as in all cases when

relying on analysis results, a thorough validation process is vital. An accurately representative material model capable of capturing the essential mechanical processes of the material under varying stress and loading rates is vital in order to successfully simulate structural response.

In an attempt to provide a fundamental explanation for the sudden increase in concrete strength Cotsovos and Pavlovic' [78] developed a finite element model to reproduce experimental data. As the material properties of the concrete were assumed to be independent of the loading rate, the effect of the loading rate on the specimen was primarily attributed to the inertia effect of the specimen mass. The concrete material model considered was brittle and independent of both stress paths and loading rate effects. The analysis was performed using a finite element 3D model of a concrete specimen. The results showed that the behaviour of concrete specimens under high rates of compressive uniaxial loading was considerably different to the behaviour under static loading. The load carrying capacity and sustained maximum axial strain exhibited by the specimen increases as the rate of loading becomes higher. One of the conclusions of the analysis is that inertia has a significant effect on the specimens' behaviour under high rates of loading. Another interesting point observed was that of the progression of the stress waves in the specimen. For high load rates (loading procedure less than 0.0001 seconds) the specimen failure preceded substantial reactions at the bottom as the stress wave was unable to reach the bottom within the time of the loading procedure. Therefore in such cases the external load does not affect the whole specimen extending to a level which the stress wave is able to reach within the loading time. On the other hand, when the loading rate is lower the stress wave bounces off the bottom of the specimen and starts to travel back and forth along the length of the specimen, trapped by the boundary conditions. In such cases it is difficult to predict where the highest concentrations of stresses will develop as the internal stress field constantly changes. Comparing the simulations to the experimental data revealed good agreement between the two. This numerical investigation shows that the change in concrete behaviour when subjected to high rates of compressive loading is mainly due to inertia effects.

In their paper Mu et al [80] discussed whether the compressive strength enhancement of concrete-like materials with strain-rate is a material property. They performed a series of 3D numerical simulations and concluded that the compressive strength enhancement with increased strain-rate is an indirect result of a lateral confining effect. Comparisons between their results with pressure-dependent material model and related tests show that the lateral confinement is caused by both the lateral inertia and the interface friction between the loading

apparatus and the loaded specimen. They also show that the main mechanisms that initiate lateral confinement include the material lateral inertia and the interface friction between the loading apparatus and the loaded specimen.

Lu and Li [88] examined the experimental methods for determining tensile strength in tension. In order to clarify whether the observed strain rate effect is a material property or a structural property (due to inertia and stress triaxility effects) they employed a hydrostatic-stress-dependent macroscopic model (K&C concrete model) with no strain rate enhancement to numerically simulate experiments. Their analyses of three different dynamic tests did not show any rate dependency and they conclude that tensile strain rate enhancement is a material effect. Further they developed a micro mechanism model and demonstrate their theory that microcrack inertia is one of the mechanisms causing the increase of dynamic tensile strength with strain-rate.

Ožbolt et al [82] numerically examined the tensile behaviour of concrete under high loading rates by employing 3D FE code for multi body dynamics with fragmentation capability. They used a rate sensitive microplane model. Based on the numerical results and their comparison with experimental results they concluded that for concrete under high strain rates the apparent strength consists of true material strength and a contribution due to the damage of concrete. The damage contribution appears once the strain rate exceeds 10/s and can be explained by either inertia invoked by material softening or by the fact that in the evaluation of numerical or experimentally measured data, damage of concrete is ignored [82]. Further Ožbolt et al claim that material strength should be accounted by the constitutive law and that the influence of inertia should be automatically introduced in the dynamic analysis. They stress that because the progressive increase of apparent stress is always related to failure modes or multiple cracks the apparent strength should never be considered as part of the constitutive law. They also warn that results of indirect tension tests, such as SHBT, require careful interpretation due to the fact that the specimen is damaged and not elastic.

As a result of their numerical investigation using a three-phase concrete (aggregate, mortar, and interface) meso-scale dynamic model into the dynamic failure under different strain rates Qin and Zhang [67] reached the following conclusions regarding the increase in concrete strength. The first is due to the non-homogeneous properties of concrete and the micro and meso defects- under dynamic loading new meso-cracks begin to expand due to propagation, reflection, and superposition of stress waves. This is why the failure patterns of concrete

under high strain rates have a dispersed formation. An additional mechanism presented is that under static/ low strain rates nearly all external work is used to accumulate strain energy compared to dynamic loads where additional external energy is needed to cause rupture of the concrete leading to further strength enhancement.

## 2.4. Steel Material Behaviour

Steel is a ductile material and its behaviour under uniaxial compression or tension is described by stress-strain curves such as the schematic representation of structural steel under uniaxial tensile loading presented in Figure 2.25. This is usually established through uniaxial tensile tests conducted on steel specimens which are considered to represent material units from which average material properties can be determined.

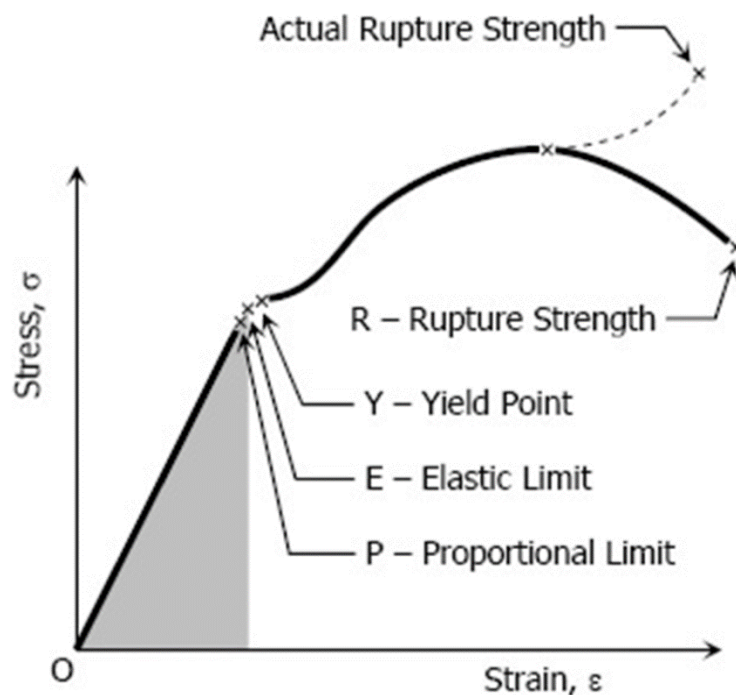


Figure 2.25. Stress-strain diagram of structural steel [100]

The behaviour of steel is characterised by the following four processes: (i) yielding, (ii) strain hardening, (iii) necking and (iv) rupture [101]. Steel initially exhibits elastic behaviour (during which deformation is recoverable after unloading) until the yield stress ( $f_y$ ) is attained. The post-yielding behaviour of steel is usually characterised by strain hardening with the total strain consisting of a recoverable (elastic) and permanent (plastic) component. Once the ultimate strength of steel is attained necking initiates (reduction in cross-section of

steel specimen). During this stage, an increase of the applied load results in further reduction of the specimen's cross-section, ultimately leading to rupture.

#### **2.4.1. Effect of Loading Rate on Steel Material Behaviour**

It has been experimentally established that the behaviour exhibited by steel specimens under high loading rates differs from that established under equivalent static loading [101]. For example, Singh et al [102] investigated the behaviour of mild steel under increasing rates of tensile loading in relation to that established under static load. They used a modified Hopkinson bar apparatus for testing under medium and high strain rates. They observed a significant increase in the yield strength of the steel with increasing strain rates. However, an increase in ultimate strength was observed for the medium strain rates and remained constant for the highest strain rates. Therefore, the yield stress of the mild steel was found to be more strain-rate sensitive than its ultimate tensile strength.

Langseth et al [103] investigated the effect of strain rate on the tensile behaviour of mild steel commonly used in offshore platforms. A high rate biaxial testing machine was used for conducting tensile tests with strain rates of  $0.0001$  to  $25\text{s}^{-1}$ , and a SHPB was employed for achieving strain rates of  $100$  to  $1100\text{s}^{-1}$ . They showed that yield strength increased significantly with the increase of strain rate. They also noted that the yield stress of mild steel is more sensitive than the stresses associated with specific values of strain in the hardening region under increasing strain rates.

In addition to the tests carried out with “dog bone” specimens, reinforcement bar specimens are also used for investigating the material behaviour of steel under static and increasing loading rates [101]. Malvar and Crawford [104] gathered and presented data obtained from experimental studies investigating the behaviour of reinforcement bars under high strain rates, presented in Figure 2.26. In order to quantify the influence of the strain rate on the yield stress of steel they defined a dynamic increase factor (*DIF*) as the ratio of dynamic yield stress to static yield stress. It can be seen that when the strain rate increases beyond a certain level the *DIF* also increases. The influence of strain rate on the *DIF* is more profound in the case of reinforcing bars in which steel is characterised by lower static yield strength values.

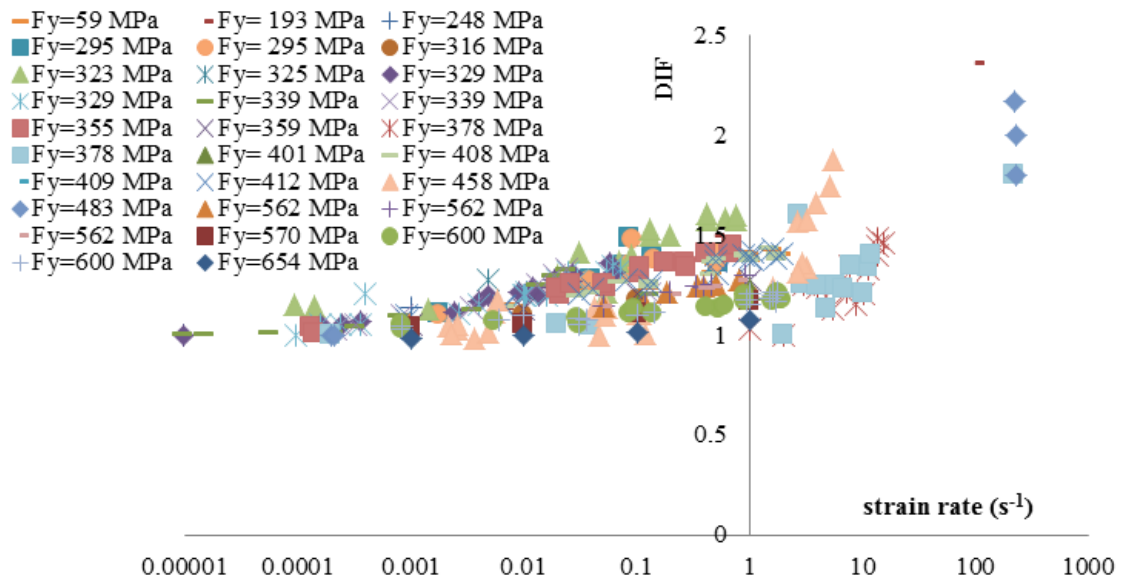


Figure 2.26. Reinforcing bars under different rates of loading [104]

However, the available test data fails to accurately quantify the observed shift and provide the reasons that cause these differences, as it is characterised by considerable scatter. This scatter is due to a number of parameters mainly associated with structural response (e.g. the experimental technique employed, the shape and size of the specimens, the different types of steel used, etc.) which vary from experiment to experiment. As a result, it is difficult to derive laws capable of realistically quantifying the change in the specimen behaviour under increasing loading rates [101].

## 2.5. Methods for Assessing RC Structural Response under Blast

There is very limited documentation providing engineers and researchers with necessary data concerning the design of structures to resist blast loads exists [105]. Therefore, structural engineers are in dire need of guidance on how to design structures to withstand various explosions. Better understanding of the factors that contribute to a structures blast resistance would allow for improvement of the structural performance. Therefore, the need for research into this topic is crucial, and the conclusions drawn from it can lead to life saving practises. Although there has been a significant amount of research in recent years dealing with the behaviour of structural elements and materials under blast loads, there is not much related to full scale structures. Most of full scale structures that have been analysed are the structures that have actually suffered from explosions.

## **2.5.1. Experimental Methods**

### **2.5.1.1. Observations**

Observations and research of actual explosions provide a great deal of data which can be utilised in the quest for a deeper understanding of modes of failure of structures.

During World War II a vast amount of data and observations were compiled, leading to tens of thousands of reports [4]. Based on the reports one of the main observations was that the most common modes of failure was due to weak beam-column connections, which generally failed due to a combination of the prying action resulting from insufficient ability to accommodate large beam end rotations and tensile loading. In general, multi storey buildings of that period in London were found to have an impressive ability to redistribute loads following substantial damage from direct hits. At that time internal partitions were usually constructed from thick masonry. The bracing effects of these masonry panel walls were able to effectively redistribute loads from badly damaged parts of the frame. These observations lead to the conclusion that the effects of the explosions on a building as a whole depend to a large extent on its internal planning.

Several insightful observations were also made after the IRA attacks and documented by Peter Rhodes, who worked for the government in Northern Ireland [4]. He noted that concrete framed structures frequently sustained severe damage to their frames, including severing of beams from columns, without leading to progressive collapse. As observed before, panel walling and diaphragm walls played a vital role in bracing severely damaged structures. The adequate tying of beams to columns is of particular importance as RC frames were found to fracture at the joints between those members when reinforcement lapped. When subjected to reverse uplift loads this area presents a significant zone of weakness as structural elements can become dislodged if not properly tied together. Two incidents, with two very different outcomes, may be used to demonstrate these points. The first incident is the bombing of the Dropping Wells Bar in Ballykelly on December of 1982. In this case blast from a small quantity of high explosive caused inadequately tied precast concrete slab units to become dislodged from their supports, crushing people and resulting in 17 deaths [106]. The other incident is the bomb attack on the Exchange's office, 30 St. Mary Axe London, on April 1992 in which 3 people were killed. In this case, although significant damage was caused to the perimeter frame, there was no progressive failure. This is mainly due to the monolithic

nature of the frame providing significant redundancy via a combination of three dimensional vierendeel actions and bracing from panel walling.

Another case which had huge impact on the structural field and led to many investigations dealing with the nature of the collapse was that of the FBI Murrah building in Oklahoma City in 1995 [7]. The blast destroyed three columns located on the front face of the building. These columns supported transfer beams that supported intermediate columns this in turn led to a widening of the zone that collapsed and to a greater destruction [4].

With limited research into the response of full scale structures to blasts several researchers have used data from real incidents to research this topic. Mlakar et al [7] investigated the bombing of the Murrah building and Luccioni et al [107] studied the collapse of the AMIA building in Buenos Aires which is further discussed in Subsection 2.5.2.

### **2.5.1.2. Experiments**

In recent years there has been much experimental research into the behaviour of structural elements under blast load, which can be divided into two main types: explosive experiments and blast simulator experiments.

There is very limited availability regarding blast experiments on full scale structures. One of those available is the a full-scale blast test on a four-story building (24.4 by 14 metres) at the White Sands Missile Range in New Mexico [108]. The experiment was conducted as part of a research and development contract from the Defence Threat Reduction Agency (DTRA) to test windows, walls and structural elements under realistic blast conditions. The front face of the structure was solid and planar. Glass windows were installed along most of the width of the fourth floor. The structure was exposed to a large detonation which loaded the front face in a mostly uniform manner [109]. Woodson and Baylott [110] conducted a quarter scale experiment on a two storey two by one frame as part of the U.S. Army Engineering Research and Development Centre. Precast panels were tested in a collaborative research between the US Air Force Research Laboratory and the Portland Cement Association [111]. They examined the blast resistance of a conventional off-the-shelf insulated concrete sandwich wall construction under full-scale blast demands in a three-story reaction structure.

Large- scale testing is very expensive and incurs many safety risks. Usually these experiments are conducted by the military, and therefore only limited information is available



to non-military researchers. Therefore, there is more information available regarding blast experiments on structural elements, such as plates, beams and columns.

Cendón et al [112] conducted a series of blast loading experiments. Their experimental setup, see Figure 2.27, allowed them to test up to four concrete elements simultaneously under the same blast load. The main advantages in the set up were the reduction of scattering on detonation tests and cost effectiveness. Cendón et al proceeded to develop numerical models and suggested, based on both experimental and numerical tests, that the ability of RC structures to withstand blast loads is primarily governed by their tensile strength.

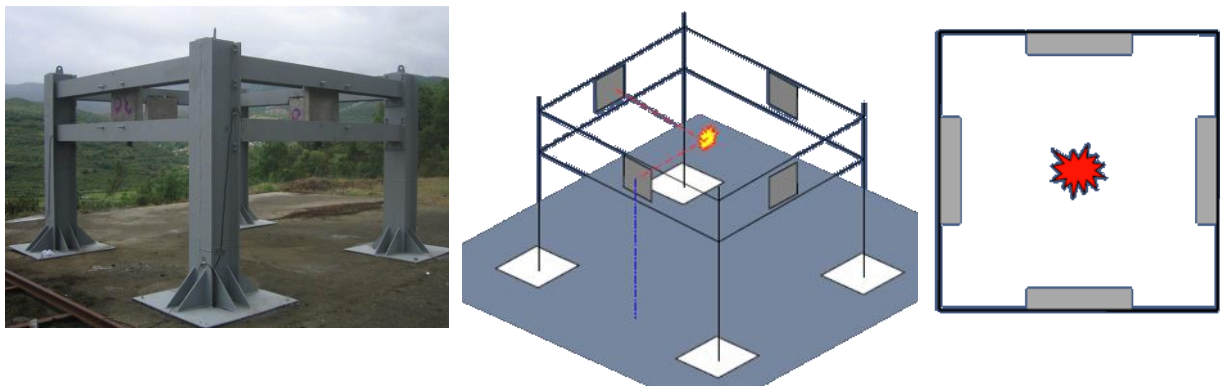


*Figure 2.27. Cendón et al [89] experimental set up*

Wang et al [113] investigated the behaviour of one-way square RC slabs subjected to a blast load through experiments and numerical simulations. The experiments were conducted under a close-in blast loading with various amounts of TNT. Different damage levels and modes were observed, mainly showing that with an increase of the explosive charge the failure mode of the RC slab gradually changed from overall flexural to localised punching mode. Wang et al [114] also conducted experiments on scaled down slabs to reduce the complications and costs associated with full scale experiments and proposed empirical equations to correct results when scaling up from a scaled down model to real size slabs.

In cooperation with the Czech Army corps and Police of the Czech Republic, Foglar and Kovar [115] were able to perform blast tests using real scale RC precast slabs with varying fibre content and concrete strength class. The specimens were designed to the scale of a small span bridge and were placed on timber posts which were fixed in position by steel tubes.

Kakogiannis et al [116] studied hollow slabs used in the construction of car park roofs. The experimental setup consisted of two tunnel RC elements with the slab located underneath, fixed on metal supports, see Figure 2.28.



*Figure 2.28. Kakogiannis et al [93] experimental setup*

RC slabs were also tested under blast conditions by Wu and Hao [117] to compare normal strength concrete with ultra-high strength concrete.

Reduced scale RC beams were experimentally investigated by Zhang et al [118] under close-in varying blast loads, as shown in Figure 2.29. They noted that with an increase in deflection, tensile fracture at the back face and compressive fracture at front face occurred.

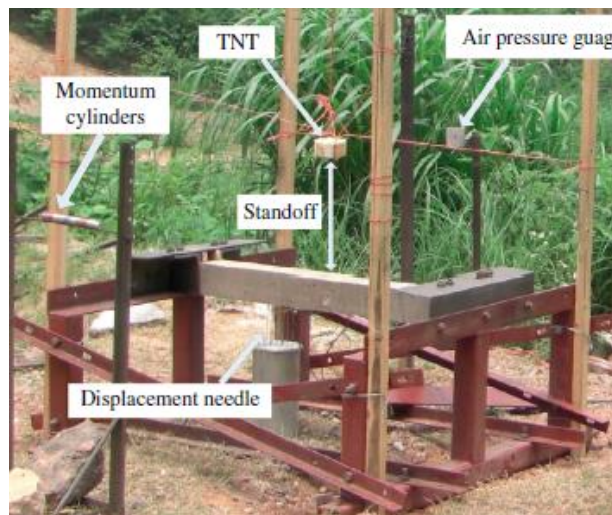


*Figure 2.29. Zhang et al [97] experimental setup*

In order to avoid dangers and complications associated with the use of explosives there have been a number of researches aimed at developing methods to experimentally simulate blast behaviour. One of these set ups is achieved by using impact to simulate blast-like loads. It has been shown that this method is capable to generate repeatable loading similar to field testing with live explosives [119]. An additional advantage of impact loading is the possibility of

using a high speed camera for collecting data as tested specimens are not obscured by a fireball. One such simulator is located at the University of California, San Diego (UCSD). The simulator is capable of generating blast-like loading on structures by using hydraulic rams; the loading can be tailored by controlling its peak load, duration and shape [119]. Freidenberg et al [119] compared results obtained using this blast simulator with corresponding field tests with live explosives that demonstrated the capability of the blast simulator to generate blast-like loading.



*Figure 2.30. Stud wall and masonry in the Blast Simulator[119]*

A similar approach was adopted by Li et al [120] in the Protective Engineering Laboratory at Nanyang Technological University, Singapore. Using the built-in Conwep suite in LS-Dyna a validated numerical model was used to predict the residual lateral deflection of RC columns subjected to an explosive attack. Three hydraulic actuators were installed horizontally to reproduce the predicted target residual lateral deflection, as shown in Figure 2.31.



*Figure 2.31. Hydraulic actuators at the Protective Engineering Laboratory in Nanyang Technological University, Singapore [120]*

### **2.5.2. Nonlinear Finite Element Analysis**

Dynamic response of blast loaded structures is very complex to analyse [23], as it involves effect of high strain rates, the nonlinear inelastic behaviour of the structural material, uncertainties of blast load calculations and time dependant deformations. Results of such an analysis are also hard to verify. However, due to the costs, risks and complications involved with experimental testing, a huge amount of research into blast loads has been conducted numerically. Simulation capabilities to accurately predict both the blast loading and subsequent structural response are important for generating improvements in blast protection. Computational methods in the field of blast engineering are generally divided into those used to predict the blast loads on the structure and those used to calculate the structural response. These programs use both first-principle and semi-empirical methods. Programs using the first-principle method can be categorised into uncoupled and coupled analyses. Uncoupled analysis calculates blast loads on a rigid structure and then transfers the obtained loads to a responding model of the structure. This method often leads to over prediction of the loads, particularly if significant motion or structural failure occurs [23]. In a coupled analysis the blast simulation module is directly linked with the structural response module. Using this method the displacements in the structure are constantly calculated during the blast calculation allowing the pressures and failure of the structure to be more accurately captured. Table 2.2 summarises computer programs currently used in the field [23].

It is recognised that the prediction of a blast induced pressure field on a structure and its response involves highly nonlinear behaviour and therefore it is essential to validate

computational methods to available experimental data. Once validated numerical analysis provides an extremely powerful tool as it can provide further insight into the damage mechanisms which cannot be observed in experiments.

Considerable studies have been conducted on the dynamic response of RC structural components in recent years [121]. Xu and Lu [122] numerically studied the damage behaviour of concrete plates subjected to air blast loads and presented an empirical spallation criterion that took the complex three-dimensional stress conditions of concrete into account. Yuan et al [123] analysed the response of RC slabs under close blast and studied the effects of explosive charge weight and reinforcement arrangement on the damage modes. Lin et al [124] investigated RC panels subjected to blast loading using the finite element code LS-Dyna, and explored the effects of charge weight, standoff distance, panel thickness and reinforcement ratio on the blast resistance of RC panels. Tai et al [125] analysed a reinforced concrete slab under a blast load using the nonlinear finite element analysis software LS-DYNA. The geometry and results of the finite element model are shown in Figure 2.32.

<b>Name</b>	<b>Purpose and type of analysis</b>	<b>Author/ Vendor</b>
BLASTX	Blast prediction, CFD code	SAIC
CTH	Blast prediction, CFD code	Sandia National Laboratories
FEFLO	Blast prediction, CFD code	SAIC
FOIL	Blast prediction, CFD code	Applied Research Associates, Waterways Experiment Station
SHARC	Blast prediction, CFD code	Applied Research Associates, Inc.
DYNA3D	Structural response + CFD (Coupled analysis)	Lawrence Livermore National Laboratory (LLNL)
ALE3D	Coupled analysis	Lawrence Livermore National Laboratory (LLNL)
LS-DYNA	Structural response + CFD (Coupled analysis)	Livermore Software technology Corporation (LSTC)
Air3D	Blast prediction, CFD code	Royal Military of Science Collage, Cranfield University
CONWEP	Blast prediction (empirical)	US Army Waterways Experiment Station
AUTODYN	Structural response + CFD (Coupled analysis)	Century Dynamics
ABAQUS	Structural response + CFD (Coupled analysis)	Simulia Inc.

*Table 2.2. Computer programs that are currently being used for modelling blast effects on structures [23]*

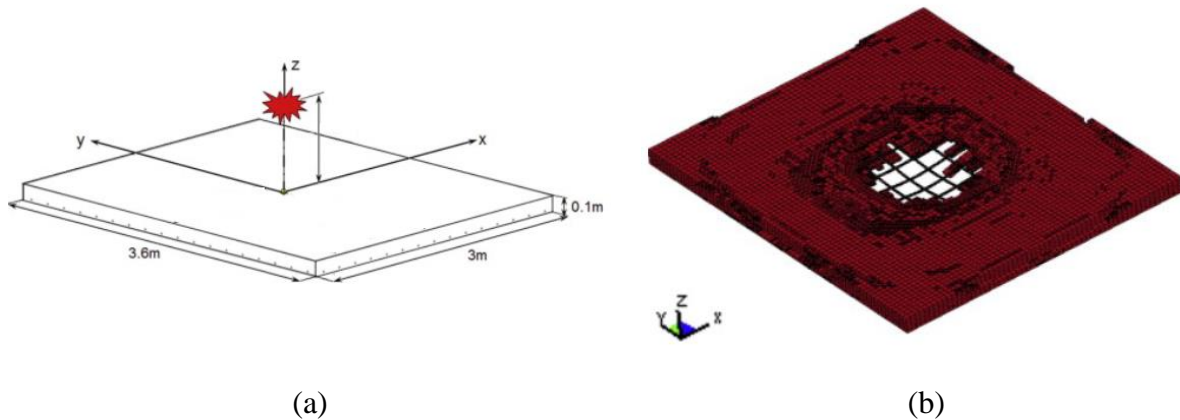


Figure 2.32. Finite element slab (a) geometry and (b) damage for a 10 kg charge at a 0.5m distance [125]

Tai et al found that mesh size is very sensitive to shock wave propagation, and that the location of damage in the slab is dependent on the amount of reinforcement present in the slab. For low reinforcement ratios damage occurred at centre slab, however for increased ratios the damage occurred at the supports.

Additionally, researchers have conducted numerical simulations in order to investigate the dynamic response of RC columns or beams under blast loads [121]. Li and Hao [126] carried out numerical simulations on RC columns subjected to blast loading and investigated the effects of column dimensions and reinforcement ratio. Shi et al [127] numerically investigated a RC column, based on the quarter scale experiment conducted by Woodson and Baylot [110]. They used LS-Dyna for the structural assessment, whilst obtaining the blast loads acting on the column front face using AUTODYN. After validating the model they carried out parametric studies to investigate the effect of column dimension, concrete strength, longitudinal and transverse reinforcement ratio on the structural response of the RC column.

Yan et al [121] carried out numerical investigation to study the damage mechanisms of RC beams under blast loading (see Figure 2.33). They used experimental results to validate their analysis which was conducted using the finite element program LS-Dyna.

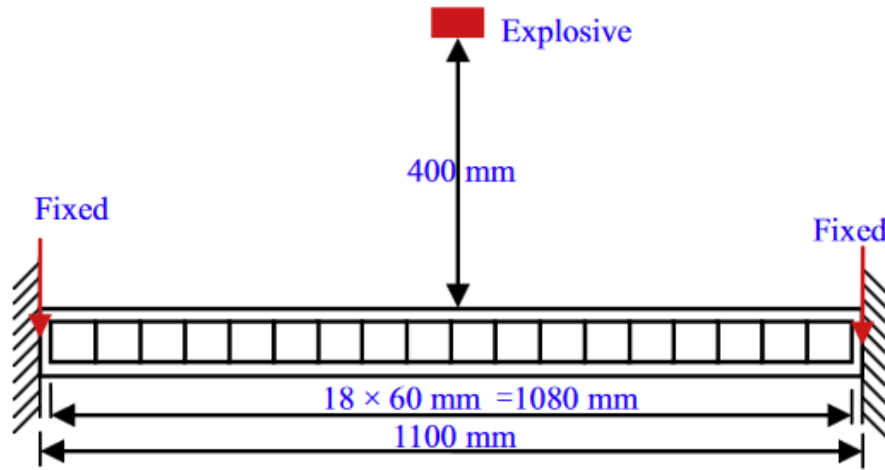


Figure 2.33. Geometry of the RC beam [121]

They found good agreement between results of the numerical model and the experiments. They observed that in this case the tensile stress wave reflected from the free bottom surface of the beam was the major reason for concrete spalling at the bottom. The development of two vertical cracks, initiating from the compressive and tensile zones, which met up led to spalling of the side-cover concrete, see Figure 2.34. This research demonstrates that numerical analysis can add additional information regarding the damage mechanisms observed in experiments.

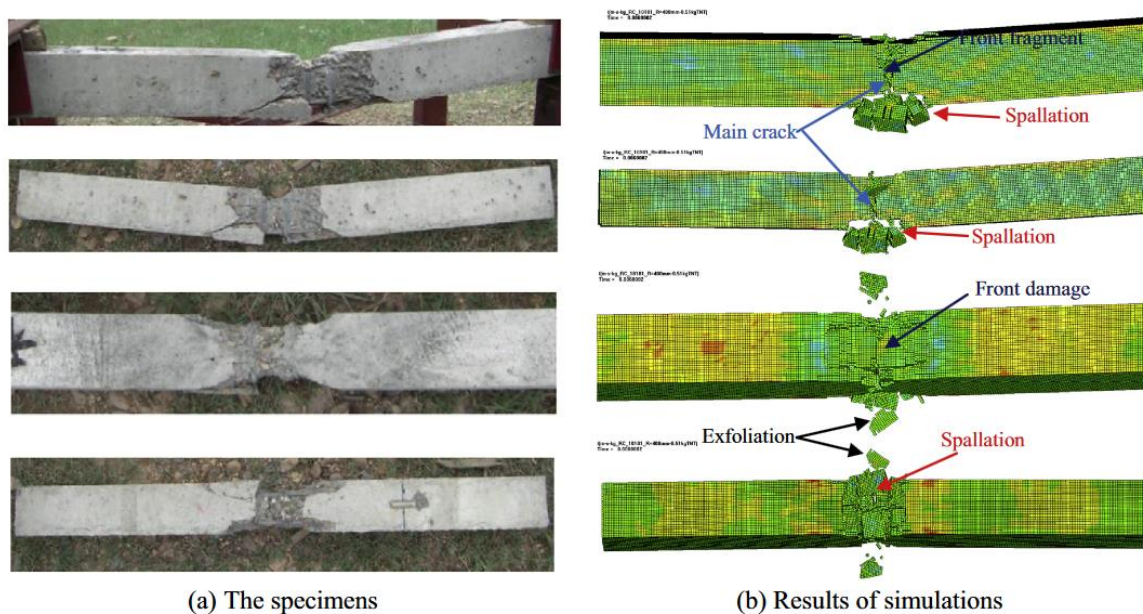
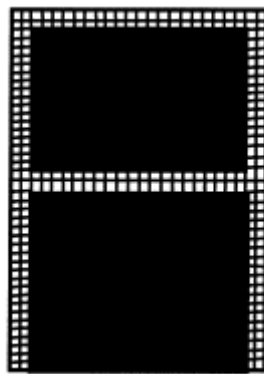


Figure 2.34. Damage comparisons between the experiment and simulation [121]

When considering complex structures, it is important to consider which components need to be taken into account and how to model the material behaviour in these components. On the

one hand, as shown in the actual results from bombing, non-load bearing structural elements can play a role in the distribution of loads, but on the other hand a very detailed model becomes very complex and calculations time consuming. The same thing can be said of material modelling - there is a need to find an optimal material model, i.e. the one that will give sufficiently accurate results but not lead to complex time consuming analysis. In their research Hao et al. [128] note that masonry infills are usually considered as secondary structures and excluded from calculations as they introduce unwanted analytical complexities. However, neglecting them may lead to inadequate assessment of the structural damage of the frames when subjected to intensive ground motions resulting from explosions. A two-storey RC frame was used to illustrate this point. The models considered were: a bare frame, infill on top floor, infill on bottom floor, full infill on both floors and infill on both floors but with openings. The ground motion in this work was derived from a numerically simulated underground explosion. The main conclusion of this work is that the stability and integrity of RC frames are enhanced with a masonry infill wall; however, the influence of masonry infill on the frame response depends on the physical properties as well as the geometry of the wall. Besides the response level, the presence of masonry infill also alters the damage pattern of the RC frame.



*Figure 2.35. Finite element model of RC two storey frame with masonry infill [128]*

Wu et al [129] linked a 3D numerical model to the computer program Autodyn3D and explored the effect of underground explosions on a two storey masonry structure, a two-storey and a six-storey RC frame (shown in Figure 2.36) filled with masonry walls. Only structural material damage was considered, while possible out of-plane damage of the masonry wall owing to rigid body movement was not taken into account. In the two-storey RC frame infilled with masonry major damage was in the infilled masonry walls at the first storey, while the second storey infilled walls suffered only moderate damage. Compared to



the masonry structure damage was less severe in the masonry walls at the first storey. This is probably because the stress wave energy propagates along the RC frame to the second storey more easily than along the masonry structure so that damage in the infilled masonry walls at the second storey was more severe. The RC columns at the first storey suffered major damage while the second storey columns experienced only slight damage, implying the vibration level of the second storey was smaller than that of the first storey. The RC frame also acts as a filter to further reduce the ground motion energy from transmitting to the second storey.

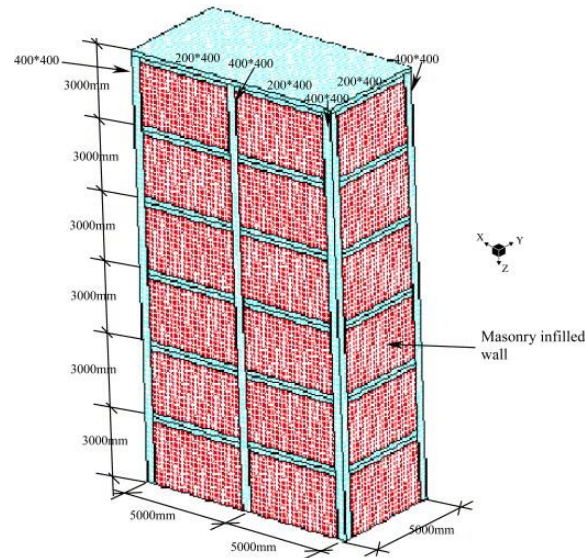
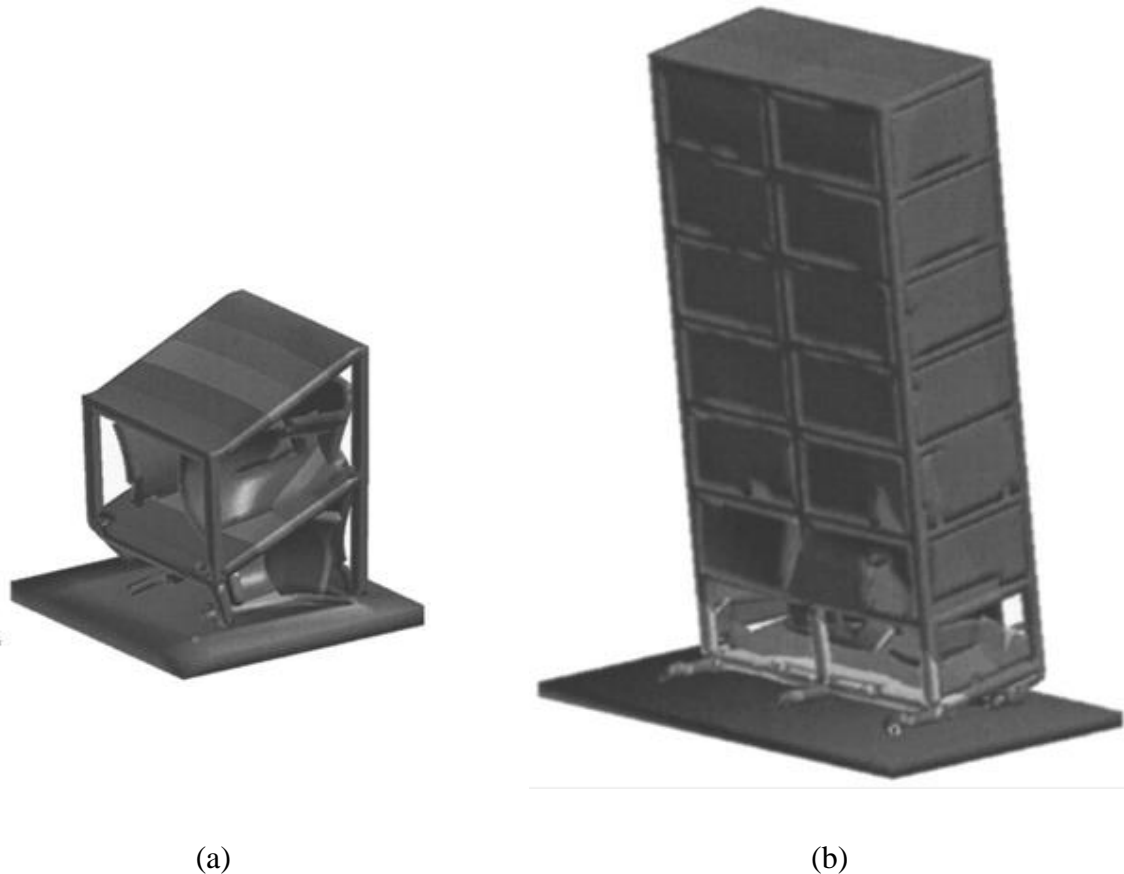


Figure 2.36. Numerical model of a six-storey building [129]

Wu and Hao [130] investigated two low-rise and one medium-rise RC frames with masonry infilled walls. Airblast pressures on the building front face simulated from AUTODYN and those on sidewalls, roof and rear walls estimated by the US Army's empirical formulas were used as input in the analysis. The computer program LS-DYNA3D was used in numerical calculations. The scaled distances corresponding to the different damage levels of the three structures' models were determined from the numerical analysis. Calculations were carried out to determine the corresponding scaled distances to various structural damage levels for the different buildings. It was found that under the blast loads from a surface explosion of the same scaled distance, the low-rise and medium-rise structures behaved differently, as shown in Figure 2.37. For the eight-storey building it is observed that the first-storey columns are not blown off, but seriously damaged by the airblast loads, resulting in the collapse of structure. Damages to the columns of the building are not as significant as to the columns of the one-storey and two-storey buildings because the sizes and reinforcement ratio of the columns of the eight-storey building are much larger than those of the low-rise buildings. It

was also found that the infilled masonry walls of the medium-rise building suffer more damage than those of the low-rise buildings. This is because the RC frame of the medium-rise building is more flexible than the low-rise structures, resulting in larger displacement response and larger storey drift and therefore more severe damage to the infilled masonry walls.



*Figure 2.37. Displacements of the (a) two storey and (b) 8 storey buildings at at 1sec after explosion at scaled distance  $0.5\text{m/kg}^{1/3}$  [130]*

An approximate validating approach was used by Luccioni et al. [107] who numerically simulated the collapse of the AMIA building in Buenos Aires, which was attacked by terrorists in July 1994. The research was conducted using the hydro code Autodyn. In the simulation the complete RC and masonry building was modelled, including non-structural elements which were shown to play an important role in the propagation of the pressure wave. The blast loading was performed in two stages using the uncoupled approach. The first stage simulated the explosion itself and the second part analysed the blast wave generated in the first stage and its effect and interaction with the building. Validation of the simulation was shown by obtaining a good agreement between the results and photographs of the actual

damage in the building. Similarity is also shown between the distribution of the building remains and the final stage of the demolition. It is important to recognise that such simulations are time consuming, with this the simulation taking 310 hours to complete.

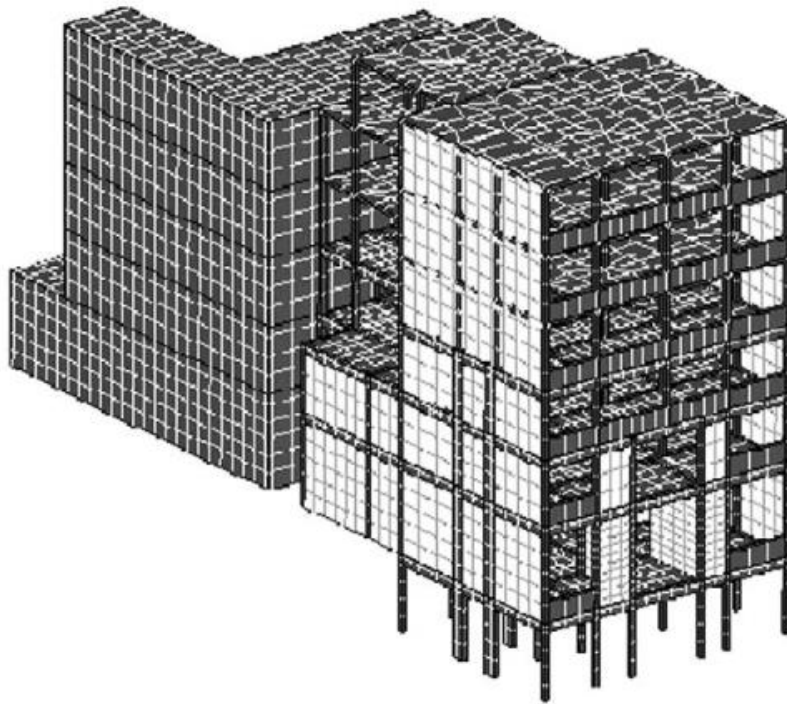


*Figure 2.38. Finite element model of the AMIA building [107]*

In his research, Esper [131] used both numerical modelling validated by laboratory and on site testing to investigate the dynamic response and the assessment of damage to buildings and their floor slabs during blast loading. A full 3D finite element model of the building was created using ANSYS. The model allowed investigation of the global response of the structure and to ascertain if there was any twisting of the structural frame. One of the main conclusions, due to the unpredictability of blast load effects was that it was more cost and time effective to implement methods such as finite elements to highlight areas of hidden damage prior to undertaking extensive intrusive structural investigations. It was also found that good detailing of beam-column connections greatly enhanced the building structural response to blast loads.

### 2.5.3. Methods Employed in Practice

#### 2.5.3.1. SDOF Models

Single degree of freedom (SDOF) models have been widely used for predicting the dynamic response of RC structures subjected to blast loading [132]. The SDOF method is the most commonly approximate method used in industry for blast loading [133]. The relative simplicity and fewer required inputs of the SDOF method make it a popular and cost effective approach to blast resistant design. The ease of calculation also led to the SDOF method being widely adopted in design codes, such as the US TM codes [134]. The results are highly dependable on how closely the response mode shape and resistance function resemble actual material and structural behaviour [132].

The SDOF method originally proposed by Biggs [135] uses a series of factors to evaluate the parameters of the system to be analysed, namely mass ( $M$ ), stiffness ( $k$ ), damping ( $c$ ) and external applied force ( $F$ ), so that the SDOF system is equivalent to the analysed structure.

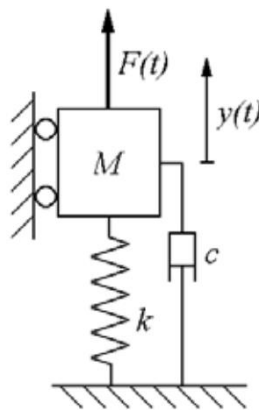


*Figure 2.39. Simple SDOF system [133]*

In this method the parameters of the governing equation of motion corresponding to distributed mass are replaced by equivalent values of a simple lumped-mass spring system. Such equivalency is based on energy approximations that rely on an assumed deflection shape of the RC structure (usually corresponding to the first eigenvector of the response). Despite its popularity, this method is associated with complications since even the application of static loading to concrete structures can lead to cracking and the development of a complex triaxial stress field within the highly nonlinear concrete medium [136]. In the case of blast loading the complexity is further accentuated since the stress wave is formed by application of external load propagation from the blast source point throughout the concrete medium.

Using simplified methods such as the SDOF iso-damage curves can be quickly generated. The most common in the area of blast studies is the pressure-impulse (P-I) diagram which provides an easy way to mathematically relate a specific damage level to a combination of blast pressures and impulses imposed on a particular structural element, see Figure 2.40. This method will be extensively covered in Chapter 3.

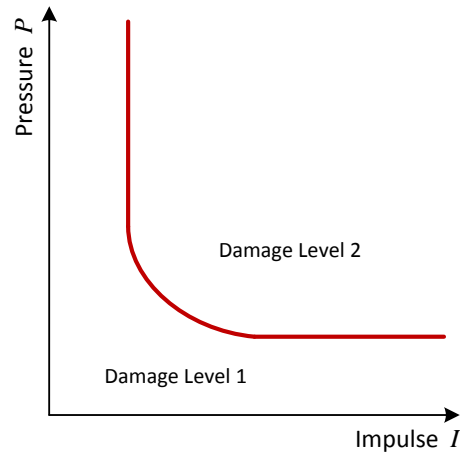


Figure 2.40. Pressure-Impulse diagram

### 2.5.3.2. Equivalent Static Methods

The truss analogy (TA), which was originally developed over a century ago [137], forms the basis of the design procedures which are present in most current Codes of Practice [89,138,139]. In the 1970s the use of the TA method was extended to describe RC structures at their ultimate limit state by incorporating concepts such as strain softening, aggregate interlock and dowel action [140]. A simple description of an RC beam at its ultimate limit state as a truss is presented in Figure 2.41. The structure starts behaving like a truss once inclined cracking occurs, with the compressive zone and the flexural reinforcement forming the longitudinal struts and ties, respectively, the stirrups forming the transverse ties, whereas the cracked concrete of the element web is assumed to allow the formation of inclined struts.

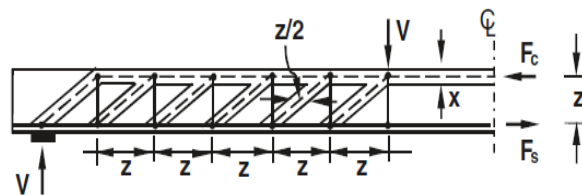


Figure 2.41. Truss modelling function of an RC beam at its ultimate limit state [140]

Although widely used due to its simplicity, the TA method is not without drawbacks. There are examples indicating that the concepts of the TA method, which form the basis of current codes of practice, do not account for the observed unexpected premature brittle types of failure suffered by RC structures in situations of overload [140]. Such examples include the collapse of the “Sleipner 4” platform in the North Sea which has been attributed to the inadequacy of the ACI shear design provisions [141] and the collapse of a multilevel car park in Wolverhampton due to punching of the top level flat slab under dead load only [142], see Figure 2.42.



*Figure 2.42. Pipers Row Car Park, Wolverhampton Partial Collapse, March 1997[143]*

A widely acknowledged alternative method of assessment is the compressive-force path (CFP) method. This method, developed by Kotsovos [140], is based on the beams’ loading capacity and failure mechanism being related to the region of the member containing the path of the compressive stress resultant which develops within the beam due to bending, just before failure occurs. This method provides a realistic description of the causes which dictate the various types of beam behaviour as established by available experimental data.

The CFP method assumes that an RC structural element at its ultimate limit state behaves essentially as an arch-like structure (for the case of a simple supported beam) or a system of arch-like structures connected at the point of contraflexure (in the case of more intricate structural configurations characterised by static indeterminacy). The latter type of behaviour is enforced by the available reinforcement. The CFP method [140] accounts for the brittle nature and triaxiality characterising concrete material behaviour. It assumes that the area of the compressive zone has a significant effect on shear capacity while the contribution of aggregate interlock and dowel action is ignored. Failure is considered to occur due to the

development of transverse tensile stresses at specific locations along the path followed by the compressive force. These locations are dependent on the value of the shear span-to-depth ratio. Four distinct behaviour patterns can be identified.

Type I behaviour is characterised by a flexural mode of failure preceded by longitudinal splitting of the concrete in the compressive zone of the beam. This occurs when concrete strength in the compressive zone is exhausted due to the development of transverse tensile stresses induced by volume dilation of concrete in the adjacent regions which include primary flexural cracks. This allows the maximum stresses developing within the compressive zone of the beam to attain values approximately equal to 1.5 times the uniaxial compressive strength of concrete  $f_c$ .

Type II behaviour is characterised by a brittle mode of failure usually caused by tensile stresses developing either in the region of change of the CFP direction (location 1 in Figure 2.43) or in the region of the cross-section where the maximum bending moment combines with the shear force (location 2 in Figure 2.43). The transverse stress resultant at location 1 is considered numerically equal to the acting shear force, and, its effect is considered to spread over a distance  $d$ , on either side of location 1.

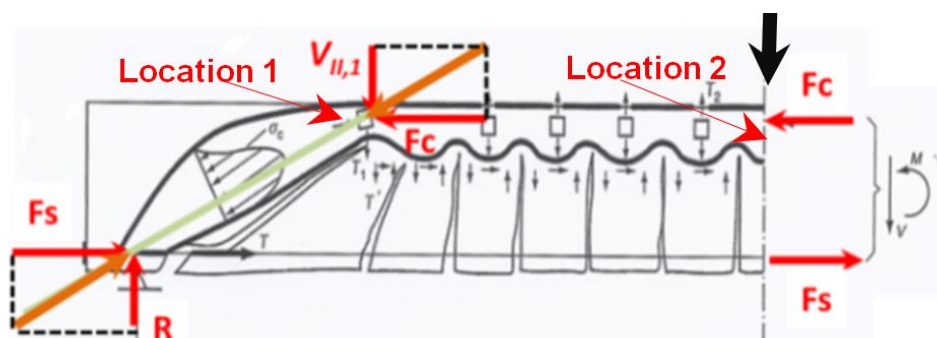


Figure 2.43. RC beam exhibiting type II behaviour

Type III behaviour, for which location 1 coincides with location 2 (i.e. the compressive zone into the shear span degenerates into a cross section within the shear span) is characterised by a brittle mode of failure caused by the deep penetration of the inclined crack into the compressive zone of the beam. This crack reduces the strength of the uncracked concrete in the compressive zone on the region where the inclined and the horizontal compressive path of the model meet (region 1, Figure 2.43), which causes a reduction on the flexural capacity of the beam.

Type IV behaviour can be characterised by two modes of failure linked with either failure of the horizontal element of the CFP model or failure of the uncracked end portion of the beam (inclined leg of the ‘frame’ of the CFP model) in compression. From the moment equilibrium of the free body in Figure 2.44, the flexural capacity ( $M_f$ ) can be easily calculated and consequently the associated load-carrying capacity can be determined.

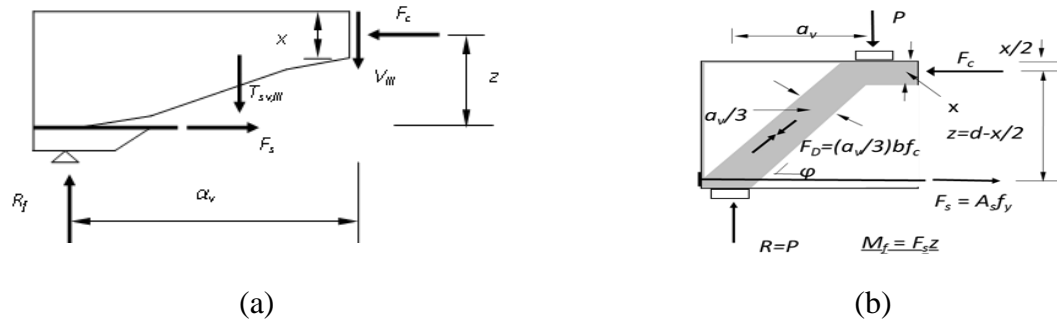


Figure 2.44. Internal actions developing in a RC beam exhibiting (a) type III and (b) type IV behaviour

## 2.6. Limitations of Existing Assessment Methods

Experimental Methods: Due to the complexity of setup, safety issues and cost there are only a limited number of available experiments related to structures subjected to explosions. Full-scale experiments are mostly conducted by the military, and therefore only limited information is available to non-military researchers. More data can be found regarding blast experiments on structural elements, such as plates, beams and columns; however, the amount is still limited. In recent years there have been some experiments which aim to simulate blast loads, such as blast load simulators and impact experiments.

The main limitations with such experiments are due to the extremely fast loading and destructive effect on the structural elements. Such tests are difficult to conduct as the intensity of the loads generated increases rapidly (in a few msec) from zero to a maximum value often leading to explosive brittle forms of failure which can in turn damage the instruments employed for measuring structural response. Data obtained from such tests is characterised by considerable scatter partly due to a wide range of parameters (associated with the experimental setup and the specimen) which differ from test to test [144–146]. This scatter predominantly reflects the difficulty in correlating the measured response to the actual physical state of the specimens; in fact, the measured maximum value of imposed load frequently corresponds to a specimen physical-state characterised by high concrete



disintegration as well as low residual load-bearing capacity and stiffness [145,146]. This stage of structural response has little practical significance as it depends heavily on post-failure mechanisms for transferring the applied loads to the specimen supports.

Methods Employed in Practice: In order to simplify the analysis and design procedures, many design codes employ equivalent simple lumped mass-spring systems for modelling individual structural elements with distributed mass and loading [147]. The equivalence is based upon energy approximations that rely on an assumed deflected shape (the first eigenvector or the deflected shape under equivalent static loading). The latter methodology relies on a number of simplifications/assumptions concerning both material behaviour and structural response. These include the use of simple uniaxial material laws, the description of post-failure behaviour, empirical amplification factors attributed to the strain-rate sensitivity of concrete behaviour, assumptions concerning the deformed shape of the structural elements and the use of elastic or elasto-plastic laws for describing structural behaviour. However, such simplifications do not allow the methodology to account for the brittle nature of concrete and its sensitivity to triaxial stress conditions, the true mechanics governing RC structural response as well as the localised response often exhibited.

Furthermore, as a structure responds to blast loads primarily at their local modes [127] these may govern the structural damage, especially when the blast load is of short duration. Therefore, the use of an SDOF model may not be suitable to analyse structural damage under blast loads. Moreover, the SDOF model is not suitable to model multi-failure modes of a structural component either. For example, a column might be damaged owing to shear failure initially and subsequently by flexural failure to collapse. Therefore, pressure–impulse diagrams generated from the analysis of a SDOF system may not give an accurate prediction of structural damage.

Nonlinear Finite Element Analysis: Detailed nonlinear finite element analysis is a widely used efficient method for investigating a wide range of structural forms, materials and loads. It is capable of providing more detailed insight on the mechanisms underlying RC structural response under blast loads. These results are limited by the element and material assumptions employed by each finite element program. Detailed modelling is very complex and is limited by computational methods and assumptions and requires an experienced analyst [148]. Additionally, as it usually employs dense 3D finite element meshes, combined with complex

constitutive material laws implemented through the use of iterative solution strategies, the required computational resources are high.

## **2.7. Concluding Remarks Concerning RC Structural Response under Blast**

Damage can affect both the global structural behaviour and the local structural behaviour. Generally, the global response is a consequence of transverse loads with long exposure time and is usually associated with global membrane (bending) and shear responses [23]. Within the four different modes of shear failure that can occur during both static and dynamic loading (diagonal tension, diagonal compression, punching shear, and direct shear) direct shear is associated with transient short duration dynamic loads that result from blast waves and depends mainly on the intensity of the pressure waves. The high shear stresses may lead to direct global shear failure and may occur within a few milliseconds of shock wave arrival to the frontal surface of the structure which can be prior to any significant bending deformations [149]. This shift in the deformation profile, as compared to the static case, means that the effects of cracking are felt closer to the supports and that the cracking mechanism is different. As the codes used to design structures to withstand blast loads [134] assume the same cracking process as in the static case, this is something that requires further investigation. The effect of steel reinforcement in the concrete is also crucial for the energy absorbing capacity of the structural concrete elements, and thereby the capacity to withstand blast and fragment loading and avoid structural collapse [149].

Local failure depends mainly on the distance of the blast source and the relative strength and ductility of the structural elements. Local failure such as localised shear or flexural failure can occur in the closest structural elements. Localised shear failure takes the form of punching and spalling, which produces low and high speed fragments. The punching effect is well known in high velocity impact applications and close range explosions. This type of failure is usually accompanied by spalling and scabbing of concrete covers as well as fragments and debris. Generally local damage does not lead to global failure, and indeed a certain amount is allowed to occur. The presence of reinforcing steel bars may limit the damage done by spalling and scabbing since they hold the concrete in place [149].

## References

- [1] J. Kelly, *Gunpowder: alchemy, bombards, and pyrotechnics: the history of the explosive that changed the world*, New York: Basic Books, 2004.
- [2] *Explosion-Resistant Buildings*, Berlin/Heidelberg: Springer-Verlag, 2006 <http://link.springer.com/10.1007/3-540-31289-7>. Last accessed on July 31, 2015.
- [3] T. Krauthammer, *Modern protective structures*, Boca Raton, FL, CRC Press, 2008.
- [4] M.P. Byfield, 'Behavior and Design of Commercial Multistory Buildings Subjected to Blast', *J. Perform. Constr. Facil. Journal of Performance of Constructed Facilities*, vol. 20, 2006, pp. 324–329.
- [5] 'Robustness and the relevance of Ronan Point today', *The structural engineer: journal of the Institution of Structural Engineers.*, vol. 88, 2010, pp. 20–25.
- [6] 'Ronan point 1968' <http://www.bdonline.co.uk/precast-disaster/3087206.article>.
- [7] S. Mlakar, Paul F, W.G. Corley, M.A. Sozen, and C.H. Thornton, 'The Oklahoma City Bombing: Analysis of Blast Damage to the Murrah Building', *Journal of Performance of Constructed Facilities*, vol. 12, 1998, pp. 113–119.
- [8] 'First Strike: Global Terror in America' [https://www.fbi.gov/news/stories/2008/february/tradebom\\_022608](https://www.fbi.gov/news/stories/2008/february/tradebom_022608).
- [9] 'The Murrah Building [Internet].' <https://www.ssa.gov/history/okc1.html>.
- [10] 'Explosions' <https://en.wikipedia.org/wiki/Explosion>.
- [11] 'Courrières mining disaster', *Britannica* <http://www.britannica.com/event/Courrieres-mining-disaster>.
- [12] 'The Oppau Disaster Report', *Ind. Eng. Chem. Industrial & Engineering Chemistry*, vol. 16, 1924, p. 635.
- [13] 'The firework disaster in Kolding, Denmark - 2004', 2005 <http://h2g2.com/entry/A3720863>.
- [14] Sugar dust explosion and fire, United States Chemical Safety and Hazard Investigation Board, 2009 <http://purl.fdlp.gov/GPO/gpo49935>. Last accessed on March 25, 2016.
- [15] 'Oppau Explosion' <http://oppau.info/2011/09/explosionskatastrophe-1921/>.
- [16] S. McGinty, *The Piper Alpha disaster*, London: Macmillan: [distributor] Macmillan Distribution (MDL), 2008.
- [17] Lac-Mégantic runaway train and derailment investigation summary., Transportation Safety Board of Canada, 2014 [http://epe.lac-bac.gc.ca/100/201/301/weekly\\_checklist/2014/internet/w14-49-U-E.html/collections/collection\\_2014/bst-tsb/TU4-25-1-2014-eng.pdf](http://epe.lac-bac.gc.ca/100/201/301/weekly_checklist/2014/internet/w14-49-U-E.html/collections/collection_2014/bst-tsb/TU4-25-1-2014-eng.pdf). Last accessed on March 25, 2016.
- [18] 'The case for safety: The North Sea Piper Alpha Disaster', *NASA Safety Centre*, vol. 7, May. 2013.
- [19] 'Fukushima Accident', 2016 <http://www.world-nuclear.org/information-library/safety-and-security/safety-of-plants/fukushima-accident.aspx>.

- [20] Design of Blast Resistant Buildings in Petrochemical Facilities. Task Committee on Blast Resistant Design, New York: Engineers ASoC., 1997.
- [21] W. Baker, P. Cox, P. Westine, J. Kulesz, and R. Strehlow, A Short Course on Explosion Hazards Evaluation, San Antonio, Texas: Southwest Research Institute, 1978.
- [22] W. Baker, P. Cox, P. Westine, J. Kulesz, and R. Strehlow, Explosion hazards and evaluation, London: Elsevier, 1983.
- [23] T. Ngo, P. Mendis, A. Gupta, and J. Ramsay, 'Blast Loading and Blast Effects on Structures – An Overview', Electronic Journal of Structural Engineering, 2007, pp. 76–91.
- [24] Fundamentals of Protective Design for Conventional Weapons, Army UDot, 1986.
- [25] The Design of Structures to Resist the Effects of Accidental Explosions - UFC 3-340-02, US Army Corps of Engineering NFEC, Air Force Civil Engineer Support Agency
- [26] S. Glasstone and P.J. Dolan, The Effects of Nuclear Weapons, [Washington]: U.S. Dept. of Defence, 1977.
- [27] Center for Chemical Process Safety (CCPS) AIoCE, Guidelines for Vapor Cloud Explosion, Pressure Vessel Burst, BLEVE and Flash Fire Hazards, New Jersey: Wiley & Sons, 2010.
- [28] J. Greenspon and J GERABM, Energy Approaches to Structural Vulnerability with Application of the New Bell Stress - Strain Laws, Defense Technical Information Center, 1976.
- [29] Design and Analysis of Hardened Structures to Conventional Weapons Effects, Departments of the US Army Navy and Airforce, 1990.
- [30] A Manual for the Prediction of Blast and Fragment Loadings on Structures, Texas: Energy UDo, 1992.
- [31] Component Explosive Damage Assessment Workbook (CEDAW), Omaha, Nebraska: US Army Corps of Engineers PDC., 2008.
- [32] J. Sperrazza, 'Modelling of Air Blast. In Use of models and scaling in shock and vibration', Philadelphia, Pennsylvania: 1963.
- [33] O. Johnson, 'A blast-damage relationship', 1967.
- [34] C.K. Youngdahl, 'Correlation Parameters for Eliminating the Effect of Pulse Shape on Dynamic Plastic Deformation', Journal of Applied Mechanics, vol. 37, 1970, p. 744.
- [35] W. Baker, Explosion in air, Austin, Texas: University of Texas Press, 1973.
- [36] R. Schumacher and B. Cummings, A Modified Pressure-Impulse Blast Damage Model., Ft. Belvoir: Ballistic Research Labs Aberdeen Proving Ground MD., Defence Technical Information Center, 1977.
- [37] G. Abrahamson and H. Lindberg, 'Peak load-impulse characterization of critical pulse loads in structural dynamics', Nuclear Engineering and Design, vol. 37, Apr. 1976, pp. 35–46.
- [38] G. Mays, Blast effects on buildings: design of buildings to optimize resistance to blast loading, London; New York: T. Telford; American Society of Civil Engineers [distributor], 1995.

- [39] Q. Li and H. Meng, 'Pressure-Impulse Diagram for Blast Loads Based on Dimensional Analysis and Single-Degree-of-Freedom Model', *Journal of Engineering Mechanics*, vol. 128, Jan. 2002, pp. 87–92.
- [40] Q. Li and H. Meng, 'Pulse loading shape effects on pressure–impulse diagram of an elastic–plastic, single-degree-of-freedom structural model', *International Journal of Mechanical Sciences*, vol. 44, Sep. 2002, pp. 1985–1998.
- [41] T. Krauthammer, S. Astarlioglu, J. Blasko, T.B. Soh, and P.H. Ng, 'Pressure–impulse diagrams for the behavior assessment of structural components', *International Journal of Impact Engineering*, vol. 35, Aug. 2008, pp. 771–783.
- [42] Y. Ding, M. Wang, Z.-X. Li, and H. Hao, 'Damage evaluation of the steel tubular column subjected to explosion and post-explosion fire condition', *Engineering Structures*, vol. 55, Oct. 2013, pp. 44–55.
- [43] *Guidelines for Evaluating Process Plant Buildings for External Explosions and Fires*, New York: Engineers CfCPSotAIOc, 1996.
- [44] *Handbook for Blast Resistant Design of Buildings*, New Jersey: John Wiley & Sons, 2010.
- [45] C. White, 'The scope of blast and shock biology and problem areas in relating physical and biological parameters.', *Annals of the New York Academy of Sciences*, vol. 152, 1968, pp. 89–102.
- [46] C. White, R.K. Jones, E.G. Damon, E.R. Fletcher, and D.R. Richmond, *The Biodynamics of Air Blast*, Ft. Belvoir: LOVELACE FOUNDATION FOR MEDICAL EDUCATION AND RESEARCH ALBUQUERQUE NM., Defense Technical Information Center, 1971.
- [47] D. Richmond, E.G. Damon, E.R. Fletcher, I.G. Bowen, and C. White, 'The relationship between selected blast-wave parameters and the response of mammals exposed to air blast.', *Annals of the New York Academy of Sciences*, vol. 152, 1968, pp. 103–21.
- [48] A.S. Fallah, E. Nwankwo, and L.A. Louca, 'Pressure-Impulse Diagrams for Blast Loaded Continuous Beams Based on Dimensional Analysis', *Journal of Applied Mechanics*, vol. 80, Jul. 2013, p. 051011.
- [49] P. Hodge, 'The influence of blast characteristics on the final deformation of circular cylindrical shells', *Journal of Applied Mechanics*, ASME, vol. 23, 1956, pp. 617–624.
- [50] Y. Shi, H. Hao, and Z.-X. Li, 'Numerical derivation of pressure-impulse diagrams for prediction of RC column damage to blast loads', *International Journal of Impact Engineering*, vol. 35, 2008, pp. 1213–1227.
- [51] J. Blasko, T. Krauthammer, and S. Astarlioglu, *Pressure-impulse diagrams for structural elements subjected to dynamic loads*, University Park, Pennsylvania: PA: The Pennsylvania State University, 2007.
- [52] J. Dragos, C. Wu, and K. Vugts, 'Pressure-Impulse Diagrams for an Elastic-Plastic Member under Confined Blasts', *International Journal of Protective Structures*, vol. 4, Jun. 2013, pp. 143–162.
- [53] J. Dragos and C. Wu, 'Single-Degree-of-Freedom Approach to Incorporate Axial Load Effects on Pressure Impulse Curves for Steel Columns', *Journal of Engineering Mechanics*, vol. 141, Jan. 2015, p. 04014098.

- [54] N. Newmark, 'An engineering approach to blast resistant design', *Transactions of American Society of Civil Engineers*, vol. 121, 1956, pp. 45–64.
- [55] J. Sperrazza, *Dependence of external blast damage to the A-25 Aircraft on peak pressure and impulsedified Pressure-Impulse Blast Damage Model.*, Maryland: Ballistic Research Labs Aberdeen Proving Ground MD Defence Technical Information Center, 1951.
- [56] J. Dragos and C. Wu, 'A new general approach to derive normalised pressure impulse curves', *International Journal of Impact Engineering*, vol. 62, Dec. 2013, pp. 1–12.
- [57] J. Dragos, C. Wu, and D.J. Oehlers, 'Simplification of fully confined blasts for structural response analysis', *Engineering Structures*, vol. 56, Nov. 2013, pp. 312–326.
- [58] T. Dunn, L. Hagler, E. Kokko, C. Noble, I. Darnell, and L. Leininger, *Concrete Model Descriptions and Summary of Benchmark Studies for Blast Effects Simulations*, Washington, D.C.; Oak Ridge, Tenn.: United States. Dept. of Energy; Distributed by the Office of Scientific and Technical Information, U.S. Dept. of Energy, 2005 [http://encompass.library.cornell.edu/cgi-bin/checkIP.cgi?access=gateway\\_standard&url=http://www.osti.gov/servlets/purl/878628-78x5Yg/](http://encompass.library.cornell.edu/cgi-bin/checkIP.cgi?access=gateway_standard&url=http://www.osti.gov/servlets/purl/878628-78x5Yg/). Last accessed on August 31, 2015.
- [59] A.H. Nilson, D. Darwin, and C.W. Dolan, *Design of concrete structures.*, New York: McGraw-Hill, 2010.
- [60] J.K. Wight and J.G. MacGregor, *Reinforced concrete mechanics and design*, Boston; Columbus; Indianapolis [etc.]: Pearson, 2012.
- [61] 'ABAQUS (2014) "ABAQUS Documentation", Dassault Systèmes, Providence, RI, USA'.
- [62] M.D. Kotsovos, 'Failure criteria for concrete under generalized stress', University of London, 1974.
- [63] M.D. Kotsovos and J.B. Newman, 'Generalised stress-strain relations for concrete', *Journal of the Engineering Mechanics Division*, vol. 104, 1978, pp. 845–856.
- [64] M. Kotsovos, *Finite-Element Modelling of Structural Concrete: Short-Term Static and Dynamic Loading Conditions*, CRC Press, 2015 <http://www.crcnetbase.com/doi/book/10.1201/b18496>. Last accessed on April 6, 2016.
- [65] ACI Committee 318, *Building code requirements for structural concrete: (ACI 318-99); and commentary (ACI 318R-99)*, Farmington Hills, Mich.: American Concrete Institute, 1999.
- [66] T. Ngo, P. Mendis, M. Hongwei, and S. Mak, 'High strain rate behaviour of concrete cylinders subjected to uniaxial compressive impact loading', Perth, Australia: 2004.
- [67] C. Qin and C. Zhang, 'Numerical study of dynamic behavior of concrete by meso-scale particle element modeling', *International Journal of Impact Engineering*, vol. 38, Dec. 2011, pp. 1011–1021.
- [68] H. Kolsky, 'An Investigation of the Mechanical Properties of Materials at very High Rates of Loading', *Proc. Phys. Soc. B Proceedings of the Physical Society. Section B*, vol. 62, 1949, pp. 676–700.

- [69] Y. Al-Salloum, T. Almusallam, S.M. Ibrahim, H. Abbas, and S. Alsayed, 'Rate dependent behavior and modeling of concrete based on SHPB experiments', *Cement and Concrete Composites*, vol. 55, Jan. 2015, pp. 34–44.
- [70] B.P. Hughes and R. Gregory, 'Concrete subjected to high rates of loading in compression', *Magazine of Concrete Research*, vol. 24, 1972, pp. 25–36.
- [71] D. Yan, S. Xu, G. Chen, and H. Li, 'Biaxial behaviour of plain concrete subjected to dynamic compression with constant lateral stress', *Structural Concrete*, vol. 15, Jun. 2014, pp. 202–209.
- [72] X. Chen, J. Zhou, and Y. Yan, 'A note on the flexural behavior of concrete under different loading rates', *KSCE Journal of Civil Engineering*, vol. 19, Sep. 2014, pp. 664–666.
- [73] 'Effect of Testing Method and Strain Rate on Stress-Strain Behavior of Concrete', *Journal of Materials in Civil Engineering*, vol. 25, 2013, pp. 1752–1761.
- [74] A. Brara and J. Klepaczko, 'Experimental characterization of concrete in dynamic tension', *MECMAT Mechanics of Materials*, vol. 38, 2006, pp. 253–267.
- [75] Erzar B and Forquin P, 'An experimental method to determine the tensile strength of concrete at high rates of strain', *Proc. Soc. Exp. Mech., Inc. Proceedings of the Society for Experimental Mechanics, Inc.*, vol. 67, 2010, pp. 941–955.
- [76] S. Shiming and S. Yupu, 'Dynamic biaxial tensile–compressive strength and failure criterion of plain concrete', *Construction and Building Materials*, vol. 40, Mar. 2013, pp. 322–329.
- [77] R. Vidya Sagar and M.V.M.S. Rao, 'An experimental study on loading rate effect on acoustic emission based b-values related to reinforced concrete fracture', *Construction and Building Materials*, vol. 70, Nov. 2014, pp. 460–472.
- [78] D. Cotsovos and M. Pavlovic, 'Numerical investigation of concrete subjected to compressive impact loading. Part 1: A fundamental explanation for the apparent strength gain at high loading rates', *CAS Computers and Structures*, vol. 86, 2008, pp. 145–163.
- [79] D.M. Cotsovos and M.N. Pavlović, 'Numerical investigation of concrete subjected to high rates of uniaxial tensile loading', *International Journal of Impact Engineering*, vol. 35, May. 2008, pp. 319–335.
- [80] Z.C. Mu, A.N. Dancygier, W. Zhang, and D.Z. Yankelevsky, 'Revisiting the dynamic compressive behavior of concrete-like materials', *International Journal of Impact Engineering*, vol. 49, Nov. 2012, pp. 91–102.
- [81] P. Bischoff and S. Perry, 'Compression behavior of concrete at high strain-rates', *Material Structures*, vol. 24(6), 1991, pp. 425–450.
- [82] J. Ožbolt, A. Sharma, B. İrhan, and E. Sola, 'Tensile behavior of concrete under high loading rates', *International Journal of Impact Engineering*, vol. 69, Jul. 2014, pp. 55–68.
- [83] H. Wu, Q. Zhang, F. Huang, and Q. Jin, 'Experimental and numerical investigation on the dynamic tensile strength of concrete', *International Journal of Impact Engineering*, vol. 32, Dec. 2005, pp. 605–617.

- [84] P. Rossi, J.G.M.V. Mier, F. Toutlemonde, F.L. Maou, and C. Boulay, 'Effect of loading rate on the strength of concrete subjected to uniaxial tension', *Materials and Structures*, vol. 27, Jun. 1994, pp. 260–264.
- [85] P. Rossi, 'A physical phenomenon which can explain the mechanical behaviour of concrete under high strain rates', *Materials and Structures*, vol. 24, Nov. 1991, pp. 422–424.
- [86] D. Zheng and Q. Li, 'An explanation for rate effect of concrete strength based on fracture toughness including free water viscosity', *Engineering Fracture Mechanics*, vol. 71, Nov. 2004, pp. 2319–2327.
- [87] Q.M. Li and H. Meng, 'About the dynamic strength enhancement of concrete-like materials in a split Hopkinson pressure bar test', *International Journal of Solids and Structures*, vol. 40, Jan. 2003, pp. 343–360.
- [88] Y.B. Lu and Q.M. Li, 'About the dynamic uniaxial tensile strength of concrete-like materials', *International Journal of Impact Engineering*, vol. 38, Apr. 2011, pp. 171–180.
- [89] fib-federation internationale du beton, *fib Model Code for Concrete Structures 2010*, John Wiley & Sons, 2013.
- [90] G.D. Williams and E.B. Williamson, 'Response of Reinforced Concrete Bridge Columns Subjected to Blast Loads', *Journal of Structural Engineering*, vol. 137, Sep. 2011, pp. 903–913.
- [91] Z. Tu and Y. Lu, 'Evaluation of typical concrete material models used in hydrocodes for high dynamic response simulations', *International Journal of Impact Engineering*, vol. 36, 2009, pp. 132–146.
- [92] A.J. Zieliński, 'Model for tensile fracture of concrete at high rates of loading', *Cement and Concrete Research*, vol. 14, Mar. 1984, pp. 215–224.
- [93] L.J. Sluys and R. de Borst, 'Wave propagation and localization in a rate-dependent cracked medium—model formulation and one-dimensional examples', *International Journal of Solids and Structures*, vol. 29, 1992, pp. 2945–2958.
- [94] H. Le Nard and P. Bailly, 'Dynamic behaviour of concrete: the structural effects on compressive strength increase', *Mechanics of Cohesive-frictional Materials*, vol. 5, Aug. 2000, pp. 491–510.
- [95] Z. Bazant, F. Caner, and M. Adley, 'Fracturing Rate Effect and Creep in Microplane Model for Dynamics', *Journal of Engineering Mechanics*, vol. 126, 2000, pp. 962–970.
- [96] X.Q. Zhou and H. Hao, 'Modelling of compressive behaviour of concrete-like materials at high strain rate', *International Journal of Solids and Structures*, vol. 45, Aug. 2008, pp. 4648–4661.
- [97] Y. Hao, H. Hao, and X.H. Zhang, 'Numerical analysis of concrete material properties at high strain rate under direct tension', *International Journal of Impact Engineering*, vol. 39, Jan. 2012, pp. 51–62.
- [98] Z. Song and Y. Lu, 'Mesoscopic analysis of concrete under excessively high strain rate compression and implications on interpretation of test data', *International Journal of Impact Engineering*, vol. 46, Aug. 2012, pp. 41–55.



- [99] G. Cusatis, ‘Strain-rate effects on concrete behavior’, *International Journal of Impact Engineering*, vol. 38, Apr. 2011, pp. 162–170.
- [100] ‘mechanics-and-strength-of-materials’  
<http://www.mathalino.com/reviewer/mechanics-and-strength-of-materials/stress-strain-diagram>.
- [101] S. Fareed, ‘Subsea Pipes under High-Mass Low-Velocity Impacts’, PhD Thesis, Heriot Watt University, 2016.
- [102] N.K. Singh, E. Cadoni, M.K. Singha, and N.K. Gupta, ‘Dynamic Tensile and Compressive Behaviors of Mild Steel at Wide Range of Strain Rates’, *J. Eng. Mech. Journal of Engineering Mechanics*, vol. 139, 2013, pp. 1197–1206.
- [103] M. Langseth, U.S. Lindholm, P.K. Larsen, and B. Lian, ‘Strain-Rate Sensitivity of Mild Steel Grade St52-3N’, *Journal of Engineering Mechanics*, vol. 117, Apr. 1991, pp. 719–732.
- [104] L. Malvar and J. Crawford, *Dynamic Increase Factors for Concrete*, Naval Facilities Engineering Service Center Port Hueneme Ca, 1998.
- [105] A. Remennikov, ‘The State of the Art of Explosive Loads Characterisation’, Wollongong: Australian Earthquake Engineering Society, 2007, pp. 1–25  
<http://ro.uow.edu.au/cgi/viewcontent.cgi?article=7176&context=engpapers>.
- [106] M. Byfield and S. Paramasivam, ‘Catenary action in steel-framed buildings’, *PROCEEDINGS- INSTITUTION OF CIVIL ENGINEERS STRUCTURES AND BUILDINGS*, vol. 160, 2007, pp. 247–258.
- [107] B. Luccioni, R. Ambrosini, and R. Danesi, ‘Analysis of building collapse under blast loads’, *JEST Engineering Structures*, vol. 26, 2004, pp. 63–71.
- [108] *Blast mitigation for structures 1999 status report on the DTRA/TSWG Program*, Washington, DC.: National Research Council (U.S.), National Academy Press, 2000  
<http://site.ebrary.com/id/10068390>. Last accessed on October 9, 2015.
- [109] C.E. Needham, *Blast Waves*, Springer Science & Business Media, 2010.
- [110] S.C. Woodson and J.T. Baylot, *Structural collapse: quarter-scale model experiments*, [Vicksburg, Miss.]: U.S. Army Corps of Engineers, Engineering Research and Development Center, 1999  
<http://www.dtic.mil/cgi-bin/GetTRDoc?AD=ADA369355&Location=U2&doc=GetTRDoc.p>.
- [111] C. Naito, ‘Blast-Resistant Design Considerations’, *ASCENT*, 2011, pp. 28–31.
- [112] D.A. Cendón, G. Morales-Alonso, F. Gálvez, B. Erice, and V. Sánchez-Gálvez, ‘Blast response analysis of reinforced concrete slabs: Experimental procedure and numerical simulation.’, *Journal of Applied Mechanics*, 2012  
<http://AppliedMechanics.asmedigitalcollection.asme.org/article.aspx?articleid=1476935>. Last accessed on October 9, 2015.
- [113] W. Wang, D. Zhang, F. Lu, S. Wang, and F. Tang, ‘Experimental study and numerical simulation of the damage mode of a square reinforced concrete slab under close-in explosion’, *Engineering Failure Analysis*, vol. 27, Jan. 2013, pp. 41–51.
- [114] W. Wang, D. Zhang, F. Lu, S.-C. Wang, and F. Tang, ‘Experimental study on scaling the explosion resistance of a one-way square reinforced concrete slab under a close-in

- blast loading', *International Journal of Impact Engineering*, vol. 49, Nov. 2012, pp. 158–164.
- [115] M. Foglar and M. Kovar, 'Conclusions from experimental testing of blast resistance of FRC and RC bridge decks', *International Journal of Impact Engineering*, vol. 59, Sep. 2013, pp. 18–28.
- [116] D. Kakogiannis, F. Pascualena, B. Reymen, L. Pyl, J.M. Ndambi, E. Segers, D. Lecompte, J. Vantomme, and T. Krauthammer, 'Blast performance of reinforced concrete hollow core slabs in combination with fire: Numerical and experimental assessment', *Fire Safety Journal*, vol. 57, Apr. 2013, pp. 69–82.
- [117] J. Li, C. Wu, and H. Hao, 'An experimental and numerical study of reinforced ultra-high performance concrete slabs under blast loads', *Materials & Design*, vol. 82, Oct. 2015, pp. 64–76.
- [118] D. Zhang, S. Yao, F. Lu, X. Chen, G. Lin, W. Wang, and Y. Lin, 'Experimental study on scaling of RC beams under close-in blast loading', *Engineering Failure Analysis*, vol. 33, Oct. 2013, pp. 497–504.
- [119] A. Freidenberg, A. Aviram, L.K. Stewart, D. Whisler, H. Kim, and G.A. Hegemier, 'Demonstration of tailored impact to achieve blast-like loading', *International Journal of Impact Engineering*, vol. 71, Sep. 2014, pp. 97–105.
- [120] B. Li, A. Nair, and Q. Kai, 'Residual Axial Capacity of Reinforced Concrete Columns with Simulated Blast Damage', *Journal of Performance of Constructed Facilities*, vol. 26, Jun. 2012, pp. 287–299.
- [121] B. Yan, F. Liu, D. Song, and Z. Jiang, 'Numerical study on damage mechanism of RC beams under close-in blast loading', *Engineering Failure Analysis*, vol. 51, May. 2015, pp. 9–19.
- [122] K. Xu and Y. Lu, 'Numerical simulation study of spallation in reinforced concrete plates subjected to blast loading', *Computers & Structures*, vol. 84, Jan. 2006, pp. 431–438.
- [123] L. Yuan, S. Gong, and W. Jin, 'Spallation mechanism of RC slabs under contact detonation', *Transactions of Tianjin University*, vol. 14, Dec. 2008, pp. 464–469.
- [124] X. Lin, Y.X. Zhang, and P.J. Hazell, 'Modelling the response of reinforced concrete panels under blast loading', *Materials & Design*, vol. 56, Apr. 2014, pp. 620–628.
- [125] Y.S. Tai, T.L. Chu, H.T. Hu, and J.Y. Wu, 'Dynamic response of a reinforced concrete slab subjected to air blast load', *Theoretical and Applied Fracture Mechanics*, vol. 56, Dec. 2011, pp. 140–147.
- [126] J. Li and H. Hao, 'Numerical study of concrete spall damage to blast loads', *International Journal of Impact Engineering*, vol. 68, Jun. 2014, pp. 41–55.
- [127] Y. Shi, H. Hao, and Z.-X. Li, 'Numerical derivation of pressure–impulse diagrams for prediction of RC column damage to blast loads', *International Journal of Impact Engineering*, vol. 35, Nov. 2008, pp. 1213–1227.
- [128] H. Hao, G.-W. Ma, and Y. Lu, 'Damage assessment of masonry infilled RC frames subjected to blasting induced ground excitations', *JEST Engineering Structures*, vol. 24, 2002, pp. 799–809.

- [129] C. Wu, H. Hao, and Y. Lu, 'Dynamic response and damage analysis of masonry structures and masonry infilled RC frames to blast ground motion', *Engineering Structures*, vol. 27, 2005, pp. 323–333.
- [130] C. Wu and H. Hao, 'Safe Scaled Distance for Masonry Infilled RC Frame Structures Subjected to Airblast Loads', *J. Perform. Constr. Facil. Journal of Performance of Constructed Facilities*, vol. 21, 2007, pp. 422–431.
- [131] P. Esper, 'Investigation of Damage to Buildings Under Blast Loading And Recommended Protection Measures', Abu Dhabi: 2003.
- [132] Hussein A.T, 'Non-linear analysis of SDOF system under blast load', *Eur. J. Sci. Res. European Journal of Scientific Research*, vol. 45, 2010, pp. 430–437.
- [133] ABS Consulting Ltd, 'Design, materials and connections for blast-loaded structures, Research Report 405', 2006.
- [134] TM5-855-1, Design and Analysis of Hardened Structures to Conventional Weapons Effects, USA: The Departments of Army, Air Force and Navy and the Defence Special Weapons Agency, 1998.
- [135] J. Biggs, *Introduction to Structural Dynamics*, New York: McGraw-Hill Book Company, 1964.
- [136] M.D. Kotsovos and M. Pavlovic, *Structural concrete finite-element analysis for limit-state design*, London: Thomas Telford, 1995 <http://www.icevirtuallibrary.com/content/book/100940>. Last accessed on March 2, 2016.
- [137] M. Ziara, 'The Influence of Confining the Compression Zone in the Design of Structural Concrete Beams', Heriot Watt University, 1993.
- [138] C.R. Hendy and R.P. Johnson, *Designers' Guide to EN 1994-2 Eurocode 4: Design of Steel and Composite Structures. General rules and rules for bridges*, Thomas Telford, 2006.
- [139] *Building Code Requirements for Structural Concrete (ACI 318-08) and Commentary*, American Concrete Institute, 2008.
- [140] M.D. Kotsovos, *Compressive force-path method: unified ultimate limit-state design of concrete structures*, 2013 <http://dx.doi.org/10.1007/978-3-319-00488-4>. Last accessed on March 2, 2016.
- [141] M.R. Collins, F.J. Vecchio, R.G. Selby, and P.R. Gupta, 'The Failure of an Offshore Platform', *CONCRETE INTERNATIONAL -DETROIT-*, vol. 19, 1997, pp. 28–36.
- [142] 'Shock collapse sparks lift slab fears and safety experts urge car park review', *New Civil Engineer*, Mar. 1997, pp. 3–4.
- [143] Institution of Structural Engineers (Great Britain), Great Britain, and Department for Communities and Local Government, *Manual for the systematic risk assessment of high-risk structures against disproportionate collapse*, 2013 <http://app.knovel.com/hotlink/toc/id:kpMSRAHRSH/manual-for-the>. Last accessed on March 30, 2016.
- [144] D.M. Cotsovos, N.D. Stathopoulos, and C.A. Zeris, 'Behavior of RC Beams Subjected to High Rates of Concentrated Loading', *J. Struct. Eng. Journal of Structural Engineering*, vol. 134, 2008, pp. 1839–1851.

- [145] Cotsovos D.M and Pavlovic M.N, 'Modelling of RC beams under impact loading', Proc. Inst. Civ. Eng. Struct. Build. Proceedings of the Institution of Civil Engineers: Structures and Buildings, vol. 165, 2012, pp. 77–94.
- [146] D.M. Cotsovos, 'A simplified approach for assessing the load-carrying capacity of reinforced concrete beams under concentrated load applied at high rates', IE International Journal of Impact Engineering, vol. 37, 2010, pp. 907–917.
- [147] C.M. Morison, 'Dynamic response of walls and slabs by single-degree-of-freedom analysis—a critical review and revision', IE International Journal of Impact Engineering, vol. 32, 2006, pp. 1214–1247.
- [148] CREA Consultants Ltd, 'Offshore Technology Report - OTO 98174. Review of Analysis of Explosion Response', 1999.
- [149] U. Nyström, 'Concrete Structures Subjected to Blast and Fragment Impacts- Numerical Simulations of Reinforced and Fibre-reinforced Concrete', 2008.

## **Chapter 3: Pressure Impulse Diagrams**

### **3.1. Introduction**

The pressure-impulse (P-I) diagram method is a effective tool widely used for the analysis, assessment and preliminary design of structures subjected to extreme loads such as those generated during explosions. P-I diagrams are used for relating the structural response (e.g. beams, plates, shells) to certain characteristics of the imposed loading (peak load, duration, loading rates, etc.) [1]–[3]. Each curve of the P-I diagram describes a certain level of damage sustained by the structural component or structure considered and can be potentially used for assessment of structural safety and resilience. This method is recommended by various design codes [4]–[12].

This chapter begins with a comprehensive discussion of the P-I diagram method, a review of the existing approaches for the derivation of P-I diagrams and an extensive state-of-the-art review of existing formulae used for analytically describing the form of the curves consisting the P-I diagrams. These approaches are classified and discussed on the basis of the techniques and algorithms used, while the formulae (which describe analytically the subject P-I diagrams) are categorised according to the procedures adopted for their formulation/derivation.

Further in the chapter, the efficiency of the P-I diagram method is examined using an elastic beam subjected to a transverse load. Different spatial load distributions and time histories typically used in modelling of extreme and accidental loading events, such as blast loads, are presented and discussed. P-I diagrams are built for the elastic beam under a uniformly distributed pressure load and a number of different time histories. The accuracy of several existing P-I curve formulae is then assessed using the derived P-I diagrams.

### **3.2. Literature Review**

The analysis of (i) data obtained from extensive air blast tests conducted during 1940's and 1950's at Aberdeen Proving Ground in Maryland, USA [13] and (ii) the damage caused to houses by bombs dropped on the UK during the Second World War [14] indicated that P-I diagrams were well suited to describe the damage caused by explosions. In early applications, the P-I diagrams derived from the analysis of the level of damage sustained by masonry houses when subjected to blast loads were successfully applied for the assessment of small civil and industrial buildings [14]. Further attempts to derive P-I diagrams for structures,

humans and military targets using experimental, analytical and numerical methods were made in 1950's [15], [16], 60's [17]–[21], 70's [1]–[3], [22]–[28] and 80's [4], [29], [30]. It was reported in [3], [4] that the level of damage sustained by structures or structural components due to blast loads can be predicted using a unique scaling law which was formulated depending on the normalised target distance and the explosion intensity (associated with the quantity and type of the explosive material used to generate the explosion). The extent of damage was found to be highly sensitive to the form of the pulse and the load rise time [15], [25].

Nowadays, the P-I diagram method is a well know and widely used technique for assessing the peak load and the residual (post-loading) behaviour (e.g. stiffness, load-bearing capacity) of a structure or a structural element subjected to a blast load [5]–[12], [15], [24], [28], [29], [31]–[47], [47]–[64] as well as the evaluation of the safe stand-off distance by overlaying additional 'range-charge weight' curves [28], [32], [42]. The P-I diagrams are usually built for certain types of individual structural elements, e.g., beams, columns, walls, plates, etc., though the application of P-I diagrams to frames [4] and even whole buildings [65] is also possible. Since the description of the load in the P-I diagram method includes the load time history, both maximum pressure and impulse can be evaluated for a chosen failure criteria. Essentially, the P-I diagram is an *iso-damage* curve [24], [29], [32], [66] since, the P-I curve represents a specific level of damage caused to the structure by different combinations of pressure and impulse. It can be seen as a boundary between states characterised by different levels of damage. Each P-I curve is built for a unique combination of loads acting on a specific structural configuration/form and for a specific level of damage and type of failure. Even slight variations in structural geometry, material parameters or in the time history of the load immediately invalidate the diagram. This high sensitivity of the P-I diagrams to various parameters has been intensively studied. The following lists the specific aspects influencing the P-I diagrams:

- geometrical dimensions [38], [58], [60], [67]–[70]
- ductility [35], [51], [57], [68]
- strain rate [51]
- damping ratio [35], [50]
- longitudinal and hoop reinforcement ratios [16], [38], [58], [70]
- reinforcement configuration [55], [69]

- material nonlinearity [54], [61], [63], [64], [71]
- concrete strength [16], [38], [58], [70], [71]
- reinforcement strength [16], [38]
- strength and thickness of FRP retrofitting wraps and strips [53]
- axial force [39], [41], [44]
- number of degrees of freedom [57]
- load time history [25], [28], [30], [33], [34], [36], [41], [45], [46], [59], [63], [71]

Consequently, the P-I diagram method lacks flexibility to a certain extent and could be quite cumbersome especially when it is used for a multi-parametric structural analysis, e.g., for assessment of different degrees of damage in similar structures under different load cases. In this situation a number of P-I curves representing different degrees of structural damage for each geometry, material properties or loading conditions have to be built [13], [16], [20], [35], [38], [39], [41], [42], [44], [46], [50], [51], [53]–[55], [57]–[60], [63], [67]–[71].

It is necessary to point out that the P-I diagram is actually a particular case of a more general *load-impulse* diagram [66]. Abrahamson and Lindberg [28] called the P-I diagram the “*peak load-impulse characterisation scheme*”. The peak load vs. impulse diagram was used in [35], [67] for assessing the response exhibited by a reinforced concrete (RC) beam when subjected to a concentrated impact load. The popularity of the P-I diagram method led, nevertheless, to the use of this term even when other types of loads were considered [29], [32], [35], [67].

A typical form of the P-I diagram, as illustrated in Figure 3.1 and its shape forms a close fit to a rectangular hyperbola.

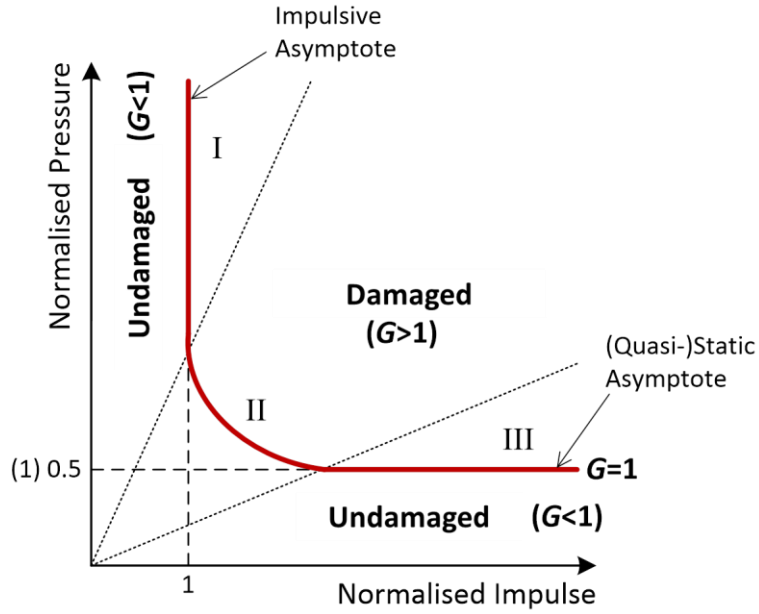


Figure 3.1. Normalised P-I diagram

In Figure 3.1,  $G$  is the limit state function representing the degree of structural damage sustained due to the application of a specific load type which can be expressed as [33], [34], [36], [40], [47], [47], [48], [72]

$$G(I, P) = \lambda / \lambda_{\max} \quad (3.1)$$

where  $\lambda$  is the failure criterion. The region of the diagram for which  $G \geq 1$  corresponds to the state of structural failure.  $G$  can also represent the degree of structural resilience/safety if its formulation in Eq. (3.1) is changed to  $G(I, P) = 1 - \lambda / \lambda_{\max}$  [15], [41]. Different studies have adopted different definitions for  $\lambda$  associated with different aspects of the exhibited structural response such as: the principle deflection at mid-span of a structural element [4], [24], [28], [29], [33], [34], [38], [40], [41], [43]–[46], [50], [52], [55], [57], [61], [63], [64], [68]–[71], [73] or at its supports [40], [50], [52], [60], [70], the maximum sideway deflections and maximum rotations [4], the residual axial load-carrying capacity [37], [38], [53], the maximum strain [56], [74], von-Mises yielding criterion [24], [29] and Tresca yielding criterion [30]. It is important to note here that the maximum mid-span displacement is not a reliable parameter to measure in a damaged structure, especially when brittle modes of failure are exhibited. Therefore, the residual axial load-carrying capacity and other structural parameters, such as residual flexural and shear strength represent a much better choice in the evaluation of the structural damage level.



A typical P-I curve can be divided into a vertical asymptote, a hyperbolic curve and a horizontal asymptote as shown in Figure 3.1. These three parts represent the following regimes: (I) an impulsive regime, (II) a dynamic regime and (III) a (quasi-)static regime [29], [33], [38], [39], [42], [46], [49], [53], [57], [64]. In the case of a normalised P-I diagram the position of the horizontal asymptote varies from 0.5 to 1.0 and strongly depends on the initial part of the load time-history [66]. When the load increases slowly without generating any inertia effects, the asymptote crosses the normalised pressure axis at 1.0 and is called static. When the load has zero rise time, i.e., step load, the inertia effects are generated and the asymptote crosses the normalised pressure axis at 0.5. The latter asymptote is called quasi-static. For a load with a relatively short rise time (time from load start to peak) the position of the (quasi-)static asymptote is in between 0.5 and 1.0 depending on the degree of the inertia effects generated [66]. Further in this work, the horizontal asymptote is referred to as static or quasi-static depending on the form of the imposed pulse load. When the loading regime is not defined as either static or quasi-static, the asymptote is referred to as (quasi-)static. The P-I curve in the dynamic domain is also sensitive to the load rise time, thus loads with finite rise time may result in series of peaks and dips in the elbow of the curve [66]. This is demonstrated by the P-I diagram generated using the sinusoidal time history later shown in Section 3.5.

The impulsive and (quasi-)static asymptotes are distinctive features of the P-I curves. The orientations of the asymptotes in parallel to the abscissa and ordinate practically eliminate influence of impulse or pressure in the (quasi-)static and impulsive regimes, respectively, while in the dynamic regime both pressure and impulse are important. Therefore, these three regimes are also called: (I) impulse controlled, (II) pressure-impulse controlled and (III) pressure controlled regime [11]. As mentioned earlier in this section, the shape of the impulse affects only the pressure-impulse controlled regime in a normalised P-I diagram [33]–[35], [66].

The impulsive, dynamic and (quasi-)static regimes depend on the load duration  $t_0$  and the time of maximum structural response  $t_m$  Figure 3.2. A structure is considered to be in the impulsive regime (Figure 3.2a) when its maximum response occurs in the post-loading phase, well after the loading ends, i.e.,  $t_0 \ll t_m$ . In the (quasi-)static regime the maximum structural response develops at the early stage of the loading phase (i.e.,  $t_0 \gg t_m$ ), while the load  $P_0$  remains approximately constant (Figure 3.2b). In the dynamic regime, the structure reaches its maximum response near the time of the load end, i.e.,  $t_0 \approx t_m$  (Figure 3.2c).

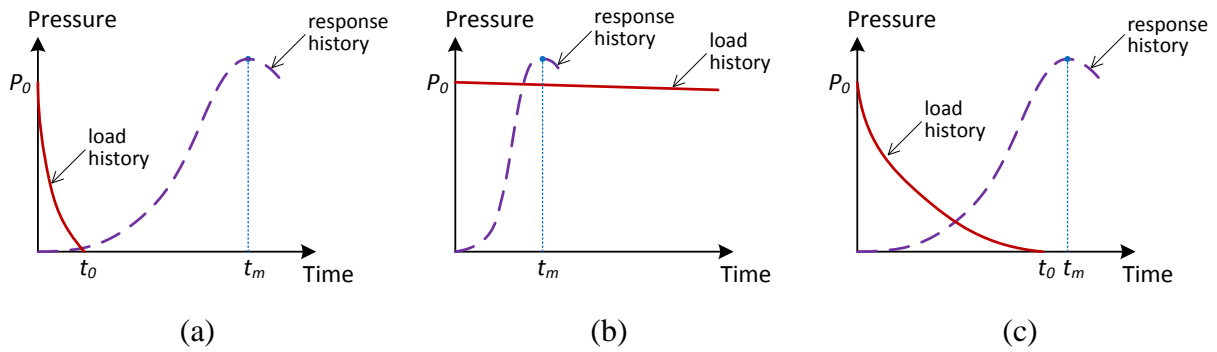


Figure 3.2. Load-response regimes: (a) impulsive, (b) quasi-static and (c) dynamic

It is important to note that the P-I diagram is commonly applied to describe the response of structures subjected to pulse pressure loads generated by external blast loads. The applicability of P-I diagrams for internal (confined) blast loads is complicated by the fact that typical confined explosions are characterised by very irregular pressure time histories with multiple peaks, longer lasting gas pressure and so without any distinguishable pulse load shape [62]. The reason for the irregularity of the pressure time history lays in multiple reflections of the blast waves from surrounding surfaces. This topic is not be considered in this work.

### 3.3. Derivation of P-I diagrams

The process of deriving P-I diagrams usually consists of two stages. The first stage focuses on assessing experimentally, analytically or numerically the degree of damage sustained by the structural element considered, thus creating a point on the P-I plane. In the second stage the next most suitable point on the P-I plane is searched for using an algorithm. Due to the high sensitivity of P-I diagrams to various factors associated with the form of the imposed load and the structural form considered, the choice of a suitable: (i) method for studying/predicting/determining the structural response and (ii) search-algorithm is essential for the derivation of the P-I diagram. The methods employed for predicting the structural response and the search algorithms adopted are discussed below.

#### 3.3.1. Methods of investigating structural response

There are three methods employed for predicting structural response exhibited under high rate loading conditions (i.e. associated with blast and impact problems) that are commonly applied for the derivation of single points on the P-I plane. They can be classified as experimental (i.e. drop-weight or shock-tube tests), analytical or semi-analytical (i.e. based on the use of simplified models that can provide analytical expressions describing certain

aspects of structural response) and numerical modelling (based on the use on nonlinear dynamic finite element analysis).

#### **3.3.1.1. Experimental methods**

The experimental methods employed for the assessment of the structural response (see Section 2.5.1) exhibited due to blast loading have many restrictions mostly introduced by the safety requirements during tests involving explosions and budget constraints. Furthermore, as a result, the number of tests is usually limited and the test data are not sufficient for derivation of whole P-I curves. Additionally, experimental results are often obtained with a significant degree of scatter due to the uncertainties associated with materials, geometry, supporting and loading conditions, etc. This scatter predominantly reflects the difficulty in correlating the measured response to the actual physical state of the specimens; in fact, the measured maximum value of imposed load frequently corresponds to a specimen exhibiting high concrete disintegration as well as low residual load-bearing capacity and stiffness [75], [76]. This stage of structural response has little practical significance as it depends heavily on post-failure mechanisms for transferring the applied loads to the specimen supports. In view of the above, it is difficult to obtain detailed insight into the mechanisms underlying RC structural response from available test data.

The aforementioned drawbacks led to the development of supporting techniques that extend limited sets of test data for derivation of whole P-I curves [68], [69], [71], [74]. This technique is based on using a single-degree-of-freedom (SDOF) system which has been calibrated using available test data.

#### **3.3.1.2. Analytical methods of structural analysis**

The most basic analytical method utilises a SDOF system [11], [24], [28], [29], [32]–[34], [36], [38], [40], [42], [45], [52], [55], [57], [61], [63], [64], [71], [77]. A typical SDOF system simulates the response of an individual structural component and consists of an equivalent mass, stiffness and often damping. The stiffness is modelled using a resistance-deflection relationship, which can differ in complexity (e.g., linear, bilinear and multi-linear) and can account for material and/or geometrical nonlinearities. The SDOF system is formulated to simulate the dominant response of a structure, which in the case of dynamic analysis is the fundamental mode of vibration. As a result, the SDOF system is modelled to fail in accordance with the dominant mode of structural failure. Since local modes of failure may be governing the response of the structure to the blast load, the SDOF model may lead to

an invalid estimate of the post-loading structural condition, especially when the loading is impulsive [38], [40], [52], [55], [57]. Additionally, the SDOF system cannot be used for modelling multiple interacting modes of failure. Special techniques were developed to overcome these drawbacks. For example, a model consisting of two loosely coupled SDOF systems was applied to take into account both the shear and flexural modes of failure of RC beams subjected to localised impact loads [52] and RC slabs under uniformly distributed blast loads [47]. Another technique was developed based on considering transverse velocity fields generated during failure of a rigid-plastic beam [40]. This enabled multiple shear, flexural and combined modes of failure to be taken into account (see Section 3.4.1 for further discussion).

### **3.3.1.3. Nonlinear finite element analysis (NLFEA)**

The most popular numerical approach for derivation of P-I diagrams is the finite element (FE) method [37], [38], [43], [44], [49], [53], [55], [56], [78]. It utilises advanced numerical algorithms and is the most versatile and robust modelling approach. Several advantages of the FE method include high level of structural detailing, the possibility of capturing multiple and combined failure modes, the use of separate complex nonlinear material models in one FE model, and the use of complex interaction models, e.g., for modelling the bond between concrete and steel reinforcement. The major drawback of the FE method lies in the fact that the increasing model complexity leads to a dramatic increase in computation time. This can further increase when multiple analyses are needed due to the probabilistic nature of the problem. NLFEA is used as a safer and more efficient method for investigating a wider range of RC structural forms. It is capable of providing more detailed insight on the mechanisms underlying RC structural response under high-rate loading compared to drop-weight testing. However, as it usually employs dense 3D finite element meshes, combined with complex constitutive material laws implemented through the use of iterative solution strategies, the required computational resources are high. As a result, its use is generally limited to the analysis of relatively simple structural forms. Moreover, its ability for providing realistic predictions of RC structural behaviour is, in most cases, linked with the use of case-study dependent constitutive models often incorporating empirical amplification factors to account for the effect of strain-rate sensitivity on concrete material behaviour [79].

#### **3.3.1.4. Combined methods**

One possible method for the reduction of computational time is based on derivation of an equivalent SDOF system [37], [42], [46], [59], [66] from a detailed FE model. In this method a displacement-controlled nonlinear static FE analysis of a structural element is applied to obtain a displacement-resistance function, equivalent load and mass characteristics needed for the SDOF model. Li and Hao [80] developed a two-step method, which represented a symbiosis between the analytical and numerical methods, to improve computational efficiency in the modelling of structures under blast loads. This method was based on the separation of the analysis process into the forced and free vibration phases. The forced vibration phase was analysed using an elastic-plastic SDOF system while the free vibration phase using a detailed FE model. The authors improved the SDOF system originally proposed by Biggs in [77] by including the shear mode of failure additionally to the flexural one. The continuity between the phases was achieved through the application of the deflection and velocity profiles obtained from the SDOF model as initial conditions in the FE model. As a result, this method did not lose the accuracy of the results due to inherent assumptions of the SDOF system.

El-Dakhkhni et al [57] developed another computationally efficient numerical method which was based on a multiple degree of freedom (MDOF) system derived using a lumped mass approach. The MDOF model was obtained through the discretisation of a structural element into a number of segments. The mass, material and mechanical properties of each segment are concentrated at its centre (i.e., node) leading to a model consisting of a series of discrete connected nodes. Dynamic analysis of this model was carried out using the finite difference technique.

#### **3.3.2. Search Algorithms**

The derivation of P-I diagrams using linear analytical models, e.g., an elastic SDOF model, is usually straightforward and requires only algebraic manipulations on the analytical expressions of model deflections. An illustrative example of such procedure is given below in Section 3.5.2. Complex nonlinear analytical models, as well as the experimental and numerical methods, require application of search algorithms for tracing the P-I limit states. These search algorithms can be generally divided into basic and advanced ones. Although any experimental, analytical or numerical method can potentially be used with any search algorithm, the application of certain methods together with certain algorithms can be limited

by a number of practical and economic factors. For example, it is common to apply the experimental methods in combination with a basic search algorithm because the limited budget of a test programme and the uncertainties associated with the procedure render the application of more advanced search procedures impossible ([68], [69], [71], [74]). In current practice, both the sophisticated SDOF and FE models are used together with the basic search algorithms (e.g., [37], [38], [49], [53], [55], [56]), while only the SDOF models are used with the advanced ones ([47], [48], [72]).

The basic algorithms rely on generating a sufficient number of threshold points followed by curve fitting using single or multi-parametric regression analysis techniques. In this case each point on the P-I curve may be the result of a large number of tests or analyses. This may be expensive in the case of the experimental method or time consuming when the FE method is used. The derivation of P-I diagrams can be carried out using either a pressure-controlled, an impulse-controlled or a mixed one-directional searching algorithm, as shown in Figure 3.3.

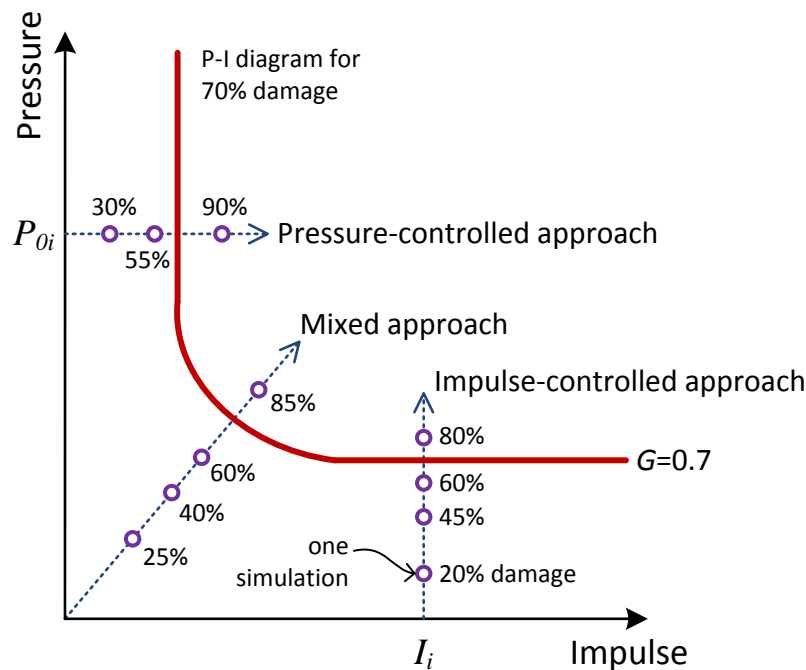


Figure 3.3. Numerical derivation of P-I diagrams

The pressure-controlled search is based on the gradual increase of the duration of the blast load  $t_0$  (and hence its impulse) in each simulation, while maintaining the peak pressure  $P_0$  constant (see Figure 3.4a). The duration  $t_0$  is increased till the limit state condition (e.g.,  $G \leq 1$ , see Eq. (3.1)) is satisfied. This search results in a horizontal series of points on the P-I plane for each  $P_0$  (see Figure 3.3). The impulse-controlled search is based on the gradual

increase of  $P_0$  in each simulation till  $G \geq 1$ . In this case,  $t_0$  is gradually decreased in order to keep the impulse  $I$  constant (see Figure 3.4b). This searching algorithm results in a vertical series of points on the P-I plane generated for each  $I$  (see Figure 3.3). In the mixed search both  $P_0$  and  $I$  (and so  $t_0$ ) gradually increase in accordance with a certain linear proportionality rule  $P_0 = \alpha I$  (see Figure 3.4c), where  $\alpha$  is a proportionality coefficient. This searching algorithm results in a series of points along an inclined line emerging from the origin of the P-I coordinates (see Figure 3.3). The inclination angle of the line is governed by  $\alpha$ .

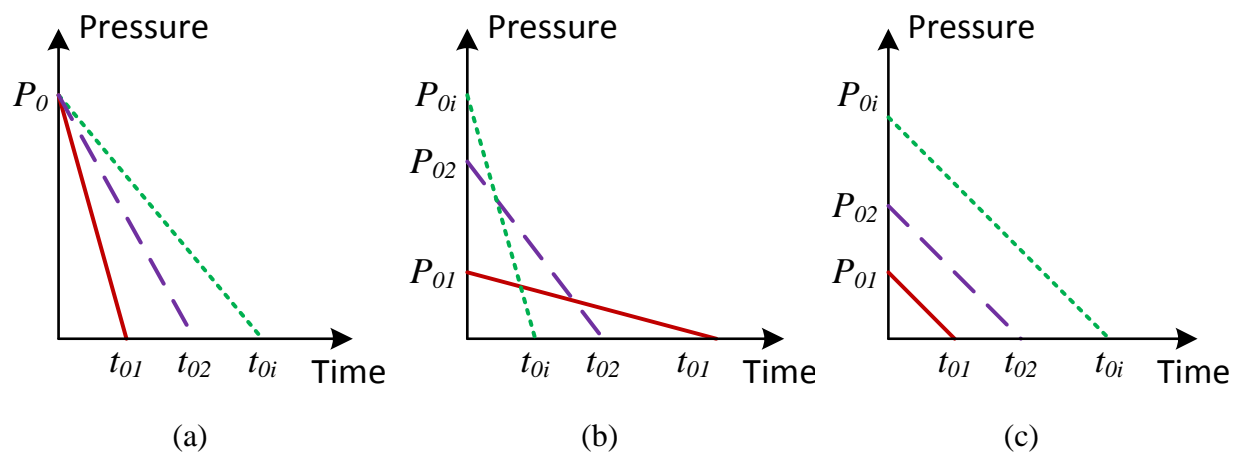


Figure 3.4. Search algorithms for the derivation of P-I diagrams: (a) Pressure-controlled, (b) impulse-controlled and (c) mixed search algorithms

It is important to emphasise again that each point on the P-I plane represents the result of a single computational simulation of an explosion incident. It is highly unlikely that any point on the P-I plane calculated using the FE analysis will exactly correspond to the case when  $G = 1$  (see Figure 3.3). Therefore, linear or nonlinear interpolation methods are used by researchers to realistically determine the location of each threshold point on the P-I curve. Figure 3.3 shows an arbitrary example of the derivation of a P-I diagram for 70% structural damage ( $G = 0.7$ ). As can be seen, the pressure-controlled approach is in essence a horizontal searching algorithm, the impulse-controlled approach is a vertical searching algorithm, whereas the mixed approach is a polar search algorithm. The pressure-controlled search is especially suitable for derivation of the impulsive asymptote, the impulse-controlled search for the (quasi-)static asymptote, while the mixed search for the part of the P-I curve in the dynamic regime. Shi et al [38], for example, applied pressure-controlled and impulse-controlled searching algorithms for the derivation of the impulsive and static asymptotes for 20%, 50% and 80% of structural damage in a RC column. The asymptotes were further used

as input for the closed-form P-I diagram (presented below in Eq.(3.28) of Section 3.4.1). Finally, it should be noted that the combination of these three search algorithms seems to be the most efficient approach for the derivation of P-I diagrams. However, despite its potential efficiency the combined searching algorithm is not used. In practice, the pressure-controlled search is the most popular approach used in many studies (e.g., [37], [38], [49], [53], [55], [56]), probably due to the convenience of changing only one parameter, i.e.,  $t_0$ .

The advanced search algorithms employed for the derivation of P-I diagrams [47], [48], [72] were originally developed using analytical methods. They can be divided into two types of sophisticated search procedures: the point-to-point progress (two directional searching) and single point search (one directional searching). In the former procedure, the search for a new point depends on the locations of previously found points, while in the latter there is no such dependency. These algorithms also differ in computational intensity and stability. Rhijnsburger et al [72] developed the branch-tracing algorithm, which consists of the predictor and corrector stages. In the predictor stage, a new point is located using extrapolation of the slope obtained from the previously calculated points. In the corrector stage, the point location is further adjusted through step by step converging onto the P-I curve until the limit state condition of Eq. (3.1) is satisfied within a certain tolerance.  $G$  was formulated similarly to [33] as the ratio between the maximum displacement calculated for the pressure and impulse at the current point, to the displacement at yield. This algorithm was found to be unstable due to necessity of time discretisation [35], [47].

Soh and Krauthammer [47] proposed a search algorithm based on a large number of dynamic analyses performed for combinations of each pressure and impulse sets within limits specified by the impulsive and (quasi-)static asymptotes. This method is numerically stable, but considerably more expensive computationally.

Ng and Krauthammer [47] developed the ‘threshold curve’ algorithm which is similar to the bisection method. In this numerical procedure each new point is found by setting a new constant value of pressure and gradually converging onto the P-I curve from both sides by increasing/decreasing the impulse with smaller and smaller increments till  $G(I, P) \approx 1$ . This method is also computationally expensive since a large number of analyses are needed to generate a sufficient amount of points on a P-I curve.

Blasko et al [48] derived normalised P-I curves using the bisection method in a polar coordinate system. This method starts by setting the origin (pivot point) of the polar



coordinate system in the ‘damage’ zone, i.e., where  $G(I, P) > 1$ . The region of searching is on the P-I plane and the angle of increment, which is directly related to the number of searched points, is defined. Each point of the P-I curve is searched for on a line connecting the polar origin and the abscissa  $I$  or the ordinate  $P$  using the bisection method till  $G(I, P) \approx 1$ . New points are found by increasing the angle of line inclination and repeating the search. The authors noted that the ideal location of the polar origin lay on the line connecting the origin of the P-I coordinate system and the point of intersection of the impulsive and (quasi-)static asymptotes. A randomly selected origin might reduce the efficiency of the method, since the origin could be too close to or too far from one or both asymptotes.

### 3.4. Classification of P-I diagrams

The final step in the process of derivation of a P-I diagram is the fitting of the points obtained on the P-I plane to derive a formula describing the whole P-I curve. Various formulae describing the P-I diagram have been proposed in the literature starting from 1950’s. Generally, the P-I curve equations can be divided into three groups: closed-form, open-form consistent and open-form mixed formulations.

#### 3.4.1. Closed-form formulation

A P-I curve equation is classified here as closed-form when all the impulsive, dynamic and (quasi-) static regimes are described by a single analytical expression. One of the first closed-form P-I diagram formulae was suggested by Sperrazza [13] based on the analysis of the results of blast tests

$$(P_0 - P_{cr})(I - I_{cr}) = C \quad (3.2)$$

where  $P_0$  is the peak pressure,  $I$  is the total impulse delivered by the blast, i.e., the area under the pulse load time history  $P(t)$ ,  $P_{cr}$  and  $I_{cr}$  are the step load and zero duration impulse required to produce the critical displacement, e.g., at the onset of plastic deformations, and  $C$  is the constant determined from the fitting to experimental results. The total impulse  $I$  was defined in an integral form as

$$I = \int_{t_s}^{t_f} P(t) dt \quad (3.3)$$

where  $t_s$  and  $t_f$  are the times of the start and finish of the part of the  $P(t)$  curve with  $P(t) > P_{cr}$ .

Expression (3.2) was found to be sensitive to the shape of the  $P(t)$  curve [2], [6], [9]. Capitalising on the analysis of rigid-plastic structures (beams, circular plates, circular and cylindrical shells, etc.) under transient distributed and localised loads, Youngdahl [25] suggested that the shape dependency could be effectively eliminated by introducing an additional parameter derived from the pulse load time history, namely, the characteristic time  $\bar{t}$  defined as:

$$\bar{t} = \frac{1}{I} \int_{t_s}^{t_f} (t - t_s) P(t) dt \quad (3.4)$$

Note that  $\bar{t}$  represents the location of the centroid of the critical pulse loading area corresponding to the time of the onset of the critical displacement,  $t_s$ . To determine  $t_s$  and  $t_f$  in the case of a complex shape of the  $P(t)$  curve, Youngdahl introduced an iterative procedure based on the equality

$$P_y(t_f - t_s) = \int_{t_s}^{t_f} P(t) dt \quad (3.5)$$

where  $P_y$  is the static yield load. This procedure was based on the condition of zero initial velocity. As expression (3.2) was already widely used in the military engineering community, Youngdahl adjusted the extended description of the blast-induced structural damage to

$$(\bar{P} - P_{cr})(I - I_{cr}) = C \quad (3.6)$$

where  $\bar{P}$  is the normalised pressure defined as

$$\bar{P} = I/(2\bar{t}) \quad (3.7)$$

It is necessary to point out that Eqs. (3.2), (3.4) and (3.7) transform an arbitrary load time history to an equivalent rectangular shape with the constant pressure  $\bar{P}$  and duration  $\bar{t}$ . Youngdahl validated the developed method for elimination of shape sensitivity using the rectangular, triangular with zero and finite rise time, exponential and sinusoidal load time histories.

Schumacher and Cummings [27] recommended to simplify the expression (3.6) by setting  $P_{cr} = I_{cr} = 0$  when  $P_{cr}$  and  $I_{cr}$  were not known. Consequently they obtained

$$\bar{P} \cdot I = DN \quad (3.8)$$

where  $DN$  is the damage number, which depends only on the pulse pressure.

Abrahamson and Lindberg [28] modified the expression (3.2) into the form of a rectangular hyperbola

$$(P_0/P_{cr} - 1)(I/I_{cr} - 1) = 1 \quad (3.9)$$

They obtained the normalised P-I diagram by plotting Eq. (3.2) in the  $P_0/P_{cr} - I/I_{cr}$  plane. The authors noted that the relationship (3.2) approximated well only the response of simple structures such as beams and plates, which can be accurately represented by equivalent linear elastic and rigid plastic SDOF systems. The analysed load time histories included the rectangular, triangular (with zero rise time), exponential and sinusoidal shapes (see Fig. 2.2). It was reported that the impulsive and static parts of the P-I curves derived for linear elastic SDOF systems coincided for the all three load time histories. The deviation of the P-I curves in the dynamic regime was between 20-40%. The authors also proposed to use combined iso-damage curves for assessment of complex structures such as shells, which can only be accurately represented by multiple-degree-of-freedom systems. These iso-damage curves were obtained as the most conservative envelopes of combinations of the iso-damage curves corresponding to each degree of freedom.

Li and Meng [33] developed an empirical form of the normalised P-I diagram, which was almost insensitive to the pulse shape. The P-I curves were derived for the rectangular, triangular and exponential pulse shapes using the limit state function  $G(i, p) = u_m/u_{cr} = 1$ , where  $u_m$  is the maximum deflection achieved by the structure. The expression of the normalised P-I diagram was postulated as

$$p = n_1/(i - 1)^{n_2} + 0.5 \quad (3.10)$$

where  $p$  and  $i$  are the non-dimensional equivalent pressure and impulse, defined as

$$p = P_0/(u_{cr}K) \quad (3.11)$$

$$i = I/(u_{cr}\sqrt{MK}) = p \int_0^{\tau_0} P(\tau)/P_0 d\tau \quad (3.12)$$

In Eqs. (3.11) and (3.12)  $u_{cr}$  is the critical structural deflection. The non-dimensional parameter  $\tau_0$  is defined as

$$\tau_0 = t_0/\sqrt{M/K} \quad (3.13)$$

where  $t_0$  is the loading duration. The definitions of  $p$  and  $i$  are close to similar dimensionless parameters introduced earlier in [24], [29]. Li and Meng [33] derived the non-dimensional parameters  $n_1$  and  $n_2$  in second order polynomial form by using the least-square fitting of the

formula (3.10) to the response of an undamped elastic SDOF system with mass  $M$  and stiffness  $K$ . The values of  $n_1$  and  $n_2$  found in [33] for the rectangular, triangular and exponential load time histories are presented in Table 3.1.

Load time history	$n_1$	$n_2$
Rectangular (Fig. 2.2a)	0.035	0.850
Triangular with zero rise time (Fig. 2.2b)	0.150	0.700
Exponential (Fig. 2.2g) $C_x = 2.8$ defined in Table 3.2	0.300	0.700

Table 3.1. Coefficients  $n_1$  and  $n_2$  for the normalised P-I diagram [33]

The authors adopted Youngdahl's approach [25] to formulate the coefficients  $n_1$  and  $n_2$  as functions of a single geometric characteristic of the pulse shape, and the location of the centroid. The proposed method proved to be efficient for elastic structures and structural elements subjected to pulse loads of rectangular, triangular and exponential shapes usually associated with external blast loads. However, later studies [35], [46], [63] reported certain limitations of this empirical method, which were attributed to the single-parameter definition of the load shape and the sensitivity of the normalised iso-damage curves to the relationship between the load function and the structural response. The uniqueness of the load-response relationship becomes especially pronounced in the dynamic and the quasi-static regions of the P-I curve.

Later Li and Meng [34] extended their approach to elastic-plastic SDOF systems where the linear resistance given as  $R = Ku$  was substituted by a bilinear elastic-perfectly plastic resistance function  $R(u)$ . It was noted that the response of the elastic-plastic SDOF system was highly dependent on the dimensionless parameters  $\bar{p} = P_0/R_{cr}$  and  $v = R_{cr}/(u_{cr}K)$ , where  $R_{cr}$  is the critical resistance. Three regimes of structural response of the SDOF model were distinguished in the  $v$ - $\bar{p}$  domain: elastic, elastic-perfectly plastic and rigid-perfectly plastic response. A closed-form expression of the dimensionless P-I diagram was developed for the rigid-perfectly plastic response of the SDOF model based on Youngdahl's idea [25] given in Eqs. (3.4) and (3.7). It reads

$$1/\bar{p} + (u_m/u_{cr})(2/t^2) = 1/v \quad (3.14)$$

with

$$\bar{p} = \frac{i}{(2\bar{\tau})} \quad (3.15)$$

$$\bar{\tau} = \frac{p}{i} \int_0^{\tau_0} \tau P(\tau) / P_0 d\tau \quad (3.16)$$

where  $p$  and  $i$  are defined in Eqs. (3.11)-(3.13). The parameters  $i$ ,  $\bar{\tau}$  and  $\bar{p}$  are the dimensionless effective impulse, characteristic time and effective pressure corresponding to Youngdahl's parameters  $I$ ,  $\bar{t}$  and  $\bar{P}$ , respectively, given in Eqs. (3.3), (3.4) and (3.7). The ratio  $u_m/u_{cr}$  is similar to the ratio  $\lambda/\lambda_{max}$  appearing in Eq. (3.1) and represents the level of structural damage. The dimensionless parameter  $r$  can be seen as a measure of ductility of a structure. It is necessary to note that the ratio  $R_{cr}/K$  in the expression for  $v$  represents the elastic yield deflection, which is constant for a given material. As a result, in addition to the loading shape the P-I diagram of Eq. (3.14) is influenced by  $u_{cr}$  (through  $v$ ) even when  $u_m/u_{cr} = 1$ . The authors eliminated this influence by transforming the limit state function  $G(i, p)$  into  $G(i/h_2(v), p/h_1(v))$ , where  $h_1(v)$  and  $h_2(v)$  were the quadratic functions of  $v$  derived for the rectangular, triangular and exponential load time histories using the method of least squares. The validity of such normalisation of  $p$  and  $i$  is questionable when a different time history is considered.

Nystrom [45] analysed linear and rigid-plastic SDOF systems subjected to the load with rectangular, triangular and quadratic decaying time histories. The author proposed to derive the P-I diagram in two forms depending on the known initial data as

$$I/I_{cr} = f_P(P_0/P_{cr}) \quad \text{when } P_{cr} \text{ and } P_0 \text{ are known} \quad (3.17)$$

$$P_0/P_{cr} = f_I(I/I_{cr}) \quad \text{when } I_{cr} \text{ and } I \text{ are known} \quad (3.18)$$

where  $P_{cr} = R_{cr}/2 = Ku_{cr}/2$  and  $I_{cr} = R_{cr}/\sqrt{K/M}$  in the case of the linear elastic material and  $P_{cr} = R_{cr}$  and  $I_{cr} = \sqrt{2R_{cr}u_{cr}M}$  in the case of the rigid-plastic material,  $I$  is defined in Eq. (3.3);  $f_P$  and  $f_I$  ( $f_P \neq f_I$ ) depend on the type of system resistance and the shape of pulse loading.

The main disadvantage of the simplified analytical formulations based on the SDOF system, e.g., [28], [33], [34], [36], [45], lays in the limitation of the mechanism of structural failure to a single mode. Since multiple mode failures occur in real structures, the P-I diagrams generated using the SDOF system may provide invalid estimates of the post loading

condition of the analysed structure. Ma and colleagues [40] derived closed-form expressions of the P-I diagrams for shear and bending failure of simply supported and fully clamped rigid-plastic beams subject to a rectangular pulse (see Fig. 2.2a) using the mode approximation method. The authors extended the model originally proposed by Jones [81] using the transverse velocity fields corresponding to bending modes of beam failure. The improvements included incorporation of the shear modes of failure through allowing for development of shear hinges at the supports. This formulation led to five distinct modes of failure, corresponding to five transverse velocity fields, including development of: (i) shear hinges at supports, (ii) a shear hinge at supports and a bending hinge at mid-span, (iii) stationary bending hinges at supports, (iv) shear hinges at supports and a dynamic bending hinge zone at mid-span, and (v) a dynamic bending hinge zone at mid-span. The analysed beam was considered as passing through different phases of motion depending on the complexity of the transverse velocity profile and so the mode of failure. The failure modes of the beam depended on the end support conditions, the bending strength of the beam  $M_{cr}$ , the half span of the beam  $L$ , the applied constant pressure  $p_0$  (in the rectangular pulse) and the dimensionless shear-to-bending strength ratio  $v = LV_{cr}/2M_{cr}$  (originally introduced in [81]). The normalised P-I diagrams were separately found for the bending and shear types of failure depending on the failure modes as

$$\alpha/i_e^2 + 1/p_e = f_1(v) \quad \text{for shear failure} \quad (3.19)$$

$$k\beta/i_e^2 + 1/p_e = f_2(v) \quad \text{for bending failure} \quad (3.20)$$

where  $i_e$  and  $p_e$  are the dimensionless impulse and pressure defined as

$$i_e = I/\sqrt{2mV_{cr}} = I\sqrt{L/4mvM_{cr}} \quad (3.21)$$

$$p_e = p_0L/V_{cr} = p_0L^2/(2vM_{cr}) \quad (3.22)$$

$\alpha = u_s/L$  and  $\beta = u_{ms}/L$  are the normalised beam deflections at the supports  $u_s$  and mid-span  $u_{ms}$ ,  $f_1(v)$  and  $f_2(v)$  are the parameters depending on the end support conditions (either simply supported or fully clamped), the mode of failure and its transverse velocity profile,  $V_{cr}$  the shear strength of the beam,  $M_{cr}$  is the bending strength of the beam and  $m$  the mass per beam unit length. The parameter  $k$  equals  $2/3$  when the beam fails by developing bending hinges at the supports, otherwise  $k = 1$ . The P-I diagrams of Eqs. (3.19) and (3.20) were built using the limit state function given in Eq. (3.1). In the case of the bending failure, the failure criterion is defined as  $\lambda = u_{ms}$  and  $\lambda_{max} = L\beta$ , while the shear failure is characterised by  $\lambda = u_s$  and  $\lambda_{max} = 0.8\gamma_v h$ . Here  $\gamma_v$  is the average critical shear strain across the beam

section and  $h$  the height of the beam cross-section. Values of  $\beta$  and  $\gamma_v$  are given in Table 3 for different levels of damage. Both the formulas (3.19) and (3.20) are valid for both simply supported and fully clamped beams but in different ranges of the  $v$ - $p_0$  domain.

<b>Parameter</b>	<b>Light damage (%)</b>	<b>Moderate damage (%)</b>	<b>Severe damage (%)</b>
$\beta$	2.5	6	12.5
$\gamma_v$	1	2	3

*Table 3.2. Coefficients  $\beta$  and  $\gamma_v$  for the P-I diagrams for the bending and shear failure of beams, Eqs. (3.19) and (3.20)*

Ma et al. compared their P-I diagrams with those obtained using an elastic-plastic SDOF model and reported a good agreement for the simple bending failure especially in the case of large peak pressure and impulse or severe damage. It should finally be mentioned that since in real structures the combined shear-flexural failure could be equally expected, the uncoupling of the shear and bending resistance introduced in the model used for derivation of the P-I diagrams (3.19) and (3.20) limits their applicability.

Ma and colleagues [50] implemented the mode approximation method developed in [40] for the analysis of RC buried structures subjected to underground blast loads. They analysed a buried beam with a box-type cross-section, which was sufficiently long to assume that the blast loaded side wall of the structure mainly worked in the vertical (shortest) direction. This assumption allowed the study of the response of the side wall using a single vertical unit strip. This unit strip was described using the simply supported, rigid-plastic beam model proposed by Ma and colleagues in [40]. The soil-structure interaction was simplistically incorporated into the unit strip beam model as the effect of damping. The beam had the same five transverse velocity profiles and therefore the five modes of failure as discussed in [40]. The authors derived P-I diagrams for the shear and bending failures of the structure buried in different soils including dry sands, dense sands and saturated sandy clay. It was shown that the P-I diagrams are highly sensitive to the degree of damping.

Huang and colleagues [54] studied simply supported RC beams subjected to blast loads with a rectangular time history using the approach proposed in [40]. To adjust Ma and colleagues' beam for the analysis of RC columns, they introduced a multi-linear elastic-softening resistance-deformation relationship into the beam formulation instead of the rigid-plastic one. This complex material nonlinearity required the addition of the elastic and post-elastic

regimes for the evaluation of each failure mode in the loading and post-loading phases. Since the RC beams were unlikely to develop moving plastic hinges, the two modes featured in this failure type were excluded from the original five mode approximation method [40] and the RC beam was modelled to fail in the shear, bending and combined shear-flexural modes only. The normalised P-I diagrams were built for these three failure modes using the failure criteria based on the beam deflections at the supports and midspan [40]. The authors investigated the influence of the resistance-deformation relationships of different complexity, which included rigid-plastic, elastic-rigid-plastic and multi-linear curves, on the P-I diagrams. All the P-I diagrams were found to be sensitive to the material nonlinearity especially in the part of the diagram corresponding to the dynamic regime.

Shi and colleagues [52] carried out an extensive analytical analysis of simply supported and fully clamped rigid-plastic beams subjected to a triangular pulse (see Fig. 2.2b). The authors applied the method developed in [40] by extending it to include twelve combined shear-flexural response patterns (i.e., modes of failure). In this study two or three modes of failure were associated with each of the five distinct transverse velocity fields introduced in [40] depending on the complexity and sequences of the beam motions during the failure. All the failure modes were formulated as functions of the supporting conditions, the peak pressure  $p_0$ , the collapse pressure  $p_c = 2M_{cr}/L^2$  and the dimensionless shear-to-bending strength ratio  $v$ . The authors derived the normalised P-I diagrams in the following generalised forms

$$[\varphi_1(p_e) \cdot \alpha/i_e^2]^{\lambda_1} + k_1/p_e = f_1(v, p_e) \quad \text{for shear failure} \quad (3.23)$$

$$[\varphi_2(p_e) \cdot \beta/i_e^2]^{\lambda_2} + k_2/p_e = f_2(v, p_e) \quad \text{for bending failure} \quad (3.24)$$

where  $f_1$ ,  $\varphi_1$ ,  $\lambda_1$  and  $f_2$ ,  $\varphi_2$ ,  $\lambda_2$  are two sets of parameters depending on the end support conditions, the type of failure and its transverse velocity profile. The definitions of  $p_e$ ,  $i_e$ ,  $v$ ,  $\alpha$  and  $\beta$  are similar to the ones in Eqs. (3.19) and (3.20). The P-I diagrams were built using the failure criteria similar to those used for Eqs. (3.19) and (3.20), where  $\beta = 12.5\%$  and  $\gamma_v = 0.3\%$  in accordance with [40], [73]. It is necessary to mention that the P-I diagrams of Eqs. (3.19) and (3.20) represent a particular case of the P-I diagrams given above. The authors compared their method with an equivalent SDOF model describing the beam failure in pure shear and bending. It was reported that the SDOF approach yielded accurate results for pure shear failure modes (corresponding to  $v \leq 1$ ) and bending failure modes (corresponding to  $v \geq 1.5$ ), while the estimates generated by the SDOF model for the combined shear-bending modes of failure (corresponding to  $1 \leq v \leq 1.5$ ) were inaccurate.



Fallah and colleagues [36] applied Li and Meng's approach [33] for the elimination of the shape dependency of the P-I diagrams derived using the response of continuous simply supported beams to rectangular, triangular, exponential and concave pulse loads. The elastic-perfectly plastic beams were able to develop plastic hinges at the supports and mid-span. The influence of neighbouring spans was modelled by elastic-plastic rotational springs of the stiffness  $K_\theta$  located at the supports. The Li and Meng's empirical P-I diagram, Eq. (3.10) was used in its generalised form as

$$p = n_1/(i - C)^{n_2} + C \quad (3.25)$$

Using the least-square fitting of the beam response to the formula (3.25), Fallah et al. found that the constant  $C$  equals 1 for elastic and 10 for elastic-perfectly plastic beams. The additional increase in the accuracy of fitting was further achieved by extending the polynomial form of  $n_1$  and  $n_2$  (second order in [33]) to the third order. The dimensionless equivalent pressure  $p$  and impulse  $i$  defined in Eqs. (3.11)-(3.13) took the following forms in the continuous elastic-plastic beam formulation

$$p = P_0 l^4 / (u_{crp} EI) \quad (3.26)$$

$$i = I / \left( u_{crp} \sqrt{EI m / (\kappa l^2)} \right) \quad (3.27)$$

where  $u_{crp}$  is the critical plastic deflection,  $l$  is the beam length and  $EI$  is the beam bending stiffness. The dimensionless parameter  $\kappa = K_\theta l / EI$  defines the structural configuration of the beam, that is, the order of development of the plastic hinges either first at the supports or at the mid-span or simultaneously in all three locations. The authors noted that the suggested method is limited by the fixed positions of the plastic hinges.

Shi and colleagues [38] carried out an extensive numerical study on RC columns subjected to a blast generated uniform pulse with a triangular time history (see Fig. 2.2b). They developed a detailed FE model of the column and carried out an extensive parametric study. The P-I diagrams were derived using the least-square curve fitting of the numerical results in the form

$$(P_0 - P_{cr})(I - I_{cr}) = C(P_{cr}/2 + I_{cr}/2)^D \quad (3.28)$$

where  $C$  and  $D$  are the constants obtained for three degrees of damage: 20%, 50% and 80%. Here 20% damage was considered to be the boundary between low and medium damage, 50% as the boundary between medium and high damage, while 80% as the boundary between high damage and structural collapse. Similar damage classification can be found elsewhere [37], [50], [54], [77]. The values of  $P_{cr}$ ,  $I_{cr}$ ,  $C$  and  $D$  are given in Table 3.3.

Damage	$P_{cr}$ (kPa)	$I_{cr}$ (kPa ms)	$C$	$D$
20%	900	2500	11.5	1.45
50%	1200	3500	12	1.49
80%	1500	6000	12.5	1.54

Table 3.3. Values of  $P_{cr}$ ,  $I_{cr}$ ,  $C$  and  $D$  for the P-I diagram for RC columns subjected to a blast with a triangular time history, Eq. (3.28).

Shi and colleagues [38] suggested to use the following approximate values  $C = 12$  and  $D = 1.5$  for the P-I diagram of Eq. (3.28). It should be pointed out that the form of Eq. (3.28) is similar to the formulas suggested in [66], [72] for the approximation of the dynamic region of the P-I curve (see Section 3.3.2). The FE analysis showed that the failure mode of the RC column depended on the loading regime. In the impulsive loading regime the column failed in shear, in the static loading regime it failed in bending and in the dynamic loading regime it failed in the combined shear-flexural mode. In the parametric study, the authors investigated the influence of various geometrical and material parameters of the RC column on the P-I diagram. The parameters included the transverse  $\rho_s$  and longitudinal  $\rho_l$  reinforcement ratios, the concrete compressive strength  $f_c$ , column height  $h$  and depth  $d$  and the width  $w$  of the cross-section. The parameters were varied in the following ranges  $\rho_s = 0.006-0.032$ ,  $\rho_l = 0.01-0.03$ ,  $f_c = 30-50$  MPa,  $h = 3.6-5.4$  m and  $d = w = 0.4-0.8$  m. These ranges define the validity limits of the P-I diagram of Eq. (3.25), since the P-I curves have been observed to be influenced by the studied parameters in a highly nonlinear manner. The location of the P-I diagram of Eq. (3.28) on the P-I plane is defined by the location of the static  $P_{cr}$  and impulsive  $I_{cr}$  asymptotes. The expressions for  $P_{cr}$  and  $I_{cr}$  were derived in [38] using the least-square fitting method as highly nonlinear functions of the degree of damage.  $P_{cr}$  and  $I_{cr}$  were for example given for 50% damage as

$$P_{cr}(50\%) = 143 \ln\left(\frac{\rho_s}{0.01}\right) + 320 \ln\left(\frac{\rho_l}{0.01}\right) + 63 \exp\left(\frac{f_c}{30}\right) + \quad (3.29)$$

$$+ 1000 \left(\frac{h}{4}\right)^{-1.39} + 2639 \left(\frac{d}{0.6}\right) + 318 \ln\left(\frac{w}{0.6}\right) - 2271$$

$$I_{cr}(50\%) = 837 \left(\frac{\rho_s}{0.01}\right) + 36 \left(\frac{\rho_l}{0.01}\right) + 235 \exp\left(\frac{f_c}{30}\right) + \quad (3.30)$$

$$+ 1000 \left(\frac{h}{4}\right)^{-0.274} + 2271 \exp\left(\frac{d}{0.6}\right) - 998 \ln\left(\frac{w}{0.6}\right) - 5286$$

In derivation of the P-I curves Shi and colleagues used the limit state function similar to the one given in the Eq. (3.1), where  $\lambda$  represented the residual load-carrying capacity of a damaged RC column and  $\lambda_{max}$  the design load-carrying capacity of an intact column according to ACI Code [82]. The authors further used a method proposed in [41] for derivation of an equivalent elastic-perfect plastic SDOF model of the RC column, which was used to generate the P-I curves for different levels of damage. The maximum mid-height column deflection  $u_m$  was used in this case as the failure criterion. The values of  $u_m$  corresponding to three boundary levels of damage were found using the detailed FE model of the 4m high column with  $d = w = 0.5$  m,  $\rho_s = \rho_l = 0.01$  and  $f_c = 40$  MPa.  $u_m < 20$ mm corresponded to the low damage (<20%),  $20 \text{ mm} < u_m < 40 \text{ mm}$  to the medium damage (20-50%),  $40 \text{ mm} < u_m < 60 \text{ mm}$  to the high damage (50-80%), while  $u_m > 80$ mm leads to column collapse (>80%). This damage evaluation procedure seems to be rather arbitrary and further stresses the weakness of the damage criterion based on the maximum midspan deflection. The obtained P-I curves were compared with those derived in Eq. (3.28). The discrepancy between the P-I curves produced by different models was especially pronounced in the static and dynamic regions. This was attributed to the material idealisation and the neglecting of the strain rate effects in the SDOF model.

Hao and colleagues [78] carried out reliability analysis on RC columns subjected to blast generated loads. The P-I diagram of Eq. (3.28) developed in [38] together with the formulas for  $P_{cr}$  and  $I_{cr}$  corresponding to different levels of damage were used as the limit state criterion for the probabilistic assessment of the damage developed in the analysed columns.

Thiagarajan and colleagues [55] developed P-I diagrams for four types of RC columns subjected to blast loads with triangular time histories using advanced detailed FE analysis and a SDOF model developed in [83]. The columns had a 350 mm by 350 mm square cross-section, a height of 3480 mm, eight 25 mm diameter longitudinal reinforcing bars and 10 mm diameter stirrups which differed in spacing and configuration. The configurations of the stirrups included two types of rectangular ties, spiral and seismically detailed transverse reinforcement. The authors used the damage criterion based on the mid-height deflection of the column. This may be seen as a drawback, since more adequate failure criteria, e.g., based on the axial load carrying capacity [37], [38], [53], are readily available in the case of detailed FE modelling. The P-I diagrams were built for each column for low, medium and high levels of damage in order to investigate the effect of confinement developed by the

analysed transverse reinforcement configurations. It was found that mainly the parts of the P-I curve in the impulsive and dynamic regions were influenced by the configuration of the stirrups. The column with the seismically detailed transverse reinforcement showed superior resistance to the blast loads as it provided the highest degree of concrete confinement at the plastic hinge regions and the highest lateral support for the longitudinal reinforcement. The authors also reported high discrepancy between all the results provided by the detailed FE model and the SDOF model especially in the impulsive and dynamic regions of the P-I diagrams. The SDOF model tended to overestimate the strength of the RC columns. The authors also derived a closed-form analytical expression for the P-I diagram using multi-variable nonlinear regression analysis. Better correlation was achieved when the impulse  $I$  in the formula was substituted with the load duration  $t_0$ . As a result, the P-I diagram in terms of reflected pressure  $p_r$  vs.  $t_0$  was given as

$$\log(p_r) = A + B \times \Delta + C \times Col + D \times \log(t_0) + E \times \log(t_0^2) + F \times \log(t_0^3) \quad (3.31)$$

where  $A$ ,  $B$ ,  $C$ ,  $D$  and  $E$  are regression coefficients depending on the configuration of stirrups and  $\Delta$  ( $= 0.1 \div 5.25\%$ ) is the damage level of the column. Unfortunately, Thiagarajan et al. did not provide in their paper the values and meanings of the parameters  $F$  and  $Col$ .

### 3.4.2. Open-form consistent formulation

The first type of the open-form consistent approach is built on describing a P-I diagram using two different analytical expressions. Zhu and colleagues [30] analysed three different types of simply supported rigid perfectly plastic structures subjected to uniform pressure loads with rectangular, triangular (with zero and finite rise time) exponential and sinusoidal time histories (see Fig. 2). The structures included a beam, a circular plate and a cylindrical shell reinforced by circular rings. The authors used Youngdahl's approach [25] for the elimination of load shape sensitivity in development of the normalised P-I diagrams (termed "characteristic curves" and plotted in the  $P_y/\bar{P} - I/I_{cr}$  plane) that were given as

$$\frac{6}{5} \left( \frac{I}{I_{cr}} \right)^2 \left( 1 - \frac{P_y}{\bar{P}} \right) = 1 \quad \text{when } P_y/\bar{P} \leq 2 \quad (3.32)$$

$$\left( \frac{I}{I_{cr}} \right)^2 \left( 1 - \frac{4P_y}{5\bar{P}} \right) = 1 \quad \text{when } P_y/\bar{P} \geq 2 \quad (3.33)$$

where  $I$  and  $\bar{P}$  are respectively given in Eqs. (3.3) and (3.7). The static yield load  $P_y$  was estimated using the Tresca yield criterion. The expressions (3.32) and (3.33) were validated using all three types of the analysed structures under the rectangular load time history and produced P-I curves with a scatter of less than 5%. To eliminate the uncertainty concerning the integration limits  $t_s$  and  $t_f$  in Eq. (3.4), Zhu and colleagues proposed to calculate  $\bar{t}$  by integrating over the whole time interval, i.e.,  $[0, \infty)$ . In this case  $\bar{t}$  takes the following form

$$\bar{t} = \frac{1}{I} \int_0^{\infty} tP(t)dt \quad (3.34)$$

Despite being convenient this approach resulted in high discrepancy in the dynamic and impulsive parts of the P-I curves derived for different load time histories.

The second type of the open-form consistent approach is based on three different analytical expressions describing the P-I diagram in the three different regimes. In this method rigorous formulas are derived for the impulsive and (quasi-)static asymptotes, while the curve in the dynamic regime is approximated by an analytical expression.

Krauthammer and colleagues [35], [66] derived the expressions for the impulsive and static asymptotes of the P-I curve from the free and forced vibration responses of an undamped elastic SDOF system subjected to a rectangular load pulse as

$$p \sin(0.5i/p) = 0.5 \quad 1 \leq i \leq 0.5\pi \quad \textit{impulsive asymptote} \quad (3.35)$$

$$p = 0.5 \quad i > 0.5\pi \quad \textit{static asymptote} \quad (3.36)$$

where  $p$  and  $i$  are defined in Eq. (3.10). The transition between the asymptotes takes place at the point ( $i = 0.5\pi$ ,  $p = 0.5$ ). The same technique was applied for the undamped elastic SDOF system subjected to a triangular pulse, which resulted in the following expressions for the impulsive and static asymptotes, respectively,

$$(2i/p^2)^2 = 2 + (2i/p)^2 - (4i/p) \sin(2i/p) - 2 \cos(2i/p) \quad 1 \leq i \leq 1.166 \quad (3.37)$$

$$(2i/p) = \tan[(2i/p)(1 - 0.5/p)] \quad i > 1.166 \quad (3.38)$$

Another method for derivation of the P-I curves is based on the principle of conservation of mechanical energy [24], [29], [35], [41], [58], [66]. In this method the impulsive and (quasi-)static loading regimes are described by two distinct energy formulations. In the impulsive regime the maximum response of the undamped elastic SDOF system occurs in the free vibration (i.e., post-loading) phase. As the duration of the load is very short as compared to the time of the maximum response (see Figure 3.2a), the system displacement at the end of

the forced vibration phase can be ignored. Therefore, the energy of the pulse load is delivered to the system only through the initial velocity, i.e., the kinetic energy  $T$ . In the conservative SDOF system,  $T$  is balanced by the potential energy represented in terms of the total strain energy  $E$  stored in the system at the time of the maximum response [27], [28], [58]. This leads to the following condition for the impulsive asymptote of the P-I curve:

$$T = E \quad \text{impulsive asymptote} \quad (3.39)$$

In the quasi-static loading regime the peak system response occurs at the beginning of the forced vibration phase, while the maximum applied load (e.g., maximum pressure  $P_0$ ) remains approximately constant and the dynamic effects can be ignored (see Figure 3.2c). Under these conditions the maximum work  $W$  done by  $P_0$  to move the conservative SDOF system to its maximum displacement  $u_m$  equals the total strain energy gained by the system. This yields the (quasi-)static asymptote of the P-I curve as

$$W = E \quad \text{quasi-static asymptote} \quad (3.40)$$

$T$ ,  $E$  and  $W$  in the case of the undamped elastic SDOF system [35] with mass  $M$  and stiffness  $K$  have the following forms

$$T = I^2/2M \quad (3.41a)$$

$$E = Ku_f^2/2 \quad (3.42b)$$

$$W = P_0u_f \quad (3.43c)$$

In the case of a SDOF system with an elastic-perfectly plastic displacement-resistance function, the final system deflection  $u_f$  is divided into its elastic  $u_{el}$  and plastic ( $u_f - u_{el}$ ) parts. The expression for  $E$  takes the following form [58]

$$E = Ku_{el}(u_f - u_{el}/2) \quad (3.44)$$

The dimensionless impulsive and static asymptotes can be obtained as  $i = 1$  and  $p = 0.5$ , respectively, after substituting the Eqs. (3.41a) into Eqs. (3.39) and (3.40). The expressions of the impulsive and (quasi-)static asymptotes derived for several other simple SDOF systems can be found elsewhere [47], [61], [66].

The described open-form methods can only be a convenient tool for derivation of the P-I curves in the impulsive and (quasi-)static domains. The curves in the dynamic domain are approximated by a number of analytic functions. Commonly, hyperbolic functions are used for approximation of the systems subjected to triangular and exponential load pulses. Baker et

al. [24], [29] suggested to approximate the dynamic structural response using the hyperbolic tangent squared relationship that reads

$$E = W \tanh^2 \sqrt{T/W} \quad (3.45)$$

Note that for the small values of the argument  $\tanh \sqrt{T/W} \approx \sqrt{T/W}$  and the expression (3.45) approaches the impulsive asymptote of Eq. (3.39), while for the higher values of the argument  $\tanh \sqrt{T/W} \approx 1$  and Eq. (3.45) reduces to the quasi-static asymptote of Eq. (3.40).

Oswald and Skerkut [84] developed an approximate formula describing the iso-damage curve in the dynamic region by fitting of the response of a SDOF system to a rectangular pulse loading

$$(p - A_p)(i - A_i) = 0.4(0.5A_p + 0.5A_i)^{1.5} \quad (3.46)$$

where  $A_p$  and  $A_i$  are the values of the static and impulsive asymptotes, respectively. Krauthammer [66] further generalised this expression to

$$(p - A_p)(i - A_i) = C(A_p + A_i)^D \quad (3.47)$$

where  $C$  and  $D$  are constants. Krauthammer estimated the constants in the expression (3.41a) by fitting it to the P-I curves derived for an undamped perfectly elastic SDOF system subjected to the rectangular and triangular pulses. Thus, the following sets of values were reported

$$A_p = 0.5, A_i = 1.0, C = 0.01, D = 1.0 \quad \text{for rectangular pulse} \quad (3.48)$$

$$A_p = 0.5, A_i = 1.0, C = 0.08, D = 0.3 \quad \text{for triangular pulse} \quad (3.49)$$

### 3.4.3. Open-form mixed formulation

An open-form approach for constructing the P-I diagrams is classified in this paper as ‘mixed’ when the impulsive and (quasi-)static asymptotes are given as analytical expressions derived using, for example, the energy balance method. The P-I curve in the dynamic domain is then derived numerically using curve fitting to the results of FE analyses or various search algorithms. Such an approach allows to build P-I diagrams for SDOF systems with more complex (e.g., bilinear) resistance-displacement functions.

Fallah and Louca [41] adopted the approaches from Li and Meng [33] and Baker et al. [24], [29] in deriving the normalised P-I diagrams based on the dimensional analysis of a SDOF

system with bilinear elastic-plastic hardening/softening resistance displacement function. The conventional set of load time histories including the rectangular, triangular and exponential shapes was considered. The static and impulsive asymptotes were defined in terms of three dimensionless parameters as

$$p = \eta(1 - \varphi\psi^2) + 0.5\varphi(\psi^2 - \varphi\eta^2 + \eta^2\psi^2) \quad \textit{static asymptote} \quad (3.50)$$

$$i = \sqrt{2\eta(1 - \varphi\psi^2) + \varphi(\psi^2 - \varphi\eta^2 + \eta^2\psi^2)} \quad \textit{impulsive asymptote} \quad (3.51)$$

where  $p$  and  $i$  are respectively defined in Eqs. (3.11) and (3.12),  $\eta = u_y/u_{cr}$  is the inverse ductility,  $\psi^2 = K_{h(s)}/K$  is the hardening/softening index, while  $u_y$  is the deflection at the yielding and  $K_{h(s)}$  is the hardening/softening stiffness. The hardening/softening parameter  $\varphi$  was set equal to 1 for elastic-plastic hardening and -1 for elastic-plastic softening model. The P-I curve in the dynamic domain was obtained by fitting the bilinear response of the SDOF system to the nonlinear response of the FE model of a three pitch corrugated stainless steel blast wall. At least one point in the dynamic domain was required for completing the fitting procedure, which was based on numerical integration of the bilinear and nonlinear resistance-displacement functions. It should be pointed out that the proposed method is only valid for rectangular, triangular and exponential pulse shapes while for other pulse shapes new sets of differential equations have to be solved and new normalised P-I curves have to be derived [61].

The derivation of the dynamic part of the P-I curve was carried out using advanced search algorithms [47], [47], [48], [72] discussed in detail in Section 3.3.2. It is necessary to point out that the calculation of the asymptotes is not required for the algorithms suggested in [47], [48], these numerical procedures can be applied for derivation of entire P-I curves. However, the asymptotes are usually located due to their effectiveness in establishing the position of the pivot point (see Section 3.3.2). Colombo and Martinelli [58] applied the search algorithm proposed in [48] for derivation of the P-I diagrams describing the response of RC and fibre-reinforced concrete circular plates under blast loads. The plates were either simply supported or resting on a Winkler-type soil. The parametric study was carried out where the effects of different material characteristics, plate radius and Winkler's constant were analysed. The authors formulated the static and impulsive asymptotes based on the energy based approach described in Subsection 3.4.2 as



$$P = \frac{R_{cr}(u_f - u_{el}/2)}{L_{el}^*u_{el} + L_{pl}^*(u_f - u_{el})} \quad \text{static asymptote} \quad (3.52)$$

$$I = \left[ \frac{2mR_{cr}(u_f - u_{el}/2)}{\pi r^2} \right]^{1/2} \quad \text{impulsive asymptote} \quad (3.53)$$

where  $R_{cr} = Ku_{el}$  is the critical (yielding) resistance force,  $u_f$  and  $u_{el}$  the final and elastic deflections,  $m$  the mass per unit area and  $r$  the plate radius.  $L_{el}^*$  and  $L_{pl}^*$  are the elastic and plastic load multiplier coefficients obtained using load generalisation with shaper functions.

Li and Hao [70] implemented their two-step method proposed in [80] (see Section 3.5.3 for further discussion) for the sophisticated analysis of simply supported RC beams under blast loads. The authors developed partial P-I diagrams for direct evaluation of the damage degree and extent of the zones of structural damage at the end of the blast loading phase. The elastic-plastic SDOF system applied for the analysis at the blast loading phase could capture both shear and flexural modes of the RC beam failure. The damage criteria for shear and bending types of failure were based on maximum deflections at supports and midspan, respectively. As the blast loading phase was very short, the generated P-I diagrams captured only the brittle shear damage. The latter represented only the initial part of the overall damage developing in the second free vibration phase. The data obtained from the first phase were further used in the second phase for detailed FE modelling of the initial state of the analysed RC beam. It was reported that the partial P-I diagrams derived for the damage levels between 10%-50% were fitted using a simple linear equation

$$P = a \times I + b \quad (3.54)$$

where the coefficients  $a$  and  $b$  were found through fitting the results of the parametric analysis using multi-parametric regression analysis. Li and Hao considered parameters similar to the ones used in their earlier study [38].  $a$  and  $b$  were expressed, for example in the case of 50% damage, in the following forms;

$$a_{50\%} = 0.45f_c + 26.6 \frac{l}{1000} - 240 \frac{d}{1000} - 87.5 \frac{w}{1000} + 3.79 \frac{\rho_1}{0.001} + 6.86 \frac{\rho_s}{0.001} + 57.9 \quad (3.55)$$

$$b_{50\%} = \exp \left[ 0.65f_c + 6.44 \frac{l}{1000} - 4.99 \frac{d}{1000} - 87.5 \frac{w}{1000} + 3.79 \frac{\rho_1}{0.001} + 6.86 \frac{\rho_s}{0.001} + 57.9 \right] \quad (3.56)$$

where  $l$  is the length of the beam, while the definitions of the rest of the parameters are similar to those in Eqs. (3.29) and (3.30). The level of damage obtained from the partial P-I diagrams was then used in the free vibration phase to decrease the Young's modulus of concrete in the shear damage zone and the concrete strength. The developed partial P-I diagrams were used by Li and Hao in their later study [85] for the analysis of three story RC frames subjected to blast loads.

### 3.5. Sensitivity to load time history

#### 3.5.1. Analytical model

This section starts with a short description of an analytical model of an elastic beam subjected to a non-harmonic transverse load that is further used for derivation of P-I diagrams. The model utilises a continuous system formulation based on the Euler-Bernoulli beam theory. Since structural elements such as beams usually have light damping [77], [83], [86], the amount of energy it can dissipate in the short duration of motion is quite small. Thus, the effect of damping can be ignored [77], [86].

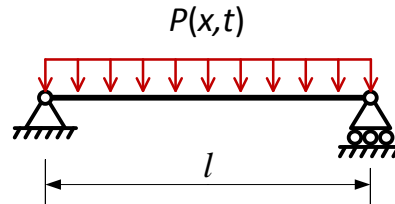


Figure 3.5. Case study beam: geometry, loading and boundary conditions

The continuous Euler-Bernoulli beam formulation leads to a system consisting of a partial differential equation of motion, an external force function, and boundary and initial conditions. This system is solved using eigenfunction expansion (i.e., mode superposition method). Herein the main equations for the analytical model are described, for the detailed equation development see the Appendix. According to the Euler-Bernoulli beam theory the response of the beam to the applied transverse load is described by the following differential equation [83]

$$EIu'''' + m\ddot{u} = P(x, t) \quad (3.57)$$

where  $u(x, t)$  is the transverse deflections,  $u'$  represents a partial derivative with respect to the space variable  $x$  and  $\dot{u}$  with respect to time  $t$ ,  $EI$  is the flexural stiffness of the beam,  $m$  is

the mass per unit length of the beam and  $P(x, t)$  is the excitation force. In order to simplify the solution of Eq. (3.57) the following parameters are used  $l = EI = m = 1$ . Since the described system is linearly elastic the use of adequate material parameters and geometrical dimensions will only introduce a certain scaling factor into the solution, which is not important for the context of this section. The effect of  $P(x, t)$  on the beam highly depends on its spatial distribution  $p(x)$  and its time history  $f(t)$ . Therefore, it is convenient to present  $P$  in the separable form

$$P(x, t) = P_0 p(x) f(t) \quad (3.58)$$

where  $P_0$  is the peak pressure. The solution of Eq. (3.57) for the maximum deflection at the midspan of the simply supported beam shown in Figure 3.5 can be expressed as [87]

$$u_m = EIP_0 \sum_{i=1}^{\infty} \Gamma_i \phi_{i,m} D_{i,m} \quad (3.59)$$

where  $\Gamma_i$  is the modal participation factor [86],  $\phi_{i,m}$  is the maximum value of the  $i^{\text{th}}$  principal mode of vibration at the beam midspan, and  $D_{i,m}$  is the maximum value of the  $i^{\text{th}}$  mode deformation response. In the current formulation,  $\Gamma_i$  represents the effect of  $p(x)$  on  $u_m$  [87]. The upper limits for  $D_{i,m}$  can be expressed as

$$D_{i,m} = \frac{1}{\omega_i} I_i(t_{m,i}) \quad \text{for the forced vibration phase} \quad (3.60)$$

$$D_{i,m} = \frac{1}{\omega_i} \sqrt{I_i^2 + (\dot{I}_i/\omega_i)^2} \quad \text{for the free vibration phase} \quad (3.61)$$

where

$$I_i = \int_0^{t_0} f(\tau) \sin[\omega_i(t_0 - \tau)] d\tau \quad (3.62a)$$

$$\dot{I}_i = \omega_i \int_0^{t_0} f(\tau) \cos[\omega_i(t_0 - \tau)] d\tau \quad (3.74b)$$

In Eqs. (3.60)-(3.62)  $\omega_i$  is the  $i^{\text{th}}$  natural frequency of the beam,  $t_0$  is the loading duration,  $t_{m,i}$  is the time of the maximum deflection of  $i^{\text{th}}$  principal mode of vibration, and  $I_i(t_{m,i})$  can be obtained from Eq. (3.62a) by substituting  $t_0$  with  $t_{m,i}$ . To produce a reasonable accuracy (error less than 1%) it is enough to consider only the first mode of vibration in the static regime, the three firsts modes of vibration in the dynamic regime and the first ten in the impulsive regime [87].

### 3.5.2. Derivation of P-I diagrams and Discussion

In this section the procedure for the derivation of the P-I diagrams for the elastic beam shown in Figure 3.5 is described. One of the most popular failure criteria used to generate P-I diagrams is the maximum structural deflection at midspan [4], [24], [28], [29], [33], [34], [38], [40], [41], [43]–[46], [50], [52], [55], [57]–[61], [63], [64], [68]–[71], [73]. This criterion in the form  $\lambda = u_m$  is used here to define the degree of structural damage. It is also assumed that  $\lambda_{max}=1$ , which is taken to represent the limit state  $G=1$  corresponding to 100% structural damage (see Eq. (3.1) and Figure 3.5).

The procedure for calculation of the P-I diagram can be summarised as follows:

1. The initial value of impulse (or, equivalently,  $t_0$ ) is set.
2.  $u_{m1}$  and  $u_{m2}$  are calculated using Eqs. (3.59)–(3.61).
3. Two values of  $P_0$  are calculated from the equations  $\lambda_{max} = u_{m1}$  and  $\lambda_{max} = u_{m2}$ , where the subscript 1 corresponds to the forced vibration phase while 2 to the free vibration phase.
4. The steps 1–3 are repeated for increasing impulse till sufficient number of points are generated for building two curves corresponding to  $\lambda_{max} = u_{m1}$  and  $\lambda_{max} = u_{m2}$ .
5. The two curves are overlaid (see Figure 3.6) and a decision is made about their validity in different regimes. The  $\lambda_{max} = u_{m1}$  curve is valid in the static regime, the  $\lambda_{max} = u_{m2}$  curve in the impulsive regime and both in turn in the dynamic regime. The final P-I curve is a combination of these two curves.

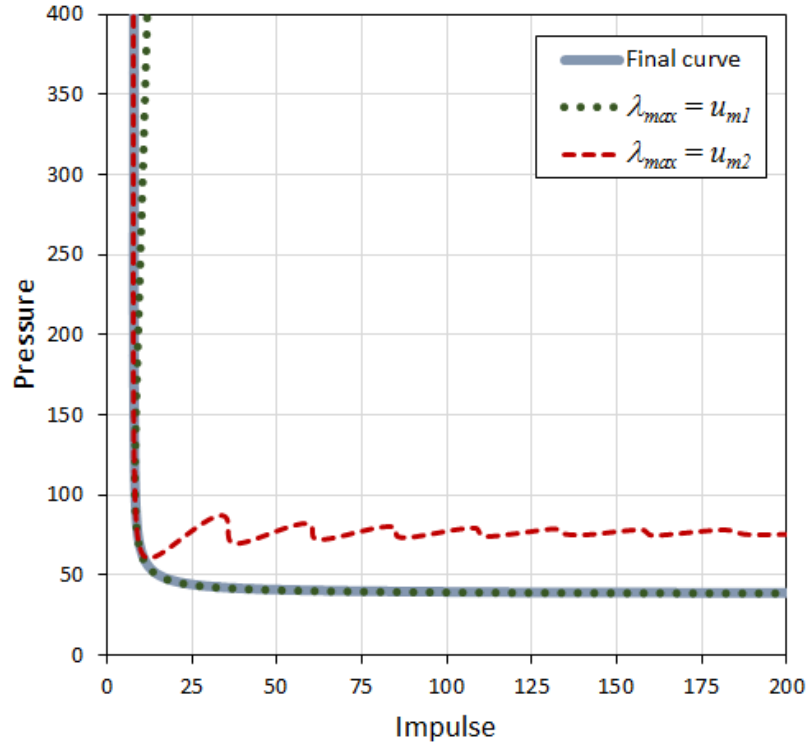


Figure 3.6. Derivation of P-I diagram for the case study beam

The P-I curves calculated for the described beam under a uniform pressure load with rectangular, triangular, concave, exponential and sinusoidal time histories are shown in Figure 3.7.

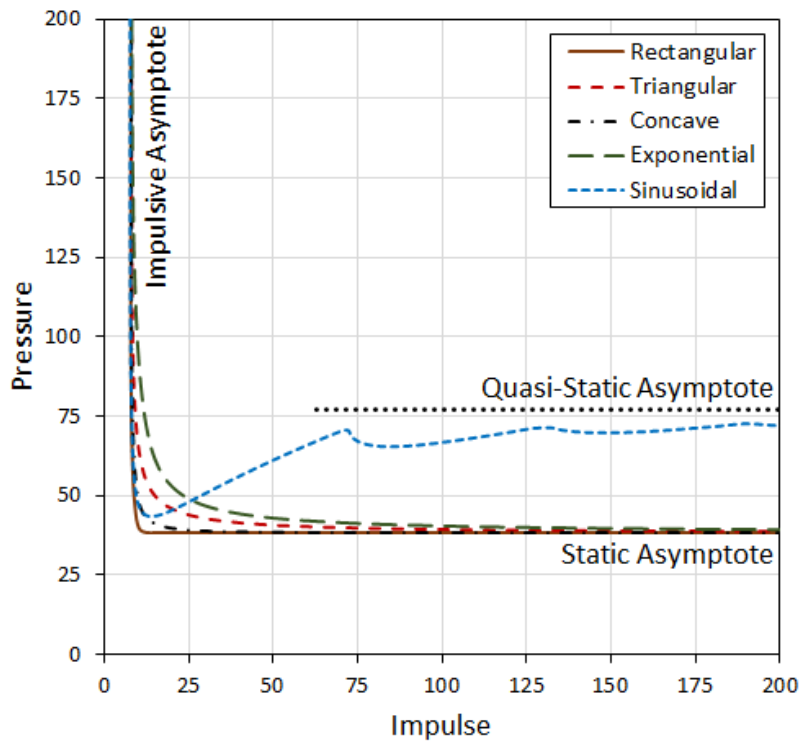


Figure 3.7. P-I diagrams for the pressure load with different time history shapes

As can be seen the analysed time histories, with the exception of the sinusoidal one, result in P-I curves which are close to the conventional hyperbolic shape. Additionally, the divergence between the P-I curves generated for the load time histories with zero rise time (i.e., rectangular, triangular, concave and exponential) mainly develops in the dynamic part of the P-I curves. As can be seen, the higher rate of the load decay (or the smaller value of the delivered impulse) corresponds to the smoother P-I curve in the dynamic regime.

The unconventional shape of the P-I curve generated by the pressure load with the sinusoidal time history can be attributed to the additional sensitivity of the P-I curve to the load rise time  $t_{P0}(= t_0/2)$ , which depends in this case on the load duration  $t_0$  (see Fig. 2.2i). Initially, the growing  $t_0$  results in larger values of impulse delivered to the beam. This situation continues till  $t_0$  becomes equal to the time of the maximum structural response  $t_m$  and the P-I curve approaches the static asymptote (see Figure 3.7). From this point on only a part of the impulse, from the load start to time  $t_m$ , contributes to the maximum structural response ( $u_m$  in the case analysed in this section). This part of the impulse is called the effective impulse in [61]–[64] and was extensively used in the development of methods for derivation of P-I diagrams describing confined explosions. In the period between  $t_0 = t_m$  and  $t_{P0} = t_m$  the effective impulse decreases with growing  $t_0$ . This leads to the need of increasing the peak pressure  $P_0$  in order to achieve the limit state condition  $G = 1$  (see Eq. (3.1)). In this period the P-I curve ascends towards the quasi-static asymptote (see Figure 3.7). Starting from time  $t_{P0} = t_m$ , the P-I curve converges on the quasi-static asymptote,  $t_m$  always coincides with  $t_{P0}$ ,  $P_0$  remains constant while the effective impulse starts growing again with increasing  $t_0$ . In the period when  $t_0 \geq t_m \geq t_{P0}$  the condition  $G = 1$  occurs during the different natural periods of the beam vibration. This leads to the development of a series of peaks and dips in the late dynamic regime of the curve. The influence of  $t_{P0}$  on the effective impulse can be represented in the case of a sinusoidal time history by the relative peak load vs. maximum response ratio  $\tau_{r0} = t_{P0}/t_m = t_0/2t_m$ , which is similar in its essence to the relative load-response relationship  $\tau_r = t_0/t_m$  introduced by Krauthammer and colleagues in [35] and extensively used by Dragos and colleagues in [61]–[64].

Each of the generated P-I curves is then compared with the P-I curves yielded by five closed-form expressions: Sperrazza [13], Youngdahl [25], Schumacher and Cummings [27], Abrahamson and Lindberg [28] and Shi et al. [38]. The aim of this comparison is to examine the fitting ability and applicability the P-I curve formulae given by Eqs. (3.2)(3.6)(3.8)(3.9)

and (3.28). To allow fitting the Abrahamson and Lindberg's P-I curve formula (3.9) was modified into

$$(P_0/P_{cr} - 1)(I/I_{cr} - 1) = C \quad (3.63)$$

where  $C$  is the fitting constant. The results of the comparison are shown in Figure 3.8 to Figure 3.12.

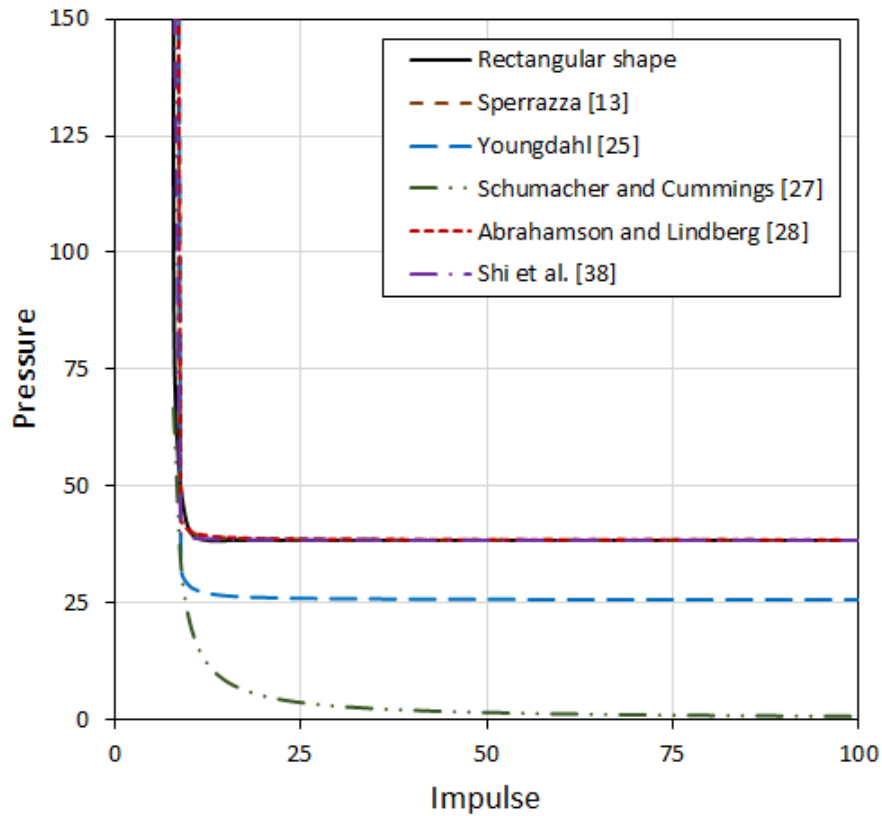


Figure 3.8. Comparison of P-I diagrams for rectangular time history

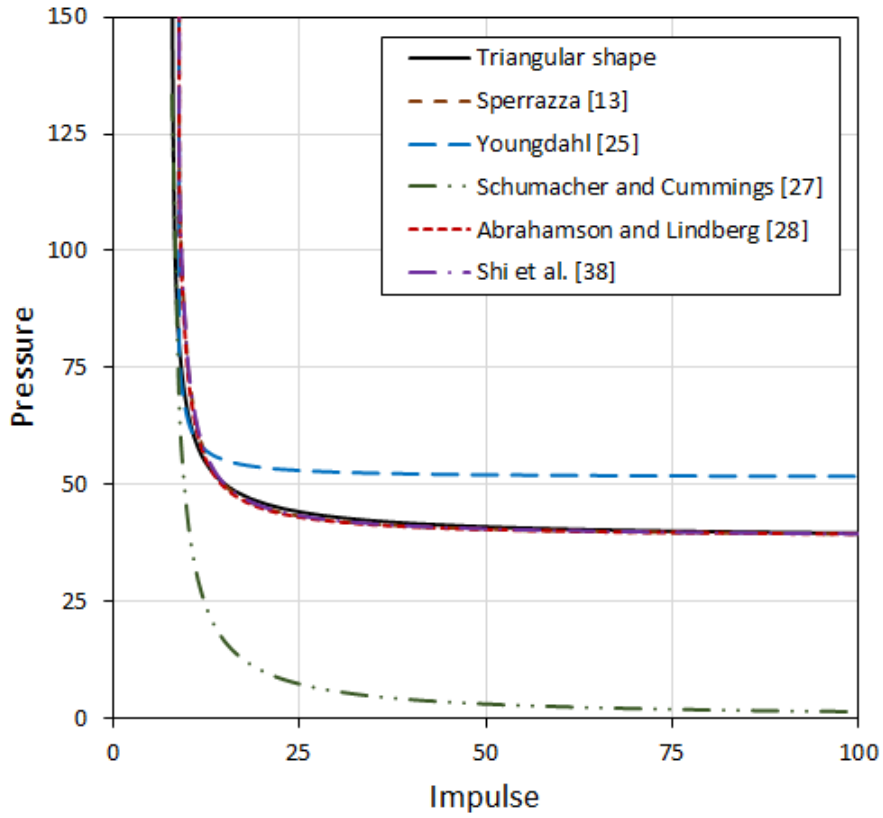


Figure 3.9. Comparison of  $P$ - $I$  diagrams for triangular time history

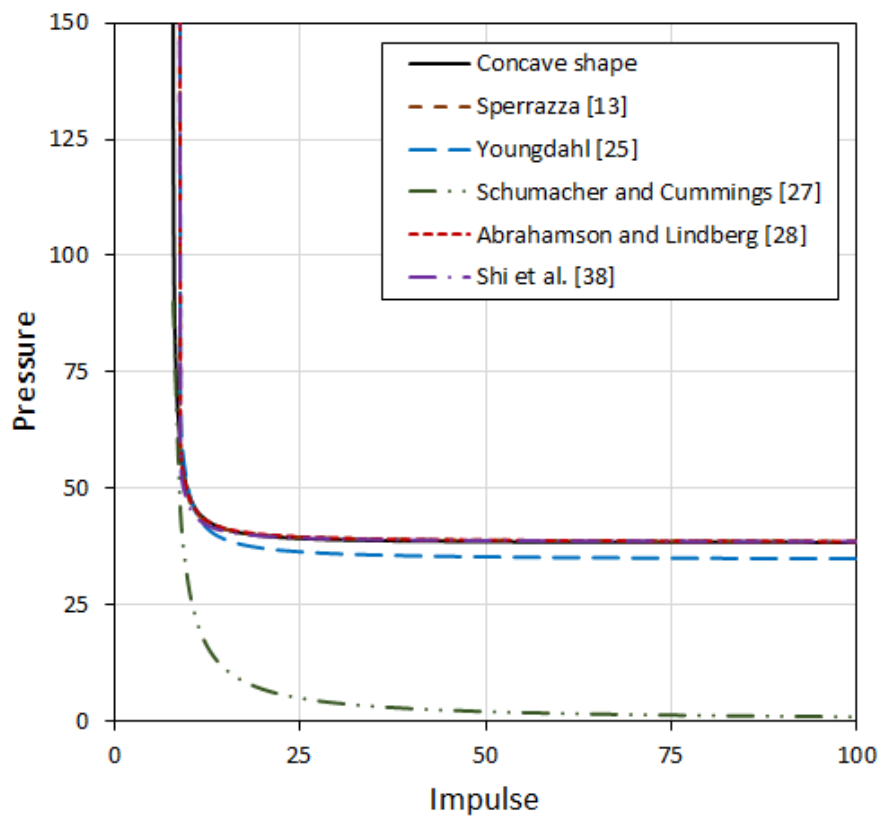


Figure 3.10. Comparison of  $P$ - $I$  diagrams for concave time history



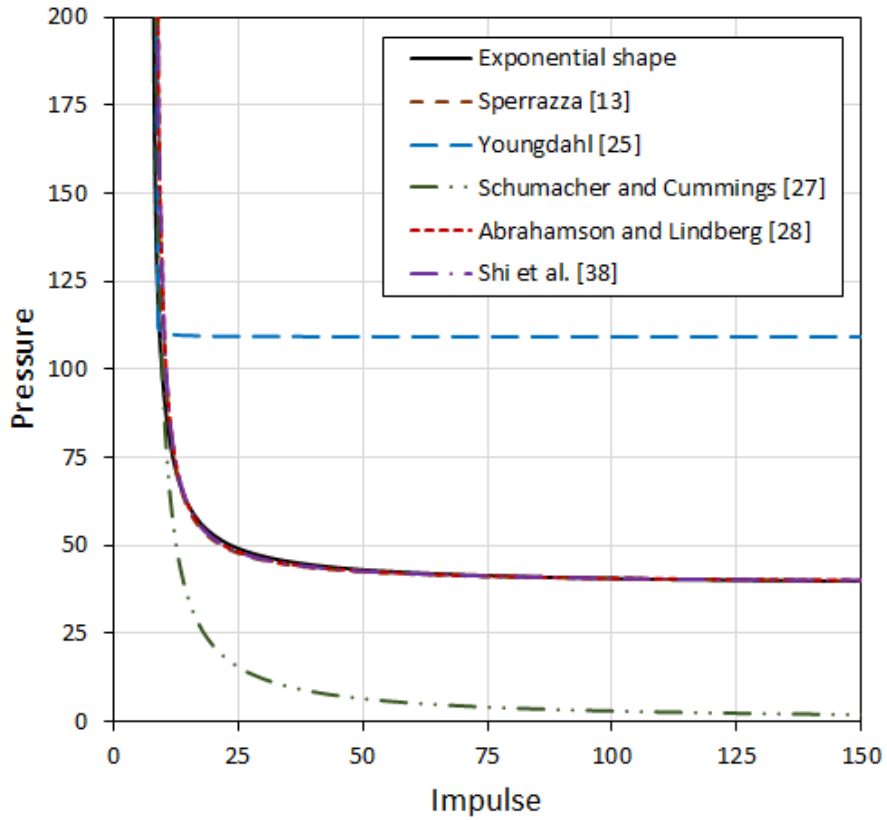


Figure 3.11. Comparison of P-I diagrams for exponential time history

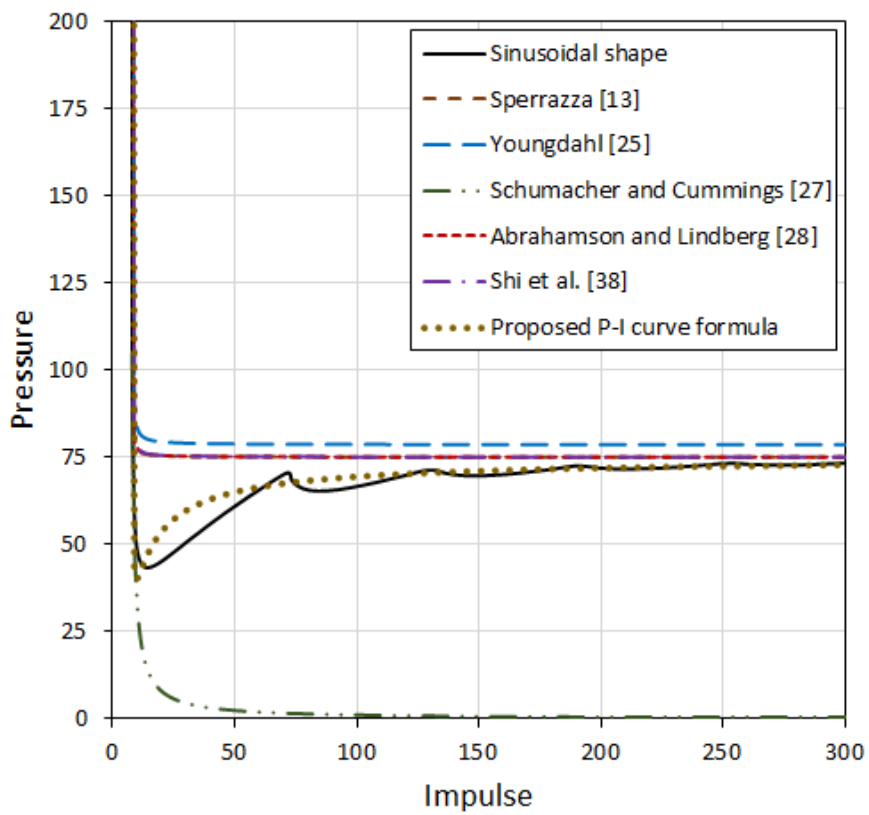


Figure 3.12. Comparison of P-I diagrams for sinusoidal time history

$P_{cr}$  and  $I_{cr}$ , which were required for the analysed P-I curve formulae, were approximately evaluated using the beam model under the loads with large values of pressure and impulse, respectively. The values of the constants in the P-I curve formulae (3.2)(3.6)(3.8)(3.28) and (3.63) obtained from fitting the analytical P-I curves generated for the rectangular, triangular, concave, exponential and sinusoidal time histories are given in Table 3.4.

P-I curve formula		Sperrazza [13]	Youngdahl [25]	Schumacher and Cummings [27]	Abrahamson and Lindberg [28]	Shi et al. [38]	
Constant		C	C	DN	C	C	D
Load time history	Rectangular	4	10	100	0.015	1	0.1
	Triangular	80	20	100	0.25	0	1.4
	Concave	20	35	100	0.07	1	0.9
	Exponential	150	1	100	0.5	1	1.6
	Sinusoidal	5	10	100	0.01	1	0.5

Table 3.4. Fitted values of constants in P-I curve formulas

Figure 3.8 to Figure 3.12 demonstrate that the P-I curve formulae [13], [28] and [38] can very accurately fit most of the analytical P-I diagrams except the unconventional P-I curve generated for the sinusoidal pulse shape. Youngdahl's [25] and Schumacher and Cummings' [27] P-I curve formulae are only consistently accurate in prediction of the impulsive asymptote. The modification introduced by Youngdahl in [25] to account for the effect of shape dependency and further simplifications proposed by Schumacher and Cummings [27] result in a loss of accuracy in the fitting of the P-I curves in the dynamic and static regimes. Consequently, Youngdahl's [25] and Schumacher and Cummings' [27] P-I curve formulae are suitable for the analysis of pressure loads in the impulsive regime only.

### 3.5.3. P-I diagram for finite load rise time history

All of the analysed P-I curve formulae were unable to fit the late dynamic and the early quasi-static parts of the P-I curve generated for the sinusoidal pulse shape (see Figure 3.12). To take into account the unconventional (non-hyperbolic) shape of this P-I diagram it is proposed to modify the static asymptote  $P_{cr}$  in the P-I curve formula (3.28) into

$$\bar{P}_{cr} = P_{cr}[1 - (A/I)^B] \quad (3.64)$$

where  $A$  and  $B$  are the fitting constants. The curve fitting of the analytical P-I diagram using the P-I curve formula (3.8) with the modification (3.64) yield  $A = 5$  and  $B = 0.85$ . The resulting P-I curve is shown in Figure 3.12.

It is seen that Sperrazza's [13], Abrahamson and Lindberg's [28] and Shi and colleagues' [38] P-I curve formulae proved to be very well adapted for the derivation of the P-I diagrams describing structures subjected to pressure loads with decaying time histories, e.g., the shock waves. Shi and colleagues' P-I curve formula (3.25) with the proposed modification [80] can be successfully used for the generation of P-I diagrams describing structures subjected to pressure loads with varying time of peak pressure in their time histories, e.g., pressure waves. Finally, it is necessary to point out that the described structural system is linear and the drawn conclusion may not hold in the case of more complex structural behaviour.

### 3.6. Sensitivity to axial loads

As previously discussed, each P-I curve represents the same degree of damage caused to a structure or a structural element by the loads with different combinations of peak pressure (or sometimes another type of loading) and impulse on the structure. Thus, the P-I curves are also termed iso-damage curves and accurate modelling of the load time history is especially important for their validity. It is necessary to point out that the P-I diagram is similar to a certain degree to the response spectrum. The main difference lies in the fact that the response spectrum represents the variation of a structural parameter (i.e., displacements) in different loading regimes. On the other hand, the P-I diagram is built for a certain failure criterion, such as maximum structural deflection at mid-span or at supports or residual axial load-carrying capacity. The most popular failure criterion however is the maximum structural deflection mostly due to the simplicity of its application with single-degree-of-freedom (SDOF) systems.

P-I diagrams using the analytical method (described above and fully demonstrated in the Appendix) were derived using the beam mid-span deflection as the failure criterion, i.e.,  $\lambda = u_m$ . The level of axial force and the shape of the time history are defined, and then the procedure previously described for the derivation of P-I diagrams is used. The beam is subjected to the same three levels of axial preload, i.e., zero axial force,  $0.5N_{b1}$  and  $0.9N_{b1}$ . The calculated P-I diagrams are shown in Figure 3.13. As can be seen, the axial loading influences both the location and shape of the P-I diagrams. The growing axial load shifts the P-I curve towards the origin of the coordinate axes signifying the decreasing peak pressure and impulse required to cause failure of the analysed structural system.

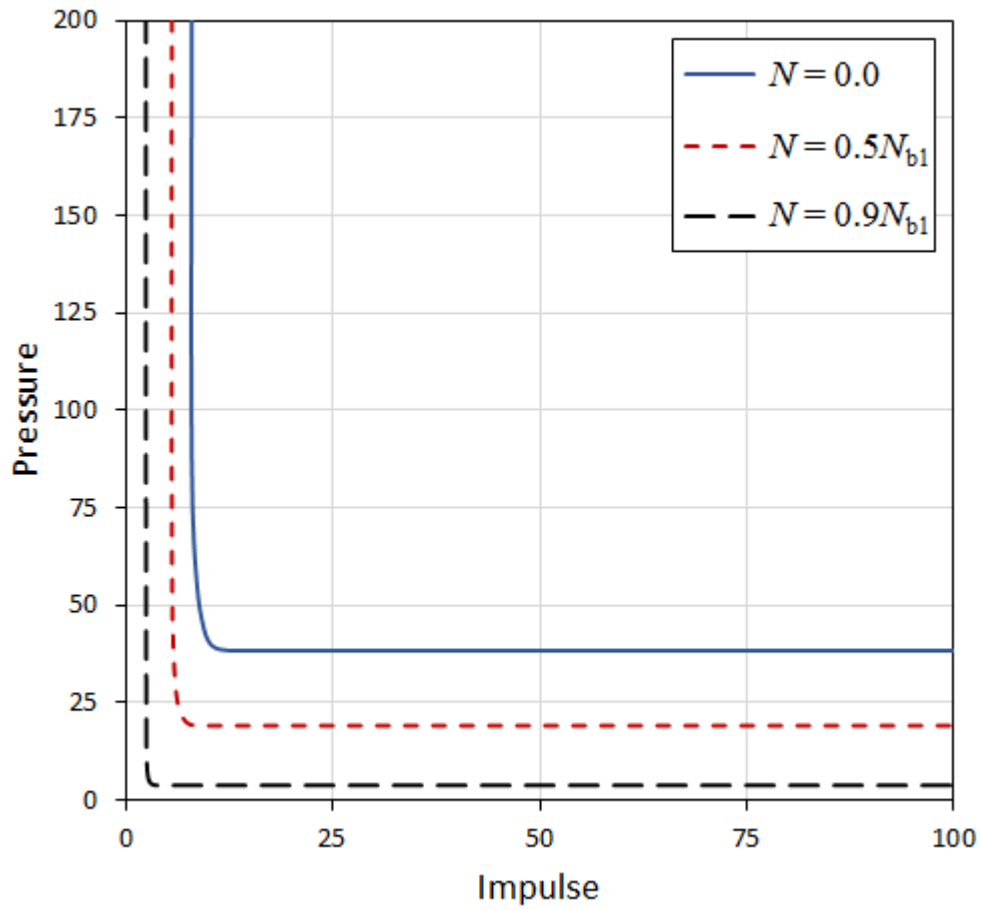


Figure 3.13. *P-I diagrams for the axially preloaded simply supported beam subjected to uniformly distributed transverse blast loading with a rectangular time history.*

### 3.7. Conclusions

Pressure-impulse (P-I) diagrams are an efficient tool widely used for preliminary assessment and prediction of damage (or survivability) of structures subjected to extreme and accidental loads. In this chapter a detailed description of the P-I diagram method and its strengths and weaknesses are presented. The methods of structural analysis and search algorithms applied in the derivation of P-I diagrams are discussed in detail and classified based on their complexity. Further, a comprehensive overview and classification of the existing formulae used for the approximate formulation of P-I curves is presented. The P-I curve formulae are divided into the closed-form, open-form consistent and open-form mixed categories based on the methods of their formulations.

A full and detailed analytical solution of an elastic beam subjected to a transverse load is presented. In this solution the beam is modelled using the continuous formulation based on the Euler-Bernoulli beam theory. The response of the beam to the excitation is decomposed into natural modes of vibration and the number of modes needed for accurate analysis is estimated. The P-I diagrams are derived for the beam under a uniform transverse pressure load with rectangular, triangular, concave, exponential and sinusoidal time histories. The sensitivity of the P-I diagram to the shape of the load time history is demonstrated. The P-I diagrams were then derived for different levels of axial force. It was shown that the P-I diagram is highly sensitive to the level of the axial force.

The efficiency of several closed-form P-I curve formulae is then examined. The P-I curve formulae introduced by Sperrazza [13], Abrahamson and Lindberg [28], and Shi et al. [38] are found to be very flexible in use and provide the best approximations of the P-I curves built for structures subjected to pressure loads with decaying time histories. It is also shown that the P-I diagram has an unconventional (non-hyperbolic) shape when it describes a structure subjected to pressure loads with a varying load rise time. The causes of the unconventional shape of the P-I curve are explained. All the analysed P-I curve formulae are found unable to fit the late dynamic and the early quasi-static parts of the P-I diagram generated for the sinusoidal load time history. A new P-I curve formula that fits such shapes is then proposed based on Shi and colleagues' P-I curve formula [38]. In the proposed formula certain modifications are made to the parameter describing the position of the quasi-static asymptote.

## References

- [1] P. Westine and W. Baker, *Energy Solutions for Predicting Deformations in Blast-Loaded Structures*. Southwest Research Institute, 1975.
- [2] P. Westine and P. Cox, *Additional Energy Solutions for Predicting Structural Deformations*. Southwest Research Institute, 1975.
- [3] J. Greenspon and J GERABM, *Energy Approaches to Structural Vulnerability with Application of the New Bell Stress - Strain Laws*. Defense Technical Information Center, 1976.
- [4] *Blast Resistant Structures*. Command NFE, 1986.
- [5] *Design and Analysis of Hardened Structures to Conventional Weapons Effects*. Departments of the US Army Navy and Airforce, 1990.
- [6] *Method for the Determination of Possible Damage to People and Objects Resulting from Releases of Hazardous Materials*. Voorburg: Committee for the Prevention of Disasters Due to Dangerous Substances; 1992. .
- [7] *A Manual for the Prediction of Blast and Fragment Loadings on Structures*. Texas: Energy UDo, 1992.
- [8] *Guidelines for Evaluating Process Plant Buildings for External Explosions and Fires*. New York: Engineers CfCPSotAIOc, 1996.
- [9] *Design of Blast Resistant Buildings in Petrochemical Facilities. Task Committee on Blast Resistant Design*. New York: Engineers ASoC., 1997.
- [10] *Component Explosive Damage Assessment Workbook (CEDAW)*. Omaha, Nebraska: US Army Corps of Engineers PDC., 2008.
- [11] *The Design of Structures to Resist the Effects of Accidental Explosions - UFC 3-340-02*. US Army Corps of Engineering NFEC, Air Force Civil Engineer Support Agency.
- [12] *Handbook for Blast Resistant Design of Buildings*. New Jersey: John Wiley & Sons, 2010.
- [13] J. Sperrazza, 'Dependence of external blast damage to the A-25 Aircraft on peak pressure and impulsedified Pressure-Impulse Blast Damage Model.', Ballistic Research Labs Aberdeen Proving Ground MD., Defense Technical Information Center, Maryland, 575, 1951.
- [14] D. Jarrett, 'Derivation of the british explosives safety distances', *Ann. N. Y. Acad. Sci.*, vol. 152, pp. 18–35, 1968.

- [15] P. Hodge, 'The influence of blast characteristics on the final deformation of circular cylindrical shells', *J. Appl. Mech. ASME*, vol. 23, pp. 617–624, 1956.
- [16] P. Symonds, 'Dynamic load characteristics in plastic bending of beams', *J. Appl. Mech. ASME*, vol. 20, pp. 475–481, 1953.
- [17] C. White, 'The scope of blast and shock biology and problem areas in relating physical and biological parameters.', *Ann. N. Y. Acad. Sci.*, vol. 152, no. 1, pp. 89–102, 1968.
- [18] D. Richmond, E. G. Damon, E. R. Fletcher, I. G. Bowen, and C. White, 'The relationship between selected blast-wave parameters and the response of mammals exposed to air blast.', *Ann. N. Y. Acad. Sci.*, vol. 152, no. 1, pp. 103–21, 1968.
- [19] I. Bowen, E. R. Fletcher, and D. R. Richmond, *Estimate of man's tolerance to the direct effects of air blast*. Albuquerque NM: Lovelace Foundation for Medical Education and Research, Defense Atomic Support Agency., 1968.
- [20] J. Sperrazza, 'Modelling of Air Blast. In Use of models and scaling in shock and vibration', presented at the Winter annual meeting of the ASME, Philadelphia, Pennsylvania, 1963.
- [21] O. Johnson, 'A blast-damage relationship'. Maryland: Ballistic Research Laboratories Memorandum, 1967.
- [22] C. White, R. K. Jones, E. G. Damon, E. R. Fletcher, and D. R. Richmond, *The Biodynamics of Air Blast*. Ft. Belvoir: LOVELACE FOUNDATION FOR MEDICAL EDUCATION AND RESEARCH ALBUQUERQUE NM., Defense Technical Information Center, 1971.
- [23] E. Damon, J. T. Yelverton, U. C. Luft, and R. K. Jones, *Recovery of the Respiratory System Following Blast Injury*. Ft. Belvoir: LOVELACE FOUNDATION FOR MEDICAL EDUCATION AND RESEARCH ALBUQUERQUE NM., Defense Technical Information Center, 1970.
- [24] W. Baker, P. Cox, P. Westine, J. Kulesz, and R. Strehlow, *A Short Course on Explosion Hazards Evaluation*. San Antonio, Texas: Southwest Research Institute, 1978.
- [25] C. K. Youngdahl, 'Correlation Parameters for Eliminating the Effect of Pulse Shape on Dynamic Plastic Deformation', *J. Appl. Mech.*, vol. 37, no. 3, p. 744, 1970.
- [26] W. Baker, *Explosion in air*. Austin, Texas: University of Texas Press, 1973.
- [27] R. Schumacher and B. Cummings, 'A Modified Pressure-Impulse Blast Damage Model.', Ballistic Research Labs Aberdeen Proving Ground MD., Defense Technical Information Center, Ft. Belvoir, 1977.



- [28] G. . Abrahamson and H. . Lindberg, ‘Peak load-impulse characterization of critical pulse loads in structural dynamics’, *Nucl. Eng. Des.*, vol. 37, no. 1, pp. 35–46, Apr. 1976.
- [29] W. Baker, P. Cox, P. Westine, J. Kulesz, and R. Strehlow, *Explosion hazards and evaluation*. London: Elsevier, 1983.
- [30] G. Zhu, Y. Huang, T. Yu, and R. Wang, ‘Estimation of the plastic structural response under impact’, *Int. J. Impact Eng.*, vol. 4, no. 4, pp. 271–282, Jan. 1986.
- [31] Center for Chemical Process Safety (CCPS) AIoCE, *Guidelines for Vapor Cloud Explosion, Pressure Vessel Burst, BLEVE and Flash Fire Hazards*, 2nd ed. New Jersey: Wiley & Sons, 2010.
- [32] G. Mays, *Blast effects on buildings : design of buildings to optimize resistance to blast loading*. London ;New York: T. Telford ;;American Society of Civil Engineers [distributor], 1995.
- [33] Q. Li and H. Meng, ‘Pressure-Impulse Diagram for Blast Loads Based on Dimensional Analysis and Single-Degree-of-Freedom Model’, *J. Eng. Mech.*, vol. 128, no. 1, pp. 87–92, Jan. 2002.
- [34] Q. Li and H. Meng, ‘Pulse loading shape effects on pressure–impulse diagram of an elastic–plastic, single-degree-of-freedom structural model’, *Int. J. Mech. Sci.*, vol. 44, no. 9, pp. 1985–1998, Sep. 2002.
- [35] T. Krauthammer, S. Astarlioglu, J. Blasko, T. B. Soh, and P. H. Ng, ‘Pressure–impulse diagrams for the behavior assessment of structural components’, *Int. J. Impact Eng.*, vol. 35, no. 8, pp. 771–783, Aug. 2008.
- [36] A. S. Fallah, E. Nwankwo, and L. A. Louca, ‘Pressure-Impulse Diagrams for Blast Loaded Continuous Beams Based on Dimensional Analysis’, *J. Appl. Mech.*, vol. 80, no. 5, p. 051011, Jul. 2013.
- [37] Y. Ding, M. Wang, Z.-X. Li, and H. Hao, ‘Damage evaluation of the steel tubular column subjected to explosion and post-explosion fire condition’, *Eng. Struct.*, vol. 55, pp. 44–55, Oct. 2013.
- [38] Y. Shi, H. Hao, and Z.-X. Li, ‘Numerical derivation of pressure-impulse diagrams for prediction of RC column damage to blast loads’, *Int. J. Impact Eng.*, vol. 35, no. 11, pp. 1213–1227, 2008.
- [39] W. W. El-Dakhakhni, W. F. Mekky, and S. H. Changiz-Rezaei, ‘Vulnerability Screening and Capacity Assessment of Reinforced Concrete Columns Subjected to Blast’, *J. Perform. Constr. Facil.*, vol. 23, no. 5, pp. 353–365, Oct. 2009.

- [40] G. W. Ma, H. J. Shi, and D. W. Shu, 'P-I diagram method for combined failure modes of rigid-plastic beams', *Int. J. Impact Eng.*, vol. 34, no. 6, pp. 1081–1094, Jun. 2007.
- [41] A. S. Fallah and L. A. Louca, 'Pressure-impulse diagrams for elastic-plastic-hardening and softening single-degree-of-freedom models subjected to blast loading', *Int. J. Impact Eng.*, vol. 34, no. 4, pp. 823–842, Apr. 2007.
- [42] D. Cormie, G. Mays, and P. Smith, *Blast Effects on Buildings*, 2nd ed. ICE Publishing, 2009.
- [43] A. A. Nassr, A. G. Razaqpur, M. J. Tait, M. Campidelli, and S. Foo, 'Strength and stability of steel beam columns under blast load', *Int. J. Impact Eng.*, vol. 55, pp. 34–48, May 2013.
- [44] S. Astarlioglu, T. Krauthammer, D. Morency, and T. P. Tran, 'Behavior of reinforced concrete columns under combined effects of axial and blast-induced transverse loads', *Eng. Struct.*, vol. 55, pp. 26–34, Oct. 2013.
- [45] U. Nystrom, *Design with regard to explosions*. Göteborg, Sweden: Chalmers University of Technology, 2006.
- [46] M. Campidelli and E. Viola, 'An analytical-numerical method to analyze single degree of freedom models under airblast loading', *J. Sound Vib.*, vol. 302, no. 1–2, pp. 260–286, Apr. 2007.
- [47] T. B. Soh and T. Krauthammer, *Pressure-impulse diagrams for reinforced concrete slabs*. University Park, Pennsylvania: PA: The Pennsylvania State University, 2004.
- [48] J. Blasko, T. Krauthammer, and S. Astarlioglu, *Pressure-impulse diagrams for structural elements subjected to dynamic loads*. University Park, Pennsylvania: PA: The Pennsylvania State University, 2007.
- [49] Y. Shi Yanchao, *A new method for progressive collapse analysis of RC frames under blast loading*. 2010.
- [50] G. Ma, X. Huang, and J. Li, 'Simplified Damage Assessment Method for Buried Structures against External Blast Load', *J. Struct. Eng.*, vol. 136, no. 5, pp. 603–612, 2010.
- [51] G. Razaqpur, W. Mekky, and S. Foo, 'Fundamental concepts in blast resistance evaluation of structures', *Can. J. Civ. Eng.*, vol. 36, pp. 1292–1304, 2009.
- [52] H. Shi, H. Salim, and G. Ma, 'Using P-I Diagram Method to Assess the Failure Modes of Rigid-Plastic Beams Subjected to Triangular Impulsive Loads', *Int. J. Prot. Struct.*, vol. 3, no. 3, pp. 333–354, Sep. 2012.

- [53] A. A. Mutalib and H. Hao, ‘Development of P-I diagrams for FRP strengthened RC columns’, *Int. J. Impact Eng.*, vol. 38, no. 5, pp. 290–304, May 2011.
- [54] X. Huang, G. Ma, and J. Li, ‘Damage Assessment of Reinforced Concrete Structural Elements Subjected to Blast Load’, *Int. J. Prot. Struct.*, vol. 1, no. 1, pp. 103–124, Mar. 2010.
- [55] G. Thiagarajan, R. Rahimzadeh, and A. Kundu, ‘Study of Pressure-Impulse Diagrams for Reinforced Concrete Columns using Finite Element Analysis’, *Int. J. Prot. Struct.*, vol. 4, no. 4, pp. 485–504, Dec. 2013.
- [56] X. Zhang, H. Hao, and G. Ma, ‘Parametric study of laminated glass window response to blast loads’, *Eng. Struct.*, vol. 56, pp. 1707–1717, Nov. 2013.
- [57] W. El-Dakhkhni, W. Mekky, and S. Rezaei, ‘Validity of SDOF Models for Analyzing Two-Way Reinforced Concrete Panels under Blast Loading’, *J. Perform. Constr. Facil.*, vol. 24, no. 4, pp. 311–325, Sep. 2009.
- [58] M. Colombo and P. Martinelli, ‘SDOF Models for RC and FRC Circular Plates under Blast Loads’, *Appl. Mech. Mater.*, vol. 82, pp. 440–445, Jul. 2011.
- [59] W. Wang, D. Zhang, and F. Lu, ‘The influence of load pulse shape on pressure-impulse diagrams of one-way RC slabs’, *Struct. Eng. Mech.*, vol. 42, no. 3, pp. 363–381, May 2012.
- [60] W. Wang, D. Zhang, F. Lu, S. C. Wang, and F. Tang, ‘The effect of span length to height ratio of reinforced concrete slabs on pressure-impulse diagram with multiple failure modes under blast loading’, *EPJ Web Conf.*, vol. 26, p. 04015, 2012.
- [61] J. Dragos and C. Wu, ‘A new general approach to derive normalised pressure impulse curves’, *Int. J. Impact Eng.*, vol. 62, pp. 1–12, Dec. 2013.
- [62] J. Dragos, C. Wu, and D. J. Oehlers, ‘Simplification of fully confined blasts for structural response analysis’, *Eng. Struct.*, vol. 56, pp. 312–326, Nov. 2013.
- [63] J. Dragos, C. Wu, and K. Vugts, ‘Pressure-Impulse Diagrams for an Elastic-Plastic Member under Confined Blasts’, *Int. J. Prot. Struct.*, vol. 4, no. 2, pp. 143–162, Jun. 2013.
- [64] J. Dragos and C. Wu, ‘Single-Degree-of-Freedom Approach to Incorporate Axial Load Effects on Pressure Impulse Curves for Steel Columns’, *J. Eng. Mech.*, vol. 141, no. 1, p. 04014098, Jan. 2015.
- [65] D. Ambrosini, B. Luccioni, A. Jacinto, and R. Danesi, ‘Location and mass of explosive from structural damage’, *Eng. Struct.*, vol. 27, no. 2, pp. 167–176, Jan. 2005.
- [66] T. Krauthammer, *Modern protective structures*. Boca Raton, FL : CRC Press, 2008.

- [67] H. M. I. Thilakarathna, D. P. Thambiratnam, M. Dhanasekar, and N. Perera, ‘Numerical simulation of axially loaded concrete columns under transverse impact and vulnerability assessment’, *Int. J. Impact Eng.*, vol. 37, no. 11, pp. 1100–1112, Nov. 2010.
- [68] A. Stolz, K. Fischer, C. Roller, and S. Hauser, ‘Dynamic bearing capacity of ductile concrete plates under blast loading’, *Int. J. Impact Eng.*, vol. 69, pp. 25–38, Jul. 2014.
- [69] J. Wesevich and C. Oswald, ‘Empirical Based Concrete Masonry Pressure-Impulse Diagrams for Varying Degrees of Damage’, *Proceeding Struct. Congr.*, ASCE2005.
- [70] J. Li and H. Hao, ‘Influence of brittle shear damage on accuracy of the two-step method in prediction of structural response to blast loads’, *Int. J. Impact Eng.*, vol. 54, pp. 217–231, Apr. 2013.
- [71] N. J. Parlin, W. G. Davids, E. Nagy, and T. Cummins, ‘Dynamic response of lightweight wood-based flexible wall panels to blast and impulse loading’, *Constr. Build. Mater.*, vol. 50, pp. 237–245, Jan. 2014.
- [72] M. Rhijnsburger, J. van Deursen, and J. van Doormaal, ‘Development of a toolbox suitable for dynamic response analysis of simplified structures’, presented at the 30th DoD Explosives Safety Seminar, Atlanta, 2002.
- [73] E. Conrath, T. Krauthammer, K. Marchand, and P. Mlakar, ‘Structural design for physical security: state of the practice’, presented at the VA: Structural Engineering Institute of American Society of Civil Engineers, Reston, 1999.
- [74] P. A. Hooper, R. A. M. Sukhram, B. R. K. Blackman, and J. P. Dear, ‘On the blast resistance of laminated glass’, *Int. J. Solids Struct.*, vol. 49, no. 6, pp. 899–918, Mar. 2012.
- [75] D. M. Cotsovos, ‘A simplified approach for assessing the load-carrying capacity of reinforced concrete beams under concentrated load applied at high rates’, *IE Int. J. Impact Eng.*, vol. 37, no. 8, pp. 907–917, 2010.
- [76] Cotsovos D.M and Pavlovic M.N, ‘Modelling of RC beams under impact loading’, *Proc Inst Civ Eng Struct Build Proc. Inst. Civ. Eng. Struct. Build.*, vol. 165, no. 2, pp. 77–94, 2012.
- [77] J. Biggs, *Introduction to Structural Dynamics*. New York: McGraw-Hill Book Company, 1964.
- [78] H. Hao, M. Stewart, Z.-X. Li, and Y. Shi, ‘RC Column Failure Probabilities to Blast Loads’, *Int. J. Prot. Struct.*, vol. 1, no. 4, pp. 571–591, Dec. 2010.
- [79] M. Kotsovos, *Finite-Element Modelling of Structural Concrete: Short-Term Static and Dynamic Loading Conditions*. CRC Press, 2015.

- [80] J. Li and H. Hao, 'A Two-step Numerical Method for Efficient Analysis of Structural Response to Blast Load', *Int. J. Prot. Struct.*, vol. 2, no. 1, pp. 103–126, Mar. 2011.
- [81] N. Jones, *Structural Impact*. Cambridge: Cambridge University Press, 1989.
- [82] *Building Code Requirements for Structural Concrete (ACI 318-11) and Commentary*. Farmington Hills, MI2011.
- [83] F. Tse, *Mechanical vibrations : theory and applications*, 2d ed. Boston: Allyn and Bacon, 1978.
- [84] C. Oswald and D. Sherkut, *FACEDAP theory manual*. Omaha, Nebraska: US Army Corps of Engineers Omaha District, 1994.
- [85] J. Li and H. Hao, 'A Simplified Numerical Method for Blast Induced Structural Response Analysis', *Int. J. Prot. Struct.*, vol. 5, no. 3, pp. 323–348, Sep. 2014.
- [86] A. Chopra, *Dynamics of structures : theory and applications to earthquake engineering*. Englewood Cliffs N.J.: Prentice Hall, 1995.
- [87] L. Chernin, M. Vilnay, and I. Shufrin, 'Blast dynamics of beam-columns via analytical approach', *Int. J. Mech. Sci.*, vol. 106, pp. 331–345, Feb. 2016.

## Chapter 4 : Graphical Method for the Derivation of P-I Diagrams

### 4.1. Introduction

This chapter focuses on the development of a new graphical method for the efficient derivation of P-I diagrams. This method is based on building complementary *loading/structural parameter vs. impulse* and *loading/structural parameter vs. pressure* graphs that describe the structural response in impulsive and (quasi-)static loading regimes. An elastic beam-column subjected to a transverse pressure load and axial force is used to illustrate and benchmark the method. In this case the axial force is chosen as the loading parameter generating the force-impulse (F-I) and force-pressure (F-P) diagrams. The techniques and algorithms necessary for implementation of the graphical method in its dimensional and normalised forms are discussed. Several P-I, F-I and F-P diagrams are derived for the beam-column subjected to different levels of axial force. It is demonstrated that while the P-I curve corresponding to the analysed structural system has a traditional hyperbolic shape, the F-I curve can be accurately approximated by a parabolic function and the F-P curve by a linear function. The derived P-I, F-I and F-P diagrams are used to demonstrate the advantages and efficiency of the proposed graphical method in both its forms.

### 4.2. New Graphical Method

As discussed at length in Chapter 3, the underlining idea of the P-I diagram approach is that every point on the P-I curve corresponds to the same level of damage caused to the structure by different combinations of pressure and impulse. It can also be seen as a boundary (or a threshold) between the damaged and undamaged structural states.

A typical P-I curve can be divided into a vertical asymptote, a hyperbolic curve and a horizontal asymptote as depicted in Figure 4.1. These three parts represent the following regimes: (I) impulsive regime, (II) dynamic regime and (III) (quasi-)static regime. The vertical asymptote is also called impulsive while the horizontal asymptote can be static or quasi-static depending on the load rise time in the load time history [1]. It should be noted

that further in the chapter the horizontal asymptote is referred to as (quasi-)static when the loading regime is unclear.

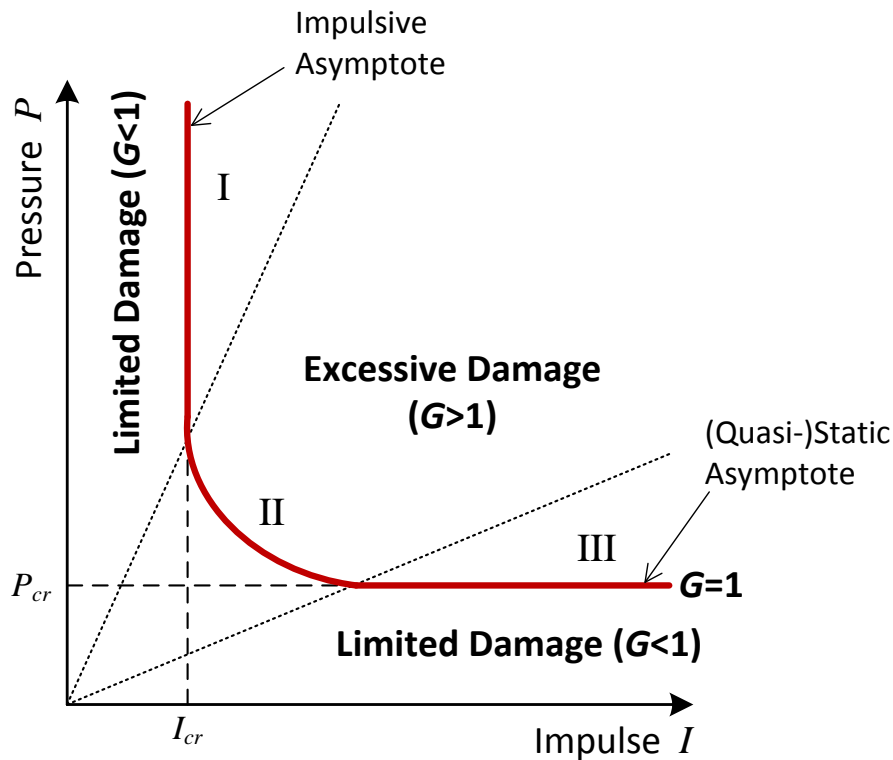


Figure 4.1. P-I Diagram

In Figure 4.1  $P_{cr}$  and  $I_{cr}$  are, respectively, the critical pressure and critical impulse required to cause structural failure. The position of each point of the P-I curve is controlled by a limit state function  $G$  representing structural damage.  $G$  can be expressed as

$$G(I, P) = \lambda / \lambda_{max} \quad (4.1)$$

where  $\lambda$  represents the failure criterion.

In a structure subjected to a blast load every structural element is already carrying a specific set of static loads generating internal forces and moments. Therefore, a combined action of a principal static load (or force) relevant to a particular structural element and the pressure pulse rather than the effect of the pressure pulse alone has to be considered in design or post-blast loading assessment. It is necessary to point out that each P-I curve is built for a unique combination of loads acting on a specific structure and for a specific level of damage and type of failure. Even slight variations in structural geometry or in the time history of the load immediately invalidate the curve. The effect of a specific loading/structural parameter on the P-I diagram, e.g., the degree of structural damage, can be taken into account by drawing

additional curves reflecting the variation in this parameter. Instead of building multiple P-I diagrams, the effect of the variation of a single parameter (e.g., axial force  $F$ , level of damage  $D$ , or post-blast fire exposure time  $T$ ) was proposed to be taken into account using a P-I band [2] or by building a three dimensional F-P-I diagram [3] a P-I-D diagram [4], or a P-I-T diagram [5]. It is suggested in [2] that the P-I bands can be used for rapid safety/survivability assessment of damaged structures. At the same time, the three dimensional diagrams, as presented by different authors such as [4], [3] and [5], have a very limited practical application providing only visual information on the influence of a corresponding parameter on the position and shape of the P-I curve. When the simultaneous effect of two parameters, e.g., different degrees of damage in similar structures with different load cases has to be considered, the P-I diagram becomes quite cumbersome and loses its flexibility. Currently, there is a lack in a reliable and efficient method that can take into account the simultaneous effect of two loading and/or structural parameters on the P-I diagram.

As the P-I diagram is very sensitive to any change in the state of the analysed structural system, a new P-I diagram has to be built each time a change occurs. In this section a novel graphical method is introduced as a means enhancing the efficiency of P-I diagrams. This unique method is based on the fact that the positions of the impulsive and (quasi-)static asymptotes are influenced by numerous loading and structural parameters. This influence can be directly taken into account by building complementary *loading/structural parameter vs. impulse* and *loading/structural parameter vs. pressure* diagrams. These two diagrams describe the structural response in the impulsive and (quasi-)static loading regimes and therefore define the positions of the corresponding asymptotes. It should be pointed out here that the variations in the positions of the asymptotes are limited to certain regions on the abscissa and ordinate of the P-I diagram near the origin (see Figure 4.2).



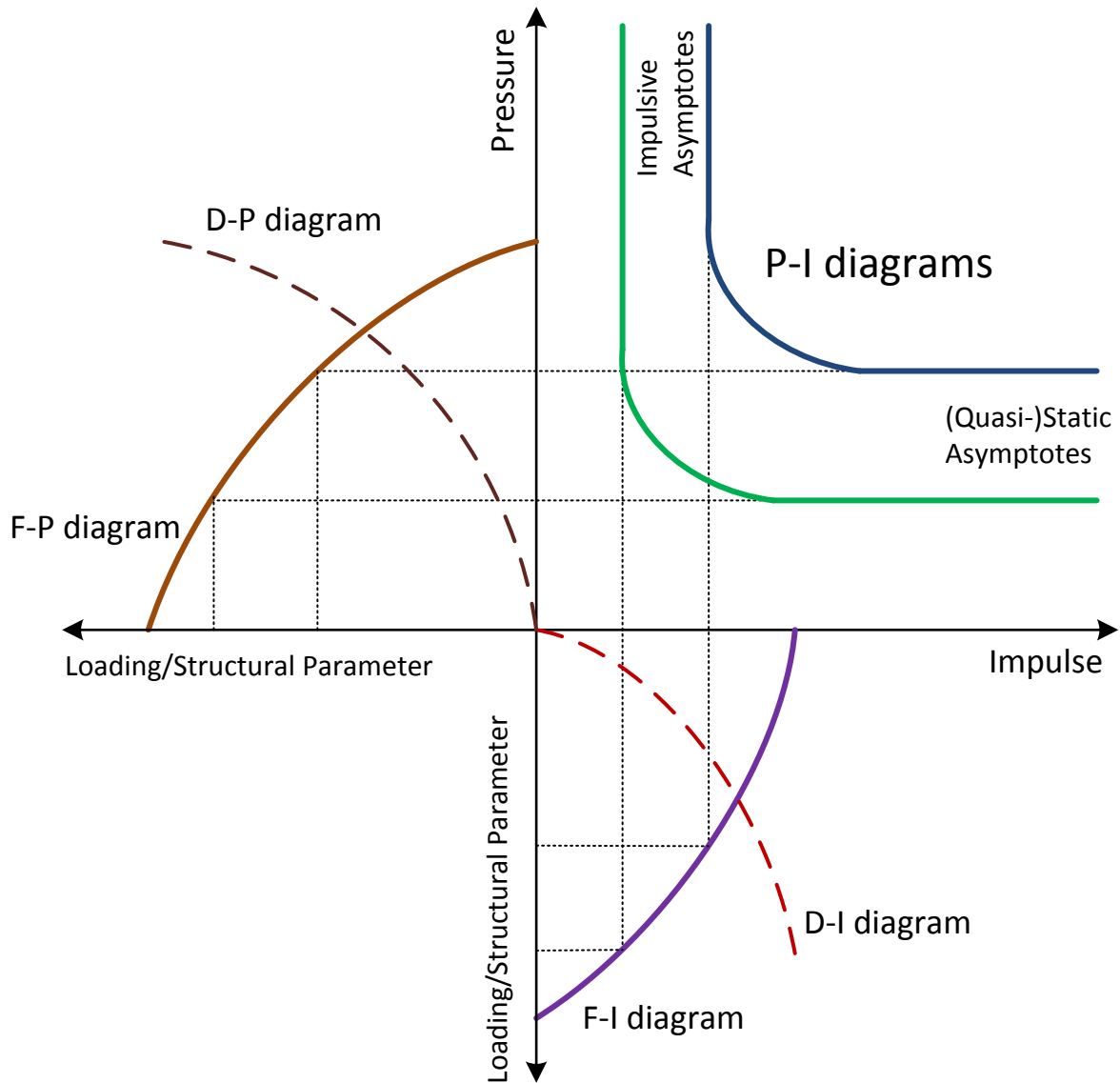


Figure 4.2. Graphical method

Any loading/structural parameter influencing the analysed structural system can be considered using the proposed method. For example, the applied force ( $F$ ) or the developed structural damage ( $D$ ) can be chosen as such parameter creating, respectively, the force-impulse (F-I) and force-pressure (F-P) diagrams or the damage-impulse (D-I) and damage-pressure (D-P) diagrams. These diagrams are schematically shown in Figure 4.2 as extensions of the P-I diagram. As an elastic beam-column subjected to an axial force and a transverse pressure load is further considered as a benchmark, the new method is introduced hereafter using the F-I and F-P diagrams. A typical normalised F-I (and F-P) diagram is shown in Figure 4.3a, where  $F$  and  $F_{cr}$  are the applied and critical axial forces,  $I$  and  $I_{cr}$  the applied and critical impulses, and  $P$  and  $P_{cr}$  the applied and critical pressures.

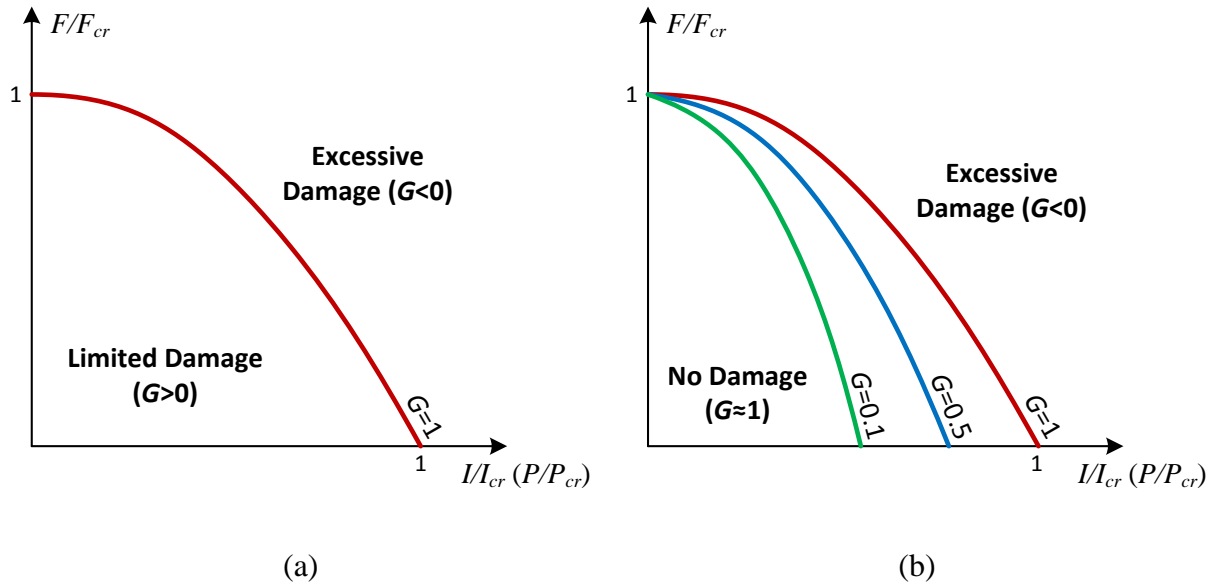


Figure 4.3. (a) Basic and (b) extended F-I (F-P) diagrams

The proposed graphical method is further divided in its dimensional and normalised forms. The dimensional method is especially efficient for the derivation of new P-I diagrams while the normalised method for the assessment of a structure in different structural states.

### 4.3. Dimensional method

The F-I diagram is suitable for the assessment of structural damage or survivability in the impulsive regime while the F-P diagram describes the structural capacity in the (quasi-)static regime. Therefore, the F-I and F-P diagrams define, respectively, the positions of the impulsive and (quasi-)static asymptotes for every practical level of the applied force. The dimensional method can utilise this feature for the derivation of P-I curves in two ways depending on the formulation of the P-I diagram. The P-I curve can be defined analytically using a formula that includes the terms  $A_P$  and  $A_I$  representing, respectively, the static and impulsive asymptotes ([6], [7], [8] and [9]). For example, Shi and colleagues [9] introduced the following P-I relationship based on an extensive numerical study on RC columns subjected to blast loads

$$(P_0 - A_P)(I - A_I) = C(A_P/2 + A_I/2)^D \quad (4.2)$$

where  $P_0$  is the peak pressure,  $I$  is the impulse delivered by the blast to a structure, and  $C$  and  $D$  are the fitting constants. In this case a new P-I curve can be simply obtained by calculating new values of  $A_I$  and  $A_P$  using, respectively, the F-I and F-P relationships.

To implement the graphical method, the complementary diagrams and one P-I curve have to be initially derived. Each new P-I curve can then be drawn by copying the existing P-I curve to a new position defined by the F-I and F-P diagrams and scaling each point of the P-I curve along the axes. The scaling is carried out using the following scaling ratios:

$$A_{I,NEW}/A_{I,OLD} \text{ along the Impulse axis}$$

$$A_{P,NEW}/A_{P,OLD} \text{ along the Pressure axis}$$

where the subscripts NEW and OLD represent the new and old values of  $A_I$  and  $A_P$ . The presented graphical method assumes that the P-I curves generated for a structural system under scaled loads have the same basic shape. This assumption is supported by the findings reported by various authors ([10], [11], [9], [12], [13], [14] and [15]).

The essential advantage of the described method lays in the fact that it also allows to account for the simultaneous effect of two loading/structural parameters on the P-I diagram. For example, P-I curves describing different degrees of damage can be drawn for a blast loaded column under different levels of axial force. For that purpose the different degrees of structural damage have to be incorporated into the F-I and F-P diagrams by building additional curves as schematically shown in Figure 4.3b. Another strength of this method is that it represents a convenient tool for quick assessment (in terms of safety and survivability) of typical structures or structural elements in a building (e.g., a floor supported by typical columns) subjected to different combinations of static, dynamic and impulsive loads.

#### **4.4. Normalised method**

The dimensional method loses its efficiency when a large number of structural states (e.g., a column under different levels of axial force developing various degrees of damage) are needed to be examined. In this situation the normalised method is more suitable. This method requires normalisation of the P-I diagram while the F-I and F-P diagrams can be used in the non-normalised or normalised forms. The normalised P-I diagram is obtained from an existing diagram by scaling it along the coordinate axes using the following normalisation factors

$1/A_I$  along the *Impulse* axis

$1/A_P$  along the *Pressure* axis

where  $A_I$  and  $A_P$  are respectively defined using the F-I and F-P diagrams (or corresponding relationships). When the F-I and F-P diagrams are normalised (see Figure 4.3a), the calculated normalised values of the asymptotes  $A_I$  and  $A_P$  have to be respectively multiplied by  $I_{cr}$  and  $P_{cr}$ .

The system composed of the three diagrams can now be used for the assessment/prediction of safety of a structure in a certain structural state subjected to a certain blast load. The F-I and F-P diagrams define the structural state (e.g., the degree of damage and the level of axial force) through the normalisation factors.

The algorithm for the assessment of safety of the structural state can be summarised as follows:

1. F-I and F-P diagrams and at least one P-I diagram are derived.
2. The P-I diagram is normalised using the normalisation factors  $1/A_I$  and  $1/A_P$  suitable to the structural state the P-I diagram describes.
3. A structural state and a blast load are chosen for examination.
4. The blast load described in terms of  $I$  and  $P$  is normalised using the normalisation factors  $1/A_I$  and  $1/A_P$  corresponding to the examined structural state. For example,  $A_I$  and  $A_P$  can be respectively calculated for the elastic beam-column loaded by a certain axial force and developing a certain degree of damage using Eqs. (4.8) and (4.11).
5. A point  $(I/A_I, P/A_P)$  corresponding to the normalised  $I$  and  $P$  is positioned on the normalised P-I diagram.
6. A check is made whether the point is in the safe or unsafe zone of the normalised P-I diagram leading to a conclusion whether the analysed blast load will cause the failure of the structure in the examined state.

The obvious advantage of the normalised graphical method is that it eliminates the need in deriving new P-I diagrams. Only one normalised P-I diagram is required and represents all the other necessary P-I diagrams. The assessment or prediction of the safety of a certain structural state can be carried out by mapping the values of  $I$  and  $P$  corresponding to the assumed or applied blast loads onto the normalised P-I plane  $(I/A_I, P/A_P)$ . Therefore, the

normalised graphical method can be used in at least two ways. First, this method can provide clear limits for multiple combinations of loads that can be applied on a structure designed to withstand a certain degree of damage. Second, this method is very efficient when multiple typical structures or structural elements (e.g., typical columns in a building floor) under varying loads (e.g., axial loads) have to be designed to or quickly assessed after an extreme event such as exposure to a blast load.

Both the dimensional and normalised methods are demonstrated in the following section.

#### 4.5. Case study: axially preloaded beam under blast load

In this section the proposed graphical method for derivation of the P-I diagrams is discussed in detail using as a benchmark an elastic beam-column subjected to an axial force and a transverse load shown in Figure 4.4.

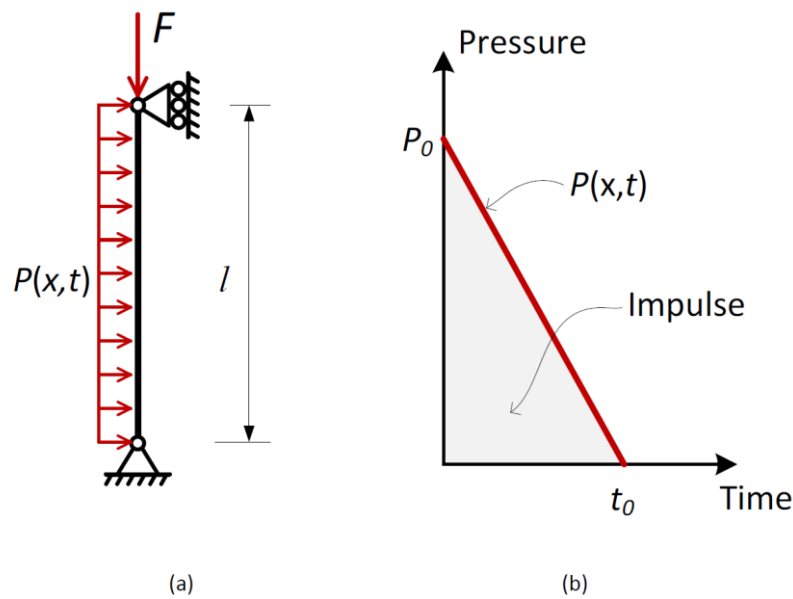


Figure 4.4. (a) Beam-column model and (b) load time history

As the primary purpose of columns is to carry axial loads, the axial force is used in the derivation of the complementary diagrams which will be renamed to N-I and N-P diagrams. The response of the beam-column to a combined action of the axial force and transverse pulse load is described using analytical modelling. This model utilises a continuous system formulation based on the Euler-Bernoulli beam ([16], [17]). It is assumed that the beam-column is statically preloaded by the axial force. The transverse load is modelled as pressure distributed uniformly over the beam-column height. The triangular load time history with

peak pressure  $P_0$  at the start and duration  $t_0$  is chosen. The model of the beam-column and the time history of the pulse load are shown in Figure 4.4b. The beam-column of the height  $l$  has pinned-pinned supports. If light damping is assumed, the amount of energy it can dissipate in the short duration of motion is quite small. Thus, its effect on the maximum response of the beam-column to a single pulse excitation can be ignored [16].

The response of the beam-column to the applied loads can be described by the differential beam equation [17]

$$EIu'''' + Fu'' + m\ddot{u} = P(x, t) \quad (4.3)$$

where  $u(x, t)$  is the beam deflection,  $u'$  represents a partial derivative according to the space variable  $x$  and  $\dot{u}$  according to time  $t$ ,  $EI$  is the flexural stiffness of the beam,  $F$  the axial force,  $m$  the mass per unit length of the beam and  $P(x, t)$  the excitation force.  $EI$  and  $m$  are assumed constant along the beam.

The detailed solution of Eq. (4.3), which has been carried out using the eigenfunction expansion method (i.e., the decomposition into the modes of vibration), is given in the Appendix. The maximum value at the beam-column mid-height  $u_m$  equals (see Eqs. (A.26) and (A.27))

$$u_m = EIP_0 \sum_{i=1}^{\infty} \Gamma_i \phi_{i,m} D_{i,m} \quad (4.4)$$

where

$$D_{i,m} = \frac{1}{\omega_i} I_i(t_{m,i}) \quad \text{for the forced vibration phase} \quad (4.5a)$$

$$D_{i,m} = \frac{1}{\omega_i} \sqrt{I_i^2 + (\dot{I}_i/\omega_i)^2} \quad \text{for the free vibration phase} \quad (4.5b)$$

The derivation of these expressions as well as the definitions of all the parameters involved can be found in the Appendix.

Since the described structural system is linearly elastic, the use of adequate material parameters and geometrical dimensions will only introduce a certain scaling factor into the solution, which is not important in the context of the paper. Therefore, to simplify the

analysis all the calculations are made for an abstract non-dimensional column with  $l = EI = m = 1$ . As in the real structures  $N$  is limited to the first Euler buckling force  $N_{b1}$ , three different levels of the axial force, i.e., zero axial force,  $0.5N_{b1}$  and  $0.9N_{b1}$ , are chosen as representing three characteristic loading situations.

#### 4.5.1. P-I diagram

As the new graphical method is based on generating new P-I curves from the existing ones, a few P-I curves are initially derived using Eqs. (4.4) and (4.5a). The most popular structural characteristic used as the failure criterion in building the P-I curves is the principal deflection of a structural element (see Section 4.2). Therefore, the maximum beam-column deflection occurring at the mid-height is used here to define the degree of structural damage. In such formulation the failure criterion takes the form  $\lambda = u_m$ . Additionally, it is assumed that  $\lambda_{max} = 1$ , which represents the limit state  $G = 1$  corresponding to 100% structural damage (see Figure 4.1). The P-I curves calculated for three different levels of the axial load, i.e., zero axial force,  $0.5N_{b1}$  and  $0.9N_{b1}$ , are shown in Figure 4.5.

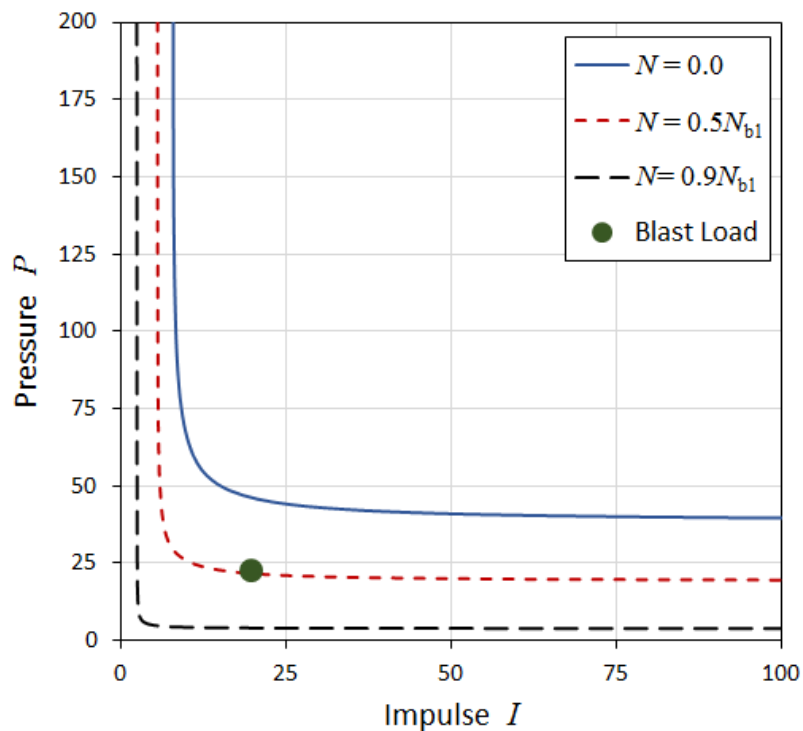


Figure 4.5. P-I diagrams

As can be clearly seen, the variation in the axial force significantly influences the positions of the P-I curve. The positions of the impulsive and static asymptotes shift towards the coordinate axes with increasing axial force. The nature of the relationships between the

impulsive and static asymptotes and the axial load is investigated in the following sections using N-I and N-P diagrams.

#### 4.5.2. N-I diagram

The F-I diagram provides the information on the degree and nature of the sensitivity of the beam-column to the axial force in the impulsive regime (see Figure 4.2). It is constructed here using the same failure criterion applied in the previous section for the derivation of the P-I diagrams. The N-I diagram is additionally normalised in order to simplify the derivation of the N-I relationship. The points of the normalised N-I diagram and the fitted curve are shown in Figure 4.6. The least-square curve fitting of these points results in the parabolic N-I relationship

$$\frac{N}{N_{b1}} + \left(\frac{I}{I_{cr}}\right)^2 = 1 \quad (4.6)$$

where  $I_{cr}$  is the critical impulse causing failure of the beam-column subjected solely to the transverse pressure load.

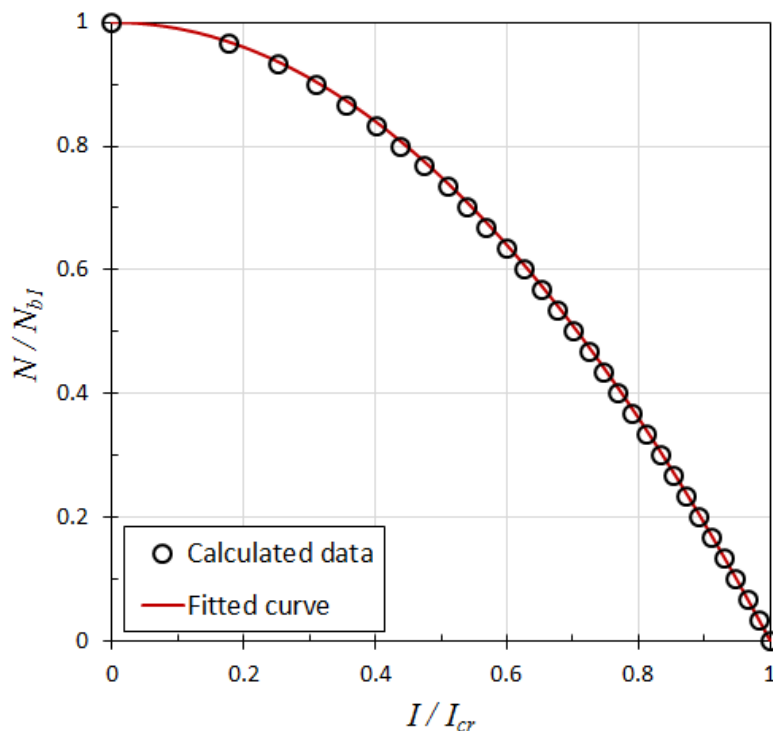


Figure 4.6. Normalised N-I diagram

It is necessary to note that the parabolic form of the N-I curve corresponds to the specific structural system analysed here. The shape of the curve may depend on numerous loading



and structural parameters such as the structural geometry, the complexity of the resistance-displacement relationship, the supporting and loading conditions, etc. The normalisation of the N-I diagram using  $N_{b1}$  and  $I_{cr}$  introduces a clear reference scale for the levels of the applied axial force and impulse. If the analysed column is short, which is, for example, the case of the majority of reinforced concrete columns [18] buckling is not likely to happen. It may be suggested that for such columns  $N_{b1}$  in Eq. (4.6) should be more appropriately substituted by the axial carrying capacity.

As in certain situations it is important to be able to assess/predict the degree of damage  $d$  caused by a blast to a structure,  $d$  can be easily incorporated into the N-I diagram by introduction of additional curves. The additional N-I curves describing different degrees of structural damage can be built using the modified limit state function (see Eq.(4.1))

$$G(I, P) = \lambda / (d \cdot \lambda_{max}) \quad (4.7)$$

$d$  is always in the range between 0 and 1 with  $d = 1$  representing the state of structural failure (100% damage). Figure 4.7 shows the N-I curves built for  $\lambda_{max} = 1$  and  $d = 1/3, 2/3$  and 1.

The N-I relationship given in Eq. (4.6) can be extended to include  $d$  in the following form

$$\frac{N}{N_{b1}} + d^{-2} \left( \frac{I}{I_{cr}} \right)^2 = 1 \quad (4.8)$$

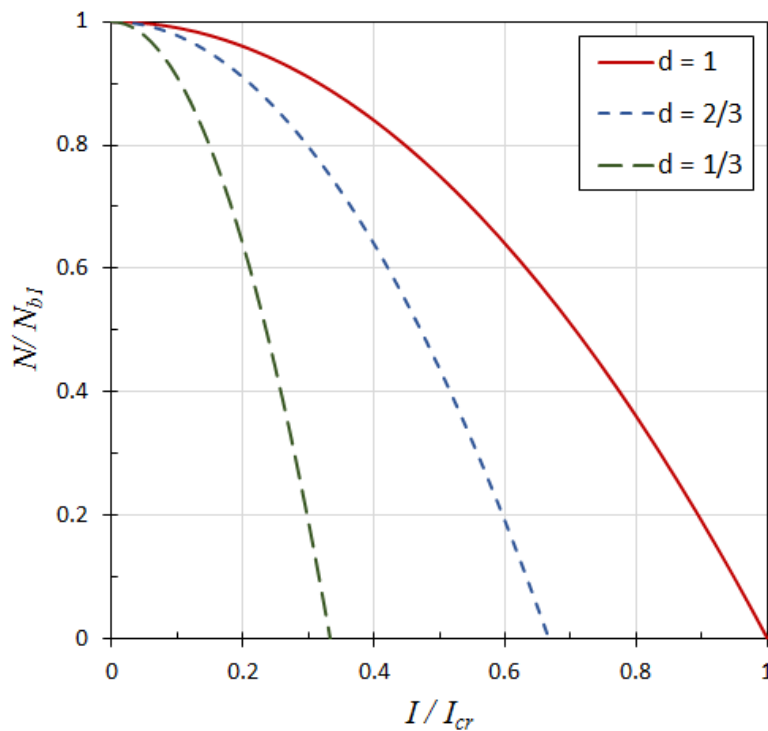


Figure 4.7. Extended normalised N-I diagram

It should be pointed out that  $d$  is always bigger than zero in the formulations of  $G$  presented in Eq. (4.7) and the N-I relationship in Eq. (4.8). In real structures  $N$  is never bigger than  $N_{b1}$  so for  $i \geq 3$  the ratio  $N/N_{bi} \cong 0$ . Thus, the axial force has a profound influence mostly on the first mode of vibration of the beam-column, which is the dominant mode of the column response [19]. An implicit analytical form of the N-I diagram can be derived using the first mode of vibration. This formulation is equivalent to using a first mode SDOF system. After substituting  $i = 1$  into Eqs. (4.4) and (4.5a) and some algebraic manipulations the following expression is obtained

$$\frac{N}{N_{b1}} + \left( \frac{\bar{I}_1}{\bar{I}_{1,cr}} \right)^2 = 1 \quad (4.9)$$

where the parameter  $\bar{I}_{1,cr} = \frac{\bar{\omega}_1 u_{1,cr}}{EI P_0 \Gamma_1 \phi_{1,m}}$  can be described as the contribution of the first mode to the impulse required to produce the critical displacement  $u_{1,cr}$  in the beam-column loaded by the transverse pressure only.  $\bar{I}_1 = \sqrt{I_1^2 + (\dot{I}_1/\omega_1)^2}$  is the first mode implicit representation of the applied impulse. It should be pointed out that the parabolic form of Eq. (4.9) is similar to the form of the N-I diagram obtained in Eq. (4.6) and shown in Figure 4.6.

### 4.5.3. N-P diagram

The N-P diagram describes the sensitivity of the beam-column on the axial force in the static regime and defines the position of the static asymptote. It is also constructed using the failure criterion applied in the derivation of the P-I diagrams. The normalised N-P diagram and the fitted curve are shown in Figure 4.8.

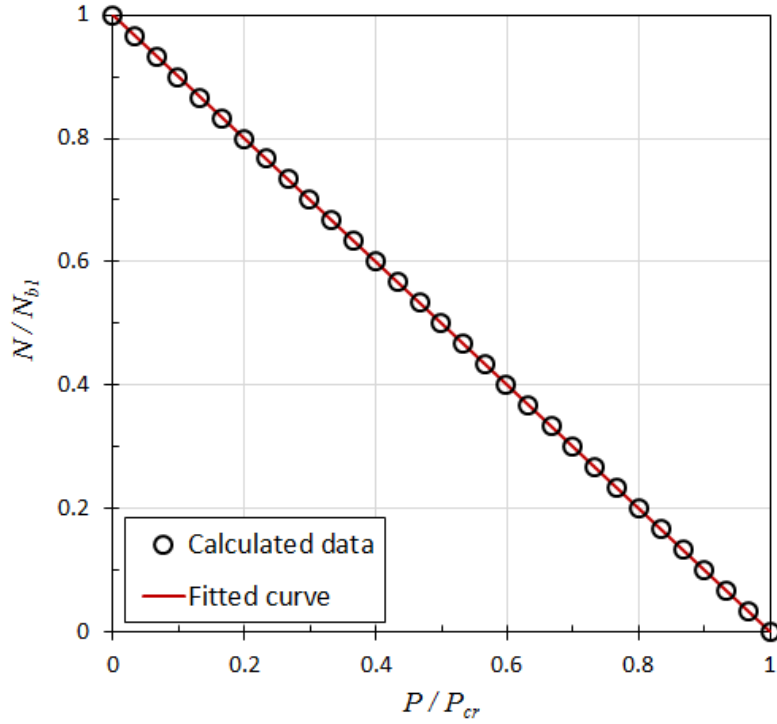


Figure 4.8. Normalised N-P diagram

Given that the elastic beam-column is in the static regime and its response is linear, the resulting N-P diagram has a linear shape. The least square curve fitting results in the following linear function

$$\frac{N}{N_{b1}} + \frac{P_0}{P_{cr}} = 1 \quad (4.10)$$

where  $P_u$  is the critical pressure causing failure of the beam-column loaded solely by the transverse pressure. The shape of the N-P diagram entirely depends on the degree of nonlinearity of the considered structural system. For example, the response of the simply supported linear elastic beam-column under the simple static load case shown in Figure 4.4 is characterised by the linear N-P curve given in Figure 4.8. The N-P curves can be highly nonlinear when the analysed structure has complex geometry, supporting and loading conditions and/or a complex nonlinear response-displacement relationship.

If it is additionally necessary to assess/predict the degree of structural damage, the N-P diagram can be extended to include extra curves in a way similar to the extended N-I diagram shown in Figure 4.7 and described in the previous section. Similarly to Eq. (4.8) the N-P relationship in Eq. (4.10) can be modified to include the degree of damage  $d$  as

$$\frac{N}{N_{b1}} + d^{-1} \frac{P_0}{P_{cr}} = 1 \quad (4.11)$$

where  $d$  is always in the range (0,1]. Figure 4.8 shows the N-P curves built for  $d = 1/3, 2/3$  and 1.

It is necessary to note that the P-I diagram is very sensitive to the shape of the load time history. This phenomena has been observed by a large number of researchers, such as [7], [8], [20], [21], [22], [23], [15], [24] and [25]. The N-I diagram, on the other hand, is utterly insensitive to the load time history and depends only on the amount of impulse delivered to a structure by the blast. The N-P diagram is only sensitive to the early part of the load time history corresponding to the load rise time since it defines whether the structure is in the static or quasi-static regime.

#### 4.5.4. Dimensional graphical method

The dimensional graphical method is demonstrated using the P-I curves and shown in Figure 4.5. For this purpose two new P-I curves corresponding to the beam-column loaded by the  $0.5N_{b1}$  and  $0.9N_{b1}$  axial forces and developing 100% damage (i.e.,  $d = 1$ ) are derived from the P-I curve corresponding to the zero axial force and  $d = 1$  by scaling the coordinates of every point of the curve using the scaling ratios  $A_{I,NEW}/A_{I,OLD}$  and  $A_{P,NEW}/A_{P,OLD}$ . The new and old values of  $A_I$  and  $A_P$  are calculated using, respectively, Eqs. (4.6) and (4.10). The new curves generated using the graphical method are compared with the original curves in Figure 4.9.

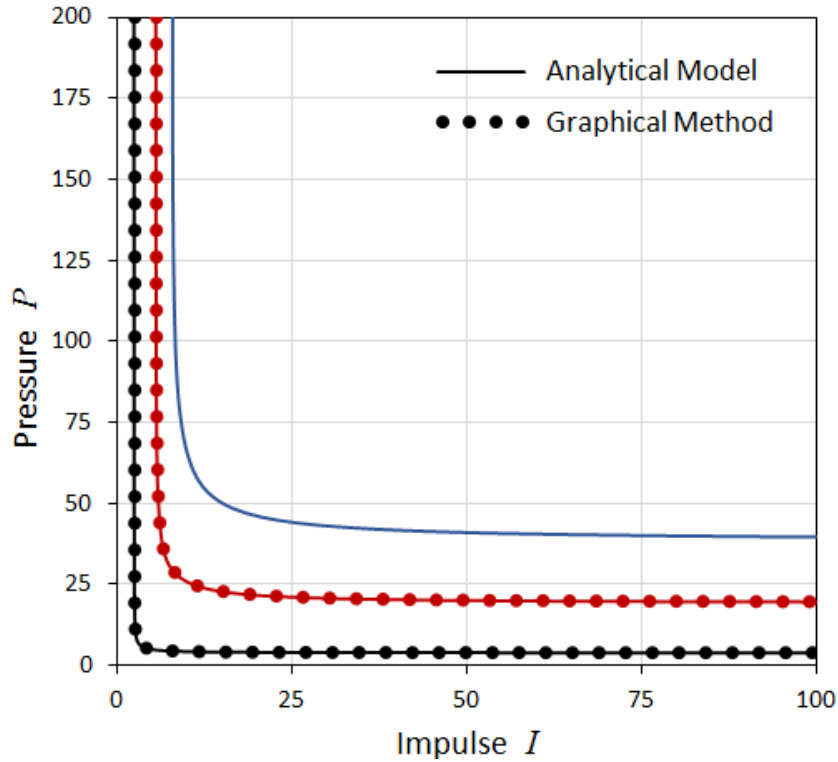


Figure 4.9. Dimensional graphical method

As can be seen from the figure the graphical method yields P-I curves identical to the previously calculated ones. Additional P-I curves can now be easily derived for any desirable degree of damage ( $0 < d \leq 1$ ) and any practical level of the axial force ( $0 \leq N \leq N_{b1}$ ) by applying Eqs. (4.8) and (4.11).

#### 4.5.5. Normalised graphical method

The normalisation process described in Section 4.4 is demonstrated using the two P-I curves in Figure 4.5 corresponding to the beam-column under the zero and  $0.9N_{b1}$  axial forces and  $d = 1$ . The values of  $A_I$  and  $A_P$  corresponding to  $N = 0$  and  $N = 0.9N_{b1}$  are respectively calculated using the N-I and N-P relationships in Eqs. (4.6) and (4.10). Figure 4.10 depicts that both normalised curves are identical. The normalised P-I curve is further fitted using the P-I relationship given in Eq. (4.2). The use of the following set of values  $A_P = 1.0, A_I = 1.0, C = 0.12, D = 1.0$  resulted in a very accurate fitting. The fitting curve is also presented in Figure 4.10.

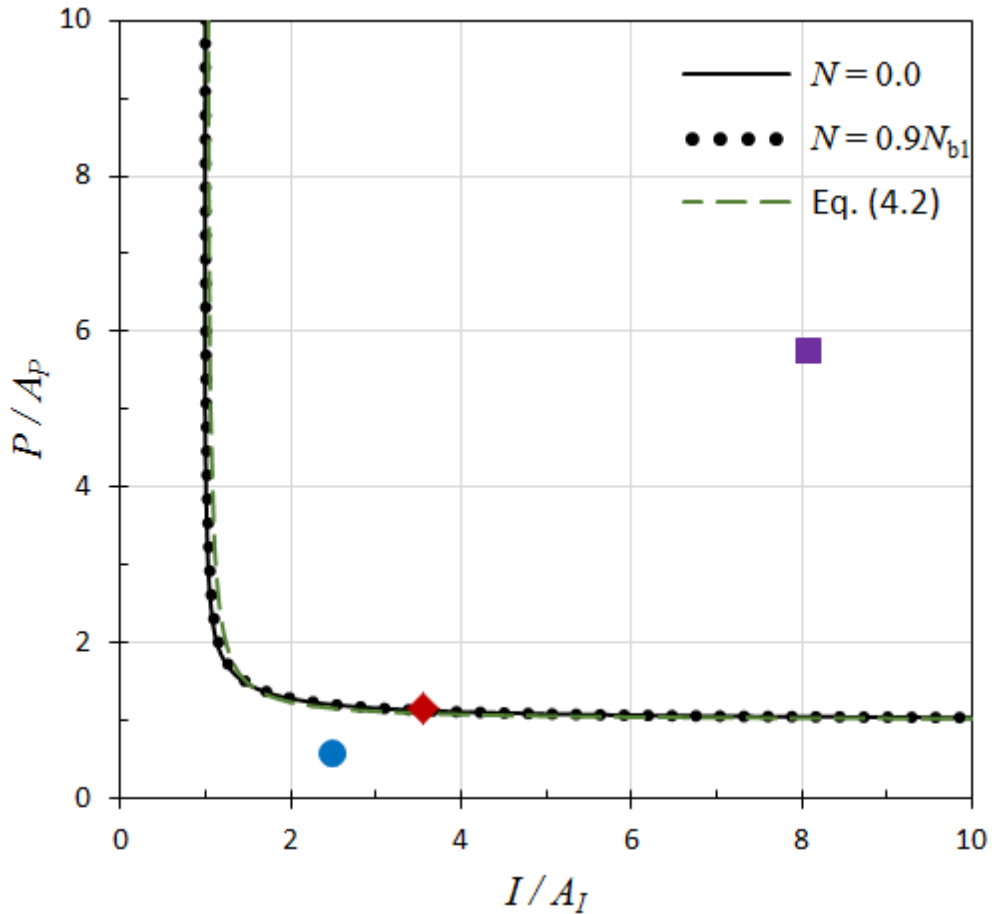


Figure 4.10. Normalised graphical method

The normalised graphical method is now applied for evaluation of the structural state of three columns subjected to zero,  $0.5N_{b1}$  and  $0.9N_{b1}$  axial forces and the same blast load with  $I = 20$  and  $P = 22$ . The P-I diagrams drawn for 100% damage and the defined levels of axial force together with the point ( $I = 20, P = 22$ ) describing the applied blast load are given in Figure 4.5. As can be seen from the figure, this point lays on the P-I curve corresponding to  $0.5N_{b1}$  axial force. It can therefore be concluded that the axially unloaded beam-column will develop only limited damage after application of the analysed blast load while the beam-columns loaded by the  $0.5N_{b1}$  and  $0.9N_{b1}$  axial forces will fail. The point ( $I = 20, P = 22$ ) is then mapped onto the normalised plane ( $I/A_I, P/A_P$ ) three times in accordance with the three sets of values  $A_I$  and  $A_P$  corresponding to the three analysed levels of the axial force.  $A_I$  and  $A_P$  are respectively calculated using the N-I and N-P relationships given in Eqs. (4.6) and (4.10). The results of mapping are shown in Figure 4.10. Point 1 in the figure represents the structural state of the beam-column under zero axial force, Point 2 under  $0.5N_{b1}$  axial force and Point 3 under  $0.9N_{b1}$  axial force. Conclusions similar to the ones for the non-normalised P-I diagram can now be made, i.e., the axially unloaded beam-column (Point 1) develops

only limited damage, while the beam-columns loaded by the  $0.5N_{b1}$  and  $0.9N_{b1}$  axial forces (Points 2 and 3) fail. Various structural states of the beam-column corresponding to different levels of axial force and different degrees of damage can now be examined using the extended N-I and N-P diagrams or relationships given in Eqs. (4.8) and (4.11). It is important to stress here that in order to assess the state of a structure only the N-I, N-P and normalised P-I diagrams need to be built and only points representing analysed blast loads are mapped onto the normalised P-I plane. This is much more efficient and less time consuming than building numerous P-I diagrams and then assessing the structural conditions. Note, the curve in the Figure was derived analytically and is not described by any of the existing formulas.

#### **4.6. Conclusions**

A new graphical method is proposed in this chapter as an efficient means for derivation of P-I diagrams or assessment of multiple structural conditions. This method is based on derivation of complementary loading/structural parameter vs. impulse and loading/structural parameter vs. pressure diagrams. These new diagrams describe, respectively, the structural response in the impulsive and (quasi-)static regimes and define the position of each P-I diagram. The proposed graphical method is presented in its dimensional and normalised forms. The techniques and algorithms necessary for the implementation of the both forms of the new method are explained in detail. The advantages and efficiency of the graphical method are examined using an elastic beam-column subjected to an axial force and a transverse blast load as a benchmark. The complementary diagrams formulated in this case are the axial force-impulse (N-I) and axial force-pressure (N-P) diagrams. The P-I, N-I and N-P diagrams are built for different levels of axial force and different degrees of structural damage. Analytical expressions are obtained for the N-I and N-P curves using least-square curve fitting. It is found that the N-I curve corresponding to the analysed structural system can be efficiently described by a parabolic function while the N-P curve by a liner function. The dimensional graphical method is demonstrated to be efficient for derivation of new P-I diagrams from an existing one, especially when the simultaneous effect of two loading/structural parameters on the P-I diagram has to be considered. The normalised graphical method is shown to be an effective means for the assessment of safety of a structure in different structural states including different load cases and different degrees of damage. Finally, it is concluded that the graphical method represents a powerful tool for preliminary design as well as quick assessment of multiple typical structures or structural elements exposed to extreme loads generated by explosions.



## References

- [1] T. Krauthammer, *Modern protective structures*. Boca Raton, FL : CRC Press, 2008.
- [2] W. W. El-Dakhkhni, W. F. Mekky, and S. H. Changiz-Rezaei, ‘Vulnerability Screening and Capacity Assessment of Reinforced Concrete Columns Subjected to Blast’, *J. Perform. Constr. Facil.*, vol. 23, no. 5, pp. 353–365, Oct. 2009.
- [3] A. A. Nassr, A. G. Razaqpur, M. J. Tait, M. Campidelli, and S. Foo, ‘Strength and stability of steel beam columns under blast load’, *Int. J. Impact Eng.*, vol. 55, pp. 34–48, May 2013.
- [4] M. Campidelli and E. Viola, ‘An analytical–numerical method to analyze single degree of freedom models under airblast loading’, *J. Sound Vib.*, vol. 302, no. 1–2, pp. 260–286, Apr. 2007.
- [5] Y. Ding, M. Wang, Z.-X. Li, and H. Hao, ‘Damage evaluation of the steel tubular column subjected to explosion and post-explosion fire condition’, *Eng. Struct.*, vol. 55, pp. 44–55, Oct. 2013.
- [6] J. Sperrazza, ‘Dependence of external blast damage to the A-25 Aircraft on peak pressure and impulsedified Pressure-Impulse Blast Damage Model.’, Ballistic Research Labs Aberdeen Proving Ground MD., Defense Technical Information Center, Maryland, 575, 1951.
- [7] C. K. Youngdahl, ‘Correlation Parameters for Eliminating the Effect of Pulse Shape on Dynamic Plastic Deformation’, *J. Appl. Mech.*, vol. 37, no. 3, p. 744, 1970.
- [8] G. . Abrahamson and H. . Lindberg, ‘Peak load-impulse characterization of critical pulse loads in structural dynamics’, *Nucl. Eng. Des.*, vol. 37, no. 1, pp. 35–46, Apr. 1976.
- [9] Y. Shi, H. Hao, and Z.-X. Li, ‘Numerical derivation of pressure-impulse diagrams for prediction of RC column damage to blast loads’, *Int. J. Impact Eng.*, vol. 35, no. 11, pp. 1213–1227, 2008.
- [10] Q. Li and H. Meng, ‘Pulse loading shape effects on pressure–impulse diagram of an elastic–plastic, single-degree-of-freedom structural model’, *Int. J. Mech. Sci.*, vol. 44, no. 9, pp. 1985–1998, Sep. 2002.
- [11] A. S. Fallah and L. A. Louca, ‘Pressure–impulse diagrams for elastic-plastic-hardening and softening single-degree-of-freedom models subjected to blast loading’, *Int. J. Impact Eng.*, vol. 34, no. 4, pp. 823–842, Apr. 2007.

- [12] Y. Shi Yanchao, *A new method for progressive collapse analysis of RC frames under blast loading*. 2010.
- [13] X. Huang, G. Ma, and J. Li, ‘Damage Assessment of Reinforced Concrete Structural Elements Subjected to Blast Load’, *Int. J. Prot. Struct.*, vol. 1, no. 1, pp. 103–124, Mar. 2010.
- [14] S. Astarlioglu, T. Krauthammer, D. Morency, and T. P. Tran, ‘Behavior of reinforced concrete columns under combined effects of axial and blast-induced transverse loads’, *Eng. Struct.*, vol. 55, pp. 26–34, Oct. 2013.
- [15] J. Dragos and C. Wu, ‘A new general approach to derive normalised pressure impulse curves’, *Int. J. Impact Eng.*, vol. 62, pp. 1–12, Dec. 2013.
- [16] A. Chopra, *Dynamics of structures: theory and applications to earthquake engineering*. Englewood Cliffs N.J.: Prentice Hall, 1995.
- [17] F. Tse, *Mechanical vibrations: theory and applications*, 2d ed. Boston: Allyn and Bacon, 1978.
- [18] J. Wight, *Reinforced concrete: mechanics and design*, 6th ed. Upper Saddle River N.J.: PEARSON PRENTICE HALL, 2012.
- [19] L. Chernin, M. Vilnay, and I. Shufrin, ‘Blast dynamics of beam-columns via analytical approach’, *Int. J. Mech. Sci.*, vol. 106, pp. 331–345, Feb. 2016.
- [20] R. Schumacher and B. Cummings, ‘A Modified Pressure-Impulse Blast Damage Model.’, Ballistic Research Labs Aberdeen Proving Ground MD., Defense Technical Information Center, Ft. Belvoir, 1977.
- [21] G. Zhu, Y. Huang, T. Yu, and R. Wang, ‘Estimation of the plastic structural response under impact’, *Int. J. Impact Eng.*, vol. 4, no. 4, pp. 271–282, Jan. 1986.
- [22] Q. Li and H. Meng, ‘Pressure-Impulse Diagram for Blast Loads Based on Dimensional Analysis and Single-Degree-of-Freedom Model’, *J. Eng. Mech.*, vol. 128, no. 1, pp. 87–92, Jan. 2002.
- [23] T. Krauthammer, S. Astarlioglu, J. Blasko, T. B. Soh, and P. H. Ng, ‘Pressure–impulse diagrams for the behavior assessment of structural components’, *Int. J. Impact Eng.*, vol. 35, no. 8, pp. 771–783, Aug. 2008.

[24] A. S. Fallah, E. Nwankwo, and L. A. Louca, 'Pressure-Impulse Diagrams for Blast Loaded Continuous Beams Based on Dimensional Analysis', *J. Appl. Mech.*, vol. 80, no. 5, p. 51011, Jul. 2013.

[25] N. J. Parlin, W. G. Davids, E. Nagy, and T. Cummins, 'Dynamic response of lightweight wood-based flexible wall panels to blast and impulse loading', *Constr. Build. Mater.*, vol. 50, pp. 237–245, Jan. 2014.

## **Chapter 5 :      Finite Element Modelling of Reinforced Concrete Structures**

### **5.1.    Introduction**

This chapter focuses on the development of finite element reinforced concrete models. Abaqus is often used by scientists and engineers for modelling of reinforced concrete (RC) structures, e.g., [1]–[5]. The choice of material models of concrete is limited in Abaqus to the smeared cracking model, the brittle cracking mode and the damaged plasticity model [6]. Each model is designed for a particular type of usage. The smeared cracking model can handle only monotonic loading and low confining pressures. This limits the range of its applicability. The damaged plasticity model is by far most complex concrete model incorporated in Abaqus that can be used in any loading regime. However, it is not ‘user friendly’, includes multiple parameters and its calibration can be very challenging. Additionally, this model does not allow damaged elements to be deleted from the finite element (FE) analysis. The brittle cracking model can be used only in the explicit loading scheme and is very ‘user friendly’ and easy to calibrate. The main disadvantage of this model is that it assumes linear elastic material behaviour in compression. As a result, the model can be reliably used only in the cases where the concrete behaviour is dominated by the tensile failure. The limited choice of the built-in concrete models combined with their shortcomings often resulted in new models introduced in Abaqus through user-defined subroutines, e.g., [1], [2]. In this paper, the brittle cracking model is extended to include the nonlinear compressive behaviour using the user subroutine VUSDFLD. The new material model is compared with the original brittle cracking model and the damaged plasticity model. It is then used to examine strain rate effects [7], [8] and also to simulate a number of benchmark cases including a three point bending test [9], a standard brittle failure test [10] and RC columns under blast [11], [12]. The limitations of model application are examined.

## **5.2. Reinforced concrete models in Abaqus**

### **5.2.1. Available models**

Currently three models exist in the commercial software finite element package Abaqus specifically for concrete. They include the concrete smeared cracking model, the cracking model for concrete and the damaged plasticity model [6]. Each model is designed for a particular type of usage within a defined time integration scheme.

The smeared cracking model is intended for use in implicit models with monotonic loading and low confining pressures. The brittle cracking model is designed for applications in which the behaviour is dominated by tensile cracking within the explicit time scheme. The damaged plasticity model is perhaps the most comprehensive of the three models, designed for use in both explicit and implicit analyses with a range of different loading intensities. The model is a continuum, plasticity-based, damage model for concrete. It assumes that the main two failure mechanisms are tensile cracking and compressive crushing of the concrete material. Apart from these models more general Abaqus capabilities can be used for the description of concrete behaviour. For example the Modified Drucker- Prager/ Cap model, which is typically used in the modelling of granular type materials, such as soils and rock, can be adapted to describe concrete behaviour [13]. Additionally, in Abaqus there is also the possibility of writing one's own material model via a user subroutine code.

In the analysis of structures subjected to extreme loads, such as blast loads the most suitable models are the latter two. This is mainly due to the limitations of both the first models- the smeared cracking model is not designed for dynamic load cases, whereas the brittle cracking model uses elastic behaviour in compression which is unsuitable when discussing extreme loads on compressive structural members, such as columns. Due to these limitations the models widely used in Abaqus to describe concrete under extreme loading are either the damaged plasticity or the Drucker- Prager models. Of these models the smeared crack model is fundamentally unsuitable for dynamic analysis. The remaining two models are discussed in the following sections.

### 5.2.1.1. Damaged plasticity model

The damaged plasticity model in Abaqus implements a damaged plasticity material model for concrete [14] which was then further modified [15]. The model is suitable for modelling concrete material under dynamic loading. The underlying constitutive theory of the model assumes that concrete behaves in a brittle manner under low confining pressure and the main modes of failure are cracking in tension and crushing in compression. However, if the confining pressure is large enough to prevent crack propagation then the concrete no longer behaves in a brittle manner. In this case failure is that of a ductile material with work hardening.

The main advantages of using this material model is that different behaviour can be specified in tension and compression in order to capture the fundamentally different behaviour, including different yield strengths, softening in tension compared to hardening followed by softening in compression and different elastic stiffness degradation in tension and compression.

As a result of the failure mechanisms in the concrete, caused by cracking and crushing, the elastic stiffness suffers a decrease in value. As the model is based on the scalar-damage theory this degradation is isotropic and characterised by a single variable, as shown below. The stress- strain relation is presented in the following equation:

$$\sigma = (1 - d) \cdot D_0^{el}(\varepsilon - \varepsilon^{pl}) = D^{el}(\varepsilon - \varepsilon^{pl}) \quad (5.1)$$

where  $D_0^{el}$  is the initial undamaged elastic stiffness of the concrete and  $D^{el} = (1 - d) \cdot D_0^{el}$  is the degraded elastic stiffness of the concrete.  $d$  is the scalar stiffness degradation variable, the range of which is  $0 \leq d \leq 1$  where the value 0 corresponds to undamaged material and 1 to fully damaged material.

The effective stress is defined as:

$$\bar{\sigma} = D_0^{el}(\varepsilon - \varepsilon^{pl}) \quad (5.2)$$

and is related to the Cauchy stress through the scalar degradation variable:

$$\bar{\sigma} = \frac{\sigma}{(1 - d)} \quad (5.3)$$

The hardening variables  $\bar{\varepsilon}_t^{pl}$  and  $\bar{\varepsilon}_c^{pl}$  represent the equivalent plastic strains in tension and compression. The micro-cracking and the crushing of concrete are represented by increasing

the values of these variables, in this way these variables control the evolution of the yield surface and the degradation of the elastic stiffness.

Uniaxial stress-strain curves are converted into stress-plastic strain curves of the following form:

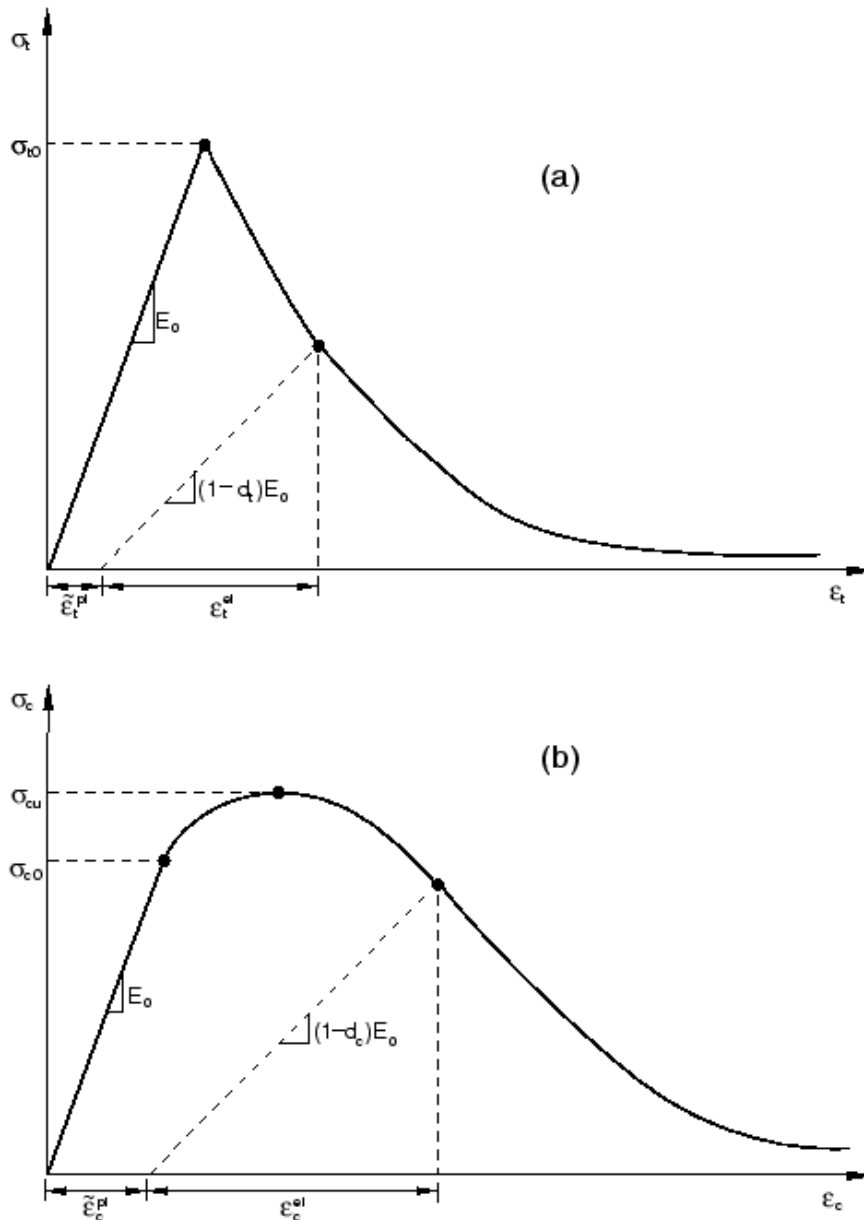
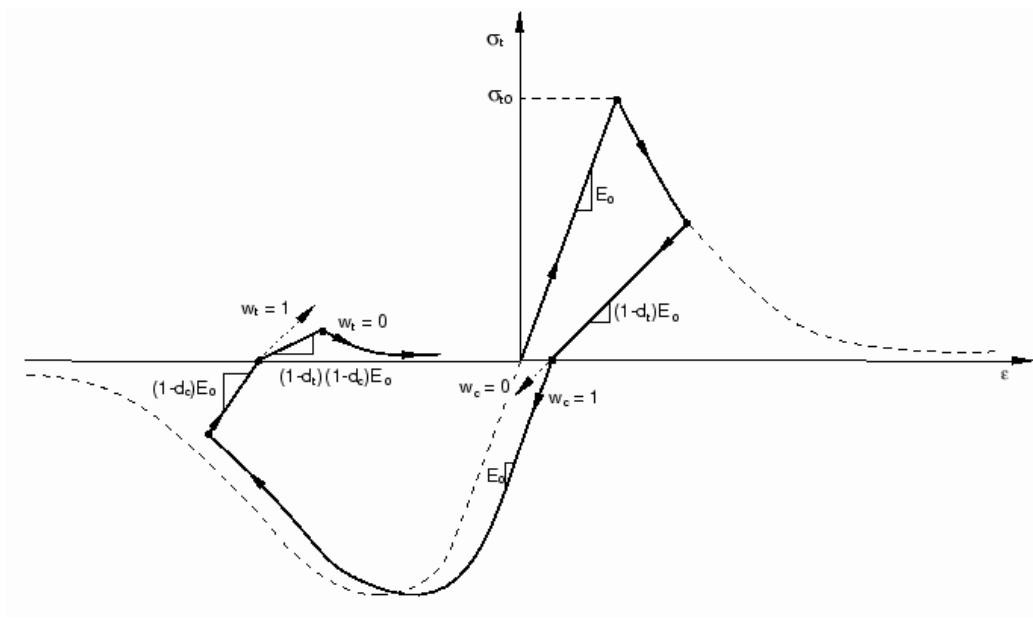


Figure 5.1. Response of concrete to uniaxial loading in tension (a) and compression (b)[6]

As shown in Figure 5.1, if unloading occurs on the strain softening branch the unloading response is weakened and the elastic stiffness degraded. The degradation of the elastic stiffness differs between compression and tension tests and is more pronounced as the plastic

strain increases. This response is expressed by using two independent damage variables,  $d_t$  and  $d_c$ , which are functions of the plastic strains, temperature and field variables.

When subjected to uniaxial cyclic conditions the degradation mechanisms in concrete, including opening and closing of previously formed micro-cracks and their interaction, become significantly more complex. Weight factors which are part of the material definitions,  $w_t$  and  $w_c$ , control the recovery of the tensile and compressive stiffness upon load reversal, as shown in the following figure.



*Figure 5.2. Uniaxial load cycle (tension-compression-tension) assuming default values for the stiffness recovery factors:  $w_t = 0$  and  $w_c = 1$ . [6]*

The postfailure behaviour of concrete under direct strain is modelled using tension stiffening. If in the model there are regions of concrete with no reinforcement the tension stiffening model defined by the stress-strain curve introduces mesh sensitivity problems into the analysis [6]. In order to overcome this failure in tension is defined by using a fracture energy cracking model. This is modelled in Abaqus by specifying the postfailure stress as a function of the cracking displacement, see Figure 5.3.



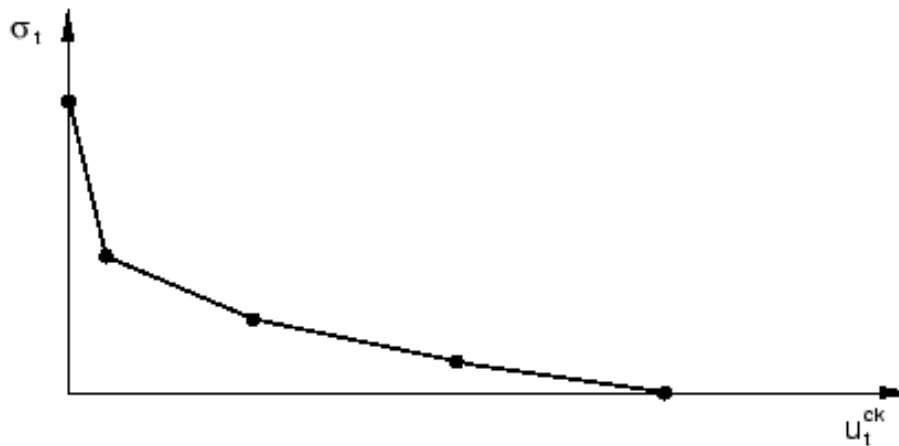


Figure 5.3. Postfailure stress-displacement curve [6]

This model seems very advantageous as it allows for different failure mechanisms in both tension and compression. The main disadvantage is that the model requires for a lot of user input and is therefore harder to calibrate. Another disadvantage is that there is no possibility to define a failure criterion removing failed elements from the analysis which could lead to numerical issues due to large deformations in the elements. Due to this cracks along the reinforcement cannot be explicitly modelled, therefore phenomena such as concrete spalling and scabbing can't be modelled, which might be advantageous in blast load analyses. Additionally it will be shown in the case studies that the results under blast loads are not satisfactory for this constitutive model.

#### 5.2.1.2. Brittle cracking model

The brittle cracking model is only available in the explicit numerical time integration scheme and uses a smeared crack model to represent the characteristically discontinuous brittle behaviour in concrete. It is an elastic cracking model with concrete between cracks considered as an isotropic linearly elastic material. In this model, the initiation and evolution of individual cracks is not tracked. Instead, a smeared crack method is utilised to present the material discontinuities. The material calculations take into account cracks via stress and material stiffness at the material point. The constitutive calculations are performed independently at each material point within the finite element model. All cracks are assumed to be fixed and orthogonal with a limit of three cracks in a 3D model. The first crack at a material point is assumed to have formed once the maximum principle tensile stress exceeds the tensile strength of the concrete. In the numerical scheme implemented in Abaqus crack

initiation is detected by a simple Rankine criterion. Once a crack is formed at a point, its orientation is stored for subsequent calculations. A new crack can form at the same point only in a direction orthogonal to the direction of an existing crack. Therefore, this model is called a fixed orthogonal crack model. Cracks are modelled as irrecoverable. They may close and reopen, but remain throughout the rest of the analysis.

If the post failure behaviour is specified using stress as a function of strain along the crack in cases with minimal or no reinforcement, the mesh will not converge. This is because finer mesh leads to narrower crack bands. In such cases it is best to characterise the concrete behaviour using a stress- displacement response [16]. Using this approach, the length of a sufficiently developed crack is primarily determined by the crack opening and is not dependent of the length of the concrete member.

The concrete model considers two modes of behaviour; Mode I and Mode II [6]. Mode I is the tension, softening/ stiffening behaviour and the crack detection scheme is based purely on this mode. Mode II is the shear softening/ retention behaviour and is based on the observation that shear behaviour is dependent on the amount of crack opening. The postcracked scheme takes into account both of these behavioural modes.

The tension softening in the direction normal to a crack is described based on the Hillerborg cohesive crack model [16], in which a stress-displacement curve is adopted from CEB-FIP Model Code 2010 [13]. Additionally, the effect of the amount of crack opening on the shear response of concrete is formulated using the shear retention model. As shown in Figure 5.4, the larger the crack the less interlocking there is so shear resistance decreases. In this model, the post-cracked shear stiffness is defined as a power function of the strain across an opening crack, reducing as the crack opens.

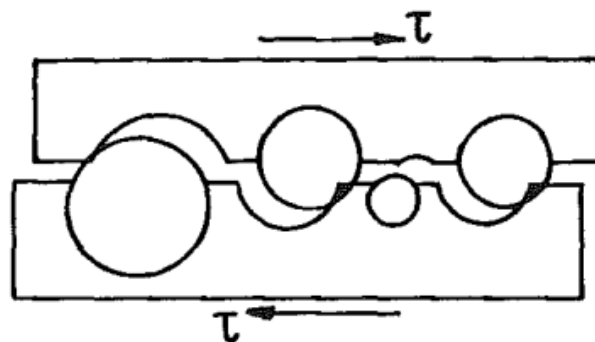


Figure 5.4. Principle of shear friction in concrete crack with unbroken aggregates [17]

Although crack initiation is based on Mode I fracture the postcracked behaviour includes Mode II behaviour. Mode II shear behaviour depends on the amount of crack opening – the shear modulus reduces as the crack opens [6]. In this model, the post-cracked shear stiffness is defined as a power function of the strain across an opening crack, shown in Figure 5.5 and taking the form of:

$$\rho(e_{nn}^{ck}) = \left(1 - \frac{e_{nn}^{ck}}{e_{max}^{ck}}\right)^p \quad (5.4)$$

where  $\rho(e_{nn}^{ck})$  is the shear retention factor,  $e_{nn}^{ck}$  is the crack opening strain and  $p$  and  $e_{max}^{ck}$  are material parameters [6].

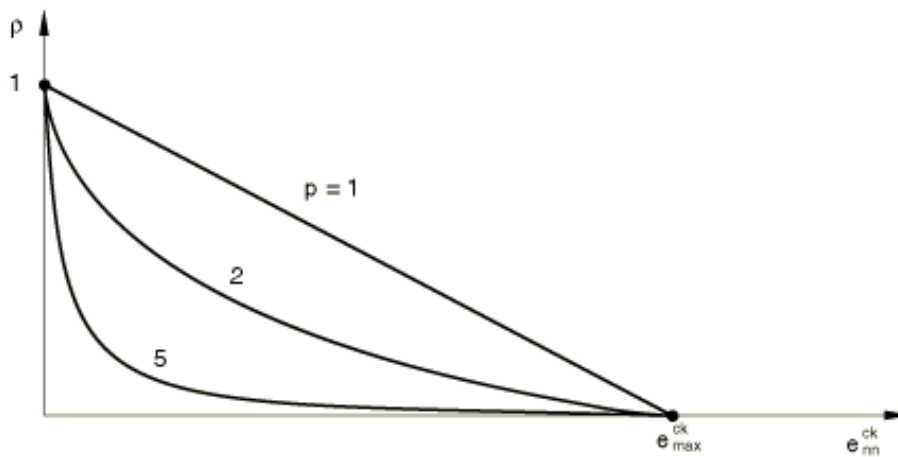


Figure 5.5. Power law form of the shear retention model [6]

Great care and understanding of the likely structural behaviour and potential failure mechanisms is required when using this material model. The advantage of a failure criterion removing an element deemed to have failed by the brittle crack criterion might not always be a valid assumption - if for example the load will reverse the analysis will not take into account the potential compressive stress capacity of the element (e.g. seismic events).

The model is suitable for the modelling of reinforced concrete as it can be used in conjunction with embedded rebar. If a concrete element were to fail according to the brittle failure criterion its contribution to the stress carrying capacity is removed, however the rebar contribution remains until the rebar failure criteria is satisfied.

The brittle cracking model is designed for cases where tensile cracking governs the overall behaviour of the structure examined. The model assumes that the behaviour of concrete in compression is always linear elastic.

In this work all the tensile input in the brittle cracking models was developed by using the known concrete properties, as given in experiment reports, and the FIB Model Code [17]. In tension the concrete behaviour was implemented according to the tensile stress-opening crack relationship for short term loading ([17], Section 5.1.8.2).

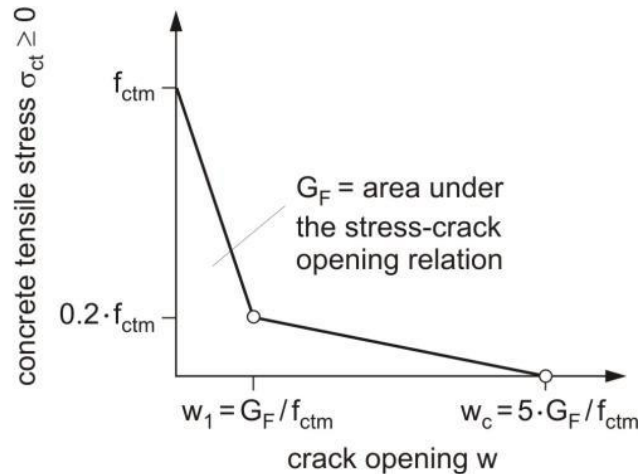


Figure 5.6. Schematic representation of the stress-crack opening relation for uniaxial tension [17]

### 5.2.1.3. Extended brittle cracking model

As discussed in the previous section, the main drawback of the brittle cracking model is that its behaviour in compression is linear elastic. This renders it inapplicable in cases where the compressive behaviour is important, either during the main loading or in the post loading analysis.

In order to overcome this shortcoming in the model a user defined subroutine was incorporated into the model. One of the great advantages of the finite element package Abaqus is that it allows the user to code and add different user subroutines. These subroutines need to be within a certain framework dictated by the program and available input and required output is also defined by the framework.

In this case, due to the behaviour of the brittle cracking model deemed satisfactory in tension and the material model weakness only being in compression, it was decided to add a user subroutine to improve only the behaviour in compression. The user subroutine scheme chosen for this task was the VUSDFLD scheme, which is only valid within the explicit time scheme. This subroutine allows certain field variables to be redefined at a material point as a

function of time or other material point quantities, such as stress, strain, temperature etc. The field variable is updated at each analysis step and the value of the relevant material property is recalculated. In this study, the nonlinear compressive behaviour of concrete is introduced into the brittle crack model by formulating the modulus of elasticity of concrete ( $E_c$ ) as a function of strain ( $\varepsilon_c$ ). To define the  $E_c - \varepsilon_c$  function, the stress-strain ( $\sigma_c - \varepsilon_c$ ) relationship describing the uniaxial compression behaviour of concrete is adopted from the CEB-FIB Model Code 2010 [17]. The code implicitly adopts concrete softening properties.

$$\frac{\sigma_c}{f_{cm}} = -\frac{k \cdot \eta - \eta^2}{1 + (k - 2) \cdot \eta} \quad \text{for } \varepsilon_c < \varepsilon_{c,lim} \quad (5.5)$$

where  $\eta = \varepsilon_c / \varepsilon_{c1}$ ,  $\varepsilon_{c1}$  is the strain at the maximum compressive stress  $f_{cm}$ ,  $\varepsilon_{c,lim}$  is the strain at crushing of concrete in compression,  $k = E_{ci} / E_{c1}$  is the plasticity number,  $E_{ci}$  is the initial modulus of elasticity of concrete and  $E_{c1}$  is the secant modulus obtained by connecting the diagram origin to the curve peak, i.e.,  $(\varepsilon_{c1}, f_{cm})$ . The  $E_c - \varepsilon_c$  relationship can be obtained from Eq. (5.5) taking into account that  $E_c = \sigma_c / \varepsilon_c$  and  $E_{c1} = f_{cm} / \varepsilon_{c1}$

$$E_c = -\frac{k - \eta}{1 + (k - 2) \cdot \eta} \cdot E_{c1} \quad \text{for } \varepsilon_c < \varepsilon_{c,lim} \quad (5.6)$$

In Eq. (5.6),  $E_c$  is the secant modulus obtained by connecting the diagram origin to a point on the  $\sigma_c - \varepsilon_c$  curve. The  $\sigma_c - \varepsilon_c$  and  $E_c - \varepsilon_c$  curves yielded by Eqs. (5.5) and (5.6) are schematically shown in Figure 5.7.

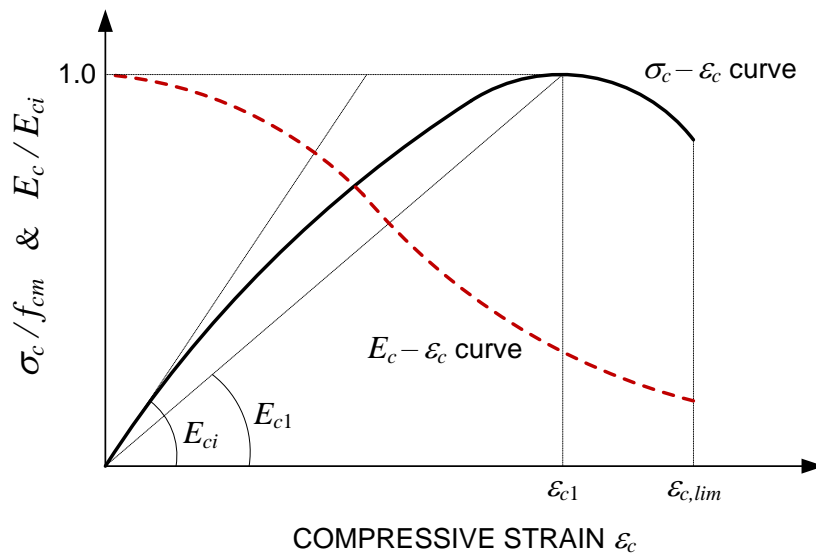


Figure 5.7. The  $\sigma_c - \varepsilon_c$  and  $E_c - \varepsilon_c$  curves describing Eqs. (5.5) and (5.6)

It is important to note that the subroutine accesses the material point properties at the start of an increment and is therefore not influenced by the results obtained during the increment [6]. This is usually not a concern as in dynamic explicit analysis the stable time increment is sufficiently small.

The variables that require user definition are the field variables at material points. These get passed into the user subroutine with values interpolated from the end of the current increment. The updated values are then used to calculate those material properties dependent on them.

An additional advantage of the extended and original brittle crack models is that they can be used together with the erosion algorithm in compression. This addition to the user subroutine finds the principle strains in each element checks if they are smaller than the allowed maximum strain (for example,  $\varepsilon_{c,max} = 0.0035$ ) and removes any failed elements, where the maximum strain has been reached, from the FE model.

### **5.2.2. Verification Studies**

In all FE simulations discussed hereafter, concrete was modelled using 8-node linear brick elements (C3D8R) with reduced integration to prevent over-stiff elements and enhanced hourglass control to avoid spurious deformation modes in the model mesh [6]. The elements were controlled during the analysis to prevent excessive distortion of the mesh.

In order to examine the concrete behaviour using the different material models described a single element cube was analysed. The cube was 1x1x1m. The bottom face of the block was constrained against the vertical movement. Additional constrains where applied at three corners of the block to prevent its rotation and movement in the plane parallel to the bottom face. Such boundary conditions allowed avoiding the development of an arching effect in the block. The displacement load was applied to the top face of the block in order to stabilise the procedure of the numerical solution. The model, boundary conditions and load for tension is shown in Figure 5.8.

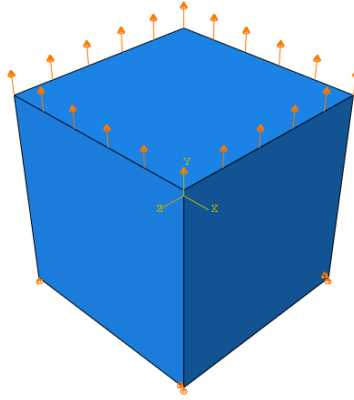


Figure 5.8. The single element concrete cube with tensile loading

Three FE models using the extended brittle cracking model, the original brittle cracking model and the damaged plasticity model were compared. The concrete materials were taken from an Abaqus benchmarked solution to a three point bending test [6], which will be further discussed in this chapter. The benchmarked solution used the damaged plasticity model and all the material parameters were taken in accordance. The general concrete parameters and the damaged plasticity parameters are presented in Table 5.1 and Table 5.2.

<b>Concrete</b>		
Young's modulus (GPa)	Poisson's ratio	Density (kg/m <sup>3</sup> )
30	0.2	2400

Table 5.1. General concrete properties

<b>Concrete Damaged Plasticity</b>				
Compressive Behaviour		Tensile Behaviour		
Yield Stress (MPa)	Inelastic Strain	Yield Stress (MPa)	Displacement (m)	Damage Parameter
20	0	3.33	0	0
30	0.0015	0.333	7.447e-5	0.9

Table 5.2. Damaged Plasticity concrete properties

The parameters were then modified for use in the brittle crack model. In this case there is no option for entering the concrete behaviour for compression, so only the tensile properties were used.

Finally, the material model was modified to use with the extended brittle crack model. For tensile behaviour no changes were needed and the tensile properties previously used were

adopted. In compression the stress- strain relationship provided by the damaged plasticity model was adapted by adding more reference points for stress and strain and then calculating the secant modulus of elasticity for each point. The results were then used as input for the user subroutine, and are presented in the following table where field 1 is representative of the strain.

<b>Concrete Extended Brittle Crack</b>	
Compressive Behaviour	
Young's secant modulus (GPa)	Field 1 (plastic strain)
30.00	0
30.00	0.000667
28.10	0.000703
24.12	0.000802
21.53	0.001001
20.00	0.0011
17.82	0.0013
16.05	0.001503
12.98	0.0021
12.04	0.0024
10.51	0.002806
10.00	0.0029
8.85	0.003305
8.03	0.003607
7.51	0.003907
6.97	0.004209
5.97	0.004913
5.00	0.0058
4.01	0.007327
3.00	0.009749
2.00	0.014505
0.10	0.02

*Table 5.3. Extended brittle crack concrete properties for user subroutine*



Additionally, the user subroutine allows the user to remove elements once maximum strain is reached in the concrete. For the following analyses using the brittle crack model the maximum allowable strain in compression was  $\varepsilon_{max,c} = 0.015$ .

As a further check the moduli of elasticity were compared for the damaged plasticity and the extended brittle crack model. The results are identical and presented in Figure 5.9.

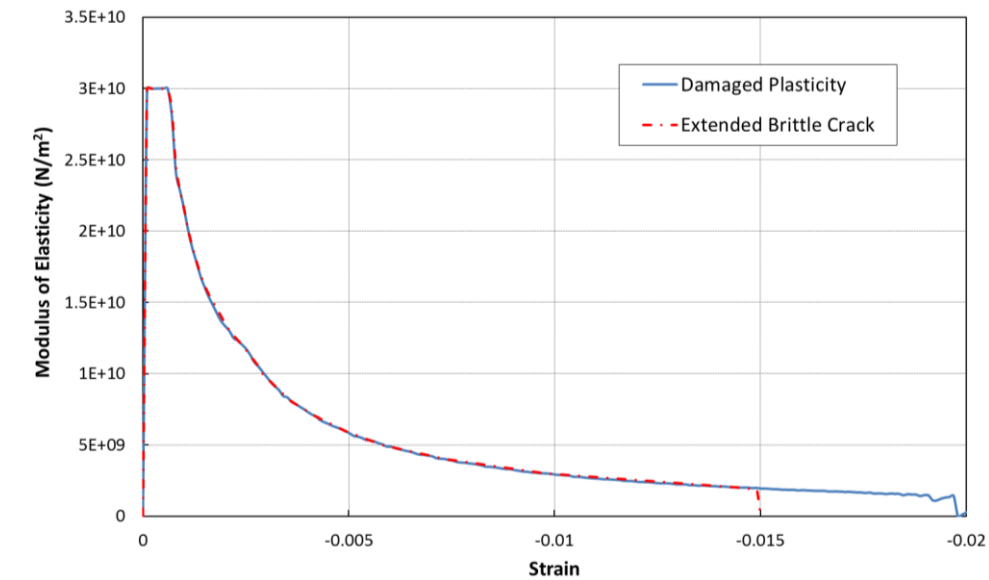


Figure 5.9. Comparison between Elastic moduli for the concrete models

The results for the single element cube in tension and compression are presented in the following sections.

### 5.2.2.1. Concrete cube under tension

The results for the concrete cube test in tension for the three different material models are presented in Figure 5.10.

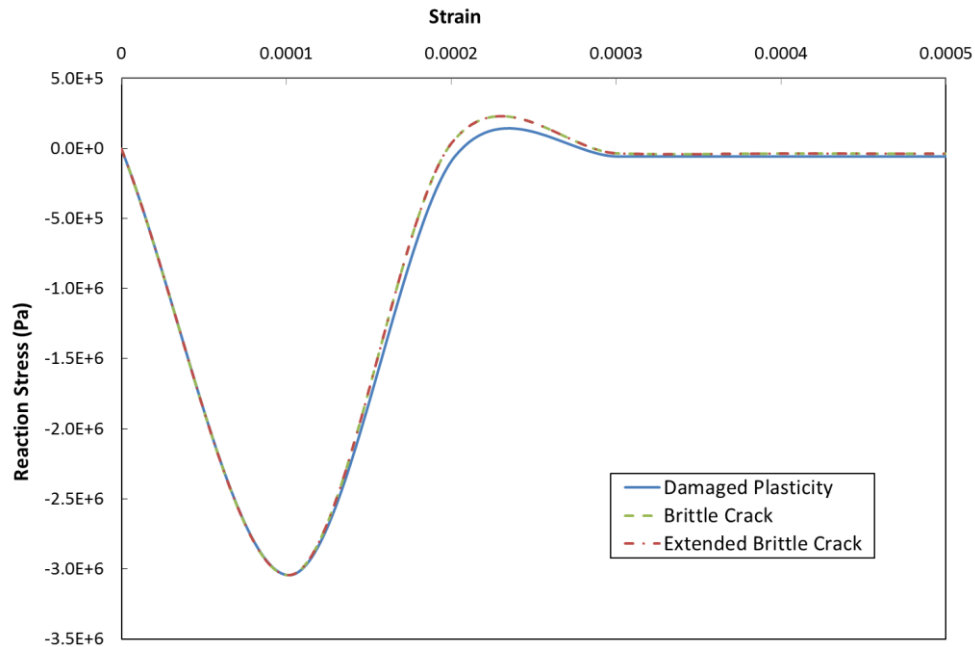
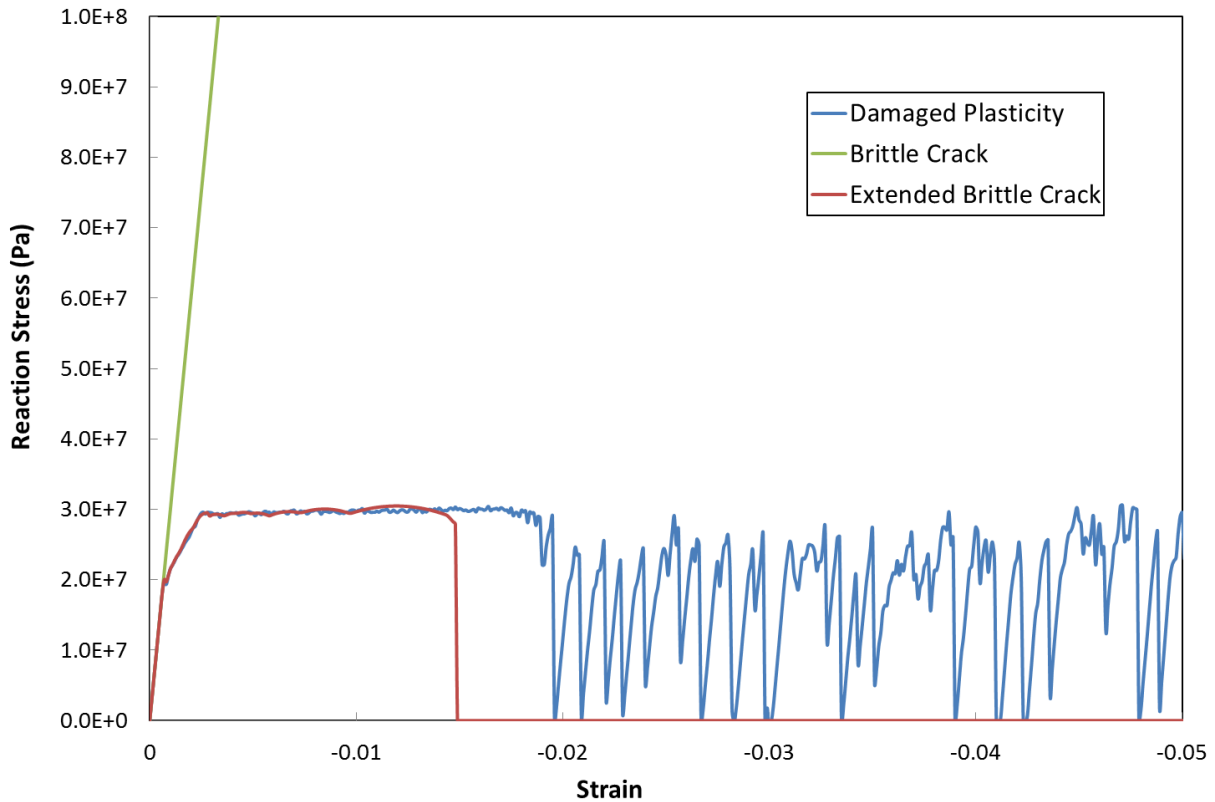


Figure 5.10. The single element concrete cube results for tensile loading

The performance of the three concrete models under uniaxial tension and compression was examined by applied a displacement load perpendicularly to the top face of the block. All the models behaved similarly under tension with a slight difference between the damaged plasticity model and the brittle cracking models developing in the part of the curves corresponding to the crack opening.

### 5.2.2.2. Concrete cube under compression

The results for the three models in compression, presented in Figure 5.11, vary significantly.



*Figure 5.11. The single element concrete cube results for compressive loading*

As presented, the behaviour of models highly diverged under compression. Figure 5.11 shows that the brittle cracking model exhibits an elastic response. The two remaining models behaved similarly until the designated maximum strain of 0.015 (corresponding to a displacement of 0.015 m), when the extended brittle cracking model failed. The damaged plasticity model failed at the strain just under 0.02 (a displacement of 0.02 m). Following its failure, the damaged plasticity model exhibited an unstable response with a series of sharp partial recoveries and failures. As a result, this model may not be entirely reliable in simulating the post-failure behaviour of concrete structures. It is important to note that the elastic-plastic response shape is determined by the benchmarked material properties of the damaged plasticity model, as previously elaborated on [6].

### 5.2.3. Strain Rate

Strain rate was examined for both tension and compression. The extended brittle cracking model does not explicitly include the effect of the rate of load application. The sensitivity of the material model to strain rate was examined using a standard concrete prism, as employed by Cotsovos and Pavlović [8], with a height of 253 mm and a cross-section of 100 mm by 100 mm [7]. Each edge of the prism cross-section was discretised into 5 elements, while the prism was discretised into 13 elements along its height. This gives 125 elements with the dimensions of 20 mm × 20 mm × 19.5 mm. The uniaxial compressive strength of concrete is assumed to be  $f_{cm} = 30$  MPa, Poisson's ratio equal to  $\nu = 0.2$  and the concrete density to  $\rho = 2400$  kg/m<sup>3</sup>. The bottom face of the prism was fixed and the load was applied to the top face at different rates.

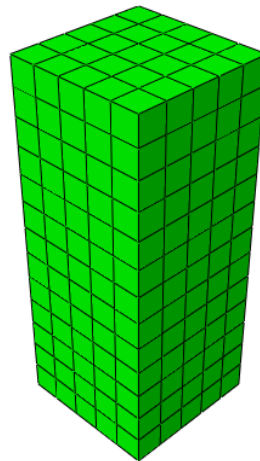


*Figure 5.12. Finite element model of concrete prism*

Initially, the effect of the tensile strain rate was examined using a displacement load. The displacement load was selected to stabilise the numerical solution during concrete failure in tension. Six different displacement rates between 10 mm/sec and 20,000 mm/sec (corresponding to the strain rates between 0.0005 sec<sup>-1</sup> and 3 sec<sup>-1</sup>, respectively) were considered. The results are presented in Figure 5.13. The increase in the tensile stresses was observed with growing strain rate.

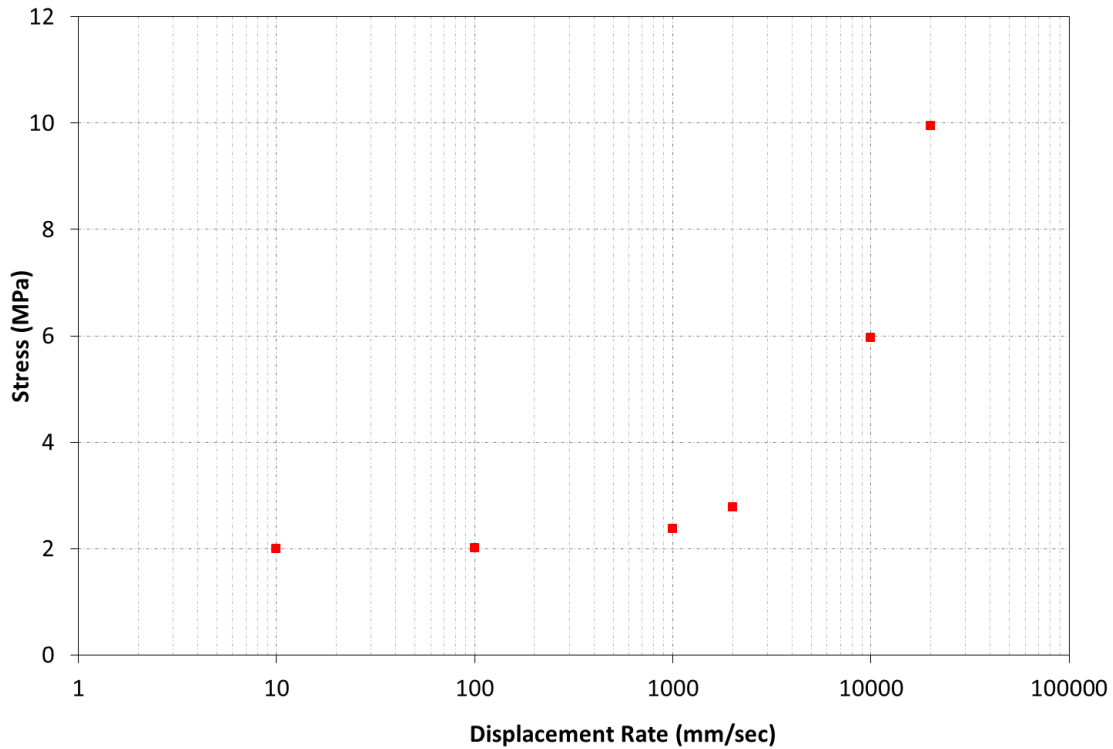


*Figure 5.13. Strain rate results in tension*

The strain rate results were plotted on a graph with all the known strain rate experimental data, as compiled by Cotsovos and Pavlović [7] and presented in Figure 5.14. The abscissa the diagram in the figure is in a logarithmic scale, and the ordinate is the maximum dynamic reaction force,  $P_d$ , at the top face of the prism normalised by the maximum static reaction force,  $P_s$ . As can be seen, the numerical results fall within the experimental scatter, and the  $P_d / P_s$  ratio increases more rapidly for the strain rates larger than  $0.1 \text{ sec}^{-1}$ . It is also necessary to note that the displacement loads with the rates larger than 20,000 mm/sec (corresponding to the strain rate of  $3 \text{ sec}^{-1}$ ) caused distortion of the finite elements, rendering the results unreliable.

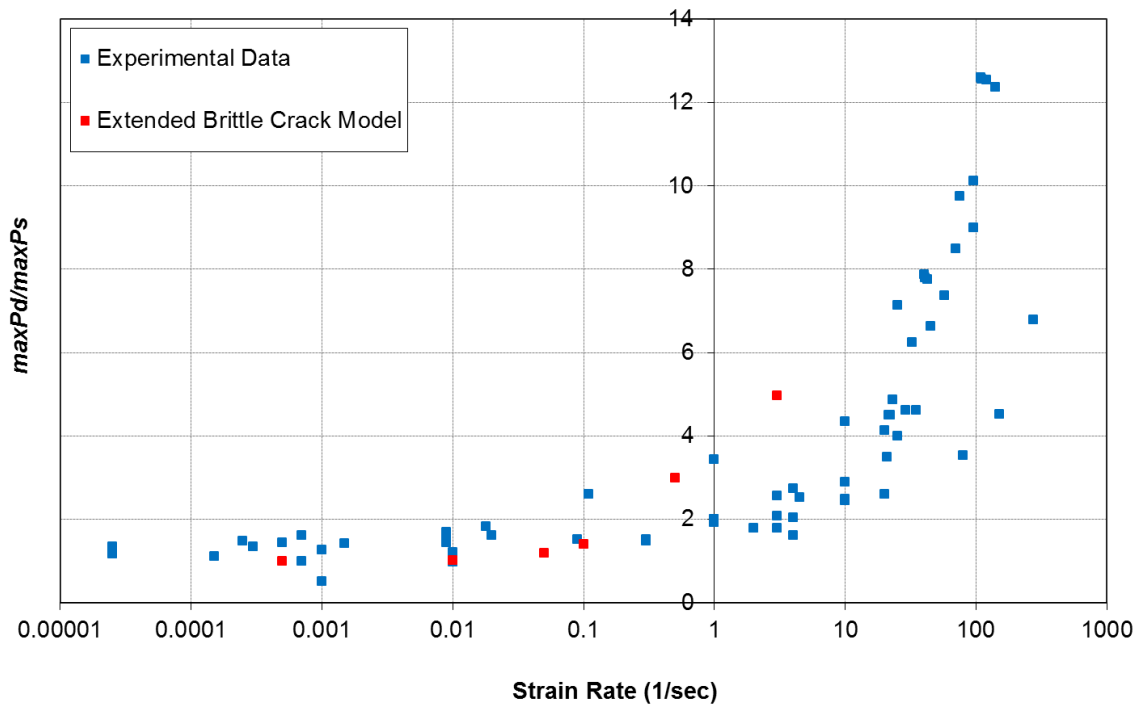


Figure 5.14. Strain rate results for tension compared to experimental results [7]

Figure 5.15 to Figure 5.20 show the development of displacements in tension until the time when maximum stress is observed. It is shown that in the lower displacement rates the displacement at the top influences the whole specimen. However in the four highest displacement rates only the top layer of the specimen is affected – the rate of loading is so high that the reaction does not have time to propagate down the specimen and the majority of the specimen remains unaffected by the load.

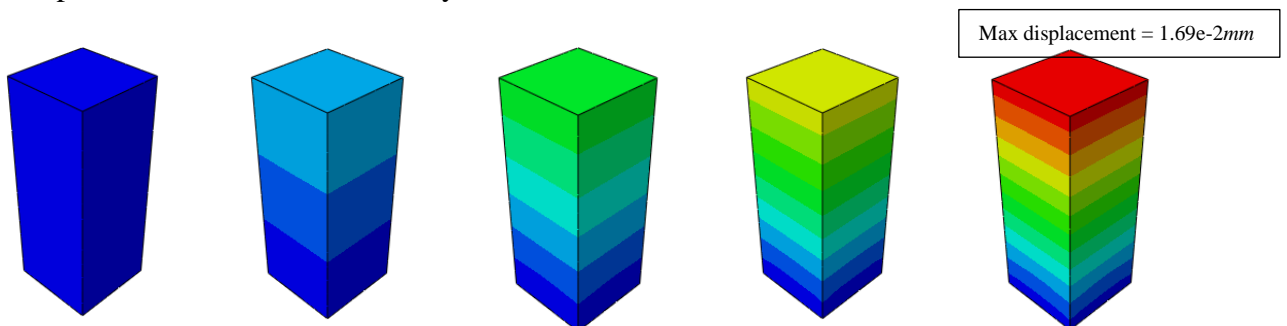


Figure 5.15. Displacement in tension for displacement rate of 10 mm/sec at  $t = 0, 25\%, 50\%, 75\%$  and  $100\%$  of time to maximum observed stress

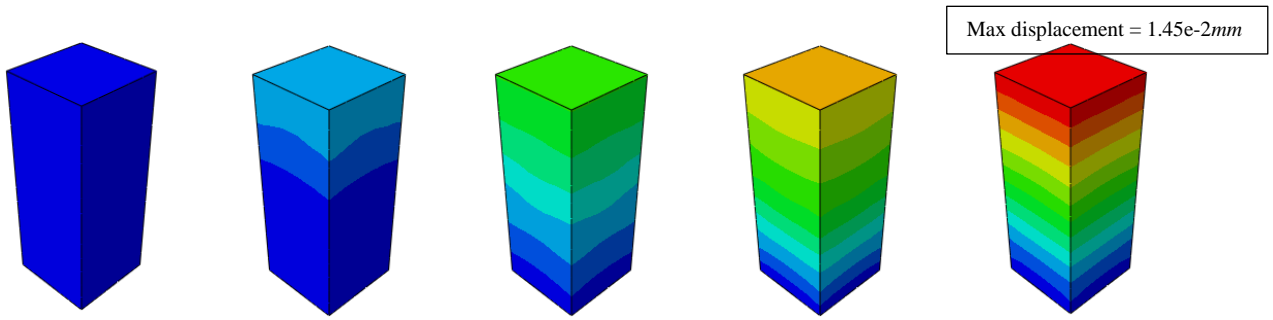


Figure 5.16. Displacement in tension for displacement rate of 100 mm/sec at  $t= 0$ , 25%, 50%, 75% and 100% of time to maximum observed stress

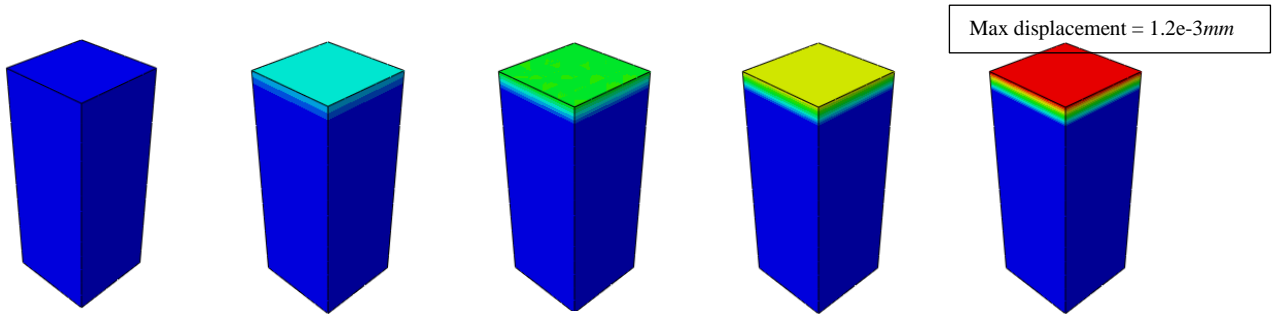


Figure 5.17. Displacement in tension for displacement rate of 1,000 mm/sec at  $t= 0$ , 25%, 50%, 75% and 100% of time to maximum observed stress

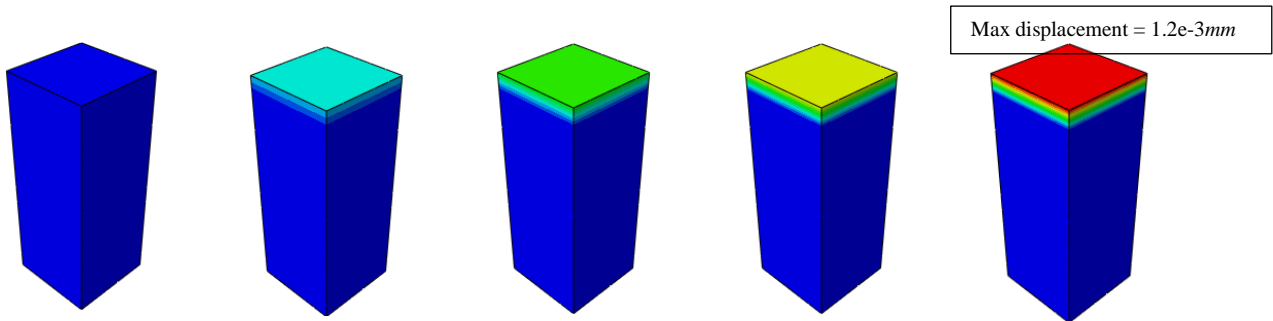


Figure 5.18. Displacement in tension for displacement rate of 2,000 mm/sec at  $t= 0$ , 25%, 50%, 75% and 100% of time to maximum observed stress

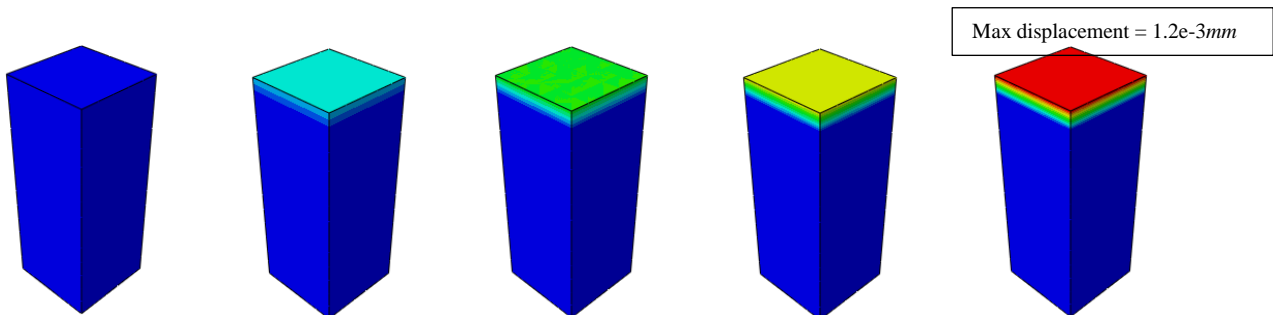


Figure 5.19. Displacement in tension for displacement rate of 10,000 mm/sec at  $t= 0$ , 25%, 50%, 75% and 100% of time to maximum observed stress

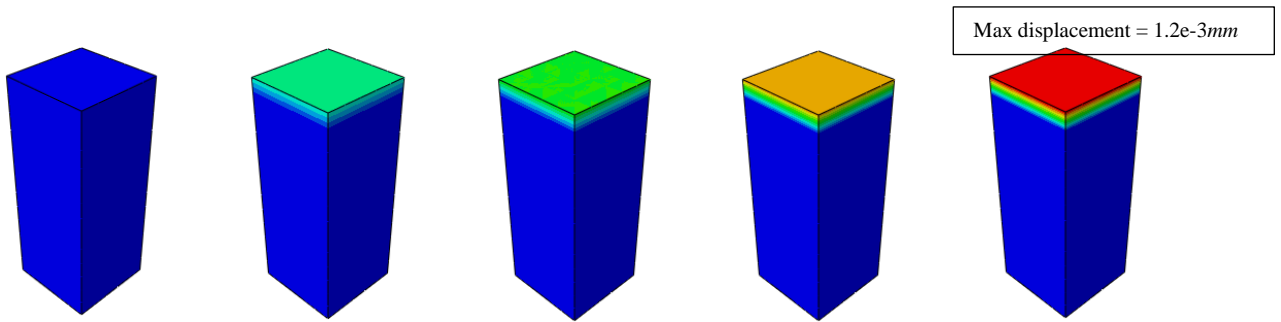


Figure 5.20. Displacement in tension for displacement rate of 20,000 mm/sec at  $t= 0, 25\%$ , 50%, 75% and 100% of time to maximum observed stress

It is worth noting that this research aims to understand concrete, and in particular reinforced concrete, at a structural level. In order to fully investigate strain rate in concrete under tension more work would be required at a meso-scale level with suitable mesh detailing due to the localised effects observed. It is recognised, therefore, that in the analyses presented there may be a certain displacement rate after which the analysis under or over estimates the concrete response.

The effect of the compressive strain rate was examined using the pressure load with the rates between 10,000 MPa/sec and 4,000,000 MPa/sec (corresponding to the strain rates between  $0.01 \text{ sec}^{-1}$  and  $70.8 \text{ sec}^{-1}$ , respectively). Figure 5.21 shows the results of numerical simulations.

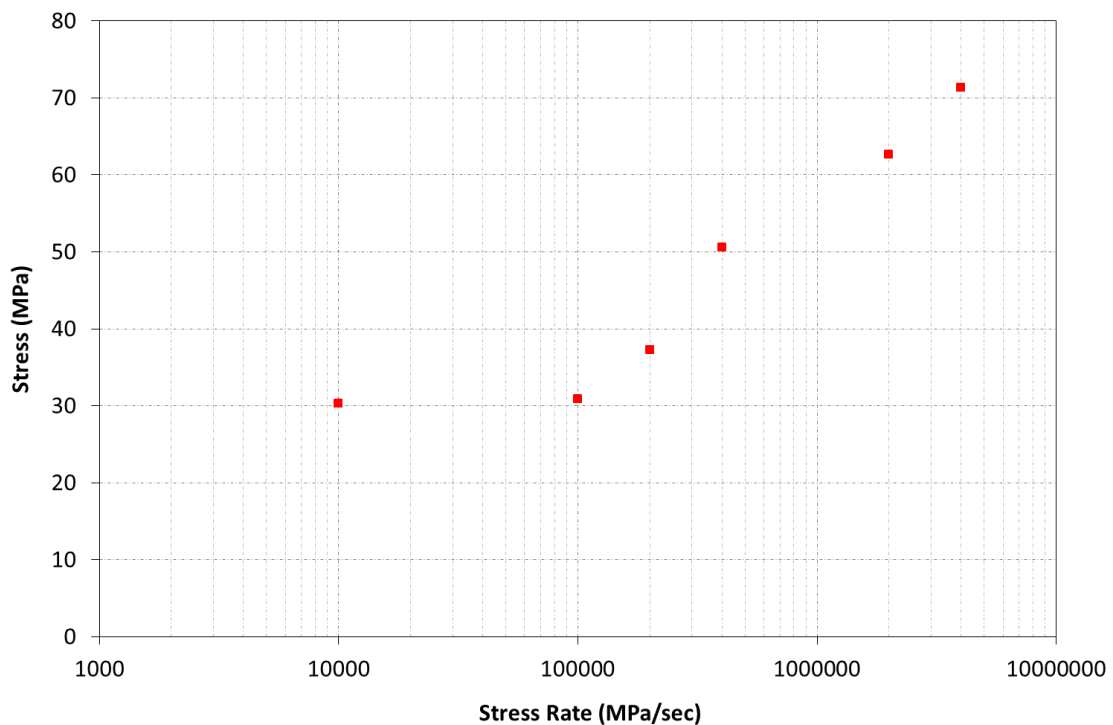


Figure 5.21. Strain rate results in compression



It was further observed that the specimen's behaviour differed under different loading rates. At the lowest loading rates of 10,000 MPa/sec and 100,000 MPa/sec the compressive stress increased gradually until the peak stress was observed and then unloading occurred and the stress reduced. In the mid rates of 200,000 MPa/sec and 400,000 MPa/sec the compressive stress increased gradually until reaching similar values to the static compressive stress, then some unloading occurred and the stress wave proceeded to the next row of elements after which additional loading was observed bringing the peak stress significantly higher than the static stress. In the highest load cases of 2,000,000 MPa/sec and 4,000,000 MPa/sec the load occurred at such a high speed that the material reaction was delayed - the stresses increased with no unloading, even when the elements were fully distorted.

The strain rate results were then plotted on a graph with all the known strain rate experimental data, as compiled by Cotsovos and Pavlović [8] and presented in Figure 5.22. The abscissa the diagram in the figure is in a logarithmic scale, and the ordinate is the maximum dynamic pressure,  $P_d$ , normalised by the maximum static pressure,  $P_s$ . It is evident that the growing strain rate leads to the increase of the  $P_d / P_s$  ratio and this increase becomes more rapid for the strain rates larger than  $0.3 \text{ sec}^{-1}$ . In addition, the numerical results fall within the wide experimental scatter.

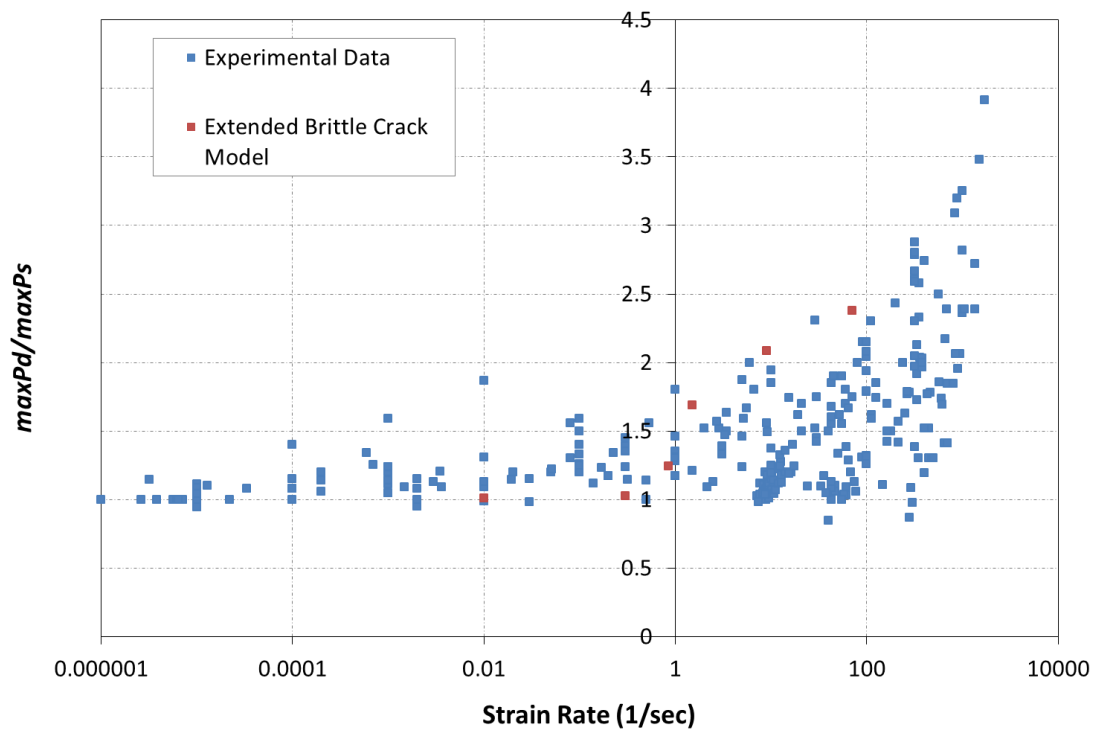


Figure 5.22. Strain rate results for compression compared to experimental results [8]

Figure 5.23 to Figure 5.28 show the development of displacements in compression until the time when maximum stress is observed. It is shown that in the lower load rates that the load progresses down the specimen. However in the two highest loading rates only the top layer of the specimen is affected – the rate of loading is so high that the reaction does not have time to propagate down the specimen and the majority of the specimen remains untouched by the load.

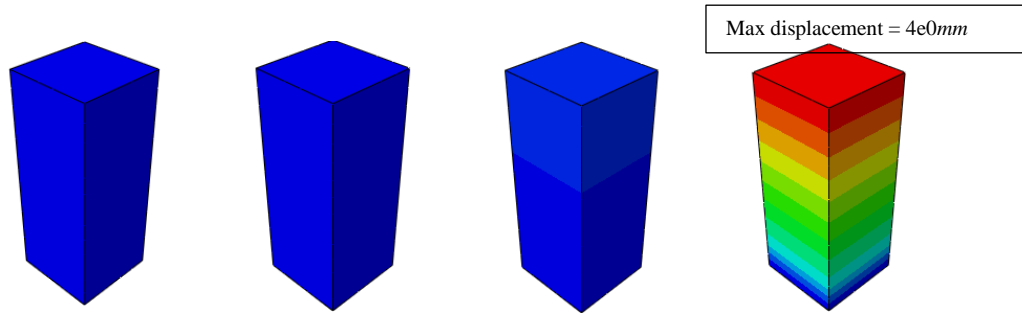


Figure 5.23. Displacement in compression for loading rate of 10,000 MPa/sec at  $t= 0, 50%, 75%$  and 100% of time to maximum observed stress

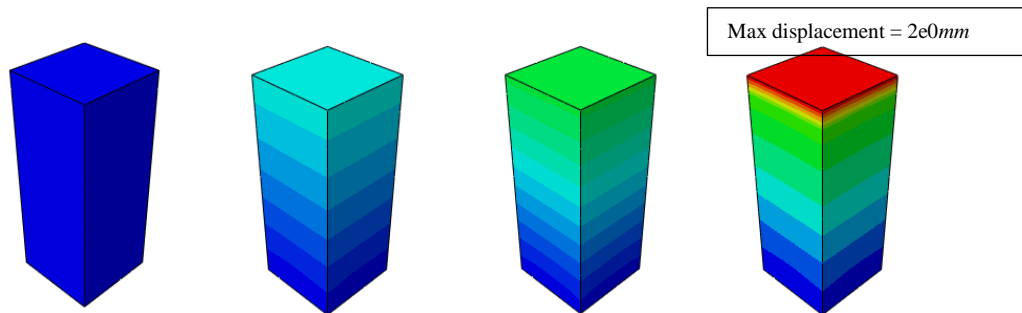


Figure 5.24. Displacement in compression for loading rate of 100,000 MPa/sec at  $t= 0, 50%, 75%$  and 100% of time to maximum observed stress

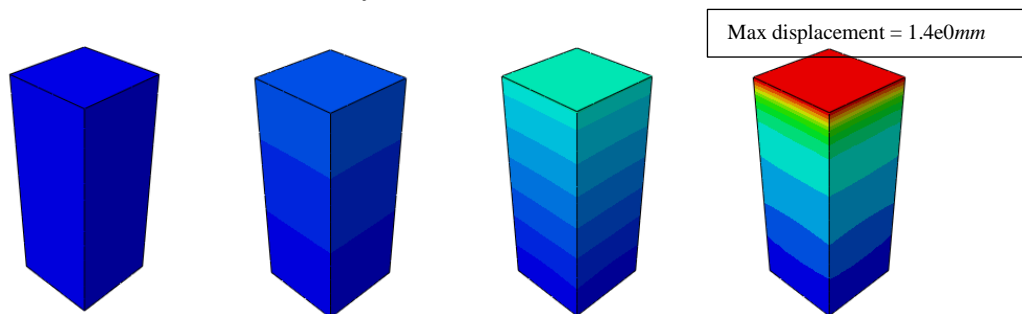


Figure 5.25. Displacement in compression for loading rate of 200,000 MPa/sec at  $t= 0, 50%, 75%$  and 100% of time to maximum observed stress

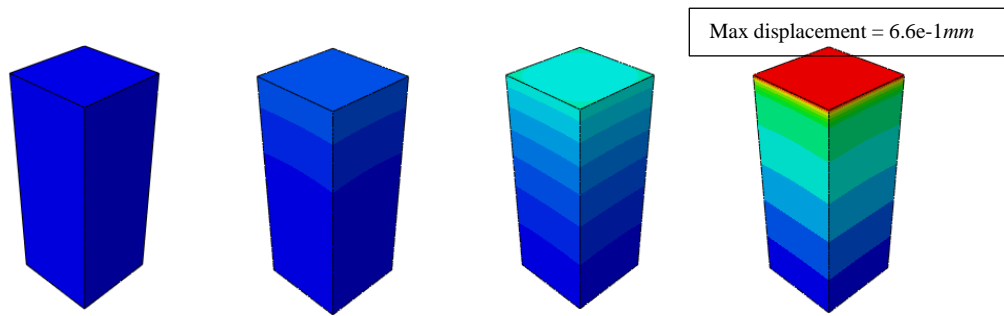


Figure 5.26. Displacement in compression for loading rate of 400,000 MPa/sec at  $t=0$ , 50%, 75% and 100% of time to maximum observed stress

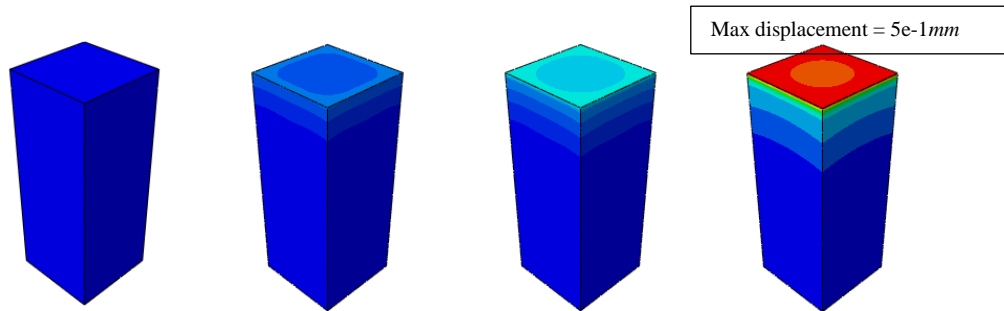


Figure 5.27. Displacement in compression for loading rate of 2,000,000 MPa/sec at  $t=0$ , 50%, 75% and 100% of time to maximum observed stress

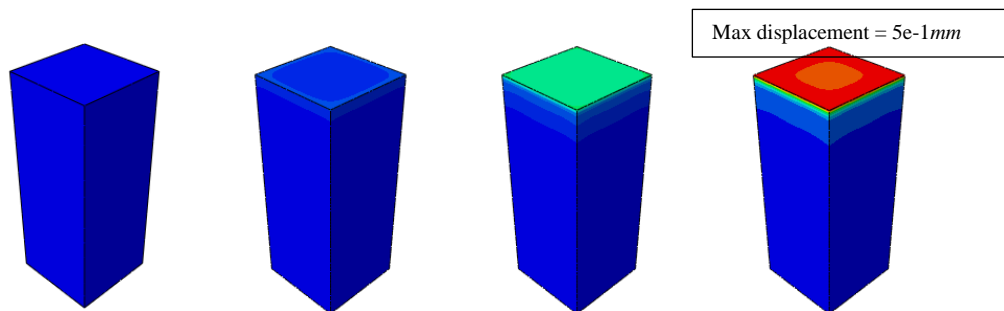


Figure 5.28. Displacement in compression for loading rate of 4,000,000 MPa/sec at  $t=0$ , 50%, 75% and 100% of time to maximum observed stress

The results show that although the subroutine written for compression has no explicit rate enhancement, the concrete stress is higher at high loading rates. This behaviour can only be attributed to inertia effects, which occur at the structural level.

#### 5.2.4. Conclusions

In this section three different concrete models were theoretically examined and then analysed using a single element cube test. The analyses confirm that the models all behave similarly in tension. In compression, however, the results diverge and the suitability of the different models can be assessed. The brittle crack model is deemed unsuitable for cases where there is

a need to consider compressive behaviour. The damaged plasticity model works well in compression until the deformations become too large and then the results are very unstable. The extended brittle crack model seems to overcome these two problems. By adding on a user subroutine written to extend the brittle crack models' capabilities in compression the behaviour in compression is as required. Additionally, adding the possibility of defining damage based on maximum strain and deleting damaged elements the material model overcomes the problems associated with the damaged plasticity model. Another advantage is that the material properties used in the extended brittle crack model are easier to obtain (using model codes, for example) than the input required for the damaged plasticity model. Overall, the extended brittle crack model offers a robust reliable concrete model.

Strain rate effects were also examined. As no material level definition was given for stress enhancement under growing strain rate any effects observed would be due to inertia effects. In both tension and compression stress enhancement under high strain rates were observed and the results favourably compared with those observed in experiments.

### 5.3. Modelling RC structural response

#### 5.3.1. Modelling of reinforcement

The steel reinforcement was modelled in Abaqus using 3D Timoshenko beam elements. The material used was a plastic, rate dependant material with a specified strain failure.

The bond between concrete and steel was modelled by embedding the steel reinforcement into the concrete elements. This technique can be readily implemented in Abaqus [6] by specifying a group of elements that lie embedded in a group of host elements whose response will be used to constrain the translational degrees of freedom in the embedded nodes. The embedded technique in Abaqus perfectly ties the embedded elements into the host elements. This is done through geometric relationships- if the node of an embedded element lies within the host element the translational degrees of freedom of the node are eliminated. In this case the relationship between concrete and steel is modelled as a perfect bond with no slip.

#### 5.3.2. Modelling Blast Loads

A number of different techniques are available in Abaqus to simulate blast loads, namely a built in CONWEP suite, incident wave formulation and the direct specification of pressure. The CONWEP ability did not prove useful in this case, as there is no way to directly control the peak pressure and impulse of the blast load. Similarly the incident wave method did not allow for direct user control on the peak pressure and impulse. The most applicable method for the analyses carried out in this research was by applying pressure directly to the column face with duration to match the impulse. As there was need to re-simulate the example many times it was deemed easiest to use and control.

#### 5.3.3. Nonlinear solution strategy

The dynamic equilibrium equation in its most general form can be written as:

$$M\ddot{u} = P - I \quad (5.7)$$

where  $M$  is the mass matrix,  $\ddot{u}$  is the acceleration vector,  $P$  is the external load vector and  $I$  is the internal vector. When the inertial force is small enough the equation reduces to the static form of equilibrium.

Both the explicit and implicit methods are mathematical approaches used in numerical analysis for obtaining solutions of time dependant equations. The implicit solution calculates

the current unknown quantities from the current information. The solution using this technique is stable, even if large time steps are taken. However, iteration and convergence checking are required and the out of balance force is used time and time again to check equilibrium which is computationally expensive. Using the explicit approach, also known as the forward Euler or central difference algorithm, the unknown quantities are obtained from information already known. Iteration and convergence checking are not required. However the time increment has to be small enough to lie on the curve.

Abaqus/Explicit has been designed to solve highly discontinuous, high-speed dynamic problems efficiently [18]. Using the explicit central difference integration rule the equations of motion are integrated for each degree of freedom (displacement or rotation) [6].

$$\begin{aligned}\dot{u}_{(i+\frac{1}{2})} &= \dot{u}_{(i-\frac{1}{2})} + \frac{\Delta t_{(i+1)} + \Delta t_{(i)}}{2} \ddot{u}_{(i)} \\ u_{(i+1)} &= u_{(i)} + \Delta t_{(i+1)} \cdot \dot{u}_{(i+\frac{1}{2})}\end{aligned}\tag{5.8}$$

where  $i$  is the increment number. The approach is explicit as the kinematic state is advanced by using the values  $\dot{u}_{(i-\frac{1}{2})}$  and  $\ddot{u}_{(i)}$  from the previous increment.

Combining the explicit integration rule with elements that use a lumped mass matrix allows Abaqus to calculate the nodal accelerations easily at any given time,  $t$ , using the following expression:

$$\ddot{u}|_{(t)} = M^{-1} \cdot (P - I)|_{(t)}\tag{5.9}$$

A lumped matrix is used due to the ease of calculating its inverse and also because the vector multiplication of  $M^{-1}$  by the inertial force requires only  $n$  operations, where  $n$  is the number of degrees of freedom in the model [6]. There is no need to create a global stiffness matrix as the internal force vector is formed from the individual element contributions.

In summary, the Abaqus/ Explicit suite is computationally efficient for the analysis of large models with relatively short dynamic response times and for the analysis of extremely discontinuous events or processes and therefore has been used in its work.

### 5.3.4. Mesh Size and Time Increment

Mesh size and stable time increment are closely linked. The stable time increment is the minimum time that a dilatational, or pressure wave, takes to move across any element in the model [18]. The stress wave speed, which consists of both volume expansion and contraction, for linear elastic material can be expressed as;

$$C_d = \sqrt{\frac{E}{\rho}} \quad (5.10)$$

where  $E$  is the elastic modulus and  $\rho$  is the material density. For simplification Poisson's ratio is assumed to be equal to zero.

In the model the mesh modelling provides each element with a characteristic length,  $L^e$ . This allows the stable time increment to be expressed as [18];

$$\Delta t = \frac{L^e}{C_d} \quad (5.11)$$

This shows that there is a direct interaction between the element length and the speed of the stress wave. Therefore reduction in element size,  $L^e$ , will reduce the stable time increment. This is of obvious importance when discussing high speed loads such as blast or impact.

In explicitly modelled blast simulations the mesh needs to be refined enough to capture the structural behaviour, but not so refined as to lead to increased time increments that will be too computationally expensive and time consuming.

Mesh convergence was studied for a column under a blast load. The column is a fixed-fixed reinforced concrete column modelled using the extended brittle crack model. It is based on the column used in this chapter (subsection 5.4.4.2) for blast verification and further used for parametric studies in Chapter 6. Full modelling details can be found in those sections. For the purpose of mesh convergence studies the mesh of the 3277mm high column was analysed using mesh sizes varying from 25mm to 100mm.

The analysis using the smallest mesh size of 25mm didn't converge due to excessive distortion elements in the model the ratio of deformation speed to wave speed was too high. This can be solved by reducing the maximum allowed time increment; however this comes at a huge computational expense. A reduction of the required time increment by one order of magnitude was not small enough to overcome the deformations developing.

The results of mid column displacement for meshes of 40, 50 and 100mm are presented in Figure 5.29. The damage pattern at the end of the analyses is shown in Figure 5.30. It can be seen that the 100mm mesh is too coarse to fully capture the structural response, whereas the 40mm and 50mm meshes are very similar in mid column displacement and residual damage.

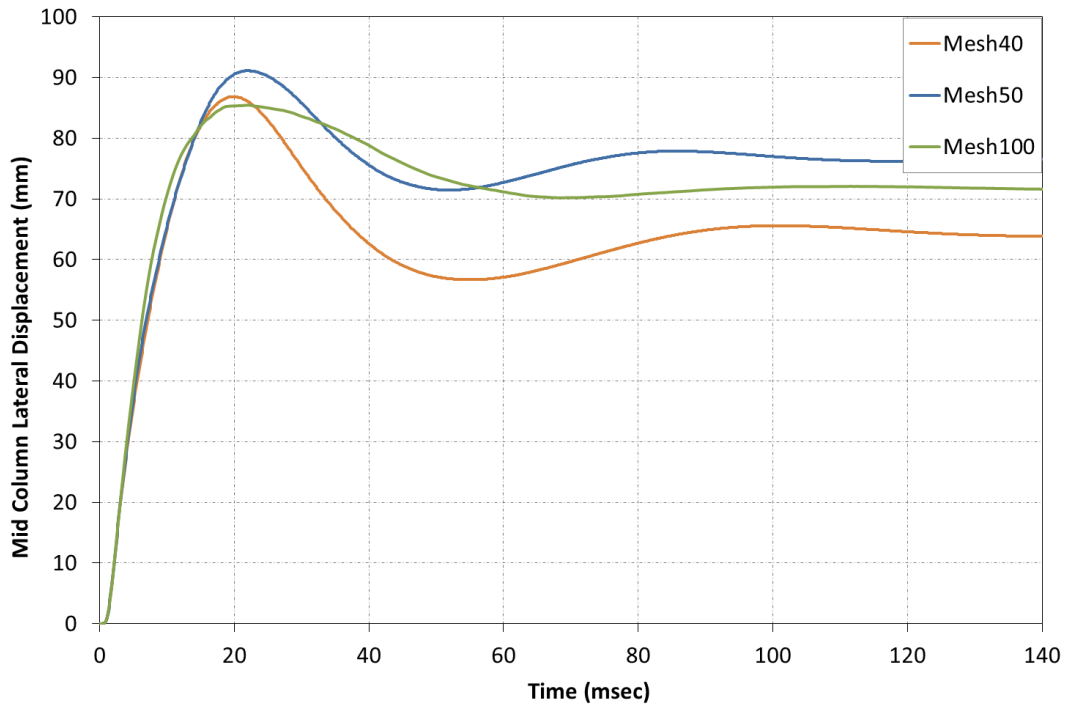


Figure 5.29. Mid column displacement for the meshes examined

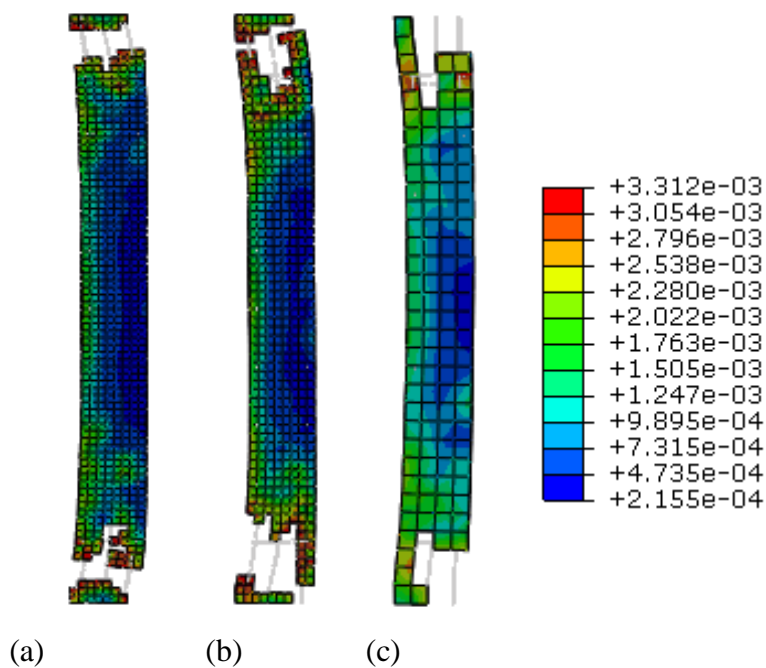


Figure 5.30. Damage patterns for the (a) 40mm (b) 50mm and (c) 100mm meshes



In order to verify that the right time increment was chosen the 50mm mesh was reanalysed with a maximum allowed time increment by one order of magnitude. In both cases the results were identical, as shown in Figure 5.31. The computational time, on the other hand grew from 1 hour of CPU time to 94.

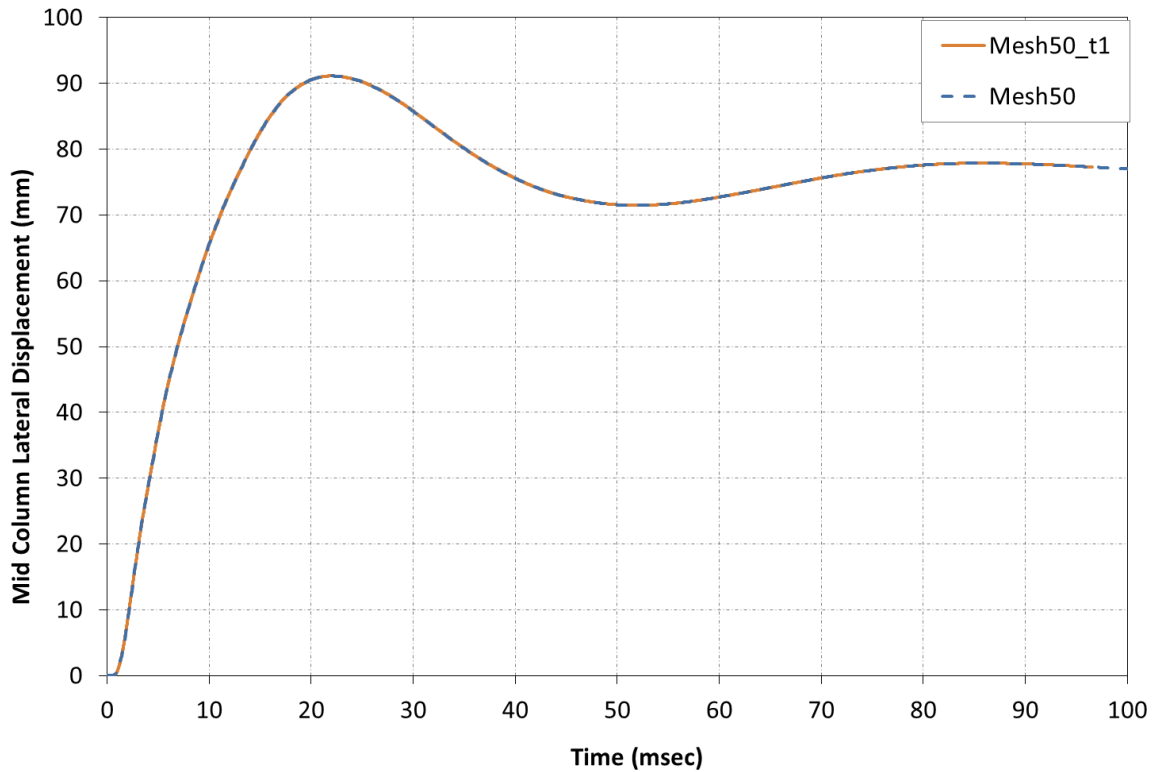
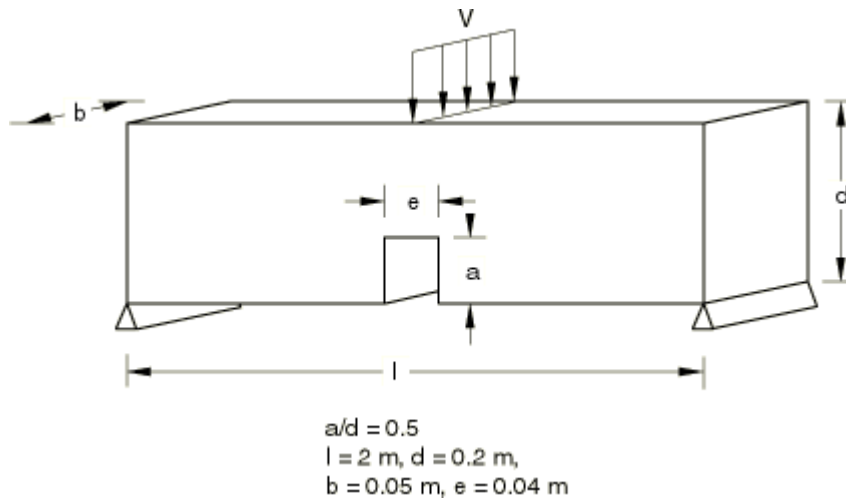


Figure 5.31. Mid column displacement for the 50mm mesh with varying time increment

## 5.4. Verification studies

### 5.4.1. Three-point bending static test

The case study of an unreinforced notched beam under 3 point bending, shown in Figure 5.32, was chosen to test the validity of the extended brittle crack model under static loading. This specific setup can be found in the literature both in terms of experimental studies [9] and analytical ones ([19]–[21], for example). The problem has already been studied in Abaqus [6] using the damaged plasticity model which gives the distinct advantage of being able to compare the two material models.



*Figure 5.32. Notched beam[6]*

The main behavioural response of the beam is Mode I cracking, so the main objective is to make sure that the tensile behaviour of the model is as expected and that the added extension does not limit it in any way.

The simply supported beam had a span equal to 2 m, a depth of 0.2 m and width of 0.05 m. The midspan notch had a depth of 0.1 m and width of 0.04 m. The beam was loaded by a knife (line) load at midspan. Taking advantage of symmetry, only half of the notched beam was modelled (Figure 5.33). The mesh consisted of 1120 three-dimensional elements of the type C3D8R [6]. The mesh around and above the notch was refined to overcome mesh sensitivity due to the possibility of cracking in the out of plane direction. The velocity load was applied to the beam very slowly to keep the inertia effects, inevitably developing when the explicit time integration was used, at a minimum and the beam in the static loading regime.

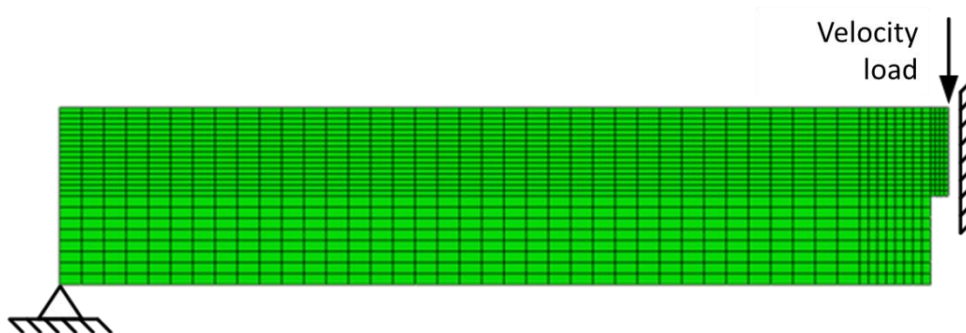


*Figure 5.33. Notched beam- finite element model*

The material properties are summarised in the following table:

<b>Concrete</b>		
Young's modulus (GPa)	Poisson's ratio	Density (kg/m <sup>3</sup> )
30	0.2	2400

*Table 5.4. Notched beam- concrete properties*

Additionally from the wealth of experimental and numerical data the cracking failure stress was known to be 3.33 MPa and the Mode I fracture energy  $G_f^I = 124 \text{ N/m}$ .

As the analysis is conducted in the Abaqus Explicit suite, which is a dynamic analysis program, it is important to ensure that the loading is done slowly to eliminate any inertia effects and to ensure a static solution. This is very important when dealing with brittle material models as the characteristic sudden drop in load carrying capacity leads to an increased response in kinetic energy [6]. In order to ensure a quasi-static solution the beam was loaded by applying a velocity that increases linearly from 0 to 0.06 m/s, the validity of which is the subject of another study [6].

The results of the FE simulations together with a comparison to the experimental data are shown in Figure 5.34. As can be seen, the use of the extended brittle crack model and the damaged plasticity model leads to similar behaviour of the notched beam which is comparable with the behaviour observed in the experiment. Small oscillations of the reaction-displacement curves still develop due to the inertial effect before cracking of concrete occurs. The amplitude of the oscillations becomes larger during the failure phase due to amplification of the inertia effect by cracking. The assumption the oscillations are due to inertia was verified by rerunning the simulation with a smaller material density.

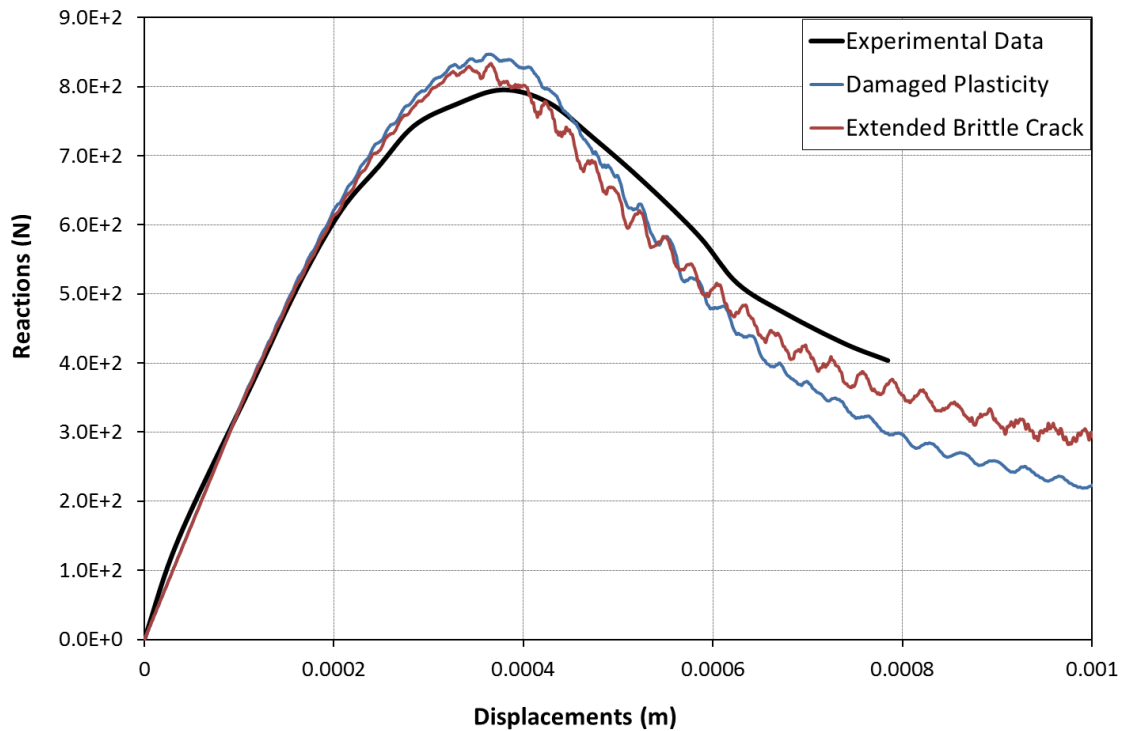


Figure 5.34. Notched beam- analysis results

#### 5.4.2. Predicting Brittle RC Failure

In order to study the response of reinforced concrete under impact, an experiment by Bresler and Scordelis [10] was modelled in Abaqus using the proposed extended brittle crack model.

The beam considered was beam C-2 from the experimental series. The beam geometry is presented in Table 5.5, and cross section presented in Figure 5.35.

Concrete			Steel Reinforcement			
Beam length (mm)	Beam width (mm)	Beam height (mm)	Longitudinal Bottom reinforcement	Longitudinal Top reinforcement	Stirrups	Cover depth (mm)
4572	155	560	4D28.65 (#9)	2D12.7 (#4)	D6.35 (#2) @208	41.275

Table 5.5. Bresler and Scordelis beam components' geometry

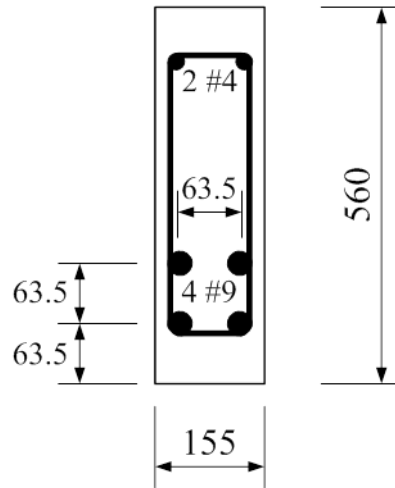


Figure 5.35. Beam cross section

The material properties for concrete were as follows

Concrete		
Young's modulus (GPa)	Nominal Strength (MPa)	Density (kg/m <sup>3</sup> )
22.924	24.13	2400

Table 5.6. Bresler and Scordelis beam- concrete properties

The steel properties are presented in Table 5.7.

Steel Type	Elastic Modulus (GPa)	Yield stress of longitudinal steel (MPa)	Ultimate stress of longitudinal steel (MPa)
#9	205.46	551.58	932.8
#4	201.33	345.42	603.98
#2	189.6	325.43	429.54

Table 5.7. Bresler and Scordelis beam- steel material properties

The loading arrangement and instrumentation is shown in Figure 5.36.

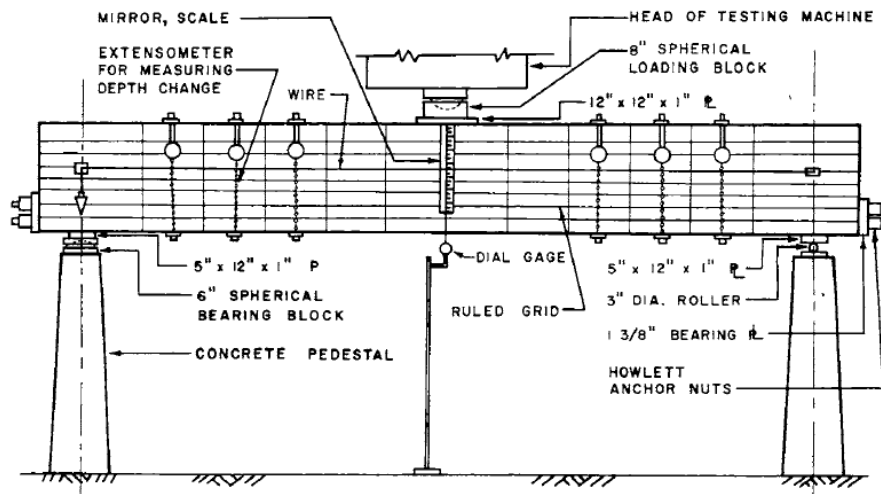


Figure 5.36. Loading arrangement and instrumentation [10]

The centre point load was applied using a 17.8 MN universal testing machine. A 200 mm spherical loading block was used at the load point. On one end the beam was supported on a spherical bearing block, whilst on the other end it was supported on a roller.

A finite element model using the extended brittle crack model was used to simulate the experiment in Abaqus. The FE model of the whole C-2 beam included 4510 three-dimensional elements of the type C3D8R. All reinforcing bars were modelled using Timoshenko beam elements (B31) and classic metal plasticity [6]. The reinforcing bar elements were embedded in the concrete elements. This formulation does not allow for failure of bond between steel bars and concrete. The finite element model with some of the concrete visually removed to allow a view of the embedded reinforcement is presented in Figure 5.37. Beam C3 was modelled although it included stirrups and therefore perhaps less of a prediction as to the behaviour of concrete as this work is aimed at looking at global structural performance.

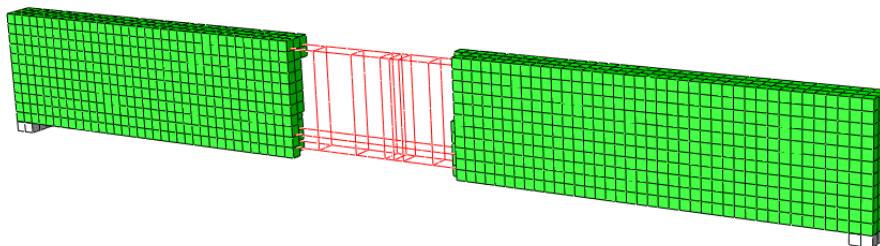


Figure 5.37. View of the finite element model of the Bresler and Scordelis beam

The concrete material in tension was modelled using the extended brittle crack model and referring to the base properties as given in the experimental data and the FIB Model Code [17], as described in Section 5.2.1.2. In compression the concrete stress-strain curve was calculated using the unconfined concrete strength in accordance with the model code. The secant Modulus of Elasticity as then calculated and used in the user subroutine, previously described, in order to capture concrete behaviour in compression. The resulting input curves are presented in Figure 5.38 for tension and Figure 5.39 for compression.

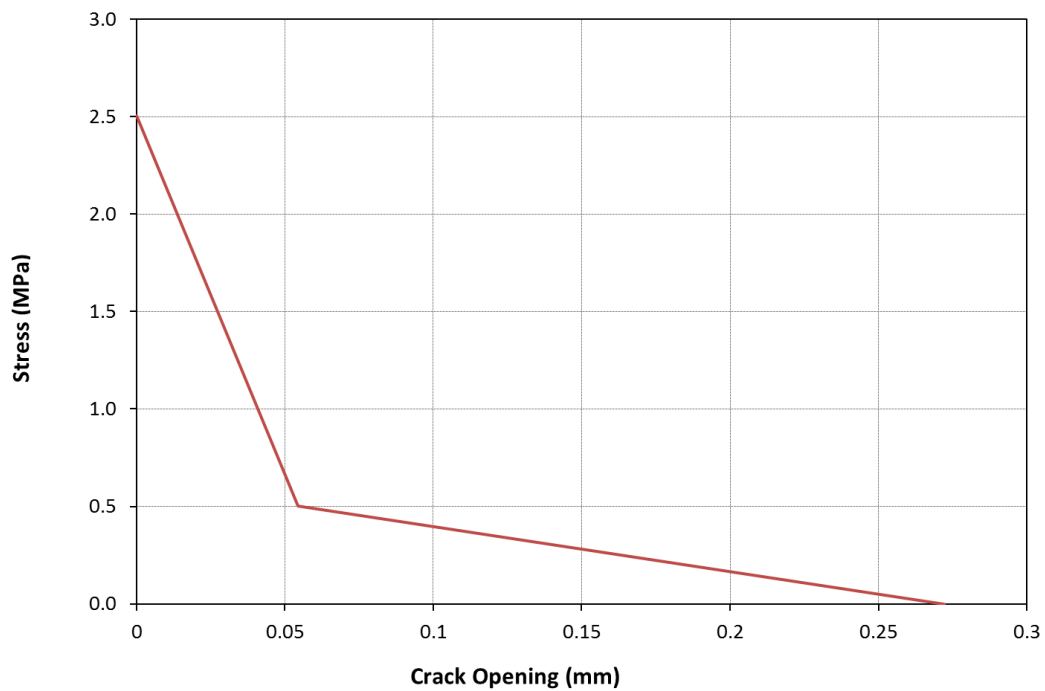


Figure 5.38. Concrete material properties in tension

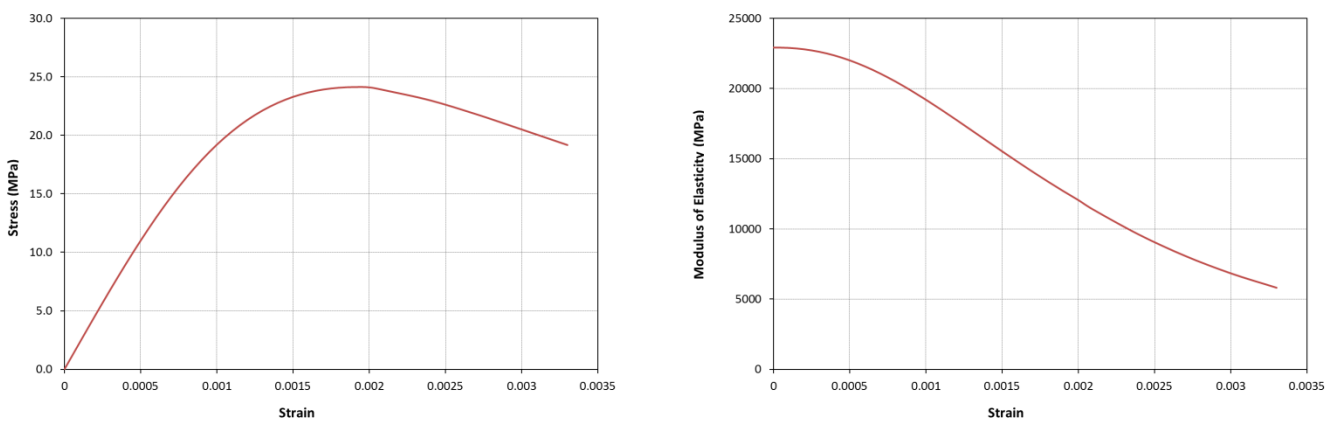


Figure 5.39. Concrete material properties in compression

The load was implemented using displacement control at the beam centre.

According to Bresler and Scordelis beam C-2 failed in shear-compression [10]. The failure took place at loads substantially higher than the load which initiated the first diagonal tension crack. The diagonal tension cracks formed at approximately 60% of the ultimate load. Additional load resulted in further diagonal cracks, but no sign of distress. As no extensive propagation of the flexural cracks at centre span occurred before failure, it was concluded that failure mechanism was that of shear-compression. The observed experimental cracks are presented in Figure 5.40.

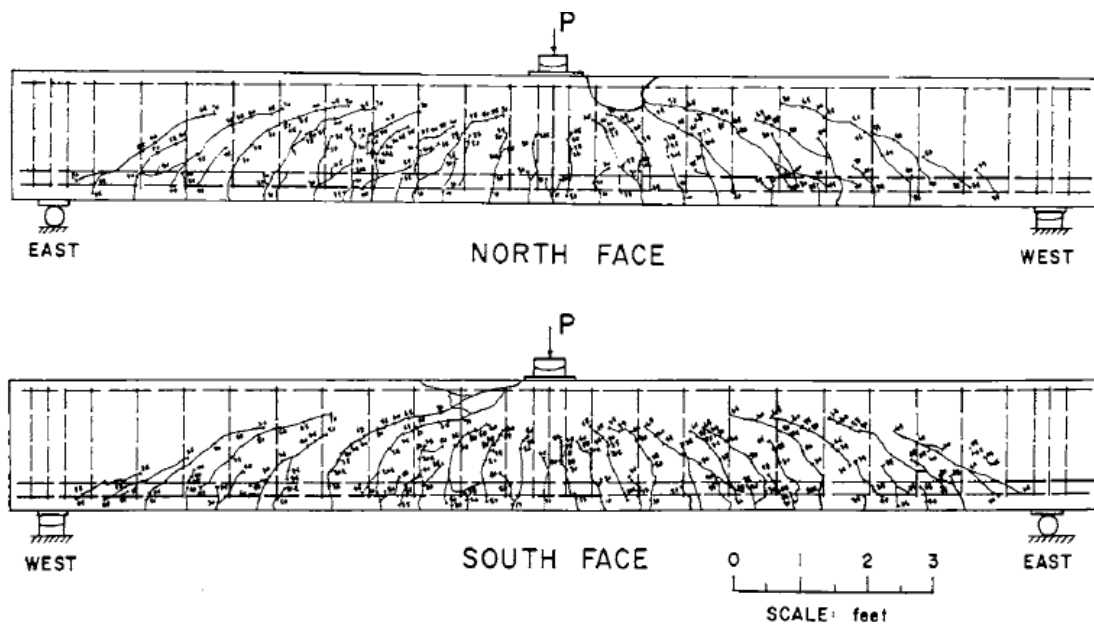


Figure 5.40. Typical crack pattern for shear-compression failure [10]

In the numerical simulation a similar crack pattern was observed, see Figure 5.41. The FE results show the strain distribution in the concrete. As can be seen, the test beam and the FE model underwent excessive cracking in the same zones. The midspan deflection of the test beam and the FE model are shown in Figure 5.42. The curves in the figure follow very similar paths till the FE model fails due to numerical instabilities introduced by excessive cracking of the concrete.



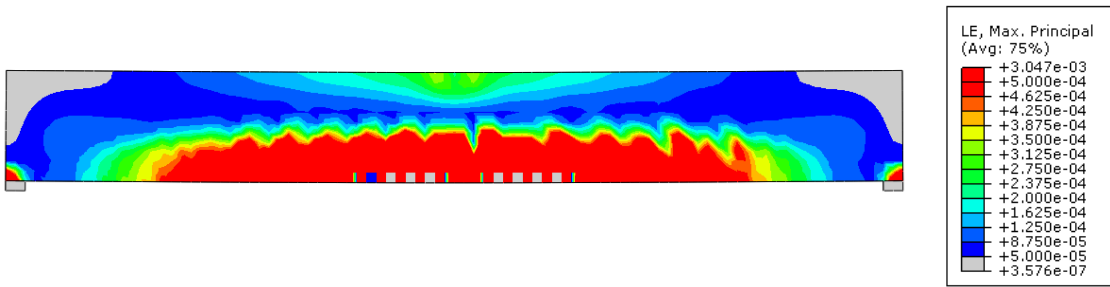


Figure 5.41. Observed crack patterns in numerical model

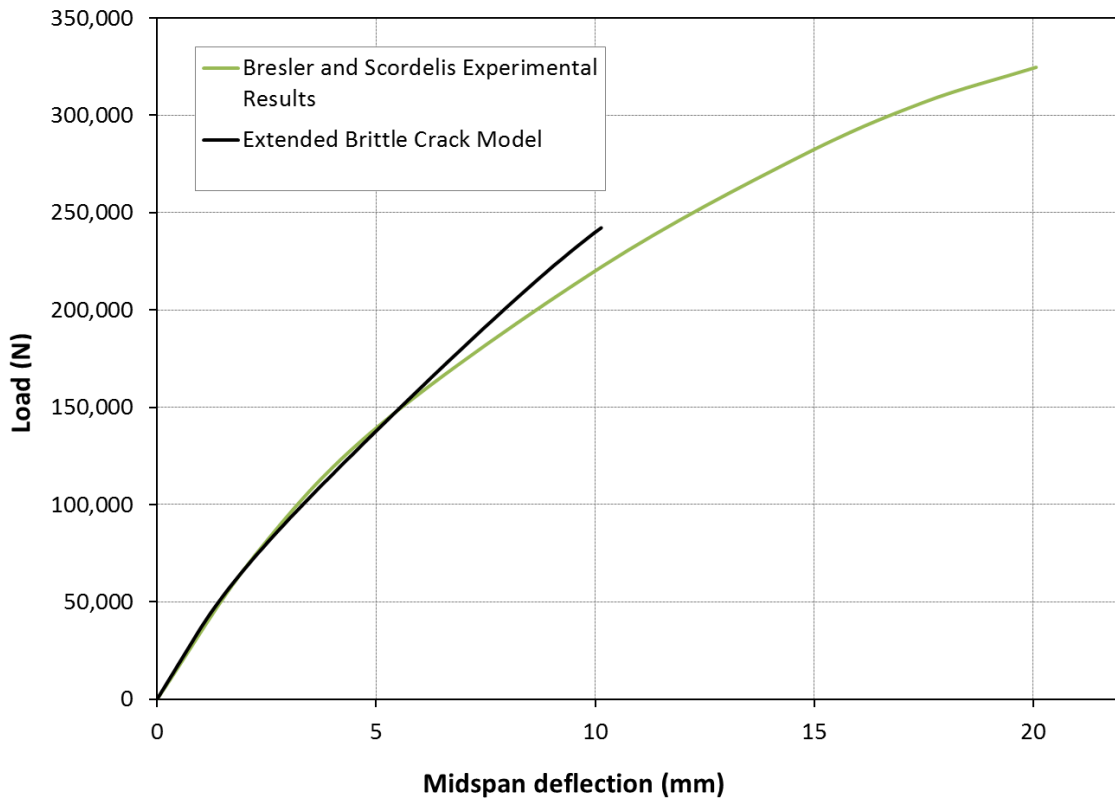


Figure 5.42. Load- Deflection curves for Bresler and Scordelis beam- experimental and numerical results

It can be seen, however, that the extended brittle crack model fails before failure is observed in the experiment (Figure 5.42). In the case of brittle failure this structural behaviour is preferable to over estimating the structural capacity. As presented in this section, the numerical model was able to capture the failure pattern and behaviour observed in the Bresler and Scordelis beam experiment.

### 5.4.3. Predicting Ductile RC Failure

Hughes and Speirs conducted numerous impact experiments on reinforced concrete beams [22]. In their experiments the beams remained elastic during the first impact and in most cases yielded subsequently at mid-span. One of the experiments was modelled in Abaqus using the proposed extended brittle crack model. The beam geometry is presented in Figure 5.43.

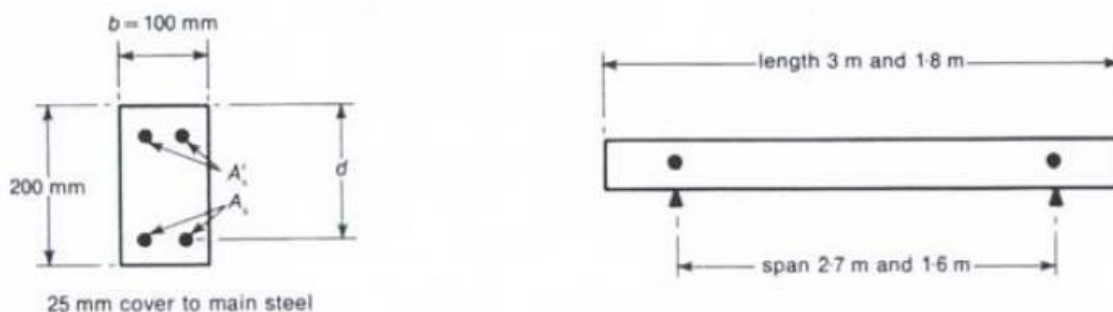


Figure 5.43. Details of test beams

The beam modelled was beam C-2 from the experimental series. The specific beam geometry is presented in Table 5.8.

Concrete			Steel Reinforcement			
Beam length (mm)	Column width (mm)	Column height (mm)	Longitudinal Bottom reinforcement	Longitudinal Top reinforcement	Stirrups	Cover depth (mm)
3000	100	200	2D12	2D6	D6@85	25

Table 5.8. Hughes and Speirs beam components' geometry

The material properties for concrete were tested and found to be in the following ranges, as presented in Table 5.9.

Concrete		
Young's modulus (GPa)	Nominal Strength (MPa)	Density (kg/m <sup>3</sup> )
28-36	30-60	2400

Table 5.9. Hughes and Speirs beam- concrete properties

The steel properties are presented in Table 5.10

Elastic Modulus (GPa)	Yield stress of steel (MPa)	Ultimate stress of steel (MPa)
206	460	560

Table 5.10. Hughes and Speirs beam- steel material properties

The loading arrangement and instrumentation is shown in Figure 5.44.

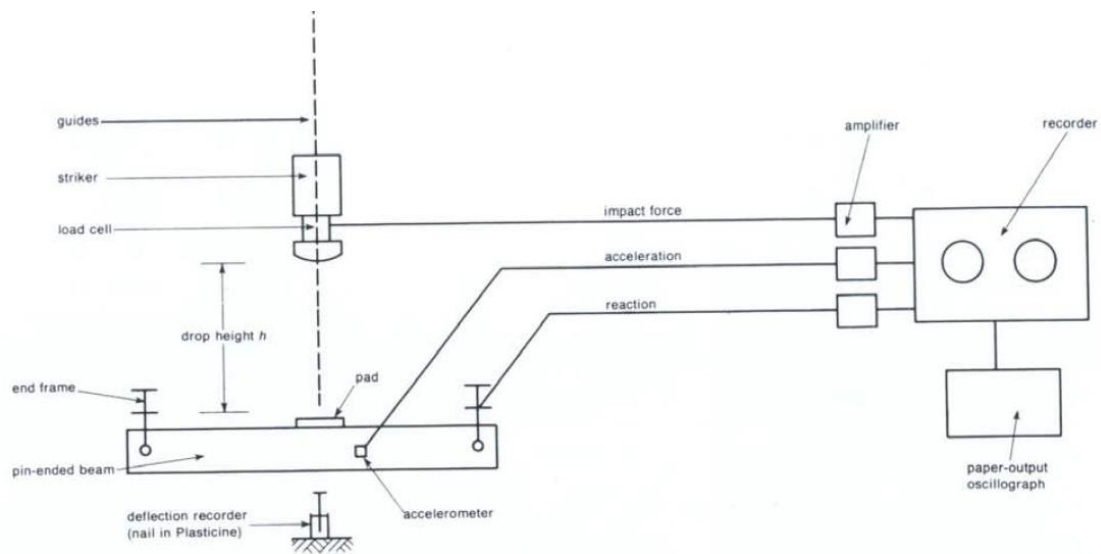


Figure 5.44. Loading arrangement and instrumentation [22]

A finite element model using the extended brittle crack model was used to simulate the experiment in Abaqus. As the beam, supports and loading was symmetric only quarter of the beam was modelled. The finite element model is presented in Figure 5.45 with some concrete elements visually removed to allow a view of the embedded reinforcement.

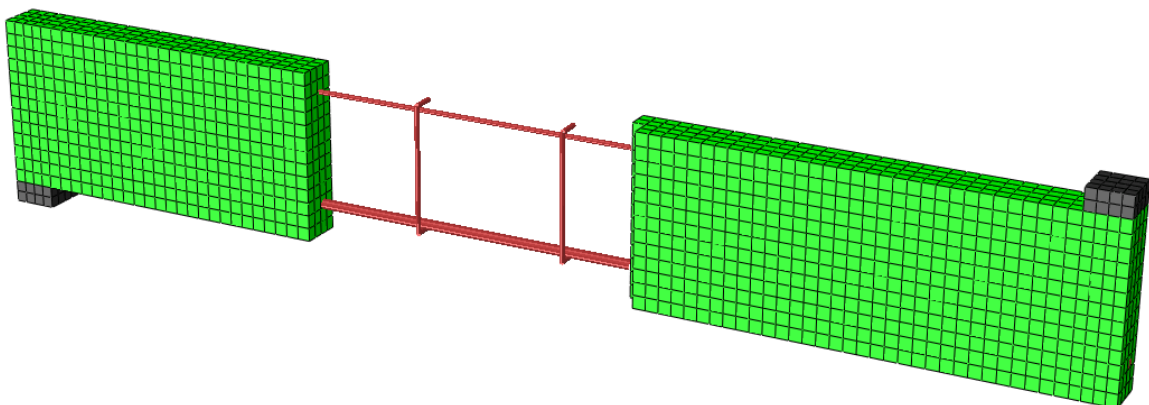


Figure 5.45. View of the finite element model of the Hughes and Speirs beam

The concrete material was modelled as before and the resulting curves presented in Figure 5.46 and Figure 5.47.

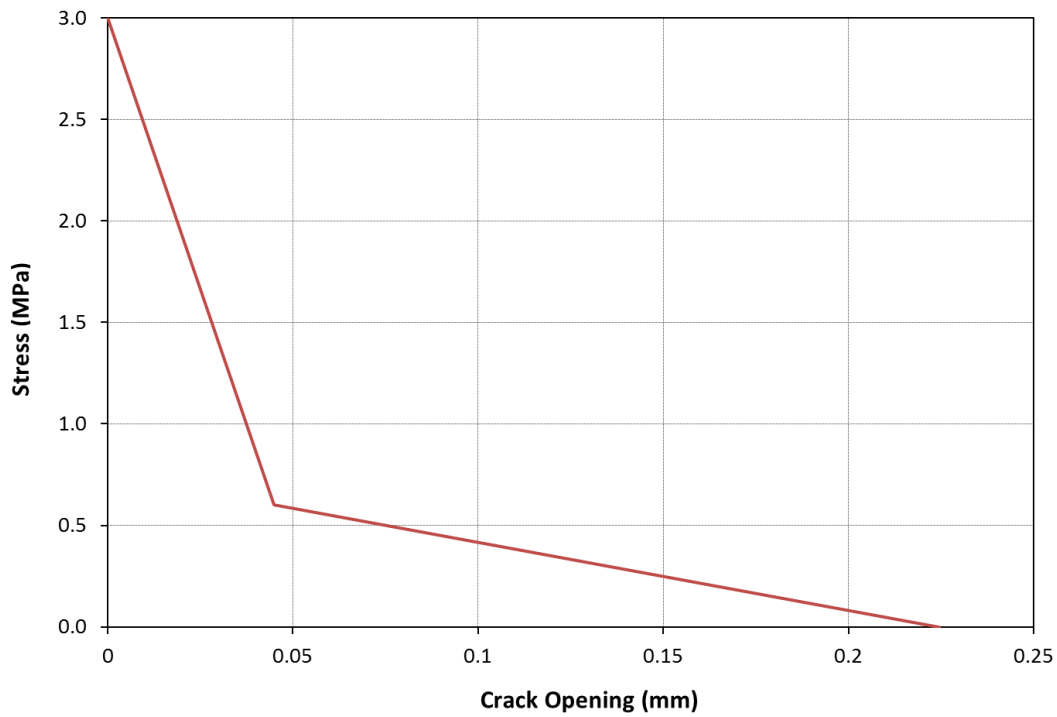


Figure 5.46. Concrete material properties in tension

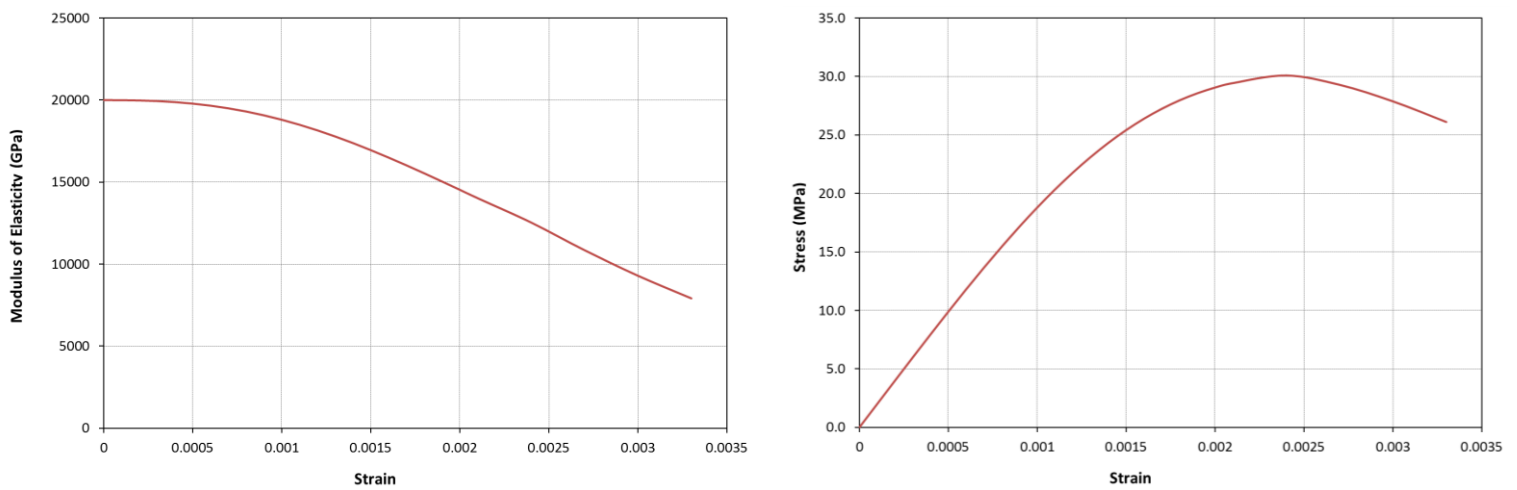


Figure 5.47. Concrete material properties in compression

The load was implemented using displacement control at the beam centre. The time-displacement curve used corresponds to the impact experiment on beam C-2 [22] and is presented in Figure 5.48.

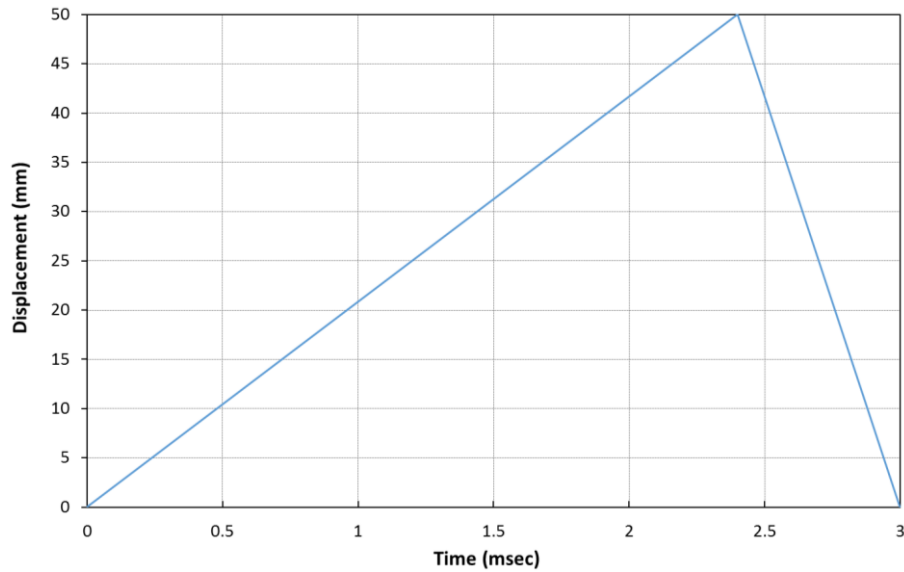
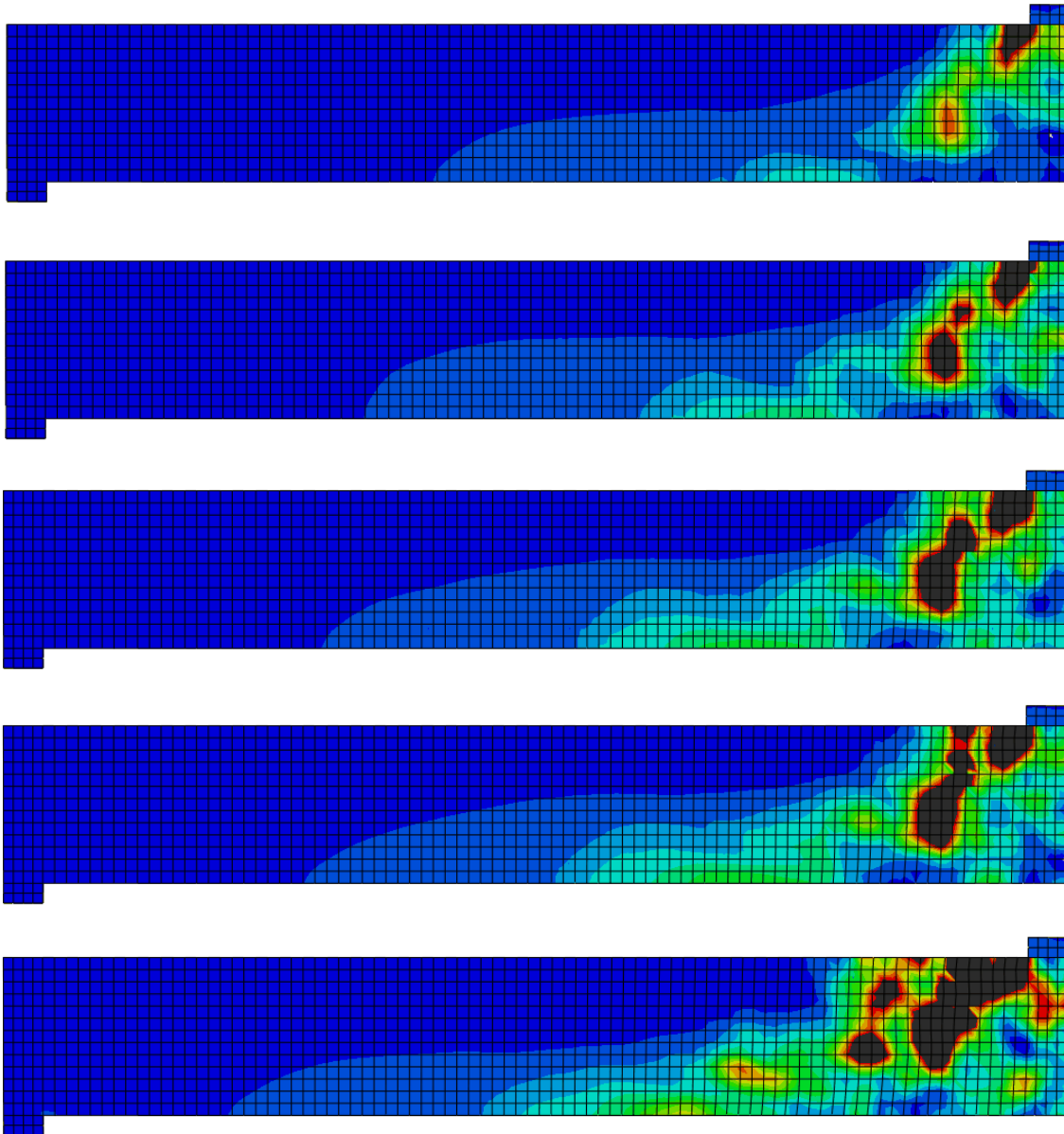


Figure 5.48. Amplitude used to simulate the impact case in experiment C-2

The maximum mid beam displacement is shown in Table 5.11. It is shown that the displacements in the numerical simulation closely follow those observed in the experiment. The crack development pattern is presented in Figure 5.49. When comparing to the observed cracks in the experiment, see Figure 5.50, the experimental pattern observed is similar to the numerical one.

C-2 Experimental Data		Numerical Simulation Results	
Mid Column Displacement (mm)	Time of max displacement (msec)	Mid Column Displacement (mm)	Time of max displacement (msec)
63	2.4	65	2.54

Table 5.11. Mid beam displacement for experiment and simulation



*Figure 5.49. Crack development for numerical simulation of Hughes and Speirs C-2 experiment*

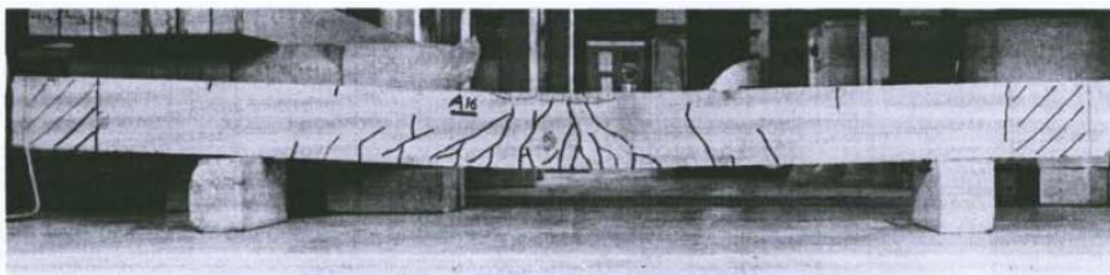


*Figure 5.50. Final observed crack pattern in Hughes and Speirs C-2 experiment*

Additionally, different rates of displacement loading corresponding to different loading rates were analysed. The results are presented alongside the results from Hughes and Speirs experimental results [22] and numerical results derived by Cotsovos [7] in Figure 5.51. It is clearly shown that the numerical results using the brittle crack model are well within the scatter.

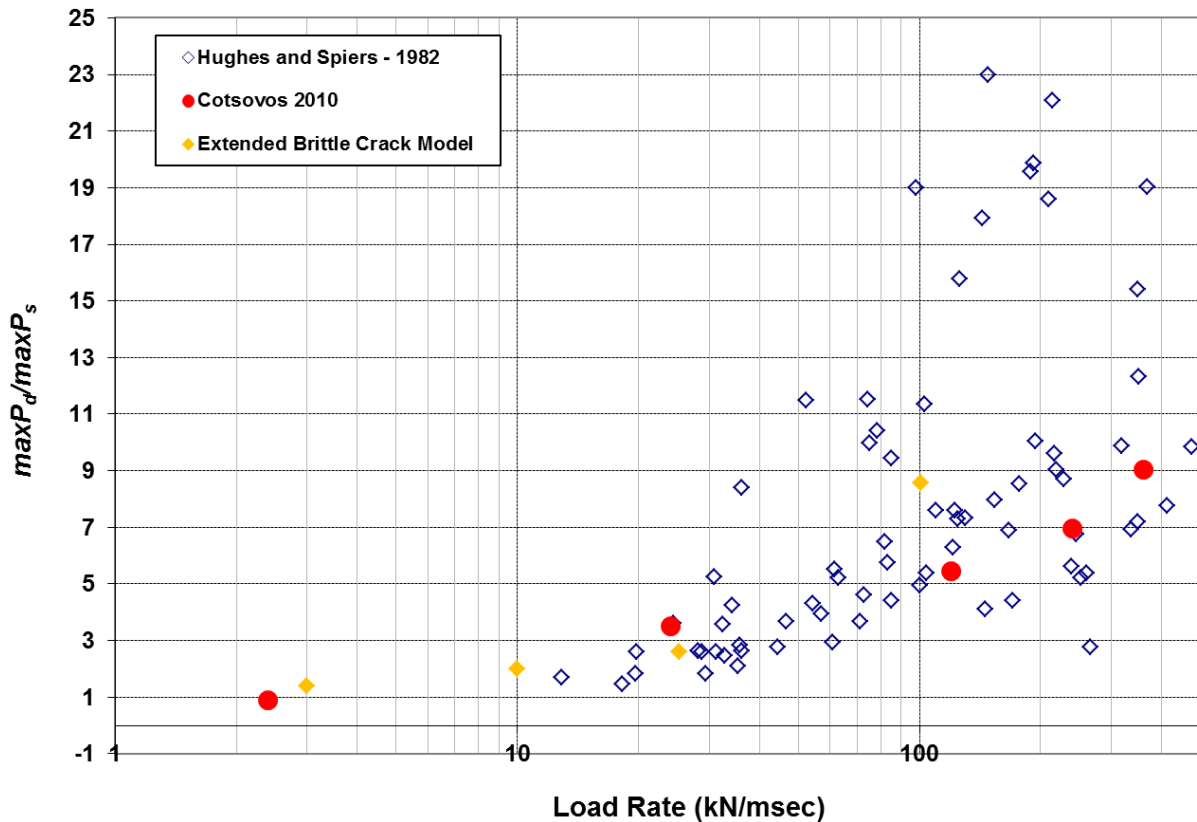


Figure 5.51. Hughes and Speirs experimental results alongside numerical results

#### 5.4.4. RC column under blast

##### 5.4.4.1. Quarter Scale Woodson and Baylot Column

In order to correctly capture the reinforced concrete behaviour under blast loads a series of simulations were carried out using Abaqus. The simulations were modelled after a blast experiment [11] and the results compared to those observed in situ.

The experiments were conducted to develop models to represent the exterior column region of a multi bay, multi-story reinforced concrete structure.

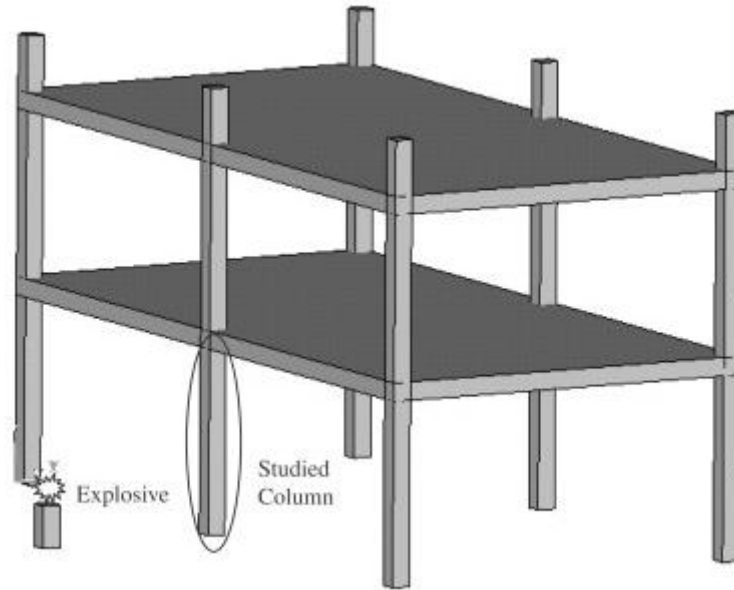


*Figure 5.52: Reinforced Concrete Column Model [23]*

The finite element model consisted of a concrete column, embedded steel reinforcement and both a column heading and footing to correctly simulate the boundary conditions of the column within the frame structure [23], as presented in Figure 5.53 and described further in this section.

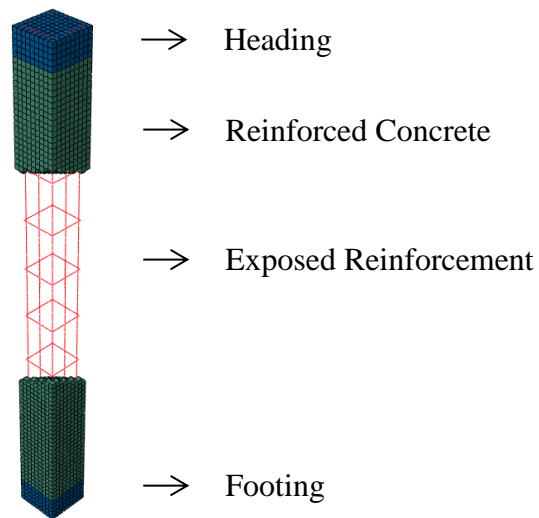


*Figure 5.53. Reinforced Concrete Column Model*



The geometry of the structural components is presented in Table 5.12.

Concrete				Steel		
Column width (mm)	Column depth (mm)	Column height (mm)	Heading/ Footing height (mm)	Longitudinal reinforcement	Cross tie/hoop	Cover depth (mm)
85	85	900	50	8D3.2	D1.6 @100	8.5

Table 5.12. Column components' geometry

The boundary conditions used simulate behaviour representative of a column within a frame structure and provided restraints between fixed and pinned. A footing and a head were included in the numerical model. The outer vertical face of the footing and head were constrained against horizontal motions and the bottom face of the footing was constrained against vertical motion.

The basic premise for the load was taken directly from the experiments. The following Figs demonstrate the reading placements on the column and the peak pressure and impulse readings.

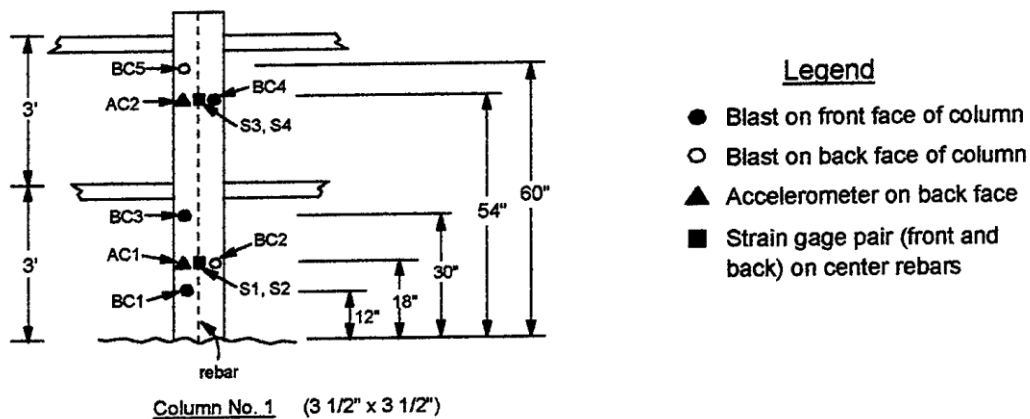


Figure 5.54. Column experiment reading placements

The blast load peak pressure and duration were 6.1 MPa and 0.000331 seconds respectively. This corresponds with the results [23] obtained for the blast loads acting on the column's front face. The load was simulated by means of a pressure load. The pressure was applied uniformly along the length of the column. In reality the spatial pressure profile decreases as distance from the blast charge point grows, however in this research as we are only discussing the length of the element the pressure was assumed to be uniform along the length.

The elements used were taken from the Abaqus explicit element library. They were of type C3D8R- 8 node linear bricks including reduced integration and hourglass control. Mesh convergence was tested and a mesh size of 1mm deemed satisfactory.

The steel material behaviour was modelled as elastic perfectly plastic with the following values:

Elastic Modulus (GPa)	Yield stress of longitudinal steel (MPa)	Ultimate stress of longitudinal steel (MPa)	Yield stress of cross tie/hoop (MPa)	Ultimate stress of cross tie/hoop (MPa)	Fracture strain of steel (%)
210	450	510	400	610	18

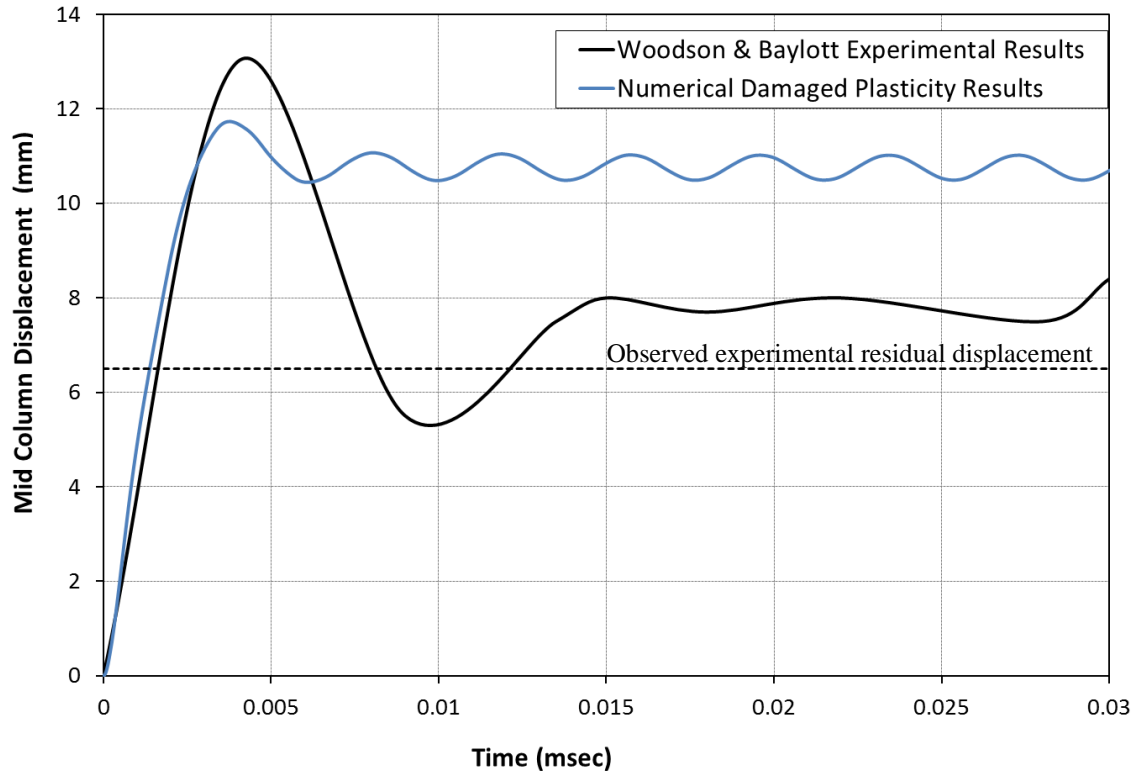
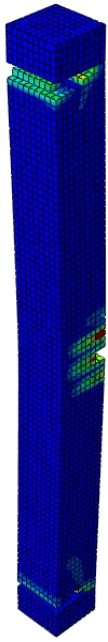
*Table 5.13. Steel Material Properties*

Concrete material modelling proved to be a more complex issue and the different modelling options were analysed. The basic concrete material properties, as per the experiment are presented in below.

Elastic Modulus (GPa)	Unconfined concrete strength (MPa)
24	42

*Table 5.14. Concrete Material Properties*

Initially the concrete was modelled using the damaged plasticity model from the Abaqus library. The results achieved using this material model were very close in the initial response to the blast load however the post blast response was not comparable to the experimental results. When used the reinforced concrete column reaches maximum displacement and then retains very large residual displacements. These seem to occur due to the columns behaviour in tension; the concrete material cracks, and the steel area is not sufficient to enable the column additional return.



(a)

(b)

Figure 5.55. Damaged Plasticity Results (a) Maximum residual strains (b) Results for mid column displacement

The Extended Brittle Crack model was then used. The concrete material was defined using the base properties, as given in the experiment report and FIB Model Code [17] as in previous simulations.

The resulting material parameters are presented in Figure 5.56 and Figure 5.57.

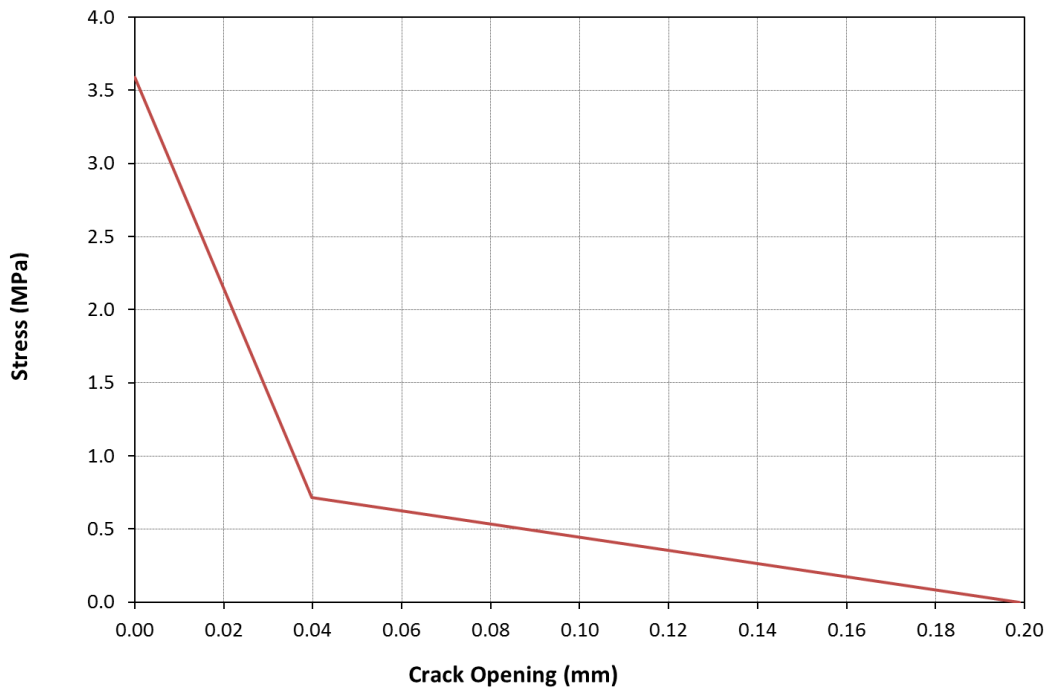


Figure 5.56. Concrete material properties in tension

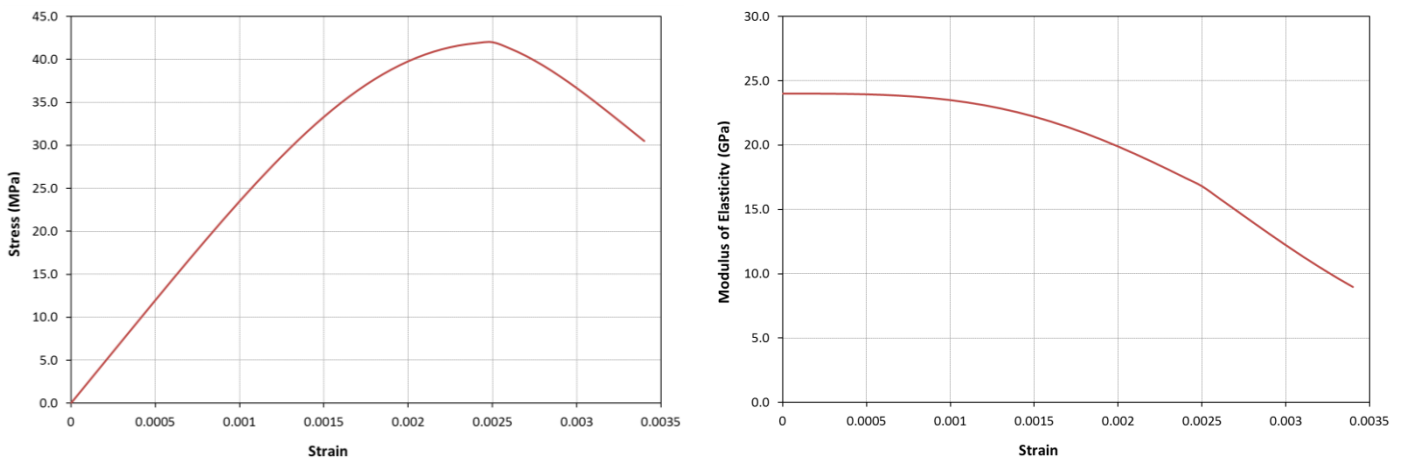


Figure 5.57. Concrete material properties in compression

Using this approach, the results from the numerical simulation are satisfactorily close to the experiment results. The maximum mid column displacement is underestimated by 1mm. Additionally the residual displacement is very close to the 6.5mm measured after the experiment as shown in Figure 5.58.

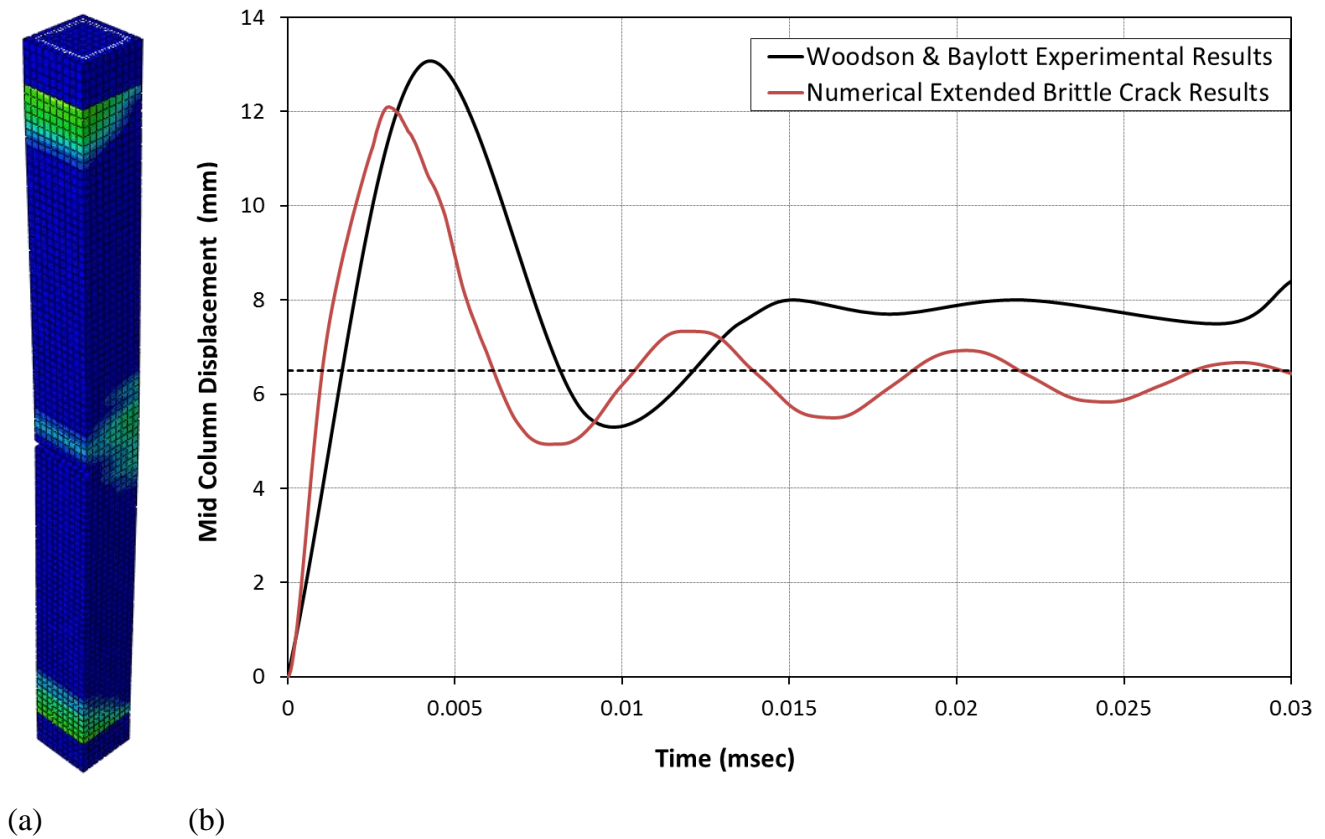


Figure 5.58. Extended Brittle Crack Results (a) Maximum residual strains (b) Results for mid column displacement

#### 5.4.4.2. Full Scale Column – Explosive Loading Laboratory

The Explosive Loading Laboratory is a simulated blast testing centre at the University of California San Diego. The laboratory was designed to simulate the impulse delivered by an actual blast to a structure and to be able to measure the structural response in a controlled environment [12]. The simulated blast loads are produced by an array of blast generators which are made up of an impacting module and a hydraulic actuator. When these blast generators impact the structure they impart a controlled blast like impact to the structure. The setup of the facility is presented in Figure 5.59.

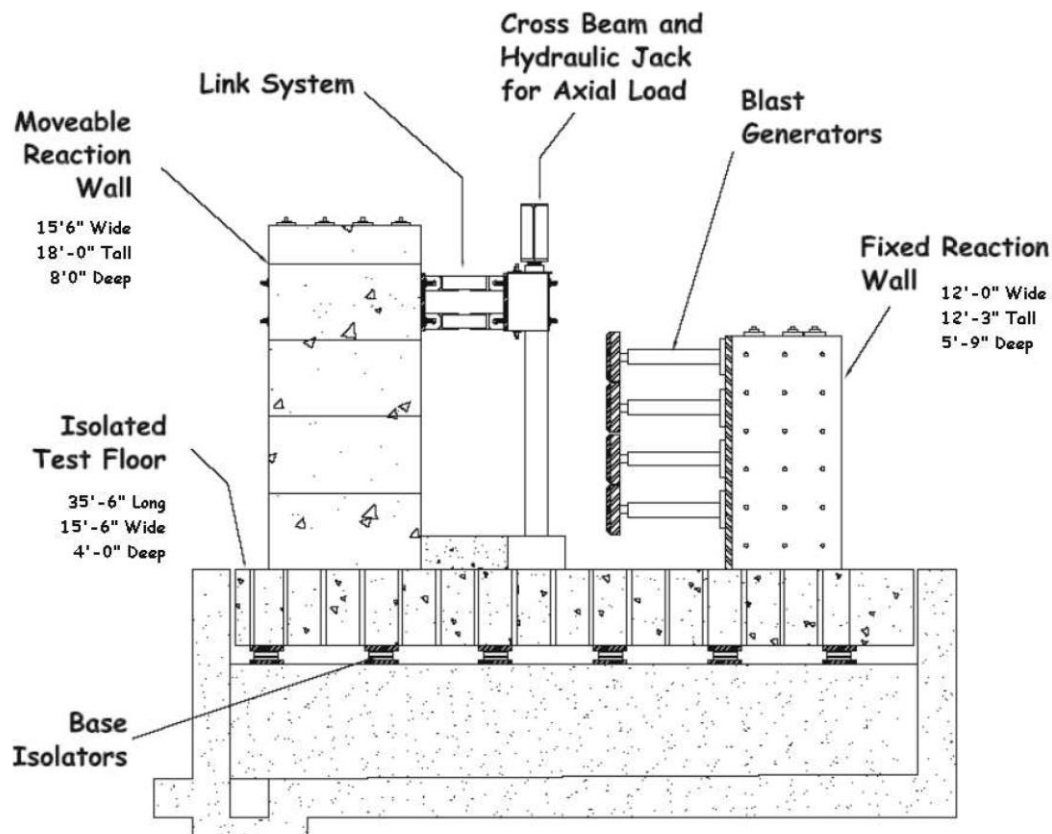


Figure 5.59. Overview of Explosive Loading Laboratory Facility with Test Setup [12]

The tested column is loaded by three or four blast generators over the column height. The connection at the base of the column is restrained in all degrees of freedom, whereas at the top a link system restrains lateral and moment directions whilst allowing vertical movement. There is a possibility of also applying axial load to the top of the column by means of three hydraulic jacks. This setup is able to simulate initial gravity loading on the column and also allows the increase of axial load when the end moves upwards due to arching action in compression.

Two of the eight test conducted on site were considered for this work; Test 7 and Test 8. Both tests utilised the same column. Although both tests aimed to subject the column to similar impact loads in practice the loads simulating the blasts differed slightly (see Figure 5.65. and Figure 5.70). The main difference between the tests, and the reason for choosing them both, was that whereas test 7 had no axial force test 8 did. This choice, therefore, allows for the validation of the concrete model and for the examination of the structural behaviour both with and without the influence of axial force.

The geometry for both tests is presented in Table 5.15

Concrete			Steel		
Column width (mm)	Column depth (mm)	Column height (mm)	Longitudinal reinforcement	Cross tie/hoop	Cover depth (mm)
356	356	3277	8#8	#3 @324	38

*Table 5.15. Column components' geometry*

The steel material behaviour was modelled as elastic perfectly plastic with the following values:

Elastic Modulus (GPa)	Yield stress of longitudinal steel (MPa)	Yield stress of cross tie/hoop (MPa)
210	335	235

*Table 5.16. Steel Material Properties*

Concrete was modelled using the extended brittle crack model with the following base parameters;

Elastic Modulus (GPa)	Unconfined concrete strength (MPa)
24	40

*Table 5.17. Concrete Material Properties*

As before, the concrete material was defined using the base properties, as given in the experiment report and International Federation for Structural Concrete Model Code The resulting material parameters are presented in Figure 5.60.

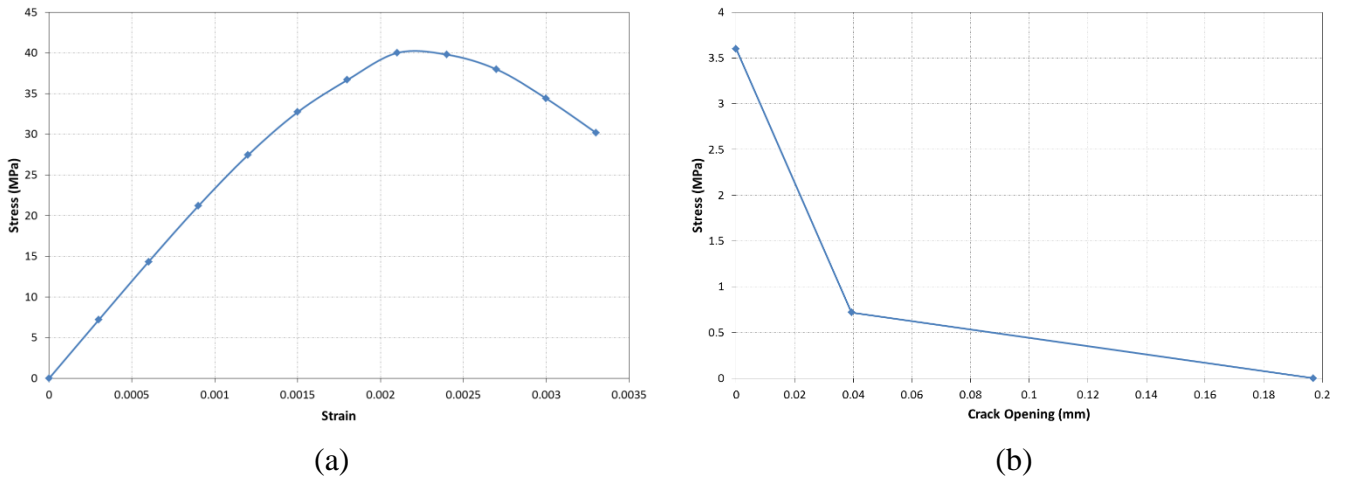


Figure 5.60. Concrete material properties in (a) compression and (b) tension

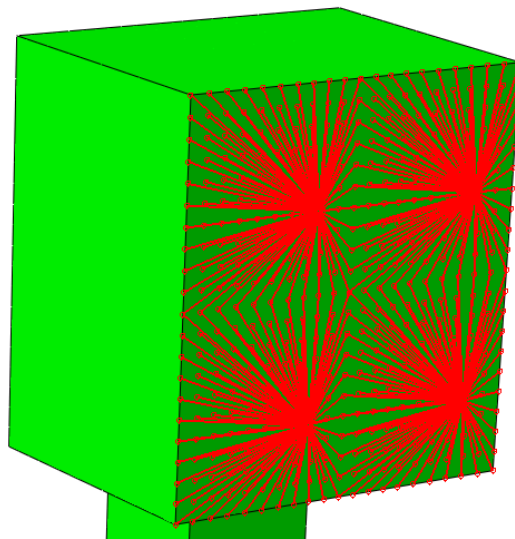
As the footing and heading were constrained and heavily reinforced they were assumed to be elastic for the conducted analyses. As per the experimental setup the footing was restrained in all degrees of freedom by restraining each of the faces in the perpendicular direction and the bottom in the vertical direction. At the top of the column a more sophisticated system was used in the experiments in the form of a link system which provided lateral and moment restraint while allowing vertical movement, see Figure 5.61.



Figure 5.61. Link system [12]



In the numerical model this system was modelled by means of a link system, as presented in Figure 5.62.



*Figure 5.62. Numerical heading constraints*

When applied, axial force was applied at the top of the heading by three hydraulic jacks, see Figure 5.63, which lock off once the target load is reached. In the numerical model axial loads were applied by means of pressure on a surface similar to the surface directly utilised by the jacks.



*Figure 5.63. Hydraulic jacks for vertical load [12]*

The resulting FE model with some of the concrete visually removed to allow a view of the embedded reinforcement is presented in Figure 5.64.

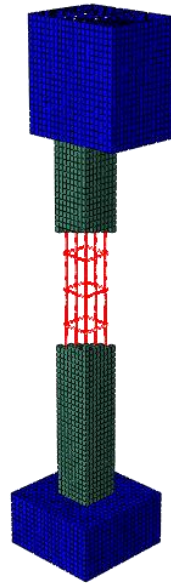


*Figure 5.64. Finite element model of full scale column*

The elements used were taken from the Abaqus explicit element library. They were of type C3D8R- 8 node linear bricks including reduced integration and hourglass control.

## Test 7

The blast load was simulated using the equivalent pressure measured in the experiment and presented in Figure 5.65.

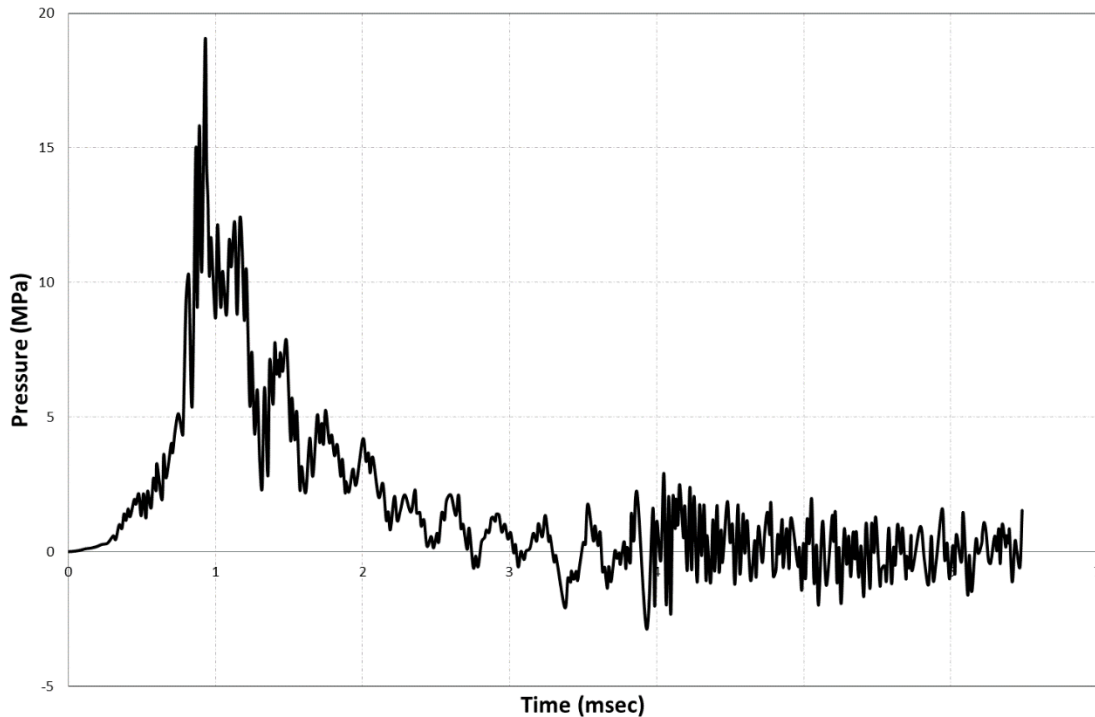
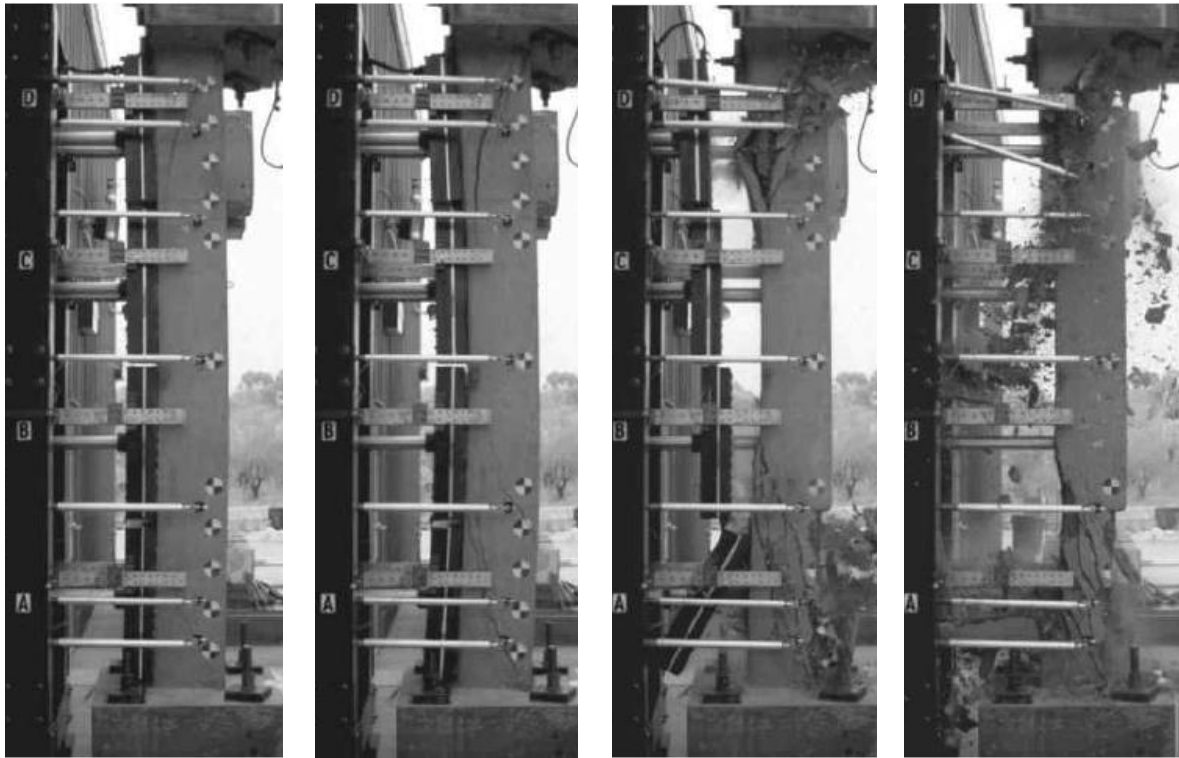


*Figure 5.65. Equivalent Pressure - Test 7[12]*

The structural response observed in the experiment consisted of shear cracks at the top and bottom of the column. As the concrete degraded secondary cracks started to appear. The spalled concrete cover then began to fall away from the column. The column descended axially and three small flexural cracks appeared mid column. The columns' response is presented in Figure 5.66, Figure 5.67 and summarised in Table 5.18.



(a) (b) (c) (d)

Figure 5.66. Test 7 experimental responses at (a) 6.7 (b) 41.7 (c) 84.3 and (d) 558 msec[12]



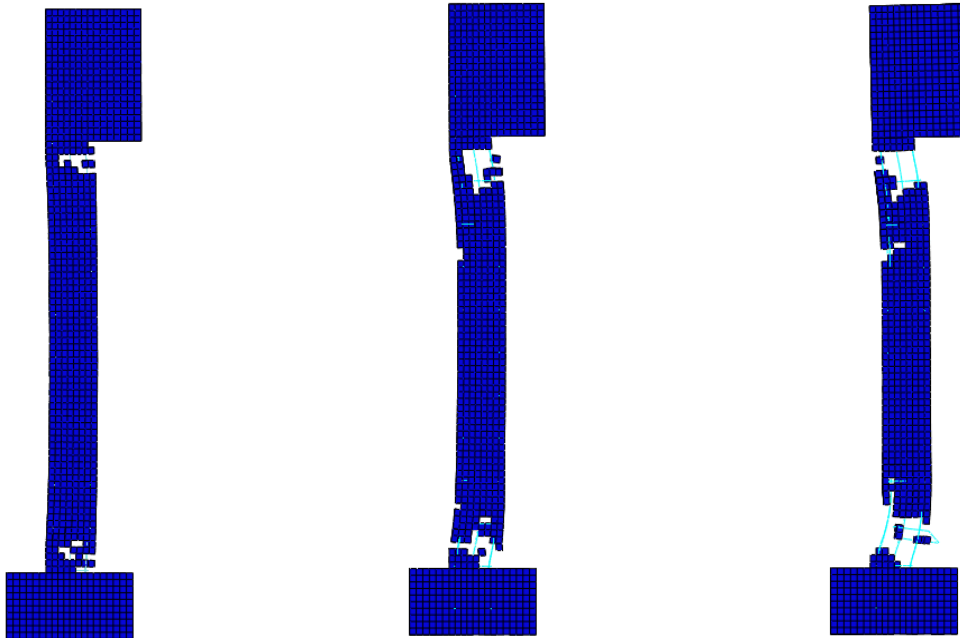
(a) (b)

Figure 5.67. Test 7 post-test damage at (a) top and (b) bottom of the column [12]

Peak deflection (mm)	Residual deflection (mm)	Damage
122 at 41.7 msec	85	Shear damage at top and bottom

*Table 5.18. Test 7 – column response*

The numerical analysis produced similar results. Shear cracks developed at both top and bottom of the column which developed until the concrete completely deteriorated. The progress of the shear failure is presented in Figure 5.68. The development of the crack pattern, shown in Figure 5.69, clearly demonstrates the shear failure at both top and bottom of the column.



*Figure 5.68. Test 7 - numerical response at 4, 10, and 150 msec*

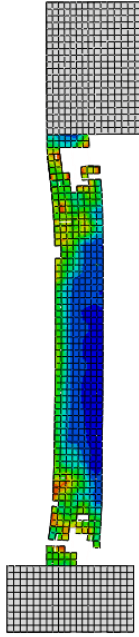


*Figure 5.69. Test 7 - crack pattern at 10 msec*

The numerical response is summarised in Table 5.19.

Peak deflection (mm)	Residual deflection (mm)	Damage
116.3 at 43.2 msec	92	Shear damage at top and bottom

*Table 5.19: Test 7 – numerical analysis response*

In this case the numerical analysis clearly follows the experimental data and provides an accurate modelling solution.

## Test 8

The blast load was simulated using the equivalent pressure measured in the experiment and presented in Figure 5.70.

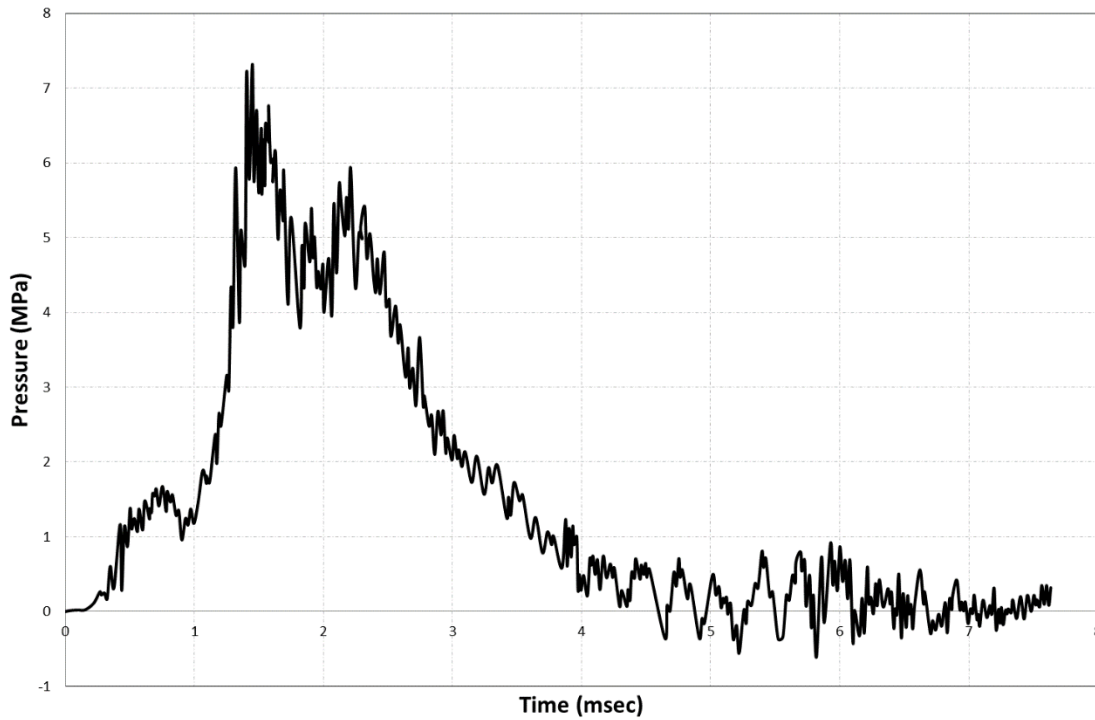


*Figure 5.70. Equivalent Pressure - Test 8[17]*

Additionally an axial force of 445 kN was applied to the column, see Figure 5.71.

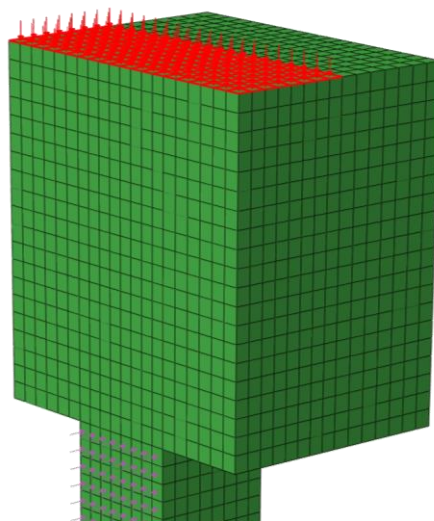


*Figure 5.71. Axial load simulation - Test 8*

In this case, due to the presence of the axial load frame, the column behaviour was not completely visible during the test. Upon inspection, after the test, the column was found to have two regions of shear failure – at the top and bottom of the column [12]. The damaged column is presented in Figure 5.72.



*Figure 5.72. Test 8- post-test, removed from fixture [17]*

The columns' response is summarised in Table 5.20.

Peak deflection (mm)	Residual deflection (mm)	Damage
157 at 47.6 msec	82	Shear damage at top and bottom

*Table 5.20. Test 8 – column response*



In this case, as previously, a similar response was observed in the numerical analysis. The blast response initiated with shear failure at the top and bottom of the column. Small flexural cracks also developed mid column. The shear cracks at top and bottom progressed until complete failure of the concrete. The response is presented in Figure 5.73.

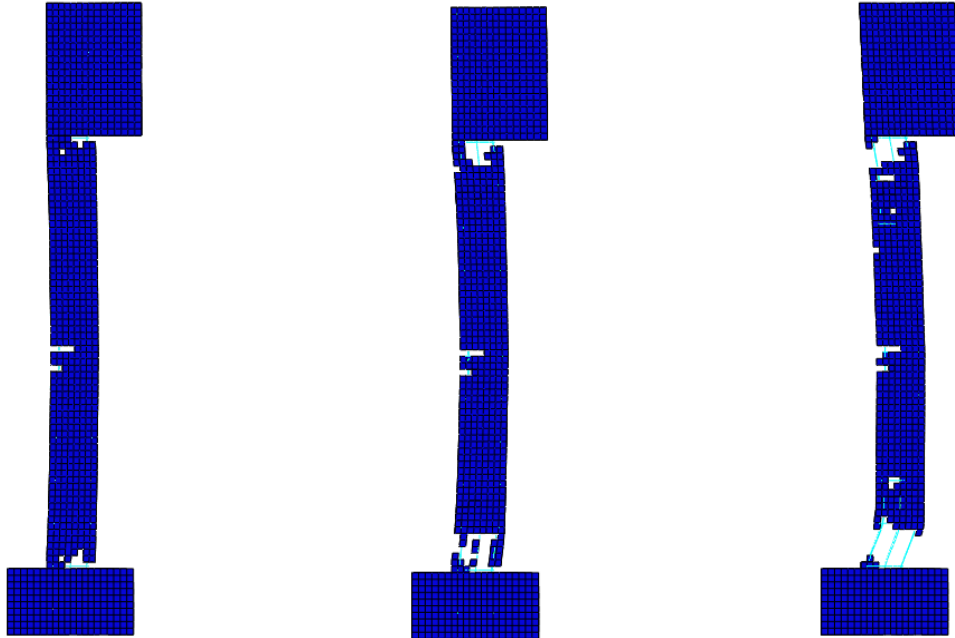


*Figure 5.73. Test 8 - numerical response at 4, 10, and 150 msec*

The crack development pattern is presented in Figure 5.74. The slightly longer shear cracking pattern at the bottom of the column as compared to the top is observed.

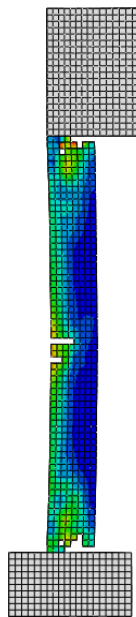


*Figure 5.74. Test 8 - crack pattern*

In the numerical analysis there was no frame providing support to the column. This led to the lateral displacement to keep on developing as the concrete at the bottom and top of the column had fully disintegrated. Therefore, it was not possible to measure any peak or residual displacements. In order to ensure that the numerical response was reasonable with regards to time the deflection was measured and compared to the peak displacement measured in the experiment. The results are presented in Table 5.21.

Deflection at experimental peak (mm)	Damage
138 at 44.7 msec	Shear damage at top and bottom

*Table 5.21. Test 8 – numerical analysis response*

In this case the modelled behaviour closely resembles the observed experimental results. However, there is one main difference – in the experimental set up the frames holding the specimen somewhat restrain deflections. As no such restraining mechanisms were used in the numerical model the post failure deflections differ. This does not deter from the comparable structural behaviour observed in the experimental and numerical models.

## **5.5. Discussion and conclusions**

In this chapter the three existing material models for concrete in the Abaqus material library were investigated and their characteristics discussed. Out of the two material models suitable for dynamic analysis the damaged plasticity was the most comprehensive, however its main disadvantages were the difficulties associated with generating the required input parameters and model instability post failure. Input for the brittle crack model is much easier to calibrate, however its main disadvantage is that only elastic behaviour can be defined in compression. An extension of the brittle crack model was suggested. This extension, achieved by means of a user subroutine, allows for plastic behaviour in compression overcoming the major drawback of the brittle crack model. Additionally, damage and erosion were both defined in the user subroutine thus eliminating failed elements and avoiding numerical difficulties.

The proposed material model was then extensively verified and validated and a number of different loading scenarios including strain rate investigation, static bending test, brittle damage benchmark and different blast load experimental set ups. In all cases the extended brittle crack model provided satisfactory results. The extended brittle crack model is robust material model suitable for successfully modelling concrete in a wide range of applications.

## References

- [1] U. Cicekli, G. Z. Voyiadjis, and R. K. Abu Al-Rub, 'A plasticity and anisotropic damage model for plain concrete', *Int. J. Plast.*, vol. 23, no. 10–11, pp. 1874–1900, Oct. 2007.
- [2] T. Yu, J. G. Teng, Y. L. Wong, and S. L. Dong, 'Finite element modeling of confined concrete-II: Plastic-damage model', *Eng. Struct.*, vol. 32, no. 3, pp. 680–691, Mar. 2010.
- [3] A. R. Mohamed, M. S. Shoukry, and J. M. Saeed, 'Prediction of the behavior of reinforced concrete deep beams with web openings using the finite element method', *Alex. Eng. J.*, vol. 53, no. 2, pp. 329–339, Jun. 2014.
- [4] A. S. Genikomsou and M. A. Polak, 'Finite element analysis of punching shear of concrete slabs using damaged plasticity model in ABAQUS', *Eng. Struct.*, vol. 98, pp. 38–48, Sep. 2015.
- [5] L. Chernin and D. V. Val, 'Prediction of corrosion-induced cover cracking in reinforced concrete structures', *Constr. Build. Mater.*, vol. 25, no. 4, pp. 1854–1869, Apr. 2011.
- [6] *ABAQUS (2014) 'ABAQUS Documentation', Dassault Systèmes, Providence, RI, USA.*
- [7] D. M. Cotsovos and M. N. Pavlović, 'Numerical investigation of concrete subjected to high rates of uniaxial tensile loading', *Int. J. Impact Eng.*, vol. 35, no. 5, pp. 319–335, May 2008.
- [8] D. Cotsovos and M. Pavlovic, 'Numerical investigation of concrete subjected to compressive impact loading. Part 1: A fundamental explanation for the apparent strength gain at high loading rates', *CAS Comput. Struct.*, vol. 86, no. 1, pp. 145–163, 2008.
- [9] P.-E. Petersson, *Crack growth and development of fracture zones in plain concrete and similar materials*. Lund, Sweden: Division of Building Materials, Lund Institute of Technology, 1981.
- [10] B. Bresler and A. C. Scordelis, 'Shear strength of reinforced concrete beams', in *ACI Journal Proceedings*, 1963, vol. 60.
- [11] S. C. Woodson and J. T. Baylot, *Structural collapse: quarter-scale model experiments*. [Vicksburg, Miss.]: U.S. Army Corps of Engineers, Engineering Research and Development Center, 1999.

- [12] T. Rodríguez-Nikl, *Experimental simulations of explosive loading on structural components reinforced concrete columns with advanced composite jackets*. 2006.
- [13] T. Krauthammer, *Modern protective structures*. Boca Raton, FL : CRC Press, 2008.
- [14] J. Lubliner, J. Oliver, S. Oller, and E. Oñate, ‘A plastic-damage model for concrete’, *SAS Int. J. Solids Struct.*, vol. 25, no. 3, pp. 299–326, 1989.
- [15] J. Lee and G. L. Fenves, ‘Plastic-Damage Model for Cyclic Loading of Concrete Structures’, *J. Eng. Mech.*, vol. 124, no. 8, pp. 892–900, 1998.
- [16] A. Hillerborg, M. Modéer, and P.-E. Petersson, ‘Analysis of crack formation and crack growth in concrete by means of fracture mechanics and finite elements’, *Cem. Concr. Res.*, vol. 6, no. 6, pp. 773–781, Nov. 1976.
- [17] fib, *fib Model Code for Concrete Structures 2010: FIB MODEL CODE 2010 O-BK*. Weinheim, Germany: Wiley-VCH Verlag GmbH & Co. KGaA, 2013.
- [18] *Abaqus/Explicit; Advanced topics*. .
- [19] J. Rots, G. Kusters, and J. Blaauwendraad, ‘The Need for Fracture Mechanics Options in Finite Element Models for Concrete Structures’, *Comput.-Aided Anal. Des. Concr. Struct. Pineridge Press Swans. U. K.*, pp. 19–32, 1984.
- [20] J. Rots, P. Nauta, G. Kusters, and J. Blaauwendraad, *Smearred Crack Approach and Fracture Localization in Concrete*, vol. 30. Delft University of Technology, 1985.
- [21] H. Ahrens, R. Meyer, and H. Duddeck, ‘Material Model for Concrete in Cracked and Uncracked States’, *J. Eng. Mech.*, vol. 120, no. 9, pp. 1877–1895, 1994.
- [22] G. Hughes, D. M. Speirs, and Cement and Concrete Association, *An investigation of the beam impact problem*. Wexham Springs, Slough: Cement and Concrete Association, 1982.
- [23] Y. Shi, H. Hao, and Z.-X. Li, ‘Numerical derivation of pressure-impulse diagrams for prediction of RC column damage to blast loads’, *Int. J. Impact Eng.*, vol. 35, no. 11, pp. 1213–1227, 2008.

# **Chapter 6: Assessing Reinforced Concrete Structural Response under Blast Loads and Pressure-Impulse Diagram Investigation**

## **6.1. Introduction**

In this chapter the effects of various parameters on the structural response of a reinforced concrete column under blast are investigated. Different scenarios are considered, the numerical analyses presented and the results for each case are discussed.

Furthermore, this chapter presents an investigation into the derivation of Pressure-Impulse (P-I) diagrams using the finite element (FE) method and the material model previously discussed and validated in Chapter 5. The graphical method, introduced in Chapter 4, is implemented here for derivation of new P-I curves for a typical reinforced concrete column, while the complementary diagrams are built with axial force being the additional parameter. The advantages of the graphical method are further demonstrated and discussed.

## **6.2. Parametric investigation**

In this section a number of different scenarios were analysed in order to establish the effects of different factors on the structural response of a reinforced concrete column subjected to blast loads. The cases considered were blast intensity, initial axial force, longitudinal and transverse reinforcement and boundary conditions. The numerical models, analyses setup, results and discussion for each case are presented in the following subsections.

### **6.2.1. Blast intensity**

The effect of blast intensity on the columns' structural response was studied using the FE model of test column 7 from the Explosive Loading Laboratory report [1] (see Chapter 5 Section 5.3.4.3.2). The blast load was modelled using a triangular time history, as shown in Figure 6.1. The intensity of the blast was gradually increased by increasing the peak pressure, while keeping the impulse constant. This formulation, therefore, led to a gradual decrease of the blast duration. The variations on blast pressure, duration and impulse are presented in Figure 6.1 and given in Table 6.1.

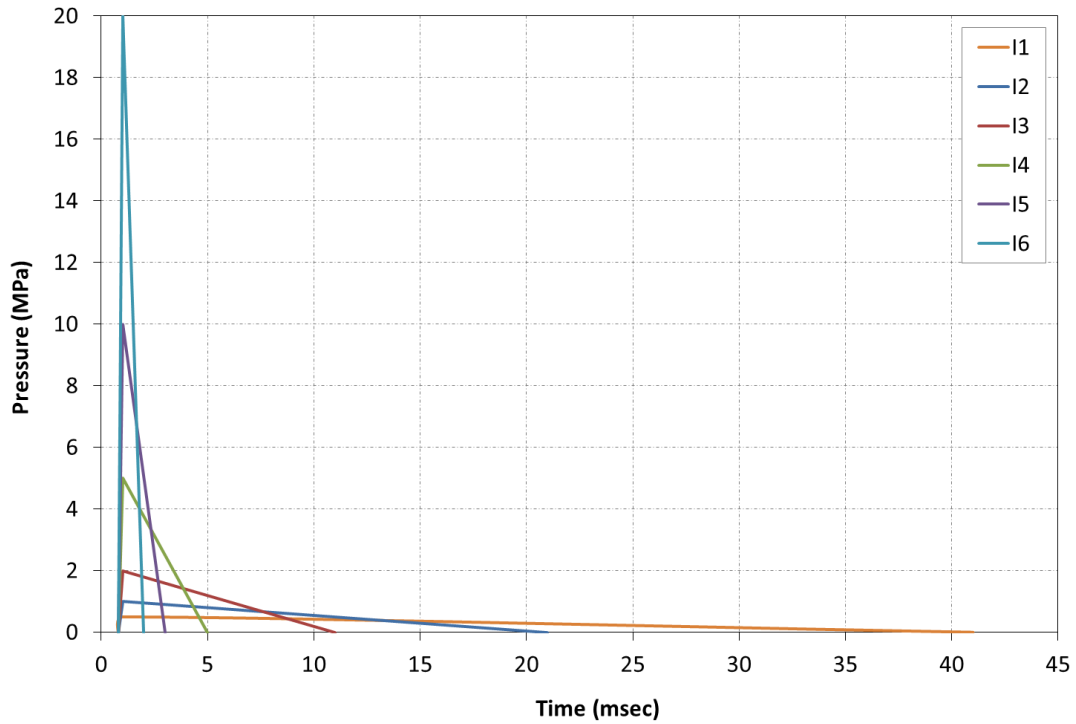


Figure 6.1. Blast loads investigated

Case	Pressure (MPa)	Duration of Blast (msec)	Impulse (MPa-msec)
I1	0.5	40	10
I2	1	20	10
I3	2	10	10
I4	5	4	10
I5	10	2	10
I6	20	1	10

Table 6.1. Levels of blast intensity investigated

The results of the numerical investigation show that under low levels of pressure the damage pattern is mainly flexural. As the pressure increases, the damaged zones concentrate near the supports effectively leading to ‘shear-off’ of the column at the supports. With further increase in pressure, the shear-induced damage becomes more pronouncedly diagonal with increasing amounts of concrete material deteriorating in the areas where shear damage occurs. The damage patterns for the column at 5 msec and at 150 msec are presented in Figure 6.2 and Figure 6.3.

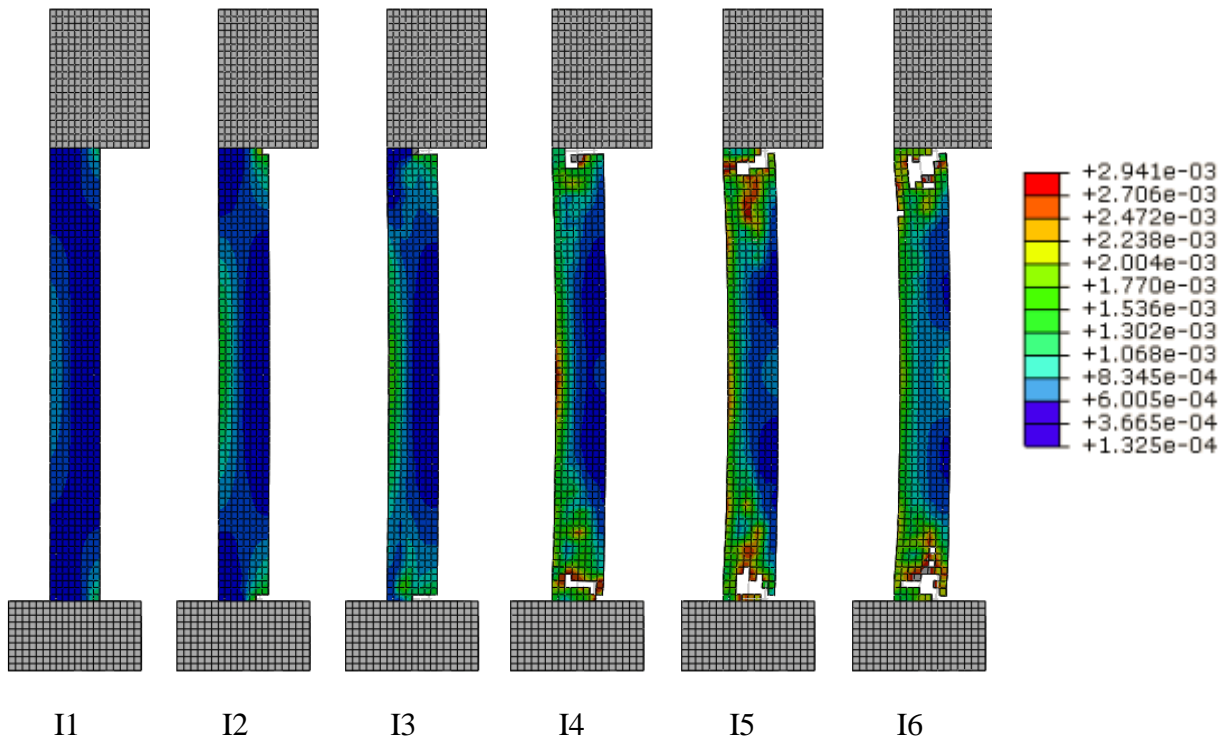


Figure 6.2. Comparison of damage patterns at 5 msec function of the user-defined variable

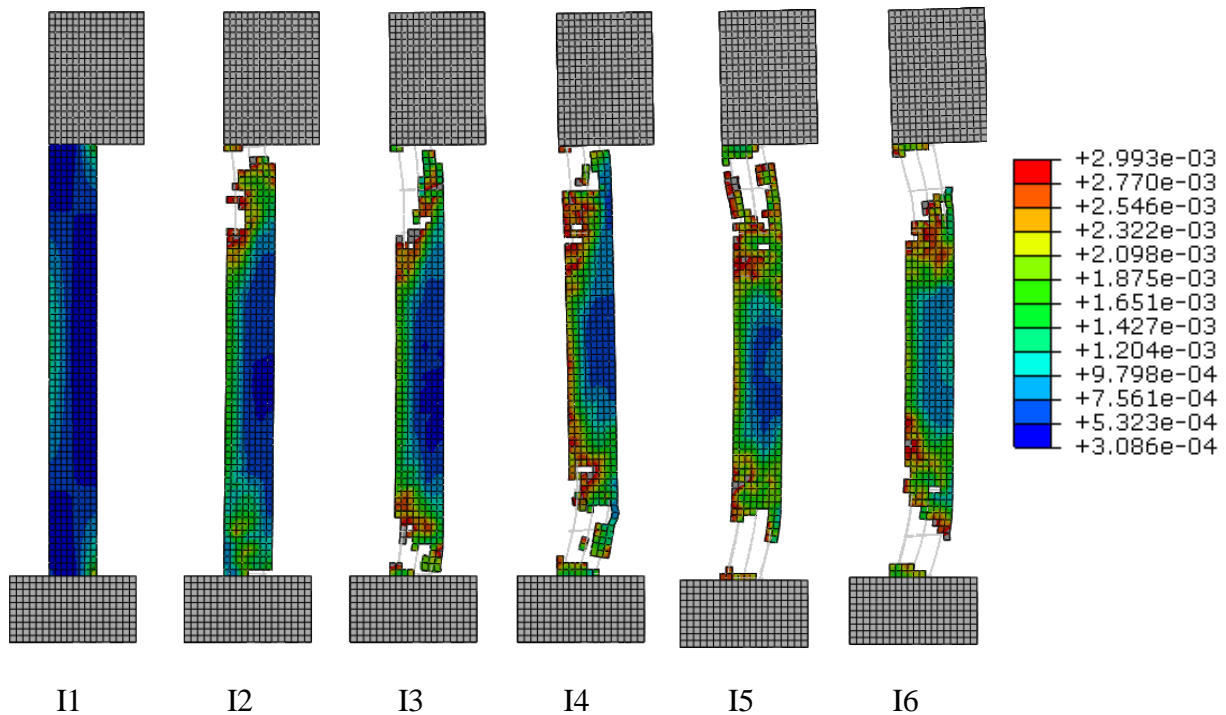


Figure 6.3. Comparison of damage patterns at 150 msec function of the user-defined variable

Figure 6.4 depicts variations of mid-height column displacement caused by blast loads with different intensities given in Table 6.1. As can be seen, the higher the blast pressure the higher the mid-column deflection and residual displacement.



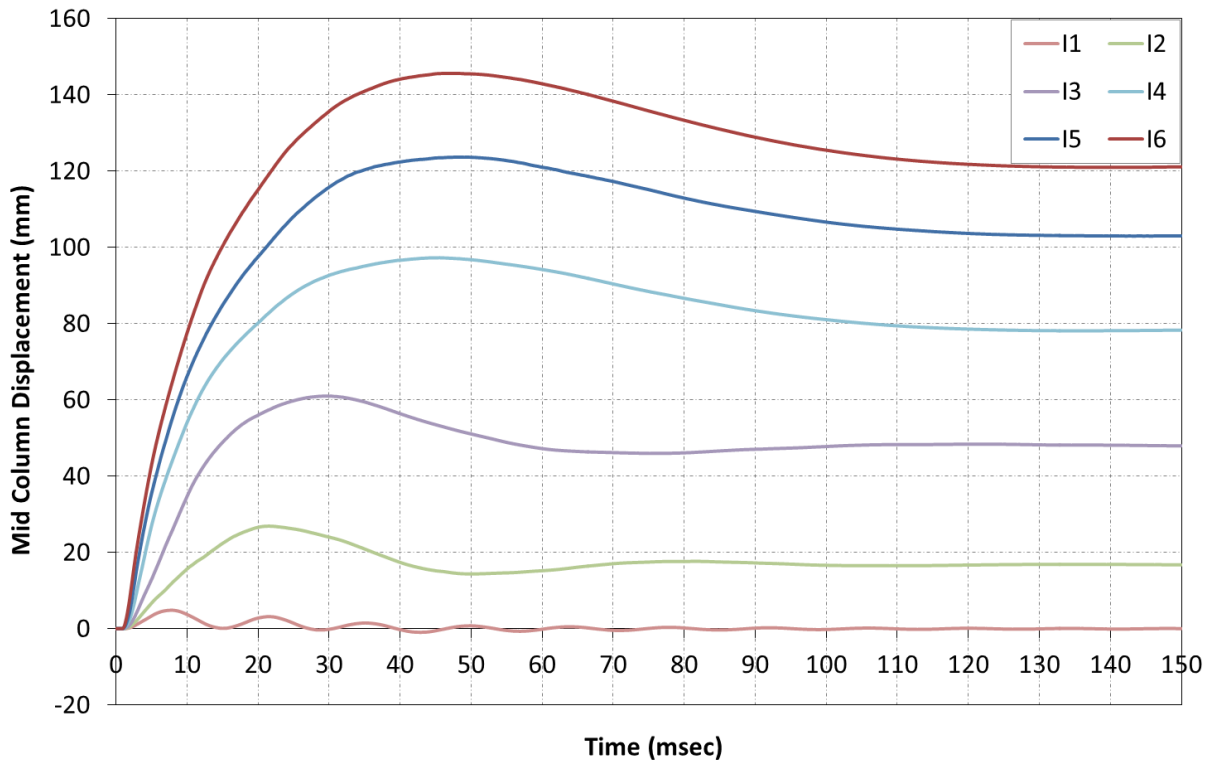


Figure 6.4. Mid column displacements for varying ratios of blast intensity

### 6.2.2. Axial Force

The influence of axial force on the structural response of a reinforced concrete column under the blast load was studied using the full scale test column 8 from the report from the Explosive Loading Laboratory [1] (see Chapter 5 Section 5.3.4.3.2).

First, the ultimate axial load for the column was found using static analysis with gradually increasing axial load. The resulting ultimate axial force was  $N_{ult} = 3264 \text{ kN}$ . This value was further used in the analyses of the column under the blast load to find the relative level of axial loading. The levels of axial force used are presented in Table 6.2, where case A3 corresponds to the original axial force applied in the experimental setup of test column 8 (see Chapter 5).

The blast load used in all the computational simulations is given in Table 6.2.

Case	Axial Force (kN)	% of Ultimate Axial Force
A1	0	0
A2	220	7
A3	445	14
A4	880	27
A5	1760	54

*Table 6.2. Levels of axial force investigated*

The results of the analysis presented in Figure 6.5 to Figure 6.9 indicate that the larger the initial axial force, the higher the level of damage caused by the same blast load. This can be seen both by the mid-column displacement (see Table 6.3) and the level of concrete deterioration (see the right columns in Figures Figure 6.5Figure 6.9, corresponding to the structural state of each column at 100 msec after the blast load was applied). It was also observed that the damage mechanism changes with the change in the axial loading. Figure 6.5 to Figure 6.9 show the progression of damage with time. In cases of lower axial force shear failure occurs both at the bottom and top of the column, with the most shear damage accumulating at the bottom of the column. As the axial load increases, flexural damage also develops at the middle of the column. With further increase, the top and bottom of the column shear off together with flexural damage appearing in the middle region.

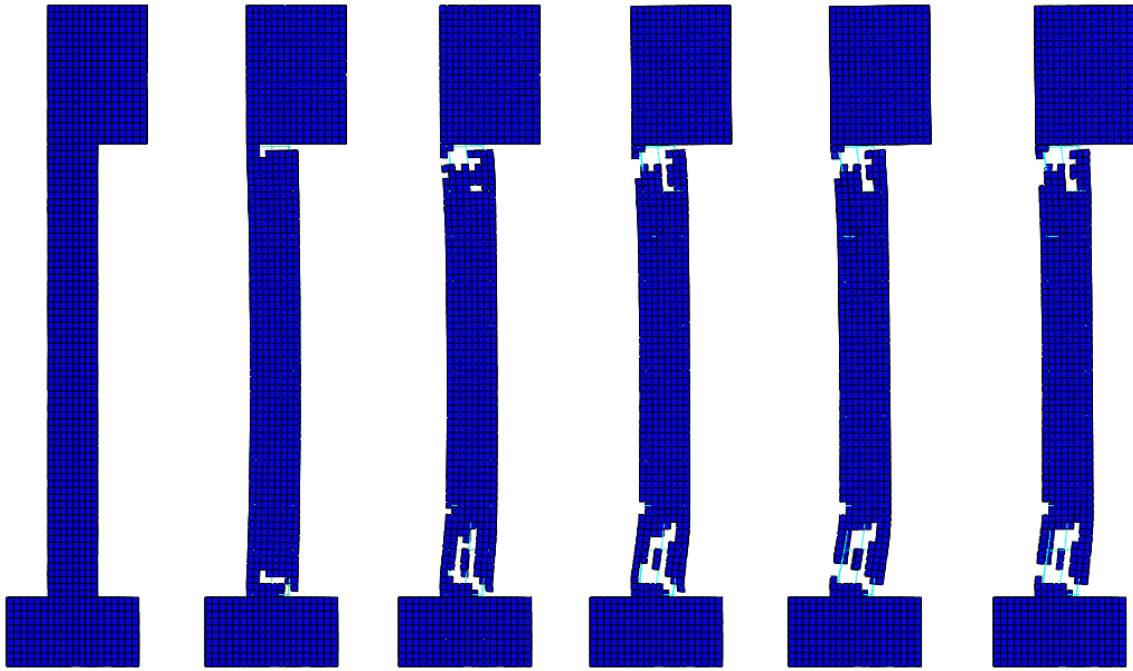


*Figure 6.5. Progression of damage in case A1 (at 0, 5, 10, 15, 30 and 100 msec)*

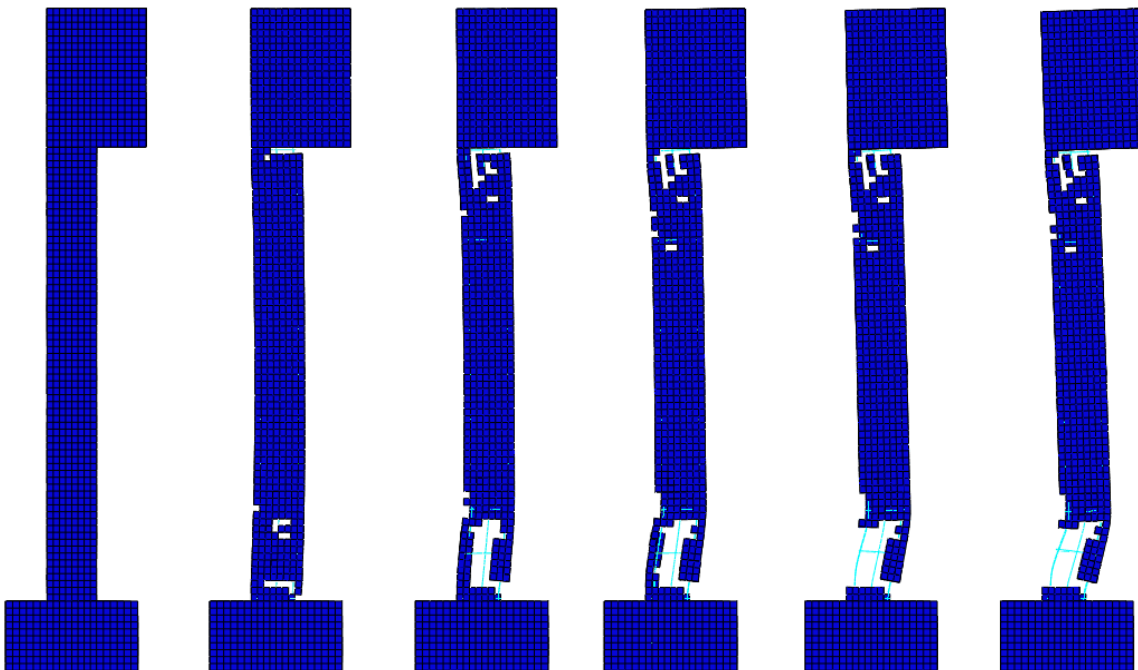


*Figure 6.6. Progression of damage in case A2 (at 0, 5, 10, 15, 30 and 100 msec)*

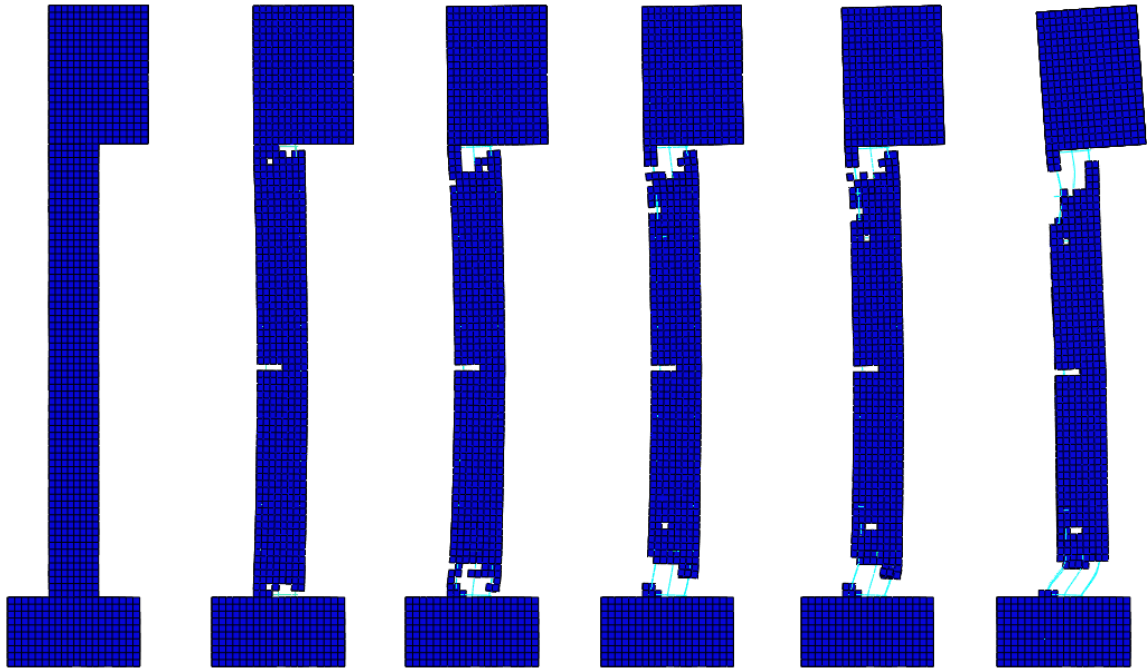


*Figure 6.7. Progression of damage in case A3 (at 0, 5, 10, 15, 30 and 100 msec)*

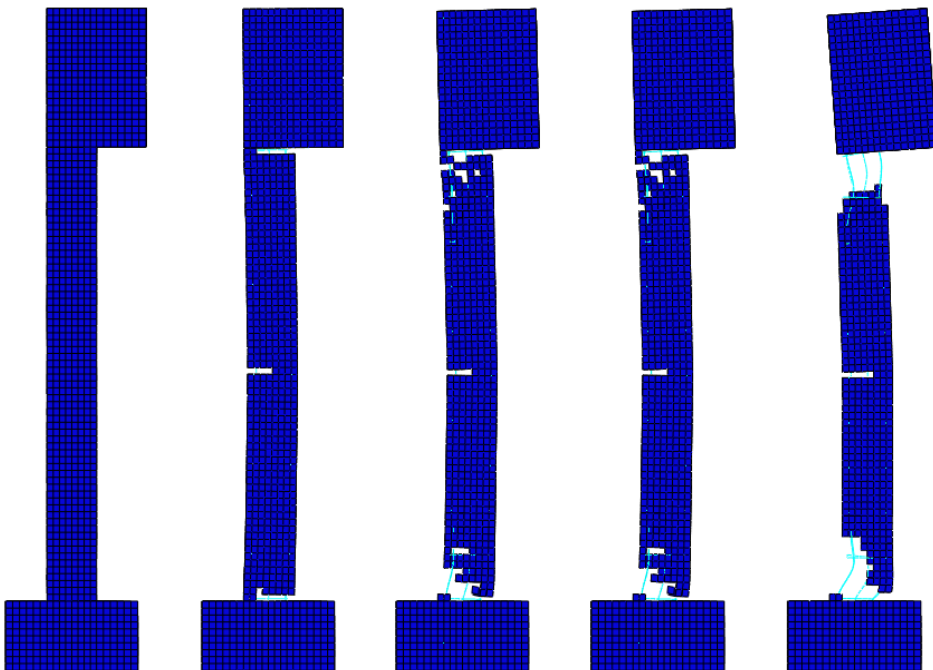


*Figure 6.8. Progression of damage in case A4 (at 0, 5, 10, 15 and 30 msec)*

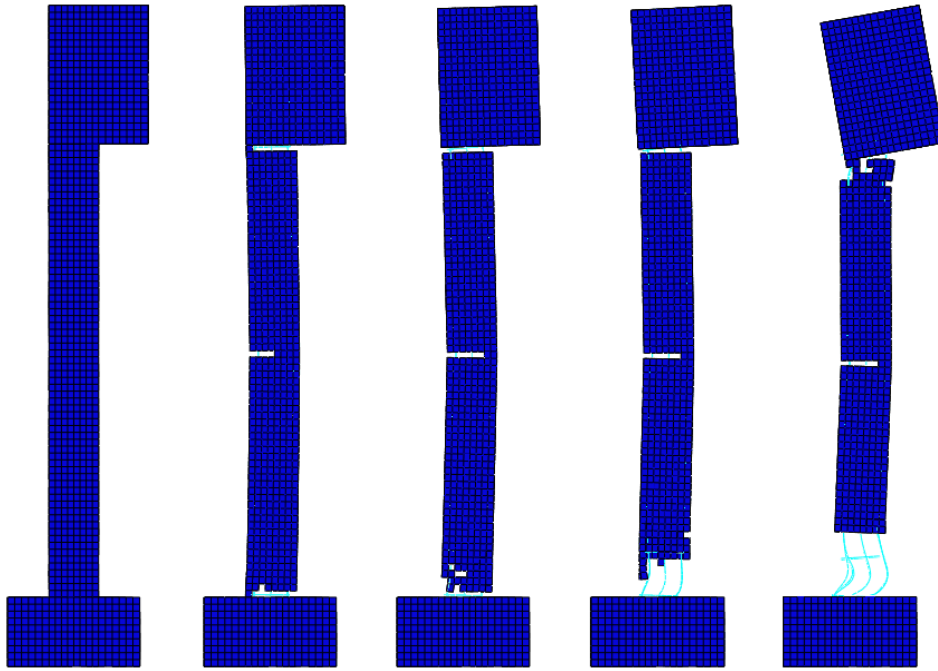


*Figure 6.9. Progression of damage in case A5 (at 0, 5, 10, 15 and 30 msec)*

Figure 6.10 shows a comparison between the damage development pattern in the cases of low and high axial force (case 2 and case 5). It can be seen that in the case of lower axial force, the shear-induced damage develops diagonally at the top and bottom of the column, with a larger portion occurring at the bottom of the column (see the left column in the figure). In the case of the larger axial force, the shear-induced damage at the top and bottom of the column develops along the supports, leading to the shear-off of the column (see the right column in the figure). Additionally, the flexural damage takes place in the middle region of the column.

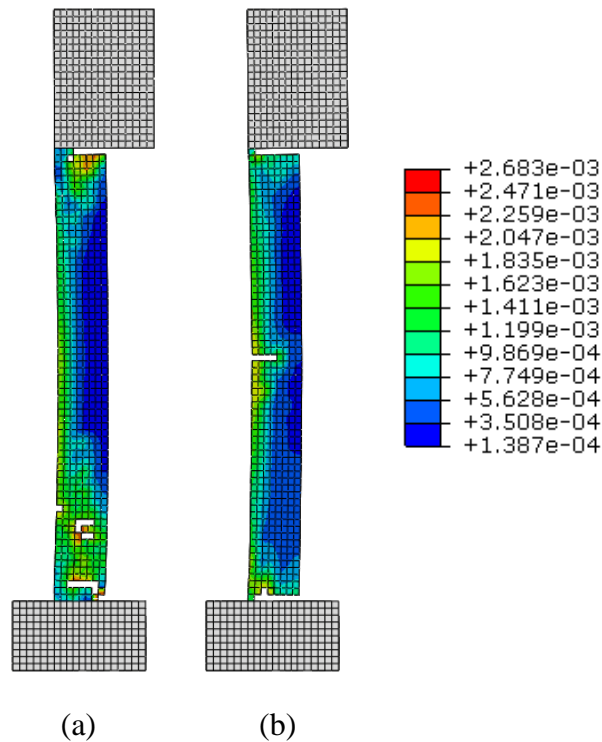


Figure 6.10. Comparison of crack pattern between cases (a) A2 and (b) A5 at 5 msec, function of the user-defined variable

The application of relatively large axial force (cases A4 and A5) led to the collapse of the column rendering the final maximum mid-column deflection meaningless. Therefore, the mid-height lateral deflections of A1-A5 columns developing at 40 msec were compared to establish the differences in displacements. The results of the comparison and the summary of mode of damage are presented in Table 6.3. It can be seen that the mid-column deflection increases with the increase in axial force and the mode of damage changes from ‘diagonal shear’ to a combination of shear-off and flexural failure.

Case	Deflection at 40 msec (mm)	Damage type
A1	106.4	Diagonal shear
A2	116.9	Diagonal shear
A3	120.5	Diagonal shear
A4	138.8	Diagonal shear and flexural
A5	172.3	Shear-off and flexural

Table 6.3. Column response under varying axial load

### 6.2.3. Longitudinal reinforcement

The effect of longitudinal reinforcement on the response of the column under blast load was investigated using a FE model of test column 7 from the Explosive Loading Laboratory report [1] (see Chapter 5 Section 5.3.4.3.2). In the experimental setup the column had 8 longitudinal reinforcing bars of #8 (25.4 mm diameter) which equate to 3% reinforcement. Four analysed columns with different reinforcement ratios are presented in Table 6.4, where the case L3 represents the reinforcement examined in the laboratory.

Case	Reinforcement scheme	% of Reinforcement
L1	8D14	1
L2	8D20	2
L3	8D25.4	3
L4	8D28.4	4

*Table 6.4. Levels of longitudinal reinforcement areas investigated*

From the numerical results, shown in Figure 6.11 to Figure 6.14, it is evident that the ratio of longitudinal reinforcement significantly influences structural response of the column under blast loads. At a lower ratio of reinforcement (Figure 6.11), the column suffers from both flexural and diagonal shear damage and undergoes substantial lateral mid-height displacement due to the lower stiffness. However, the more flexible behaviour of the column leads to crushing of relatively smaller zones of concrete. With an increase in reinforcement ratio, the column stiffness increases leading to smaller displacement but higher level of damage in terms of material deterioration. The damage mechanism becomes diagonal shear based, although as the reinforcement increases this effect becomes more localised and similar in behaviour to the shear-off effect. The differences in the damage mechanism can be observed in Figure 6.15.

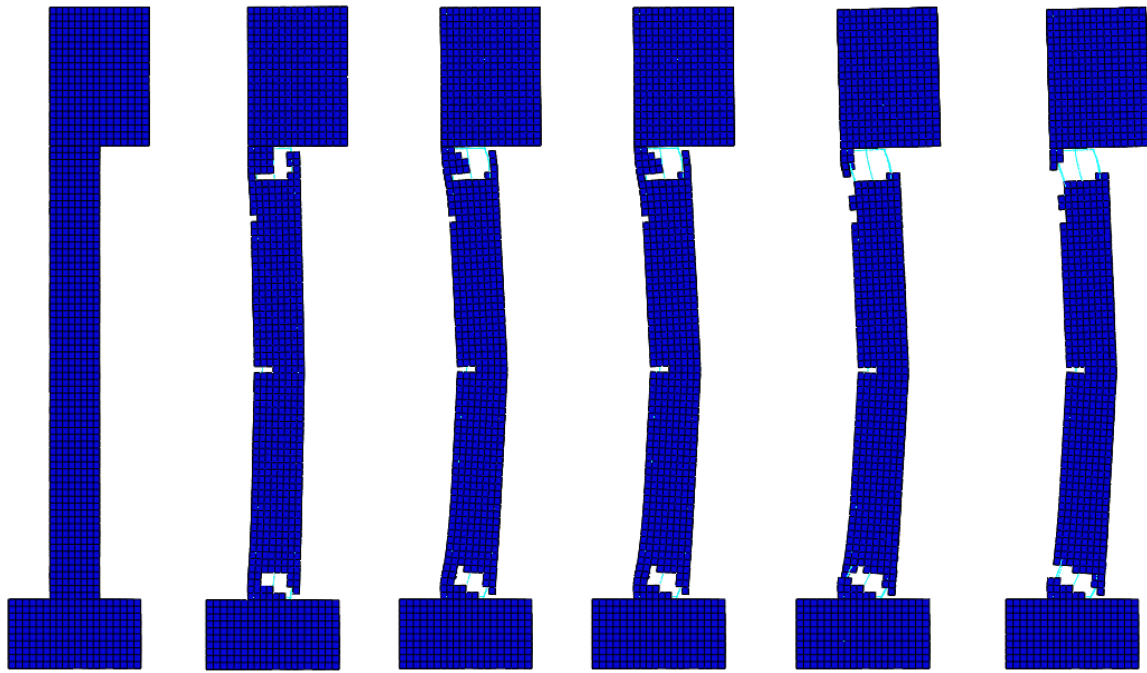


*Figure 6.11. Progression of damage in case L1 (at 0, 5, 10, 15, 30 and 100 msec)*

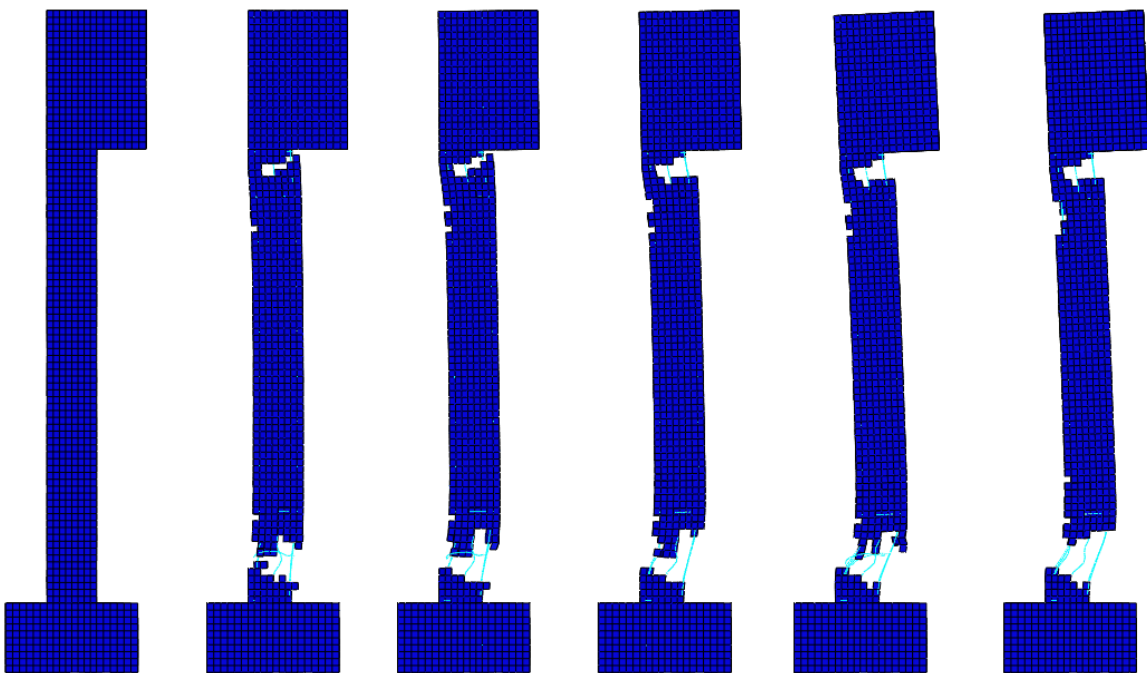


*Figure 6.12. Progression of damage in case L2 (at 0, 5, 10, 15, 30 and 100 msec)*



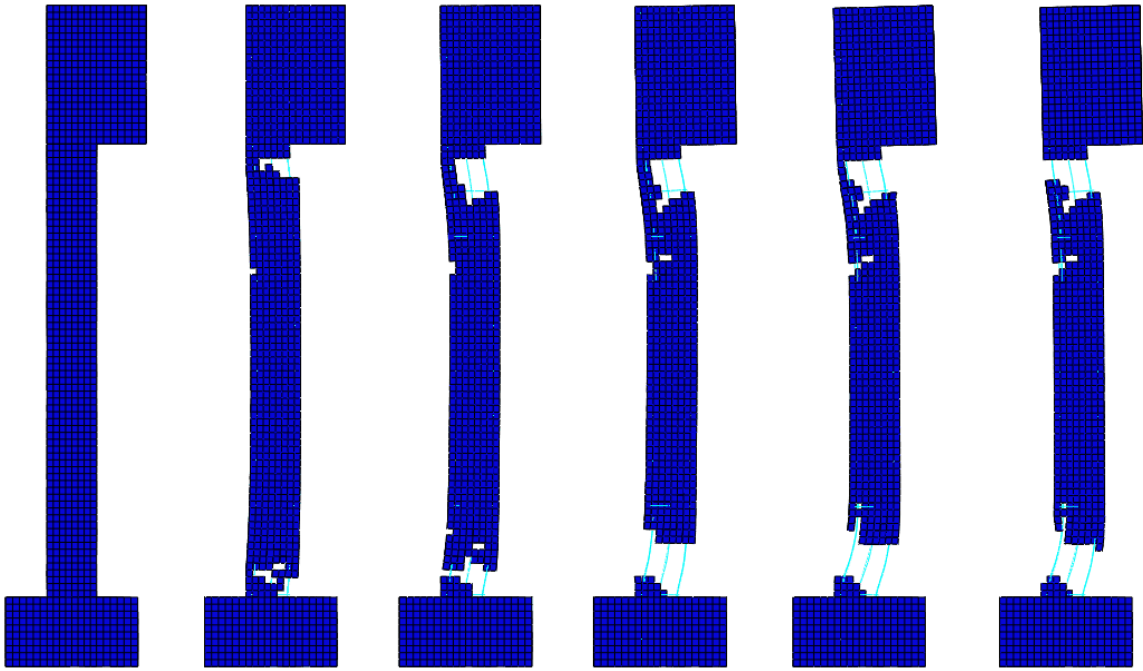


*Figure 6.13. Progression of damage in case L3 (at 0, 5, 10, 15, 30 and 100 msec)*

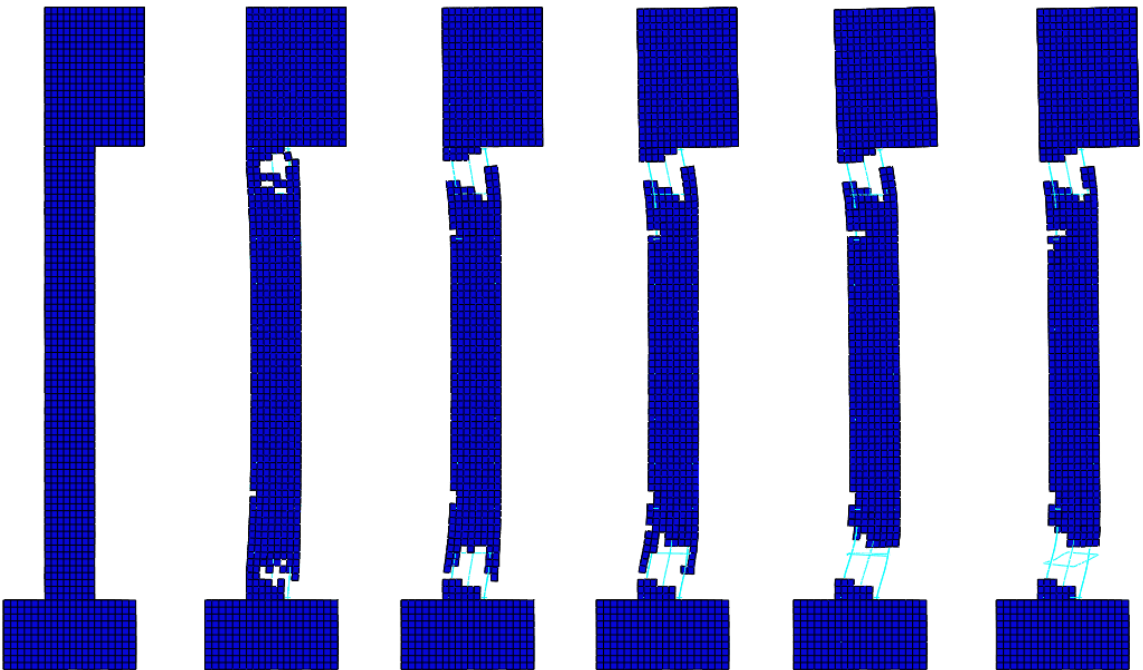


*Figure 6.14. Progression of damage in case L4 (at 0, 5, 10, 15, 30 and 100 msec)*

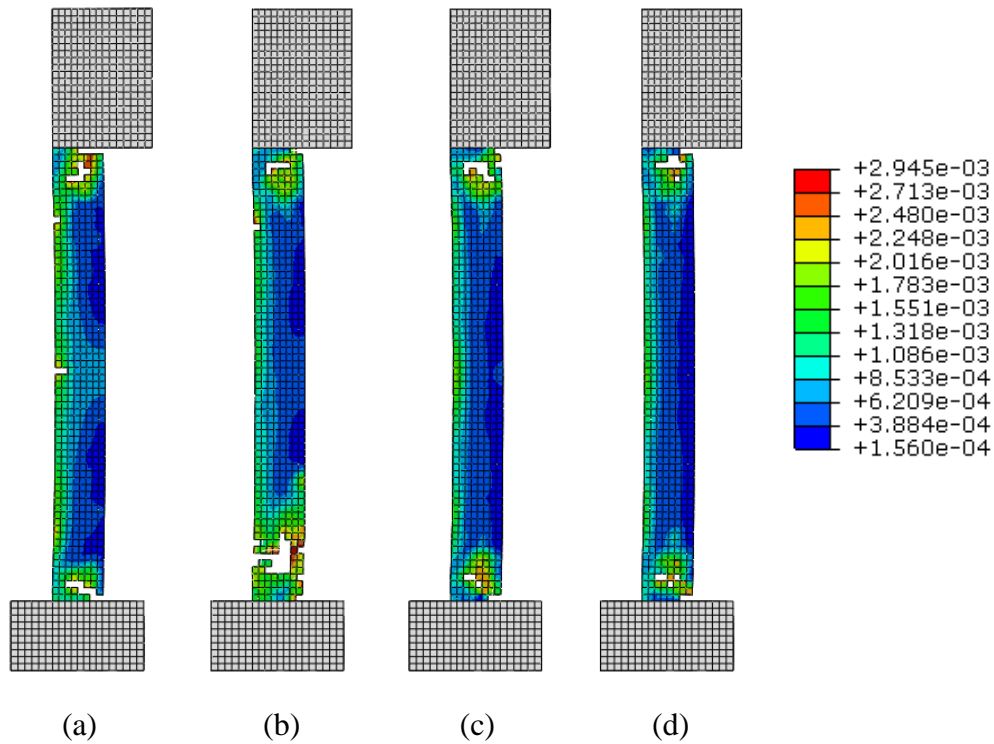


Figure 6.15. Damage pattern in cases (a) L1, (b) L2, (c) L3 and (d) L4 at 3 msec, function of the user-defined variable

As discussed above, with increase in longitudinal reinforcement ratio and therefore column stiffness the peak and residual mid column displacements reduce, as shown in Figure 6.16. The displacements and damage is further summarised in Table 6.5.

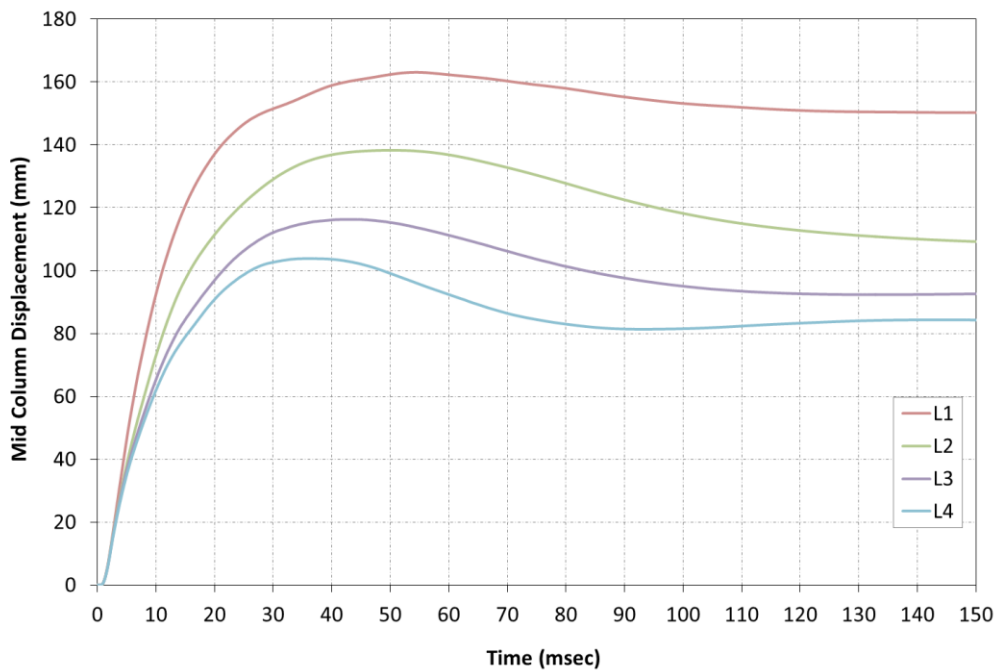


Figure 6.16. Mid-column displacements for varying ratios of longitudinal reinforcement

Case	Peak Deflection (mm)	Residual Deflection (mm)	Damage type
L1	163	150.2	Diagonal shear and flexural
L2	138.2	109.2	Diagonal shear
L3	116.3	92	Diagonal shear
L4	103.8	84.3	Diagonal shear

*Table 6.5. Column response under varying longitudinal reinforcement*

#### **6.2.4. Transverse reinforcement**

The influence of the transverse reinforcement on the structural response was investigated using the FE model of test column 7 taken from the report from the Explosive Loading Laboratory [1]. In this study, the diameter of stirrups was varied, while their spacing was kept constant. Four different diameters of stirrups used in the FE model of the column are presented in Table 6.6, where T1 represents a case of the column without transverse reinforcement and the case T3 being the original experimental setup.

Case	Stirrup Diameter (mm)
T1	0
T2	2.4
T3	4.76
T4	9.5

*Table 6.6. Diameter of transverse reinforcement investigated*

The results of the FE analysis showing the progress of damage in the columns with varying transverse reinforcement are presented in Figure 6.17 to Figure 6.20. The numerical analysis in case T2 failed at 25 msec after the blast load application due to excessive rotation in the stirrups, therefore, the fifth reading in Figure 6.18 is made at 25 msec and the 100 msec reading is missing. The damage developed in the investigated columns at 3 msec and 150 msec after application of the blast load is summarised in Figure 6.21 and Figure 6.22. As can be seen, the character of the damage is similar in all columns and the diagonal shear is the main failure mechanism. Stirrups with larger diameters can reduce the extent of material damage accumulated and influence the failure mechanism (see Figure 6.22). The comparison

of the damage patterns in the cases T1 and T4 at 150 msec clearly shows the development of a combined diagonal shear and flexural damage in the column with large transverse reinforcement.

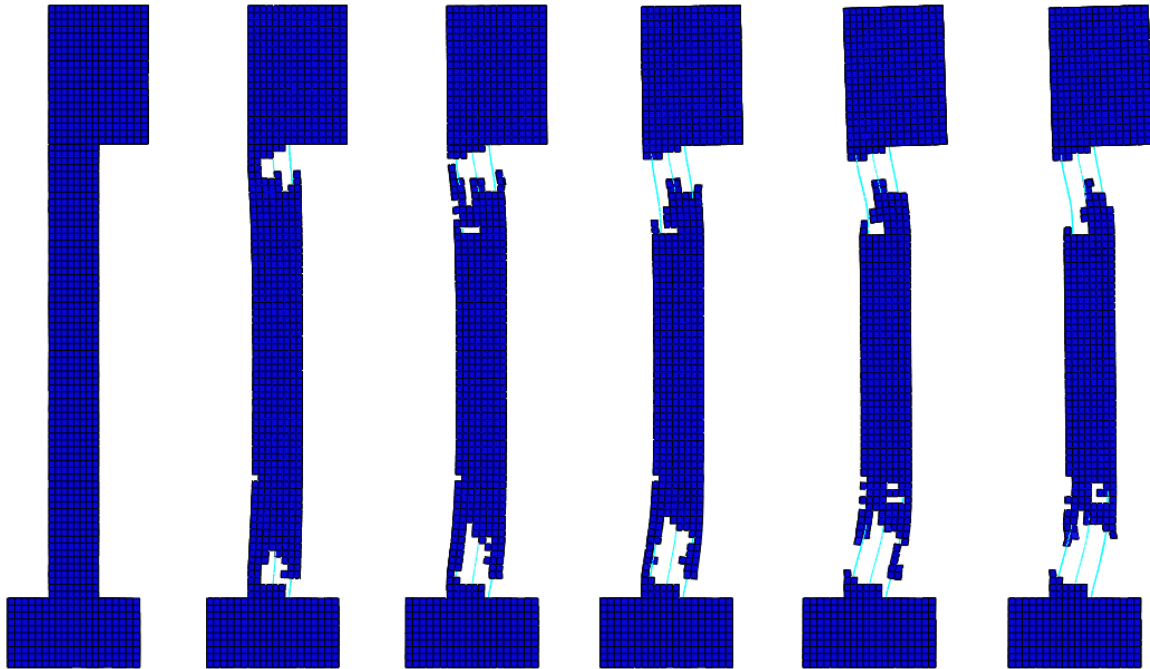


*Figure 6.17. Progression of damage in case T1 (at 0, 5, 10, 15, 30 and 100 msec after the application of the blast load)*

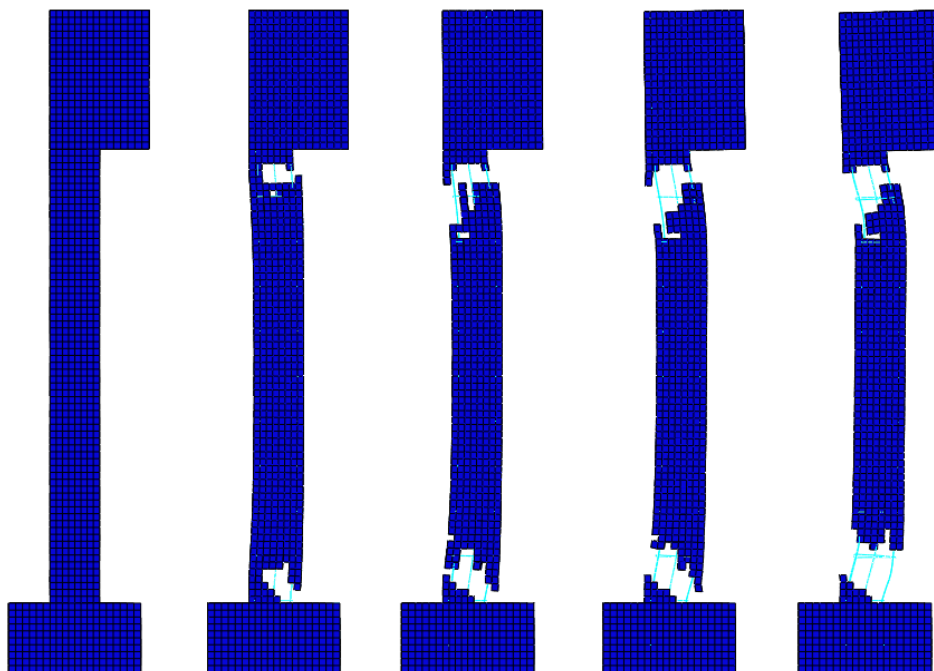


*Figure 6.18. Progression of damage in case T2 (at 0, 5, 10, 15 and 25 msec after the application of the blast load)*

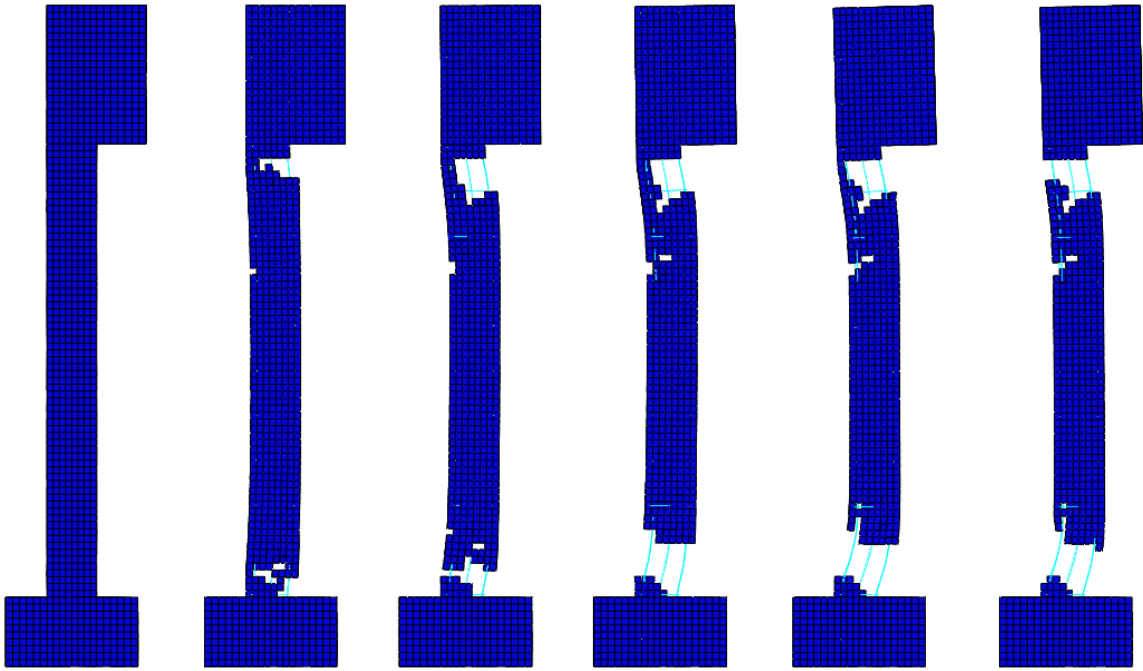


*Figure 6.19. Progression of damage in case T3 (at 0, 5, 10, 15, 30 and 100 msec after the application of the blast load)*

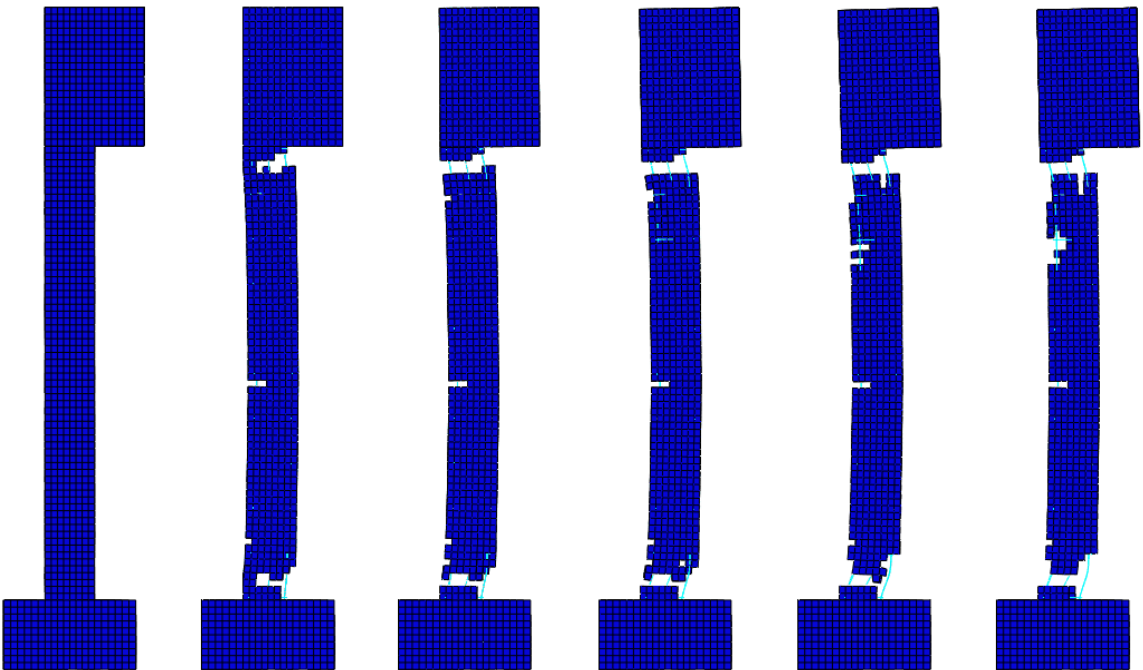


*Figure 6.20. Progression of damage in case T4 (at 0, 5, 10, 15, 30 and 100 msec after the application of the blast load)*

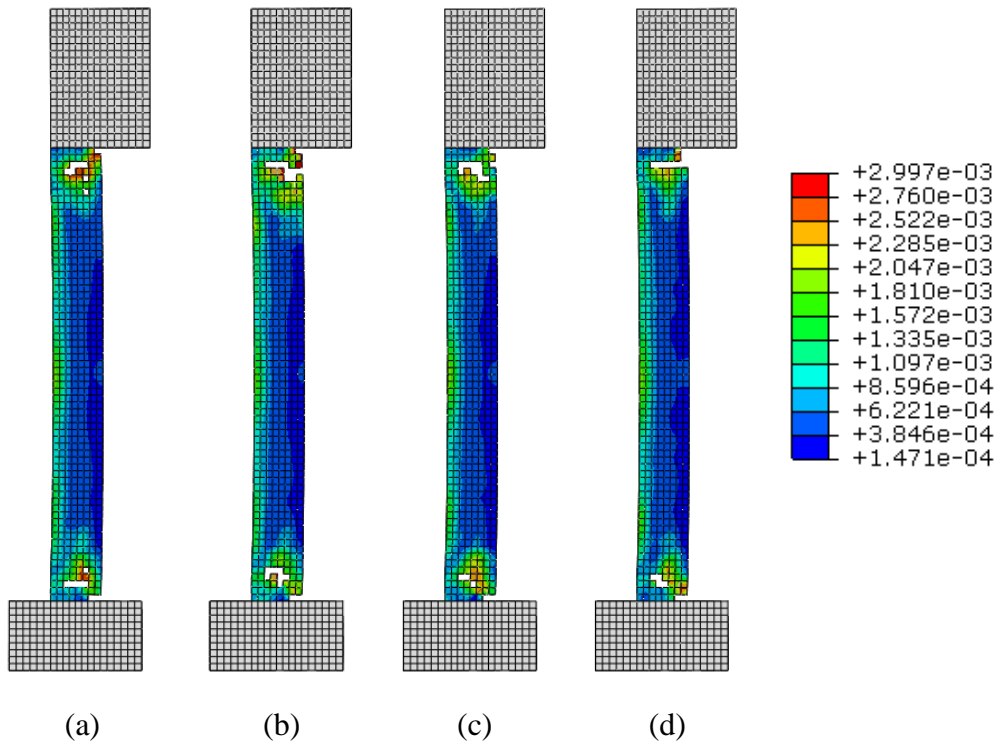


Figure 6.21. Damage pattern in cases (a) T1, (b) T2, (c) T3 and (d) T4 at 3 msec after the application of the blast load, function of the user-defined variable

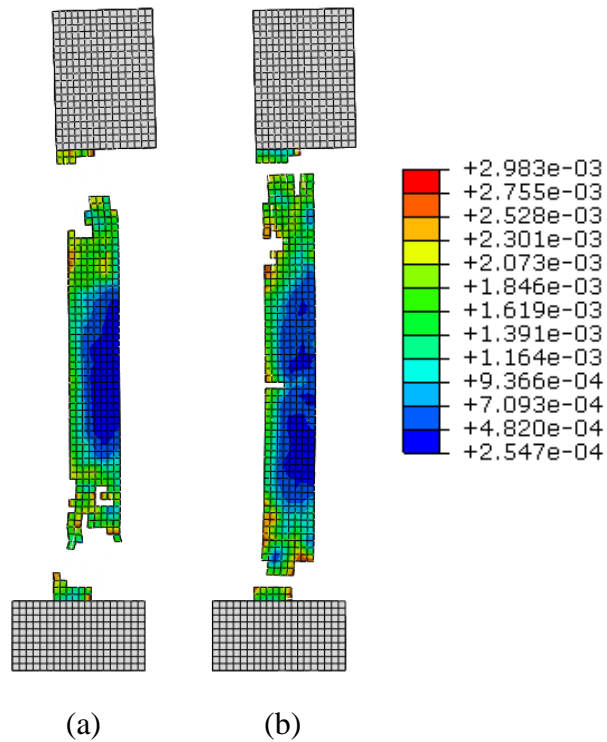


Figure 6.22. Damage pattern in cases (a) T1 and (b) T4 at 150 msec after the application of the blast load, function of the user-defined variable

The readings of the mid-height displacement of the analysed columns are shown in Figure 6.23 and summarised in Table 6.7. As can be seen, the increase in transvers reinforcement leads to an increase in column stiffness which accounts for lower lateral displacements.

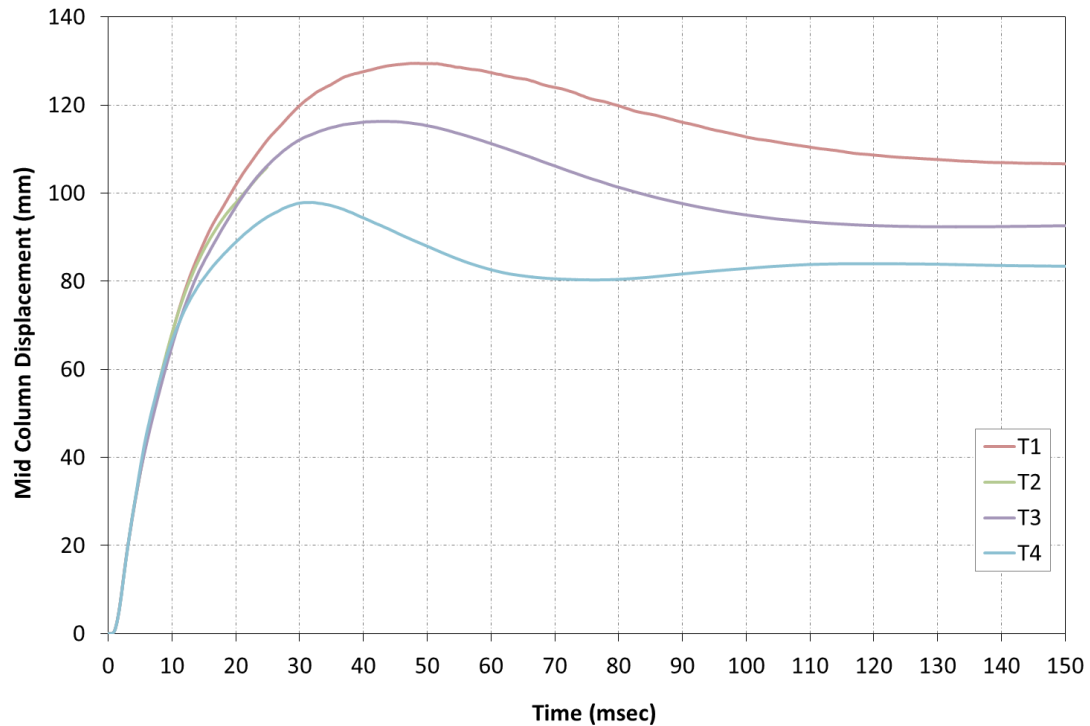


Figure 6.23. Mid column displacements for varying ratios of transverse reinforcement

Case	Peak Deflection (mm)	Residual Deflection (mm)	Damage type
T1	129.5	106	Diagonal shear
T2	-	-	Diagonal shear
T3	116.3	92	Diagonal shear
T4	97.9	83.4	Diagonal shear

Table 6.7. Column response under varying transverse reinforcement

### 6.2.5. Boundary conditions

The influence of boundary conditions on the structural response of the column was studied using three simplified cases. In all cases, the heading and footing of the column were not included in the finite element model. The three cases were fixed-fixed, pinned-pinned and

pinned-sliding simple support. The boundary conditions at each end are presented in Table 6.8.

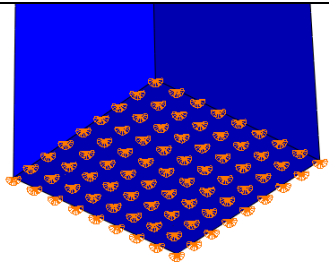
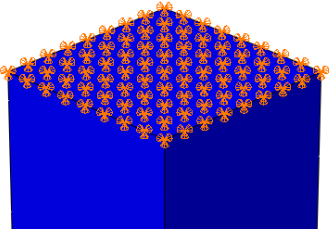
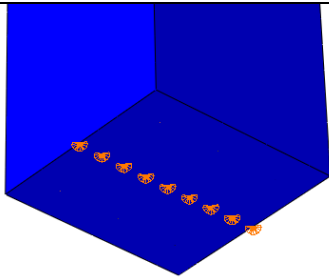
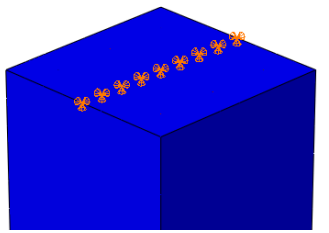
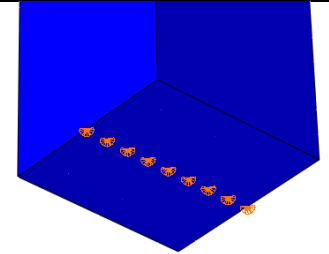
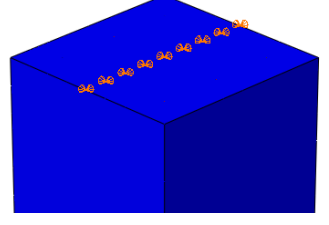
Case	Description	Bottom Boundary	Top Boundary
BC1	fixed-fixed		
BC2	pinned-pinned		
BC3	pinned-sliding simple support		

Table 6.8. Boundary conditions examined

Apart from the lack of heading and footing and the boundary conditions, the columns examined in this section were similar to the column from the experimental setup for test 7 reported by the Explosive Loading Laboratory [1]. The columns were subjected to the blast load used in test 7. The influence of boundary conditions was studied on the post-blast structural state of the columns.

The numerical results for the studied cases (see Table 6.8) are presented in Figure 6.24 to Figure 6.26. As can be seen, initial damage occurred sooner in the column with the fixed-fixed (BC1) supports than in the other two columns. Diagonal shear damage developed in all three cases, with the most severe visible deterioration in the column with the fixed-fixed supports. The nature of the pinned-pinned (BC2) and pinned-sliding (BC3) simple supports applied in this study resulted in the localisation of damage in support vicinity at early stages of column response (5-15 msec after the application of the blast load). The columns with the pinned-pinned and pinned-sliding simple supports also exhibited flexural damage, with mild



damage visible at mid-column in the first case and severer damage closer to the top support in the latter case. In the column with the pinned-sliding simple support, this also led to a large amount of material deterioration, as shown in the Figures below.

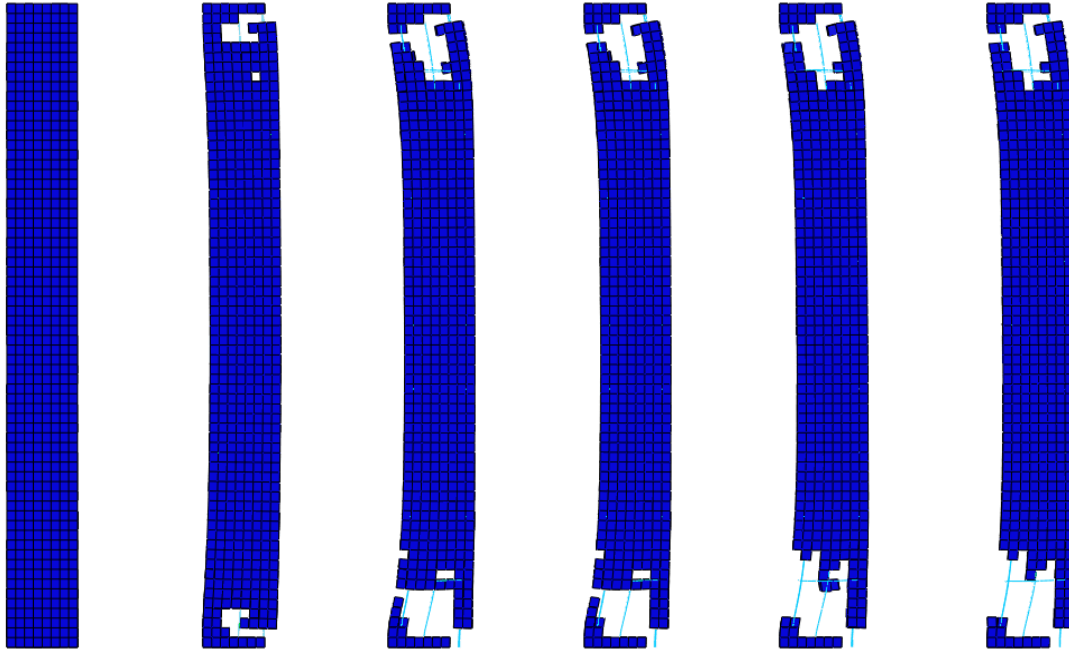


*Figure 6.24. Progression of damage in case BC1 (at 0, 5, 10, 15, 30 and 100 msec after the application of the blast load)*

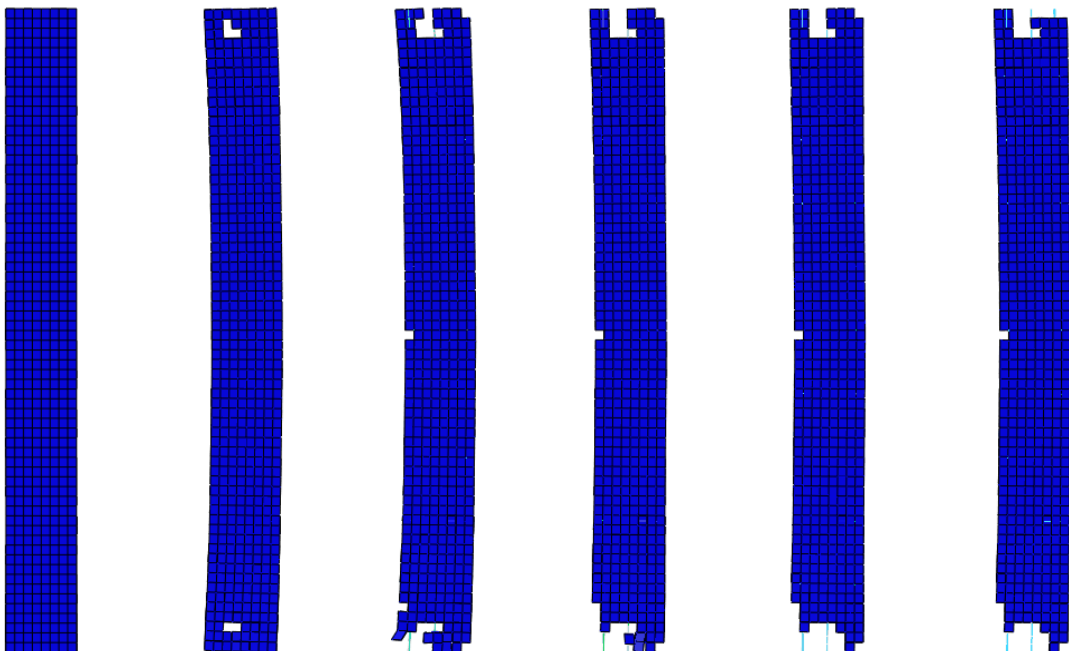


*Figure 6.25. Progression of damage in case BC2 (at 0, 5, 10, 15, 30 and 100 msec after the application of the blast load)*

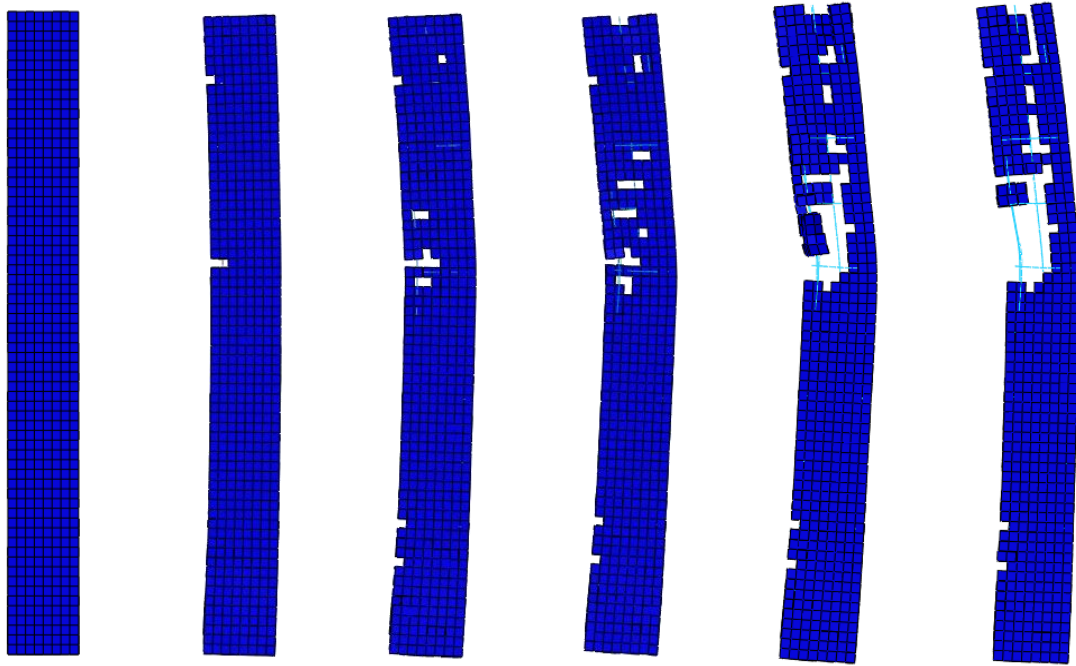


*Figure 6.26. Progression of damage in case BC3 (at 0, 5, 10, 15, 30 and 100 msec after the application of the blast load)*

The damage patterns developed in the columns with BC1-3 supports 5 msec and 15 msec after the application of the blast load are compared in Figure 6.27 and Figure 6.28, respectively. It can be concluded that the supporting conditions have a profound effect on the failure mechanism, i.e., changing it from diagonal shear damage in the BC1-2 cases to the combined diagonal shear and flexural damage in the BC3 case. The stiffer fixed-fixed supporting conditions (BC1) lead to higher initial damage, but this damage is restrained from further developing. There is also a considerably smaller mid-column displacement and a substantial re-centring of the column, as shown in Figure 6.29 and Table 6.9 by the residual displacement sustained. The pinned-sliding simple support (BC3) showed the least initial damage. However, both diagonal shear and flexural damage developed rapidly due to the large rotations at the supports, leading to substantial material deterioration and a large mid-column displacement without re-centring. Although the column with the pinned-pinned support (BC2) exhibits the lowest level of material deterioration, such supporting conditions lead to the largest mid-column displacement.

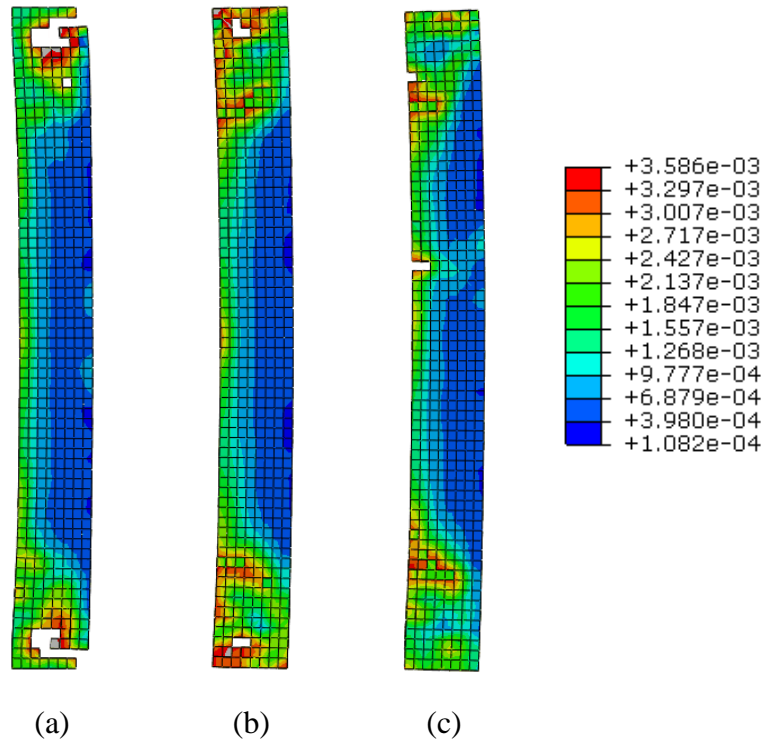


Figure 6.27. Damage pattern in cases (a) BC1, (b) BC2, (c) BC3 at 5 msec after the application of the blast load, function of the user-defined variable

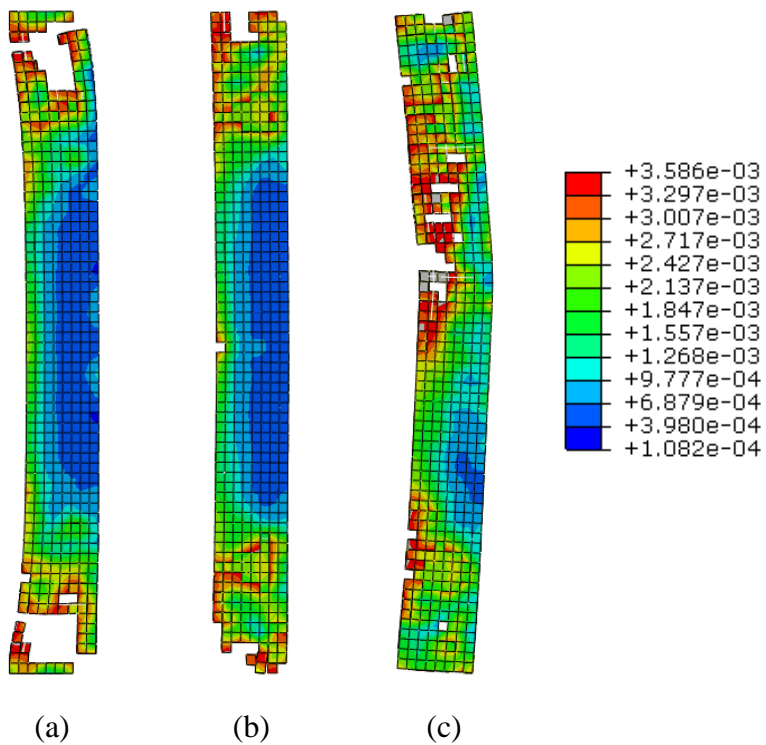


Figure 6.28. Damage pattern in cases (a) BC1, (b) BC2, (c) BC3 at 15 msec after the application of the blast load, function of the user-defined variable

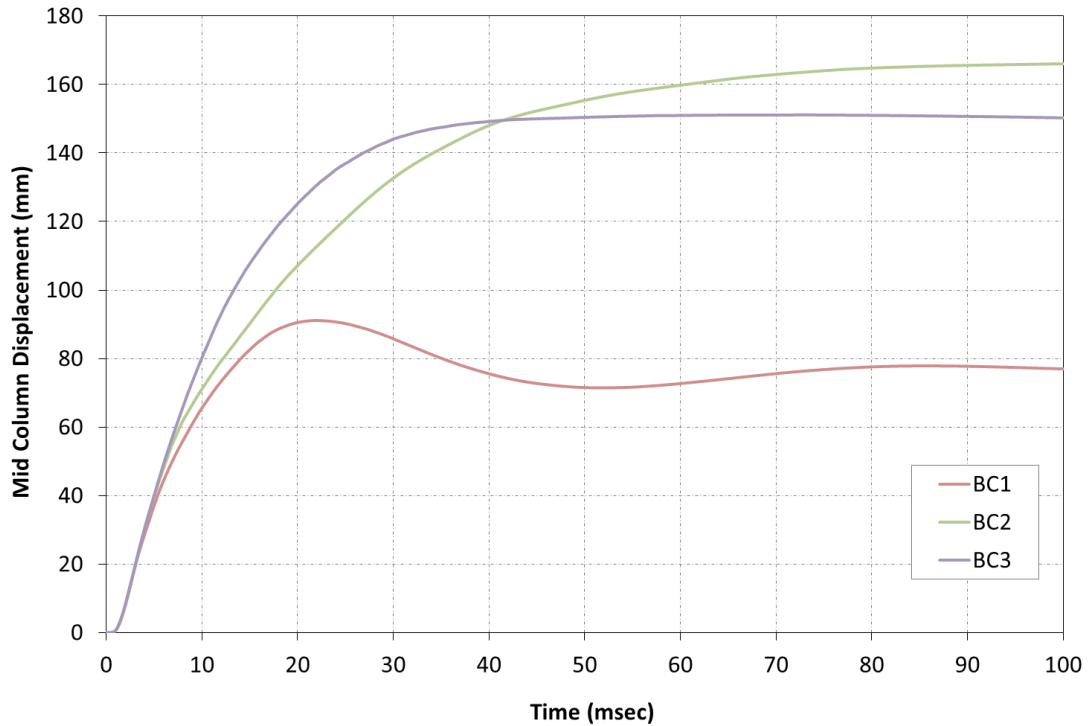


Figure 6.29. Mid-column displacements under the different boundary conditions

Case	Peak Deflection (mm)	Residual Deflection (mm)	Damage type
BC1	91.1	77	Diagonal shear
BC2	166	166	Diagonal shear
BC3	151	150	Diagonal shear and flexural damage

Table 6.9. Column response under the different boundary conditions

### 6.2.6. Static, Dynamic and Impulsive Reactions

The influence of different loading regimes on the structural response of the column was studied using the fixed-fixed column presented in Subsection 6.2.5. The cases analysed were the static, dynamic and impulsive cases. The blast loads used and their duration are presented in Table 6.10 and in Figure 6.30.

Case	Pressure (MPa)	Duration of Load (msec)	Impulse (MPa·msec)	Equivalent Load (N)
Static	0.5	200	50	583306
Dynamic	0.5	40	10	583306
Impulsive	0.5	2	0.5	583306

Table 6.10. Levels of blast pressures, durations and equivalent force investigated

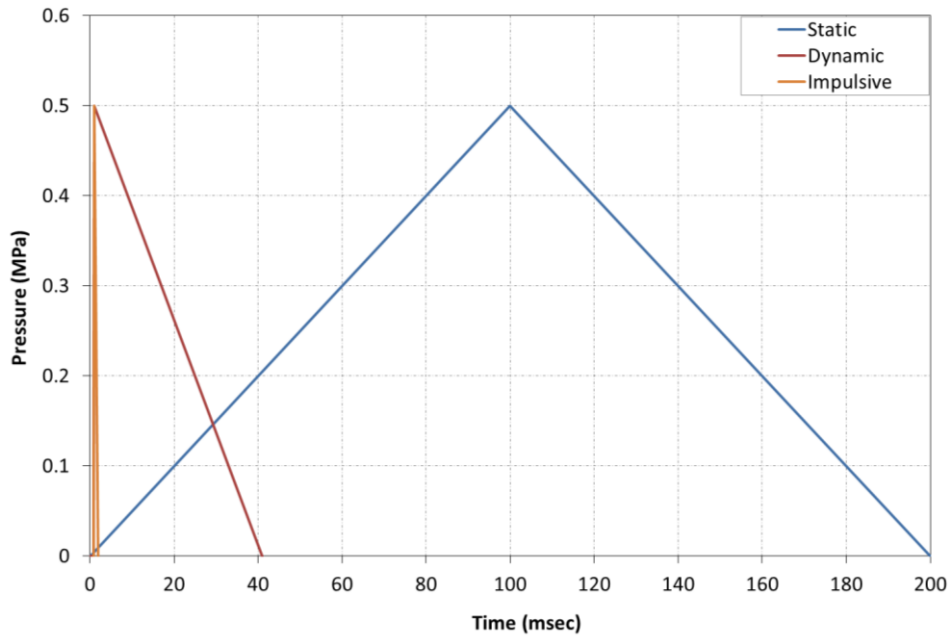


Figure 6.30. Load profiles used for static, dynamic and impulsive cases

Figure 6.31 presents the applied static force as compared to the reaction force. It is shown that when the force is applied statically the structural response follows the applied load. The damage pattern at peak load is also presented in the Figure. It can be observed that the damage at the end of the loading period, as presented in Figure 6.36 is practically identical to that observed at peak load.

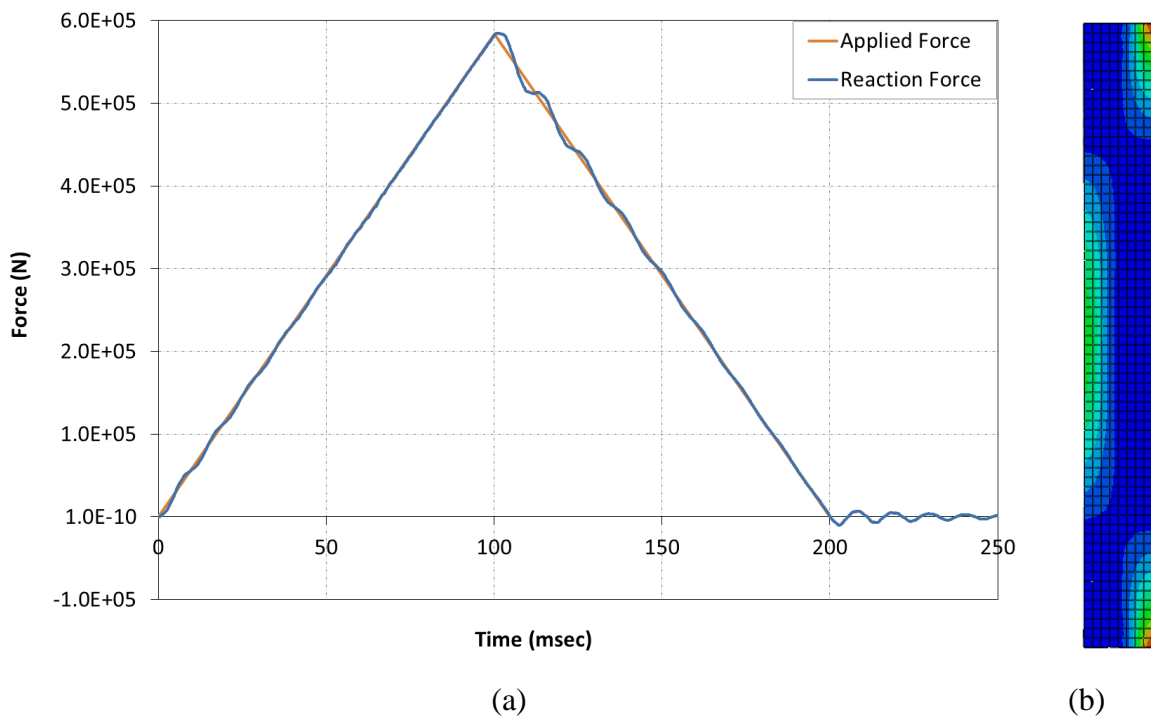


Figure 6.31. (a) Applied load vs. reaction force and (b) damage pattern at time of max reaction for static case

Figure 6.32 presents the applied force compared to the reaction force and the structural reaction at peak applied force for the dynamic case. It is shown that when the force is applied dynamically there is an increase in the structural response. This increase constitutes the dynamic amplification factor and is caused by due to the structure's inability to respond quickly to the loading [2]. It is shown that at peak load the structure has not had sufficient time to respond and no notable damage is observed.

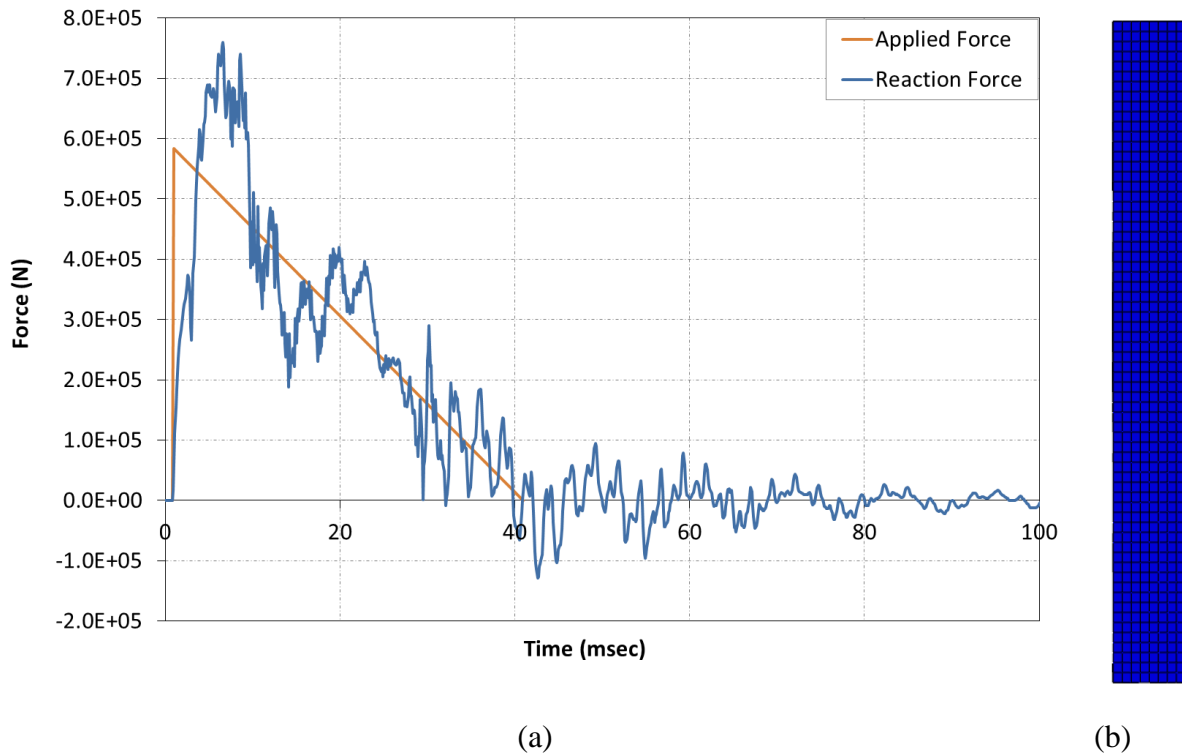


Figure 6.32. (a) Applied load vs. reaction force and (b) damage pattern at time peak load for dynamic case

The applied force, reaction force and the structural reaction at peak applied force for the impulsive case is presented in Figure 6.33. In the impulsive case with relatively low applied pressure the structure behaves as a very stiff member.

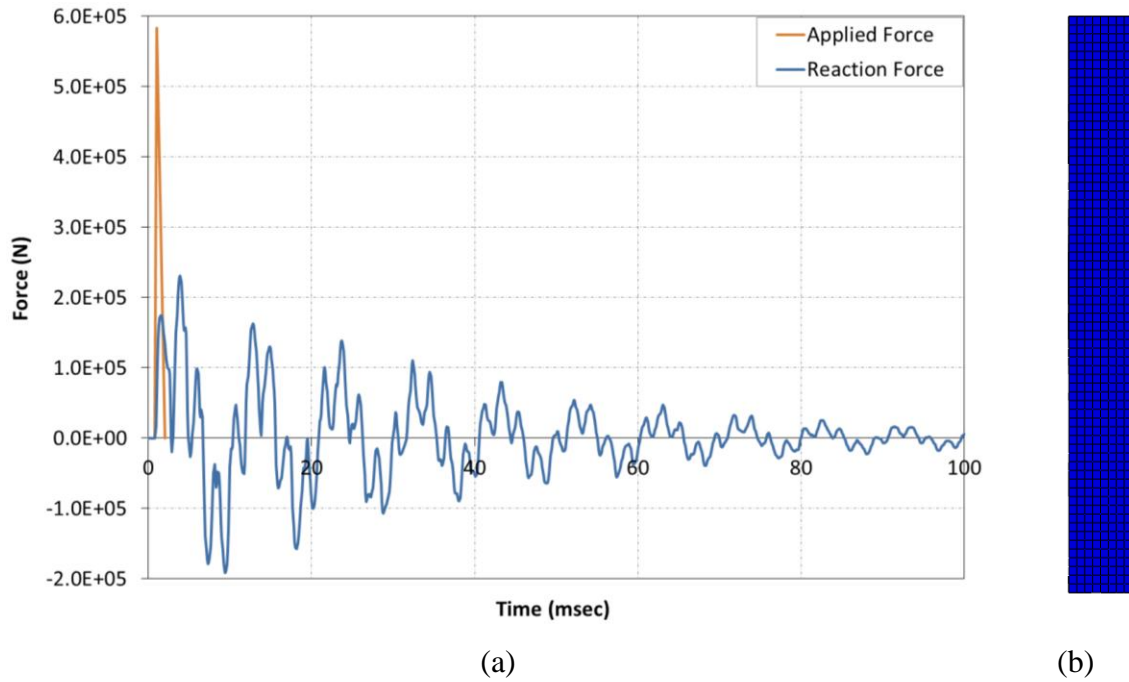


Figure 6.33. (a) Applied load vs. reaction force and (b) damage pattern at time of peak load for impulsive case

Although from the above figure the reactions for the column are very low this is due to the fact that, as in the case of strain rate, the column does not have sufficient time to react. In this case, the comparison between the total internal energy of the structure in the static and impulsive regimes, as shown in Figure 6.34, reveals that the energy in the impulsive case is significantly higher.

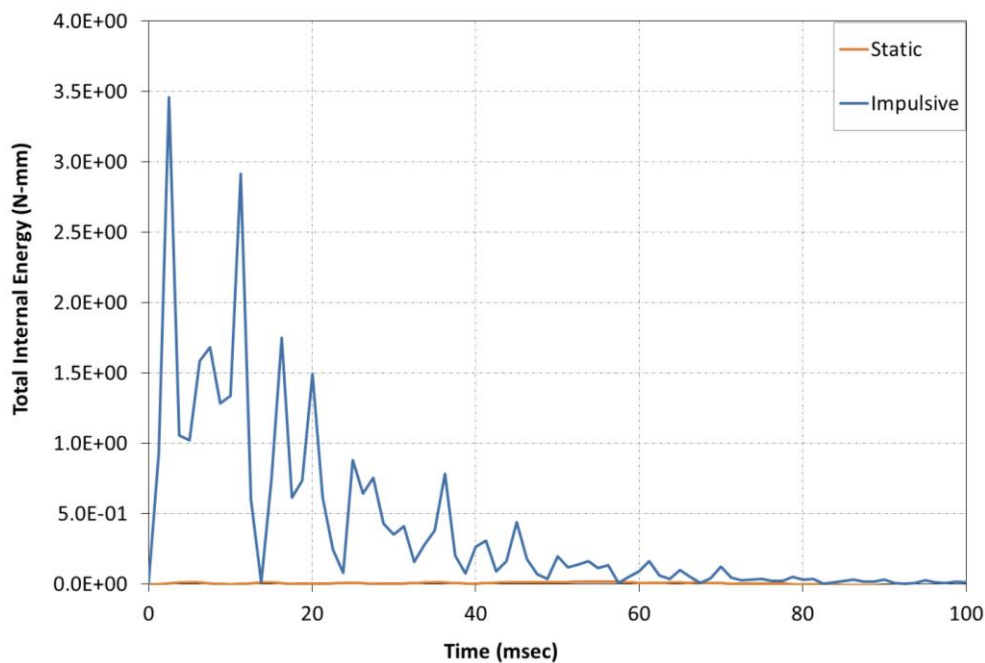


Figure 6.34. Total internal energy in the static and impulsive cases

At 5 msec damage is observed in the dynamic case. The static case has not had sufficient load at this time and the impulsive case has only reacted mildly to the applied load, see Figure 6.35. By the time the load has passed, see Figure 6.36, both the static and dynamic cases exhibit damage. The pattern is similar, however as the dynamic case is amplified the damage is more severe in that case.

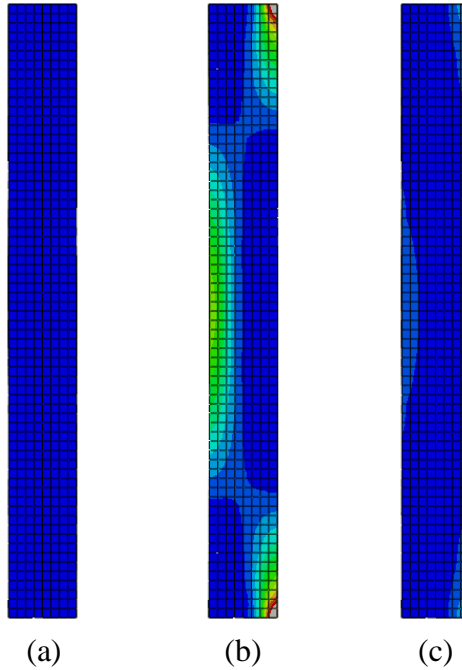


Figure 6.35. Damage pattern in (a) Static, (b) Dynamic and (c) Impulsive cases at 5 msec, function of the user-defined variable

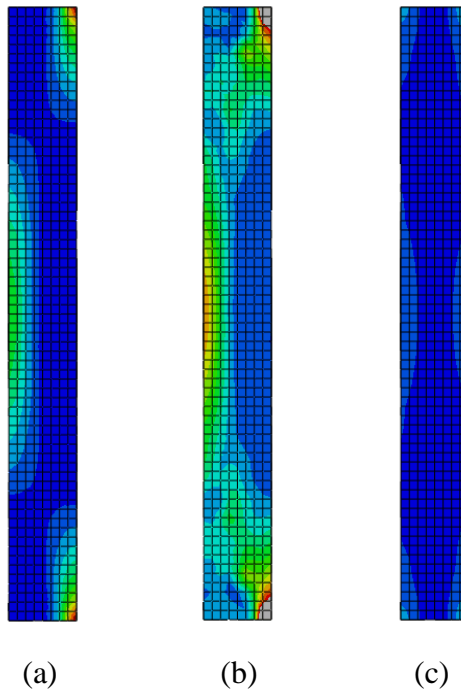


Figure 6.36. Damage pattern in (a) Static, (b) Dynamic and (c) Impulsive cases at 250 msec, function of the user-defined variable



### 6.2.7. Reaction Time

In order to investigate the reaction time under varying blast pressures and durations a number of analyses were carried out. The structural model used was the fixed-fixed column as described in Subsection 6.2.5. The blast pressures and blast durations investigated, as well as the equivalent applied forces are presented in Table 6.11.

Case	Pressure (MPa)	Duration of Blast (msec)	Equivalent Force (N)
RT1	0.5	40	583306
RT2	1	20	1166612
RT3	5	4	5833060
RT4	20	1	23332240

Table 6.11. Levels of blast pressures, durations and equivalent force investigated

The results of the column behaviour at 5 msec and at 150 msec are presented in Figure 6.37 and Figure 6.38. These results are consistent with those previously observed when examined the effects of varying blast intensities (Subsection 6.2.1), namely that as the pressure increases, the damaged zones concentrate near the supports effectively leading to ‘shear-off’ of the column at the supports. With further increase in pressure, the shear-induced damage becomes more pronouncedly diagonal with increasing amounts of concrete material deteriorating in the areas where shear damage occurs.

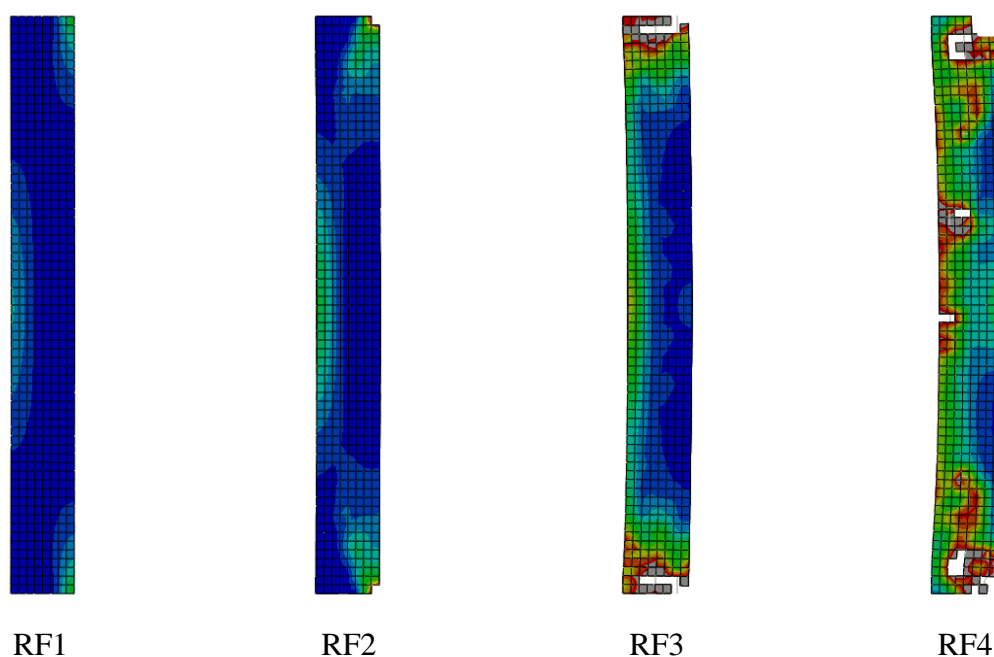
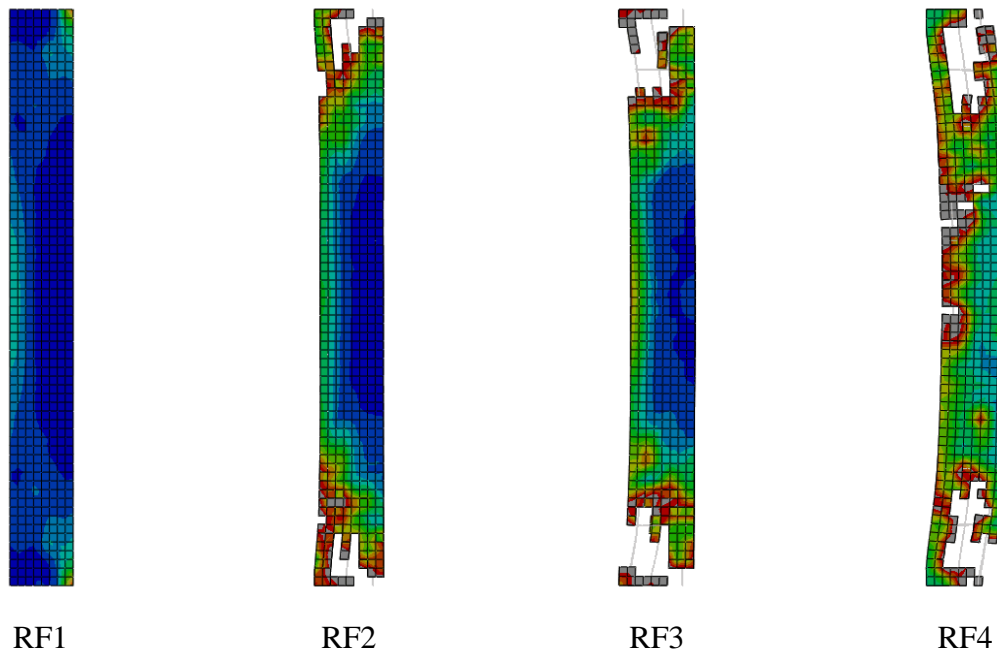


Figure 6.37. Comparison of damage patterns at 5 msec, function of the user-defined variable



*Figure 6.38. Comparison of damage patterns at 150 msec, function of the user-defined variable*

The comparison of the applied load as compared to the damage dissipation energy for each case is presented in Figure 6.39 to Figure 6.42. The reason for using energy, as opposed to reaction forces, to measure how it takes to realise structural reaction to the applied force stems from the inaccuracies when using reaction forces. As discussed in the section referring to strain rate, the higher the loading speed the less accurate measuring the reaction via the reaction forces becomes. It is shown the when the speed of the applied force is slower the reaction occurs at roughly the same time, see Figure 6.39. As the speed of the applied force grows, the maximum reaction occurs at the unloading stage and at even higher speeds even after the load has occurred, see Figure 6.40, Figure 6.41 and Figure 6.42.

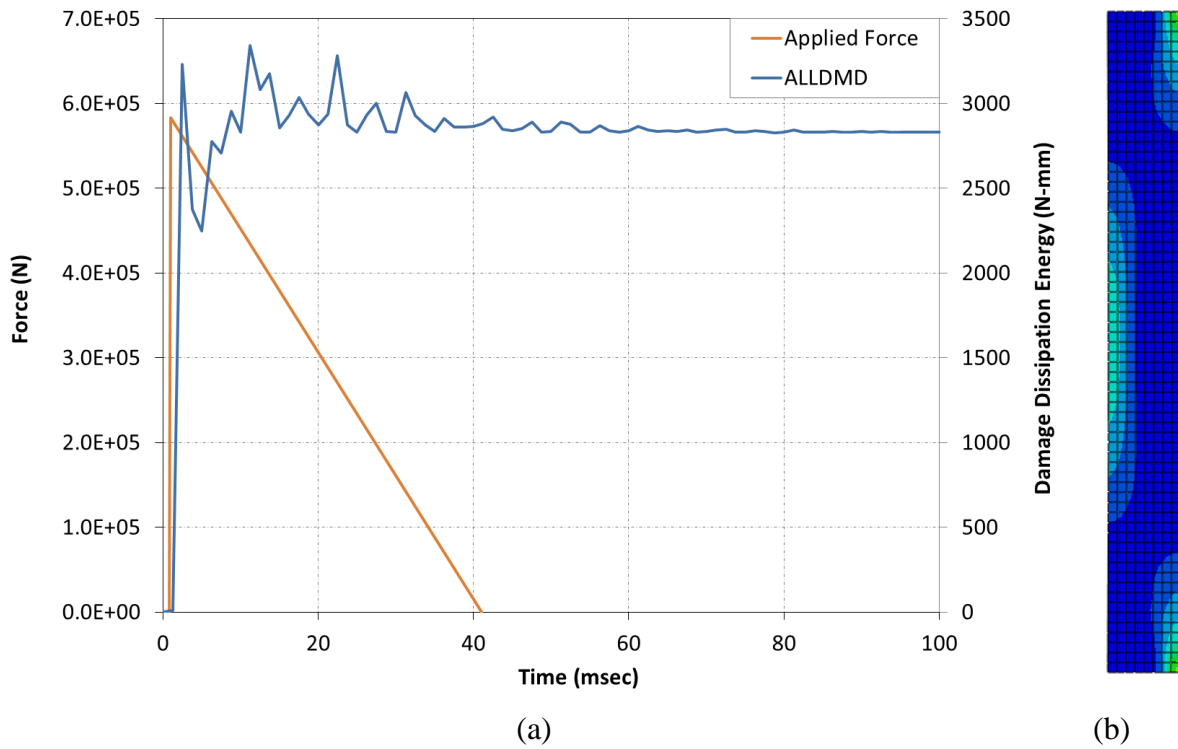


Figure 6.39. (a) Applied load vs. damage dissipation energy and (b) damage pattern at time of max reaction for case RT1

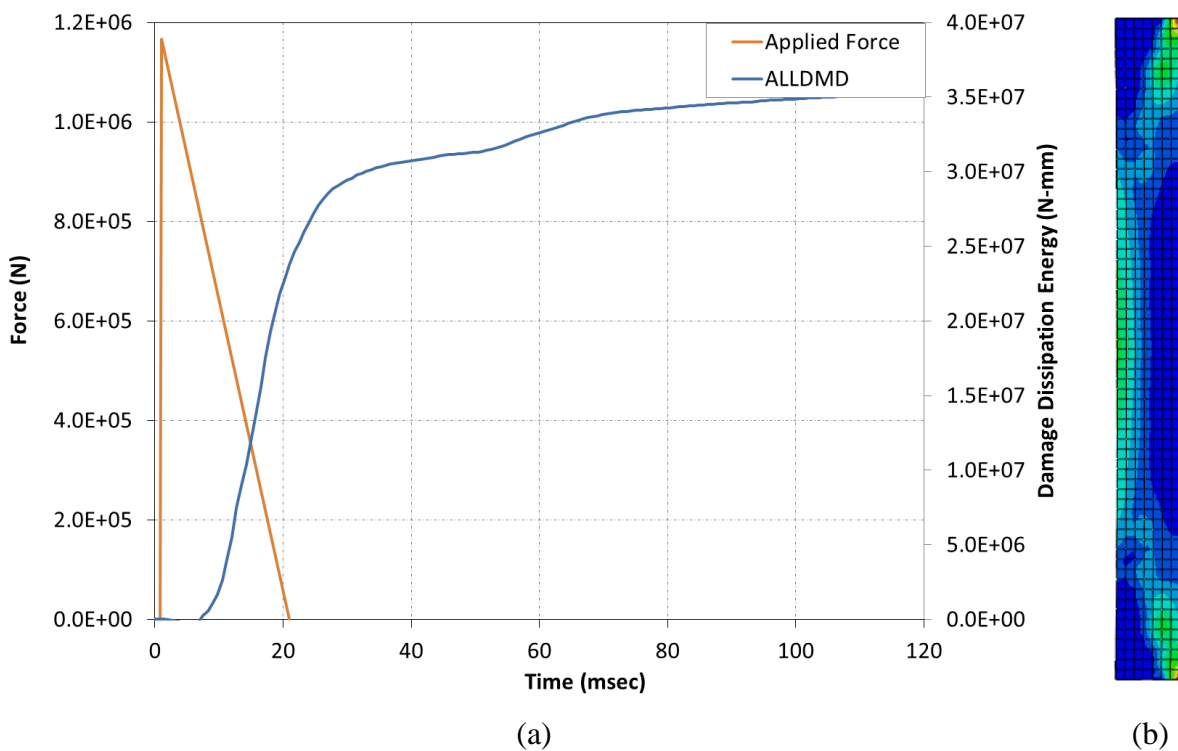


Figure 6.40. (a) Applied load vs. damage dissipation energy and (b) damage pattern at time of max reaction for case RT2

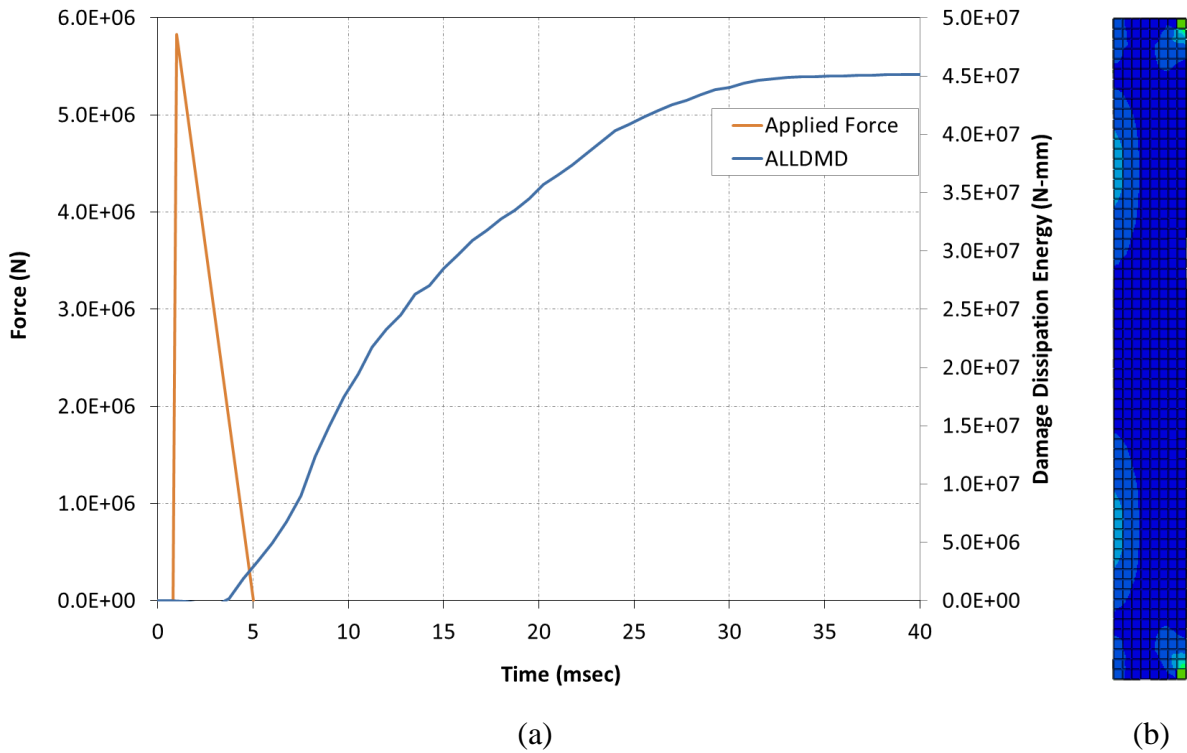


Figure 6.41. (a) Applied load vs. damage dissipation energy and (b) damage pattern at time of max reaction for case RT3

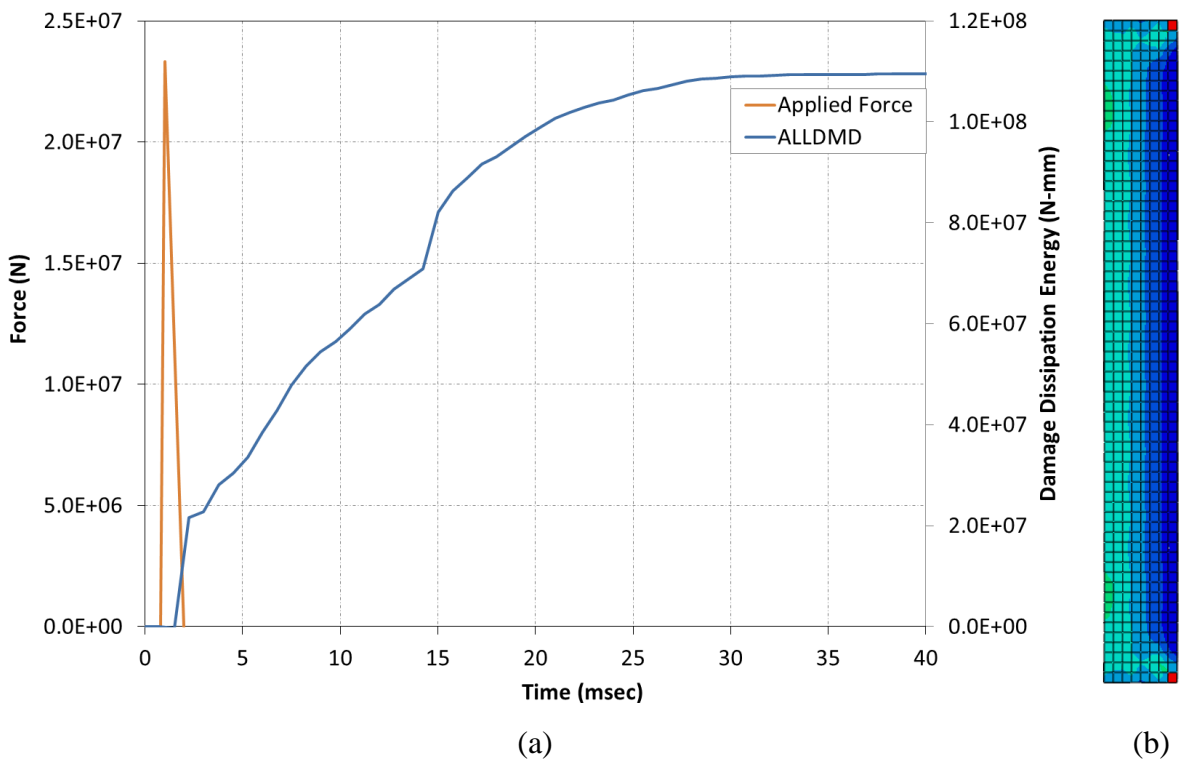


Figure 6.42. (a) Applied load vs. damage dissipation energy and (b) damage pattern at time of max reaction for case RT4

A comparison between the damage dissipation energies for the four cases shows an increase in the energy as the applied load grows, as presented in Figure 6.43.

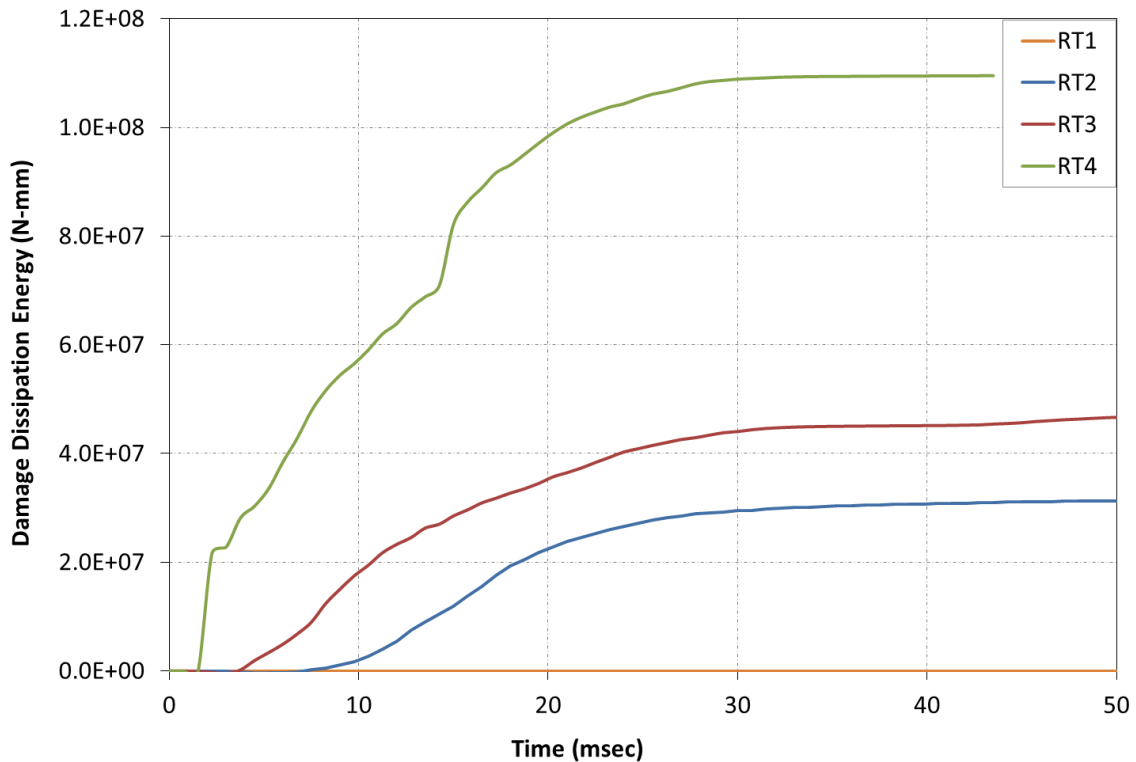


Figure 6.43. comparison of the damage dissipation energy in all four cases

### 6.2.8. Reinforcement Element Definition

The effect of the assumption of reinforcement behaviour on the columns' structural response was studied using the load assumptions made in subsection 6.2.1. The reinforcement was modelled using truss elements and compared to the assumption of beam elements, as used in all analyses carried out in this work. The assumption of beam behaviour takes into account post failure mechanisms, such as dowel and catenary behaviour. Both the beam and truss reinforcement schemes were carried out on blast intensity load model I4.

The damage patterns for the column at 5 msec and at 150 msec are presented in Figure 6.44 and Figure 6.45. At 5 msec the behaviour of the structure with reinforcement modelled as truss elements is very similar to the structure with beam modelled reinforcement. However, at 150 msec the behaviour of the two structures differs. The beam reinforced structure suffers from shear and material erosion close to the base, whereas the column with reinforcement modelled as truss elements also develops flexural damage.

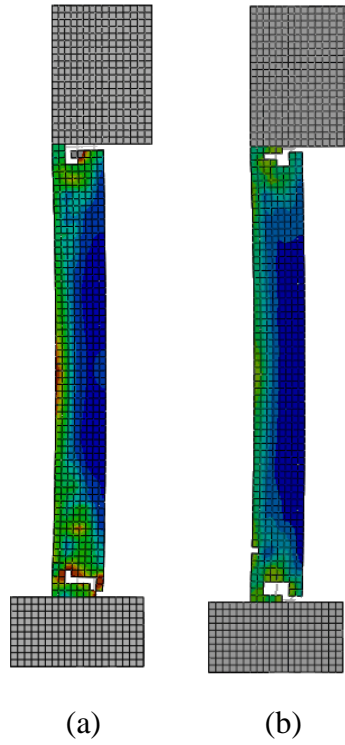


Figure 6.44. Comparison of damage patterns at 5 msec for column with (a) beam element reinforcement and (b) truss element reinforcement, function of the user-defined variable

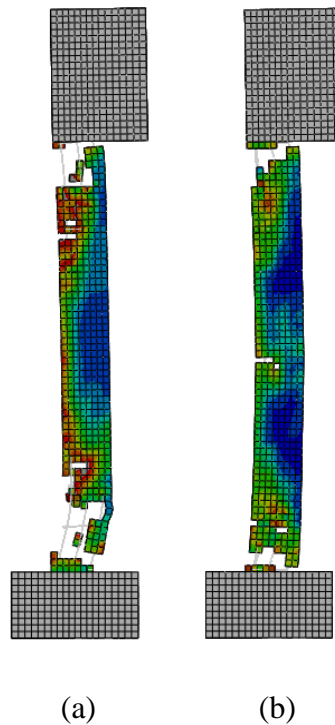


Figure 6.45. Comparison of damage patterns at 150 msec for column with (a) beam element reinforcement and (b) truss element reinforcement, function of the user-defined variable

Figure 6.46 depicts variations of mid-height column displacement caused by the different element modelling assumptions. As can be seen, the initial displacements for both the truss and beam element types are similar with the truss elements adding to the whole structural stiffness. However, when damage does occur, as seen in Figure 6.45, additional flexural damage is evident leading to overall higher mid column displacements.

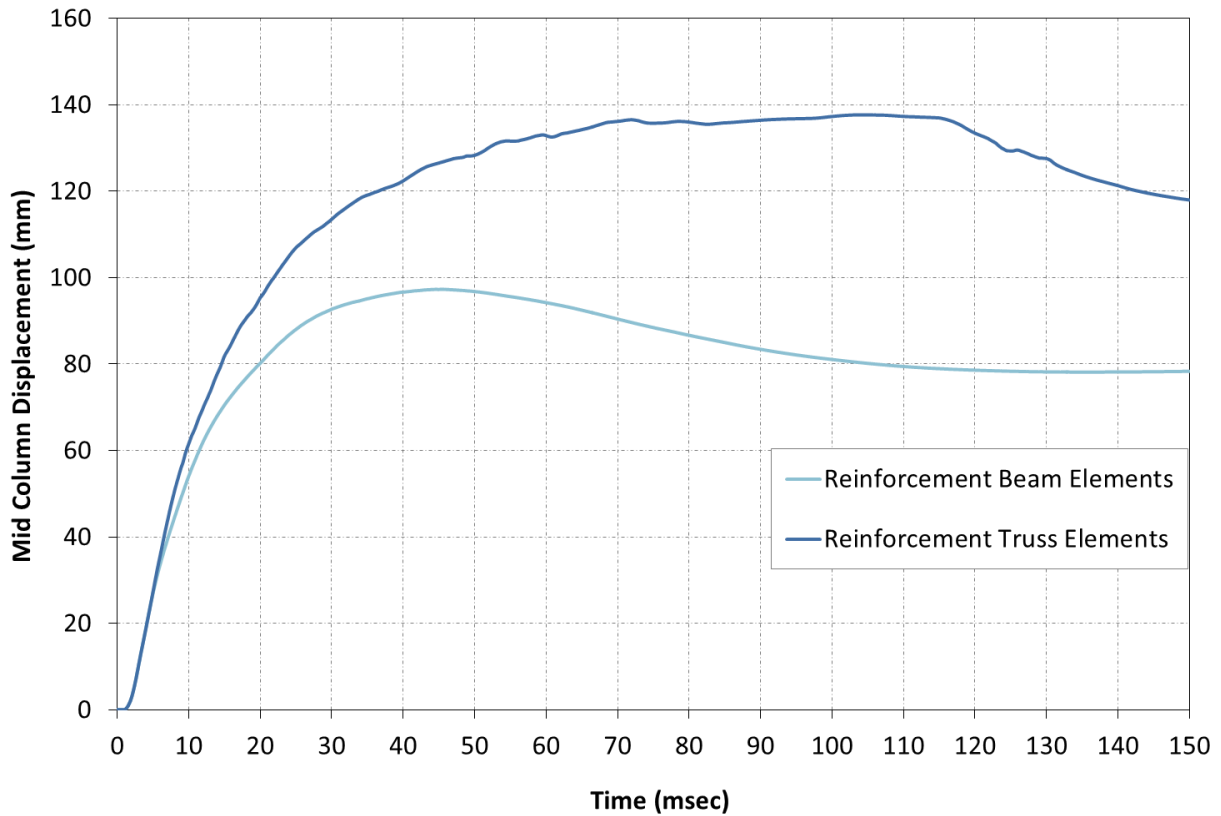


Figure 6.46. Mid column displacements for different reinforcement element definitions

This study into the type of element used for reinforcement shows that a structure using truss element reinforcement does not allow for the full benefit of the reinforcing steel. When the steel is modelled as beams it contributes to the post failure mechanisms and dissipates energy by means of catenary action and dowel effects. The modelling of reinforcement as beam elements, therefore, leads to a better overall structural representation.

### 6.2.9. Conclusions

In this chapter, the influence of various parameters on the structural response of a reinforced concrete column under a blast load was studied using FE simulations. The parameters included different blast intensities, levels of axial force, ratios of longitudinal and transverse reinforcement and boundary conditions.

The levels of blast intensity were studied using a triangular time history which differed in pressure and blast duration whilst maintaining constant impulse. The FE results demonstrated changes in the column response mechanism from flexural damage occurring under low pressures to shear damage occurring under high pressures.

The numerical study into the influence of axial force showed that the mode of failure changes from 'diagonal shear' to a combination of shear-off and flexural failure with an increase in axial load, and that the mid-column deflection increases.

The ratio of longitudinal reinforcement had a pronounced impact on the structural response of the column under blast loads. At a lower ratio of reinforcement, the column suffered from both flexural and diagonal shear damage and underwent substantial lateral mid-height displacement due to the lower stiffness. With an increase in reinforcement ratio, the column stiffness increased leading to smaller displacement but higher material deterioration. The damage mechanism was still shear damage; however it became more similar to the shear-off effect.

The results of the analysis with varying transverse reinforcement showed that diagonal shear was the main failure mechanism in all cases. Stirrups with larger diameters, however, can reduce the extent of material damage and influence the damage mechanism leading to the development of combined diagonal shear and flexural damage.

Three simplified boundary condition variations were also examined. They included fixed-fixed, pinned-pinned and pinned-sliding simple supports. Diagonal shear damage developed in all three cases, with the most severe visible deterioration in the column with the fixed-fixed supports. The columns with the pinned-pinned and pinned-sliding simple supports also exhibited flexural damage due to increased flexural stiffness.

Static, dynamic and impulsive loading regimes for low pressure were also analysed. It was observed that the static structural response mirrored the applied load, the dynamic case led to an amplification of the response and the impulsive case responded stiffly leading to less



damage. This trend was observed again in the study of reaction times. In the dynamic region the response was amplified, however in this study the pressures were increased and durations reduced leading to pronounced damage which in turn allowed for energy dissipation leading to reduced structural reaction forces.

The numerical study into the influence of reinforcement modelling showed that the beam elements contribute to energy dissipation via structural mechanisms such as catenary action. The structure with truss element reinforcement was stiffer, suffered much larger mid column displacements and had additional flexural damage.

### 6.3. Pressure-Impulse Diagram Investigation

#### 6.3.1. Description of column used in investigation

As previously in validation analyses carried out in Chapter 5, the FE model consists of a concrete column with embedded steel reinforcement. The column has both a heading and footing to approximately simulate its boundary conditions within a frame structure. The finite element model with some of the concrete visually removed to allow a view of the embedded reinforcement is shown in Figure 6.47.

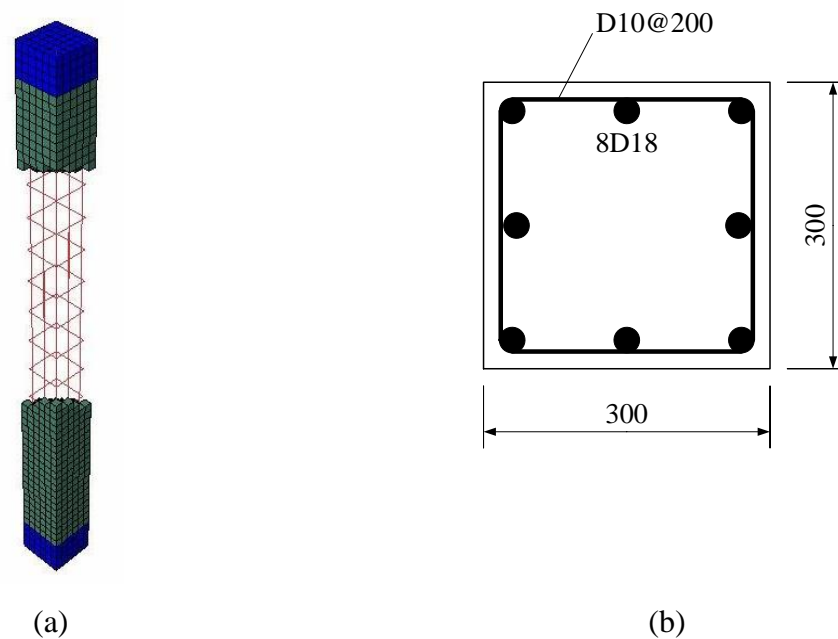


Figure 6.47. Reinforced concrete column (a) Finite element view and (b) cross section

The geometry of the structural components is presented in Table 6.12.

Concrete				Steel		
Column width (mm)	Column depth (mm)	Column height (mm)	Heading/ Footing height (mm)	Longitudinal reinforcement	Cross tie/hoop	Cover depth (mm)
300	300	3000	200	8D18	D10 @200	30

Table 6.12. Column components' geometry

As previously described in Chapter 5, the bond between concrete and steel reinforcement was modelled by embedding beam elements representing the reinforcing bars into the concrete elements (see Figure 6.47). This procedure created a perfect bond between the materials.

The footing and heading were added to the column model of the shown in Figure 6.47 to simulate behaviour representative of a column within a frame structure. The arrangement of boundary conditions allowed for small amount of rotation though footing and head deformations creating restraints that acted somewhere in between the fixed and pinned supports. The outer vertical face of the footing and head were constrained against horizontal motions and the bottom face of the footing was constrained against vertical motion.

The elements used in the model of the column were taken from the Abaqus explicit element library. The concrete modelled using type C3D8R – 8 node linear bricks including reduced integration and hourglass control. The steel reinforcement was modelled in Abaqus using 3D Timoshenko beam elements. The material used for the steel beams was a plastic, rate dependant material with a specified strain failure. A refined mesh of 50 mm was used in all FE simulations in accordance with previous element sensitivity analysis.

The steel material behaviour was modelled as elastic perfectly plastic with a failure strain of  $\epsilon = 0.18$  and the material properties given in Table 6.13.

Elastic Modulus (GPa)	Yield stress of longitudinal steel (MPa)	Yield stress of cross tie/hoop (MPa)
210	335	235

*Table 6.13. Steel Material Properties*

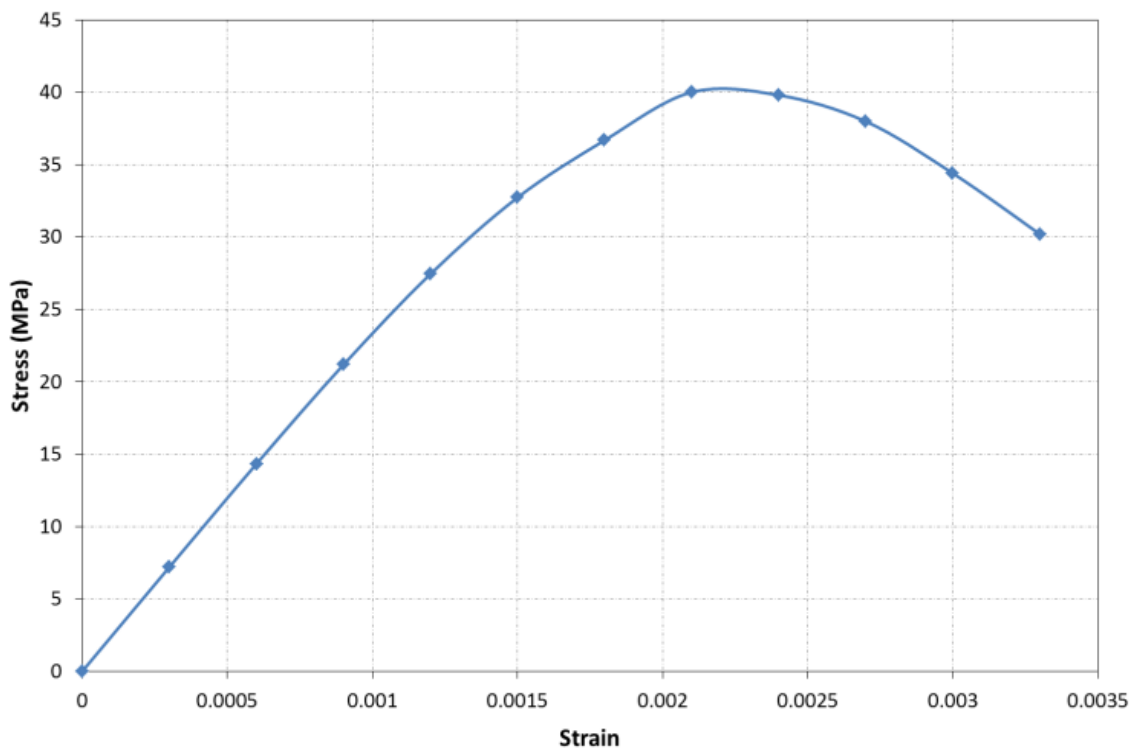
Concrete was modelled using the extended brittle crack model, described in detail in Chapter 5, with the material parameters given in Table 6.14.

Elastic Modulus (GPa)	Unconfined concrete strength (MPa)
24	40

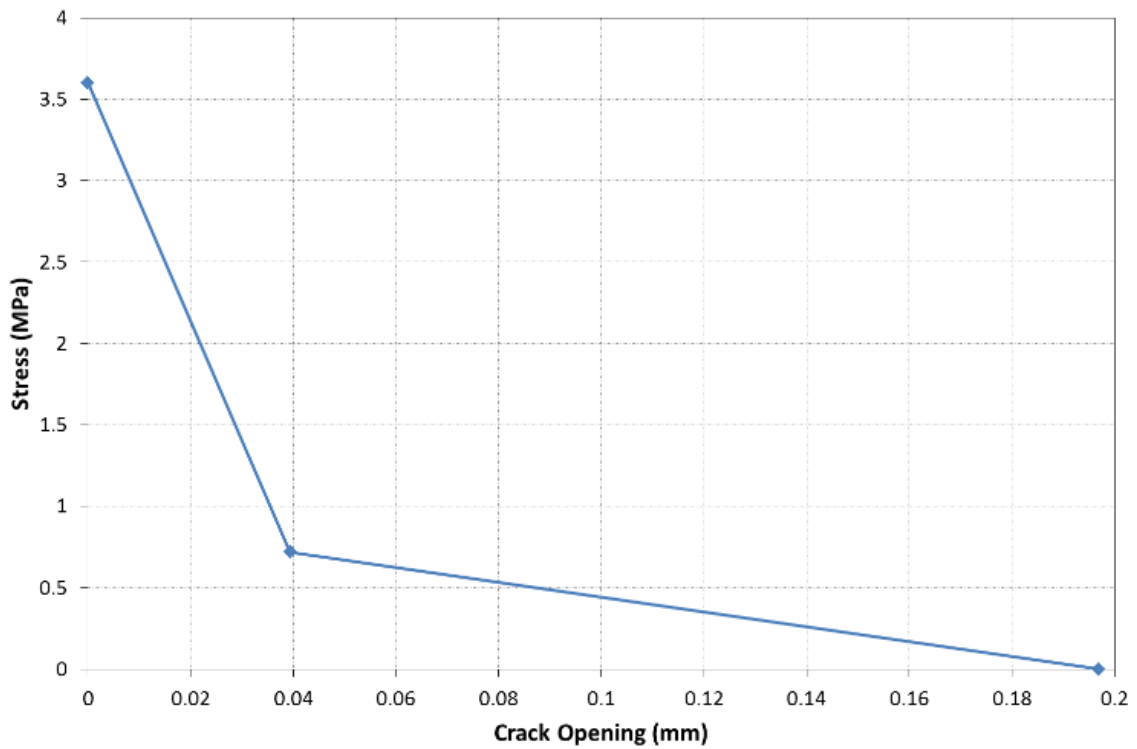
*Table 6.14. Concrete Material Properties*

The stress-strain curve describing the behaviour of concrete in compression and the stress-displacement curve describing the behaviour of concrete in tension were calculated using in

accordance with the FIB Model Code [3]. The resulting diagrams are presented in Figure 6.48.



(a)



(b)

Figure 6.48. Concrete material properties in (a) compression and (b) tension

The blast load was simulated through application of uniform pressure on one face of the column. The pressure load had a triangular shaped time history with zero rise time, as presented in Figure 6.49.

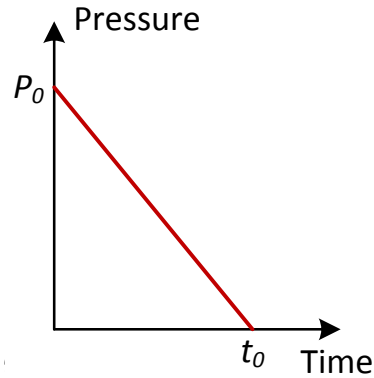
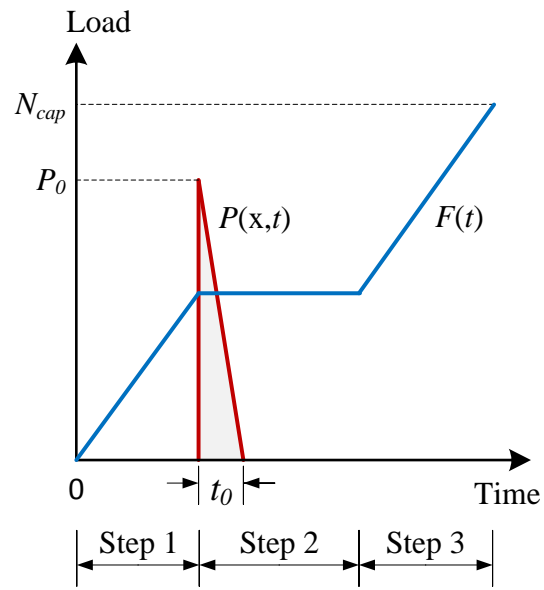


Figure 6.49. Blast load time history

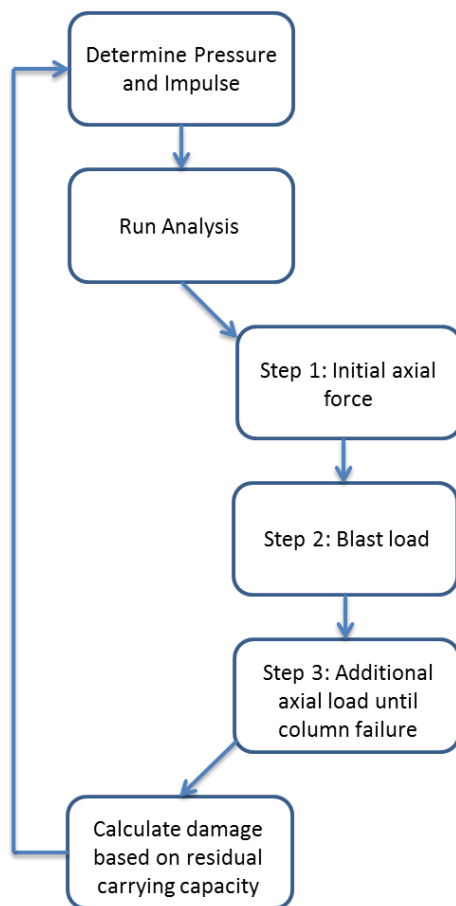
### 6.3.2. Building of P-I and complementary diagrams for different structural/loading parameters

In this section, the P-I and complementary diagrams are derived using Abaqus [4]. To enable further understanding of damage levels of reinforced concrete columns under blast loads with reference to the columns axial load, the latter is considered as the parameter influencing the position of P-I curves and, thus, used in the complementary diagrams. The remaining carrying capacity is considered as the failure criterion, since it represents the most vital characteristic of the column.

In derivations of each point on the diagrams, three main loading steps were undertaken: *Step 1* – the column was loaded by the axial force, *Step 2* – the blast load was then deployed and, finally, *Step 3* – additional axial force was introduced until the column collapsed. The time history of the loading steps and the flowchart describing main steps undertaken in each FE simulation are depicted in Figure 6.50.



(a)



(b)

Figure 6.50. (a) Loading steps and (b) flowchart describing derivation

In order to ensure quasi-static behaviour in Steps 1 and 3 the axial force was loaded in a gradual manner to avoid the development of inertia effects. In Step 2, a sufficient amount of time was given after the application of the blast load to allow the blast-induced energy to sufficiently dissipate. After the completion of Step 3 (see Figure 6.50b), the structural damage,  $d$ , was found according to the following formula:

$$d = 1 - \frac{RF_{v,3}}{N_{cap}} \quad (6.1)$$

where  $N_{cap}$  is the ultimate axial capacity obtained in a separate analysis under static loading conditions prior to the curve analyses and  $RF_{v,3}$  is the maximum axial reaction force from Step 3. The P-I curves were derived for 20%, 50% and 80% damage that represented the borderlines between low ( $d < 20\%$ ), medium ( $20\% < d < 50\%$ ) and high ( $50\% < d < 80\%$ ) damage levels, e.g., see [5].

Due to the high volumes of simulations needed to generate enough points to reliably represent damage curves (see Chapter 3, Section 3.3.2 for detailed discussion), the whole method was semi-automated. This was achieved by creating a master program in Matlab [6]. The master program manipulated the Abaqus input files in order to change displacements, loads and duration as required. The program then called the Abaqus simulation and utilised Python scripts for result processing.

### 6.3.2.1. Pressure-Impulse (P-I) Diagrams

Initially, the P-I diagrams are derived using the axially unloaded column for the 20%, 50% and 80% damage levels. In order to find points on the graph, a mixture of search algorithms were used: the pressure-controlled search, the impulse-controlled search and the combined search (see detailed discussion in Chapter 3, Section 3.2.2).

In order to minimise the amount of FE runs, the dynamic region of the P-I curve was initially investigated using the combined search method (see Figure 6.51). The first set of FE analyses (Set PI1 in Figure 6.51) allowed to estimate the pressure and impulse ranges for the impulsive and quasi-static regimes, respectively. Further, two sets of FE runs utilising the impulse-controlled (Set PI2a-b in Figure 6.51) and the pressure-controlled (Set PI3a-b in Figure 6.51) search algorithms were conducted. Additional calculations of Set PI2b and Set PI3b were carried out to validate the eventual positions of the asymptotes. The results of FE simulations of the axially unloaded column carried out during the derivation of the complementary

diagrams (see Sections 6.3.2.2 and 6.3.2.3) were also added to Figure 6.51, where Set PI4 represents the points laying on the *Impulse* axis of Figure 6.53 (i.e., Set NI1), whereas Set PI5 the points on the *Pressure* axis of Figure 6.55 (i.e., Set NP1). The inclined nature of Set PI1 is the result of the liner relationship between the peak pressure and impulse embedded in the combined search algorithm. The points of Sets PI4 and PI5 follow inclined lines because in their derivation the duration of the blast load was kept constant in order to maintain the impulsive or quasi-static regime, while the peak pressure was gradually increased, leading to the increase in the impulse.

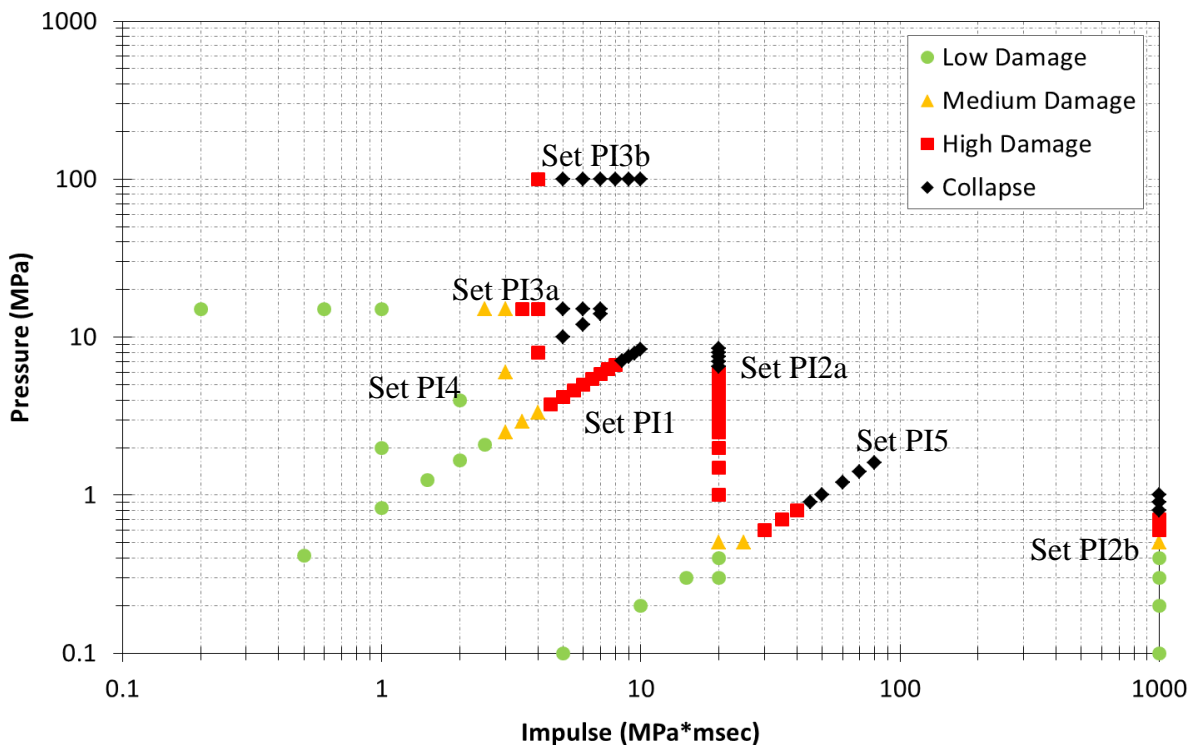


Figure 6.51. Points derived for the P-I diagram

The results of the FE analyses shown in Figure 6.51 were further used for generation of three P-I curves representing 20%, 50% and 80% damage levels. It was found that a very accurate description of the P-I curves can be given by the following equation

$$\begin{aligned} (P_0 - A_p)(I - A_I) & \quad (6.2) \\ & = (C_p \cdot A_p + C_I \cdot A_I)^D \end{aligned}$$

where  $P_0$  and  $I$  are the pressure and impulse variables, respectively;  $A_p$  and  $A_I$  represent the pressure and impulse asymptotes;  $C_p$ ,  $C_I$  and  $D$  are the fitting constants. It is necessary to point out that the shape of Eq. (6.2) is similar to Eqs. (3.28), (3.58) and (3.59) described in



Chapter 3, Section 3.4. The resulting P-I curves are obtained for  $C_P = 1$ ,  $C_I = 1$  and  $D = 0.5$  are presented in Figure 6.52.

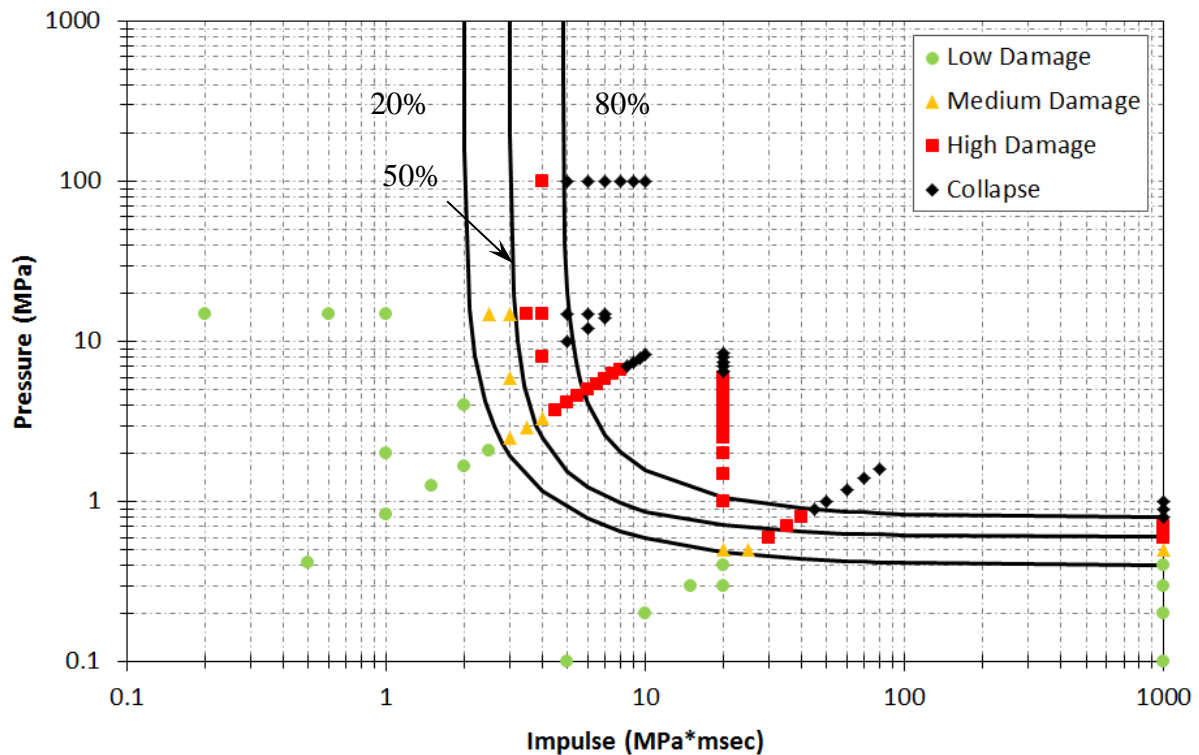


Figure 6.52. P-I Diagram fitted curves

The impulsive and quasi-static asymptotes at different damage levels are respectively described by the values of  $A_P$  and  $A_I$  given in Table 6.15.

Asymptotes		Damage
$A_I$	$A_P$	
2	0.4	20%
3	0.6	50%
4.8	0.8	80%

Table 6.15. Parameters for P-I equations

### 6.3.2.2. Axial Force-Impulse (N-I) Diagrams

The derivation of the Axial Force-Impulse (N-I) diagram started with a FE simulation of the column solely loaded by the axial force to determine its load carrying capacity. The obtained value  $N_{cap} = 2570$  kN (the point on the *Axial Force* axis in Figure 6.53) is then used to determine the increments in the axial force between four sets of FE runs. The first set of runs was carried out without axial loading (Set NI1 in Figure 6.53). The axial force was

subsequently increased by  $\Delta N = 625$  kN between each following set of runs (i.e., Sets SN2-4). In all runs, the duration of the blast load was kept constant  $t_0 = 1$  msec to generate the impulsive loading regime. This value of  $t_0$  was selected based on the analysis of the impulsive asymptotes of the P-I curves in Figure 6.52. The increase in the impulse by  $\Delta I = 1$  MPa·msec was achieved by increasing the peak pressure by  $\Delta P = 2$  MPa. The amount of damage accumulated in the column at each simulation was evaluated using the failure criterion given in Equation (6.1).

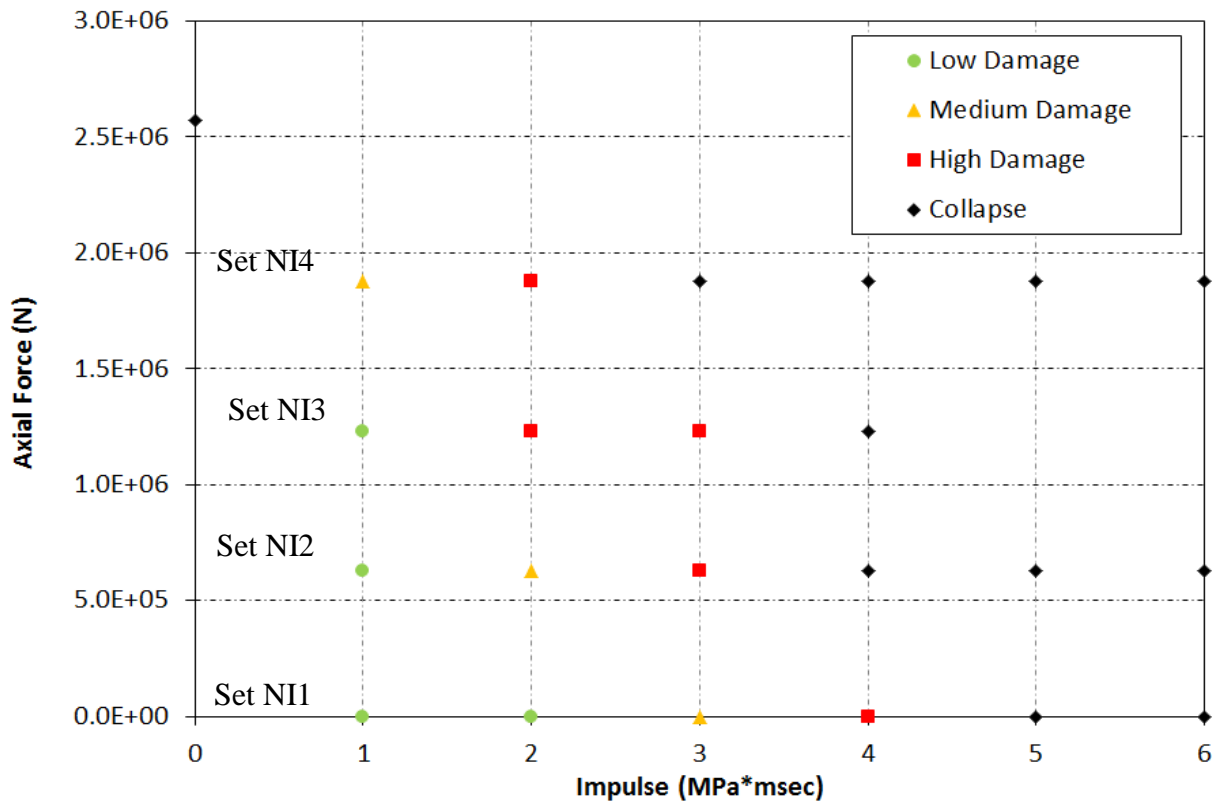


Figure 6.53. Points derived for the N-I diagram

Three N-I curves representing 20%, 50% and 80% damage levels were generated using the data points in Figure 6.53. The following equation provided the best fit for the curves:

$$\frac{N}{N_{cap}} + \left(\frac{I}{A_I}\right)^b = 1 \quad (6.3)$$

where the exponent  $b$  equals 1.5, 1.6 and 1.8 for the cases of 20% damage, 50% damage and 80% damage, respectively. The generated N-I curves are presented in Figure 6.54.

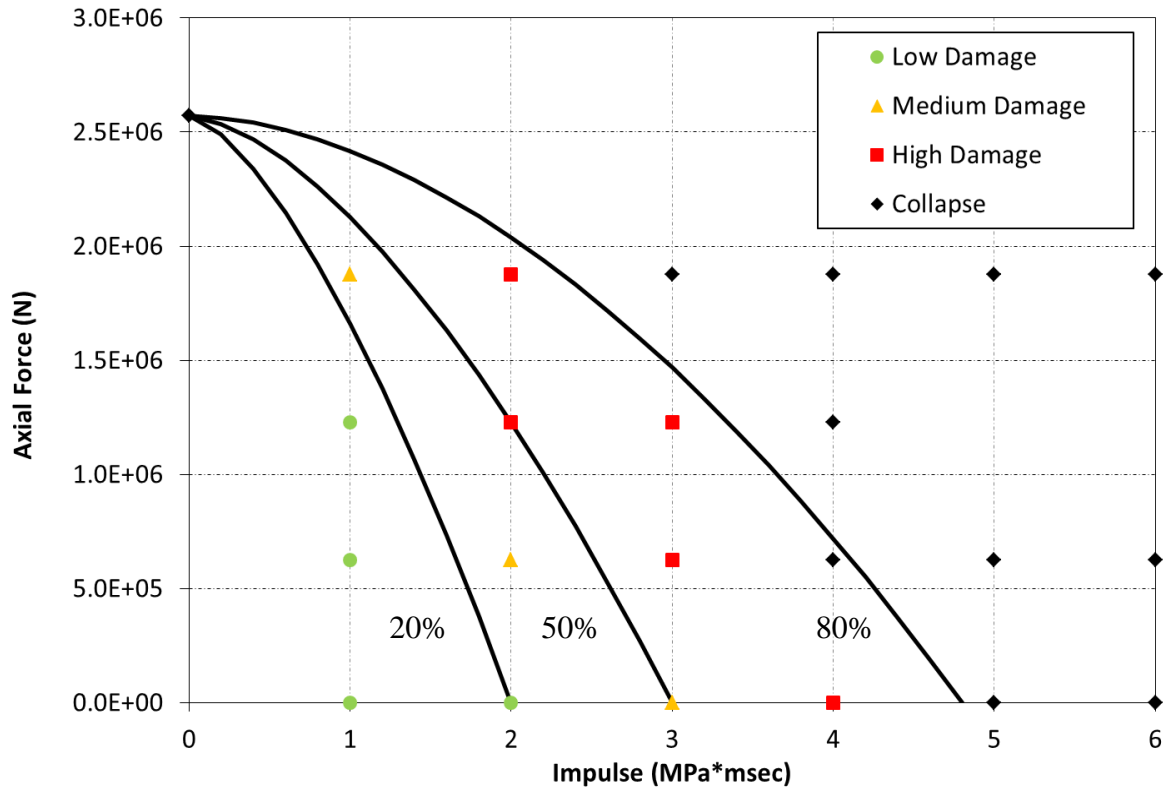


Figure 6.54. N-I Diagram fitted curves

It is necessary to note that the parabolic form of the N-I curve corresponds to the specific structural system analysed here. The shape of the curve may depend on numerous loading and structural parameters such as the structural geometry, the complexity of the resistance-displacement relationship, the supporting and loading conditions, etc.

### 6.3.2.3. Axial Force-Pressure (N-P) Diagrams

The four sets of data points (Sets NP1-4) on the Axial Force-Pressure (N-P) diagram were obtained using the increments in the axial force equal to  $\Delta N = 625$  kN and in the peak pressure to  $\Delta P = 0.1$  MPa (see Figure 6.55). The value of  $\Delta N$  similar to the one used in the derivation of the N-I diagrams was chosen for the sake of convenience. The axial load carrying capacity of the column is represented in Figure 6.55 by the point on the *Axial Force* axis. The duration of the blast load was kept constant  $t_0 = 100$  msec. This value was deemed sufficient, based on the analysis of the quasi-static asymptotes of the P-I curves in Figure 6.52, to generate the quasi-static loading conditions. The four sets of points derived in the FE analyses are presented in Figure 6.55.

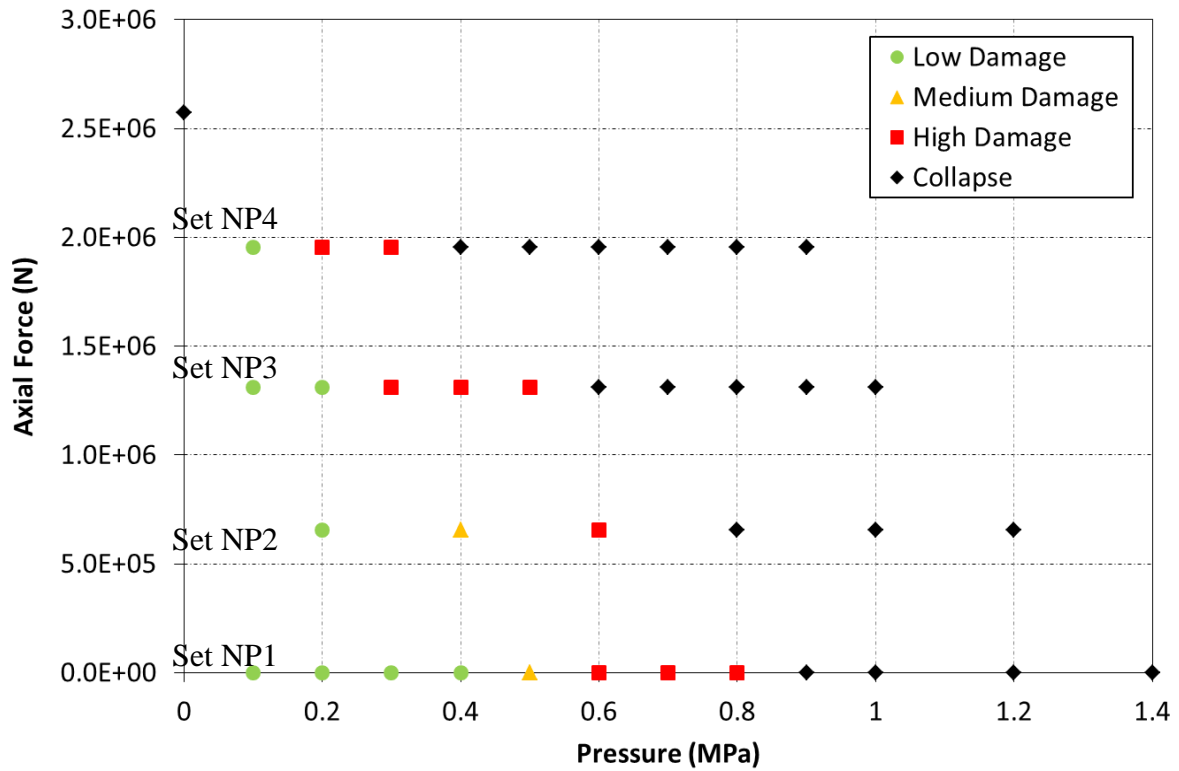


Figure 6.55. Points derived for the N-P diagram

Three N-P curves generated for 20%, 50% and 80% damage levels can be accurately described by the following expression:

$$\frac{N}{N_{cap}} + \left(\frac{P}{A_p}\right)^c = 1 \quad (6.4)$$

where the exponent  $c$  equals 1.2, 1.8 and 2.2 for the cases of 20% damage, 50% damage and 80% damage, respectively. The fitted curves are presented in Figure 6.56.

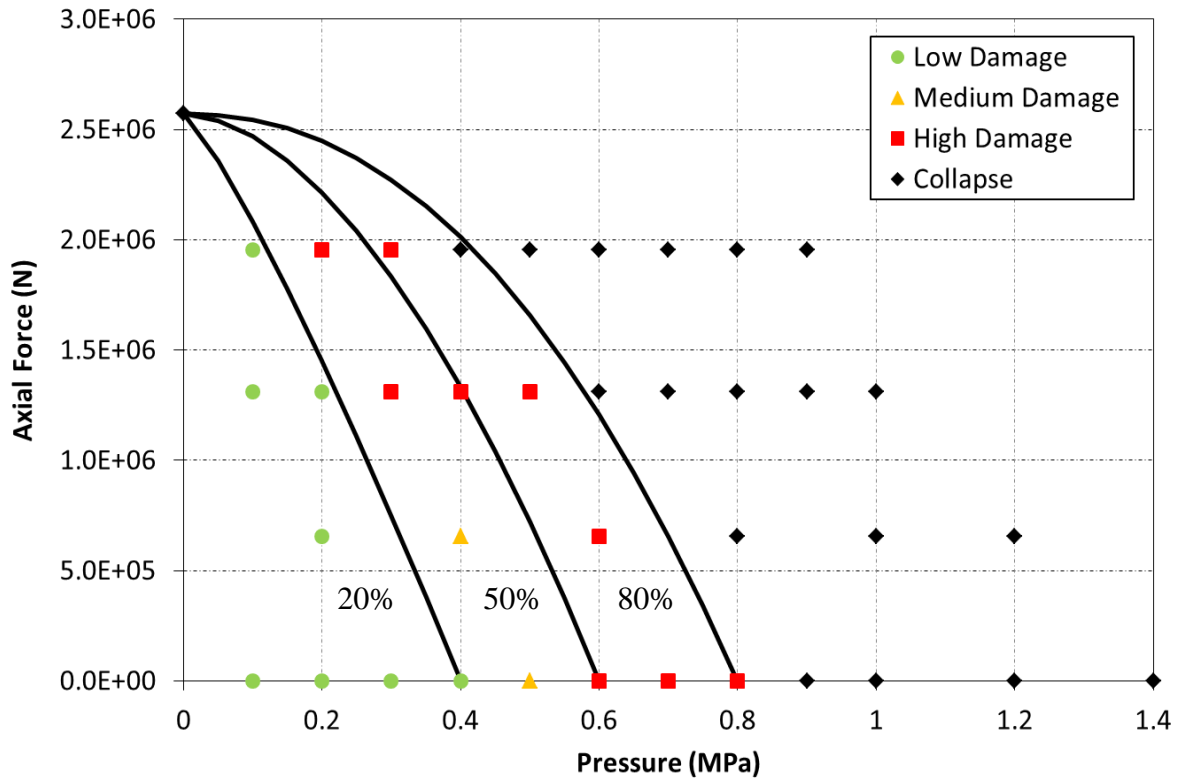


Figure 6.56. N-P Diagram fitted curves

The shape of the N-P diagram entirely depends on the degree of nonlinearity of the considered structural system. The N-P curves can be nonlinear when the analysed structure has complex geometry, supporting and loading conditions and/or a complex nonlinear response-displacement relationship, such as in our case.

### 6.3.3. Response mechanisms in different loading regimes

The response of the column to the blast load that induces three different loading regimes is investigated using the peak pressure and impulse given in Table 6.16.

Loading Regime	Pressure (MPa)	Impulse (MPa*msec)
Impulsive	15	0.3
Dynamic	3	3.6
Quasi-static	0.4	1000

Table 6.16. Pressure and impulse values used for different loading regimes

The appropriate values of the peak pressure and impulse were chosen based on the P-I diagrams generated in Section 6.3.2.1, see Figure 6.57.

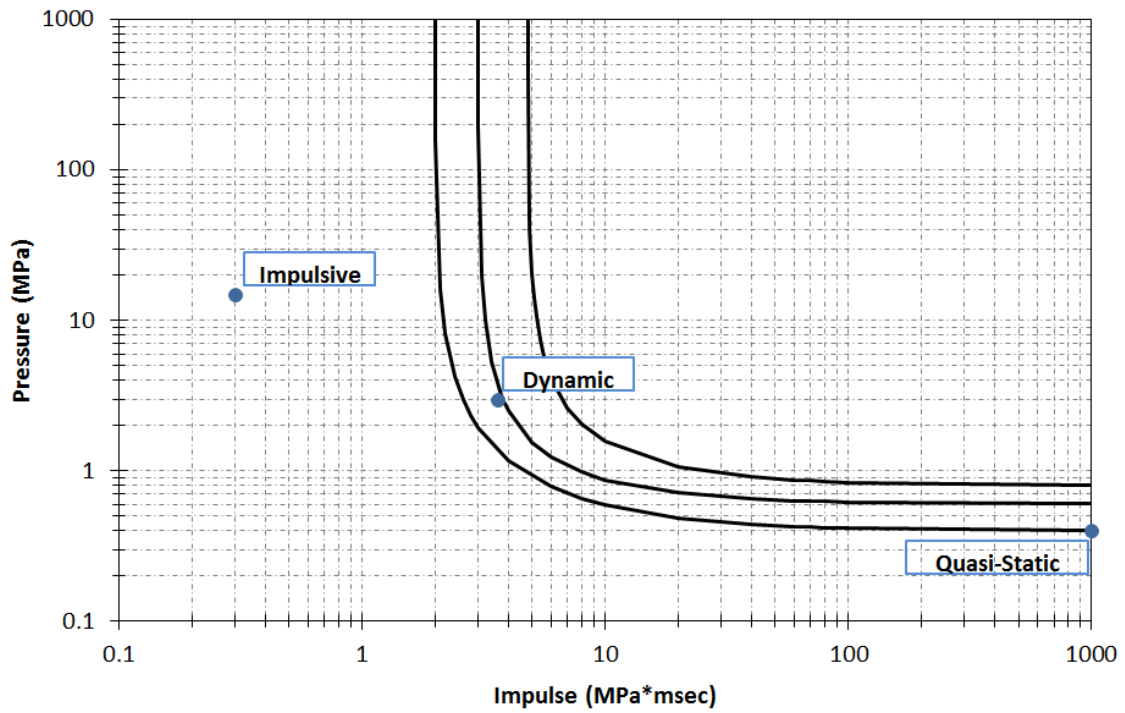


Figure 6.57. Analysis points in each regime

The reaction of the column, in terms of minimum principal stress, at 3 msec after application of the blast load is presented in Figure 6.58 for the three loading regimes.

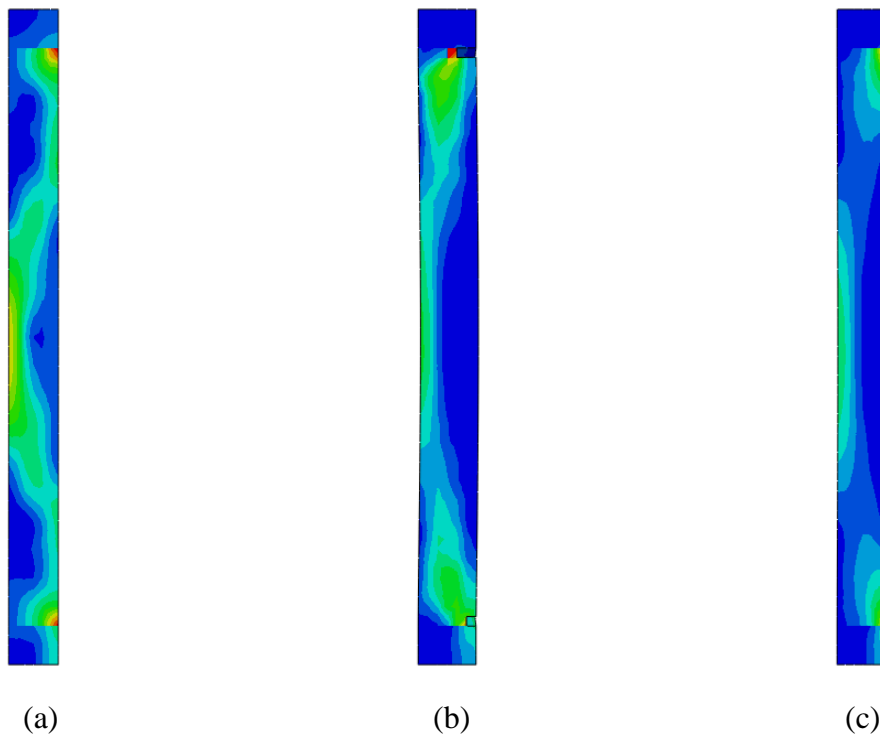


Figure 6.58. Structural response in (a) impulsive (b) dynamic and (c) quasi-static loading regimes

It can be observed in Figure 6.58 there are stress concentrations at the column mid-height and at the supports in all three loading regimes. The impulsive loading regime is characterised by the development of a clear compression arch with the span much shorter than the column length, combined with high stress concentrations at the supports (see Figure 6.58a). This eventually results in the shearing of the column off the supports, while the flexural damage does not have sufficient time to develop due to the very short duration of the blast load. Therefore, the column effectively behaves as a rigid structural element. In the dynamic loading regime, the compression arch extends through the entire length of the column (see Figure 6.58b) leading to the increase of the flexural stresses sufficient to eventually cause damage. As shown in the results, the response mechanism is dominated by both bending and shear, with the shear having a more diagonal pattern. In the quasi-static loading conditions (see Figure 6.58c), the arch is less pronounced and the concentrations of the flexural stress at the column mid-height are connected to the concentrations of the shear stresses at the supports by compression struts. In these conditions, the flexural response mechanism gradually becomes more dominant with increasing duration of the blast load. It is important to note that the presented observations correspond with the conclusions made by Shi et al. [5].

#### **6.3.4. Implementation of the graphical method**

As discussed in Chapter 3, one of the major drawbacks of the P-I diagram method is that each P-I curve is built for a specific structure and any slight change to that structure immediately invalidates it. The use of the complementary diagrams presented in Sections 6.3.2.2 and 6.3.2.3 gives the user the ability to create new P-I curves for the column with the simultaneous effect of two loading/structural parameters on the P-I diagram (e.g., reinforcement ratio and damage, axial preload and cross section area, etc.). In this section, the combined influence of structural damage and axial force on the P-I diagrams was investigated. The use of complementary diagrams allows drawing P-I curves for different levels of damage developing in the column under different levels of axial force. This can be achieved through derivation of additional complementary curves describing different levels of structural damage shown in Figure 6.54 and Figure 6.56. The graphical method is discussed at length in Chapter 4 (see Section 4.3).

The effectiveness of the graphical method is demonstrated by the derivation of new P-I curves describing the column loaded by an axial force of 1229.1 kN, which is approximately

50% of the ultimate axial capacity of the column, and developing 20%, 50% and 80% damage. The position of each P-I curve is defined by the asymptotes, while the asymptotes are controlled by the complementary diagrams. For the column considered herein, the N-I diagram defines the position of the impulsive asymptote (i.e., the value of  $A_I$ ), while the N-P diagram the position of the quasi-static asymptote (i.e., the value of  $A_P$ ). The first step, therefore, is to obtain  $A_I$  and  $A_P$  directly from the complementary curves or by using the corresponding formulas presented in Eqs. (6.3) and (6.4). The new values of  $A_I$  and  $A_P$  obtained for the 20%, 50% and 80% damage levels using the analytic expressions (6.3) and (6.4) are presented in Table 6.17. In the table, the previous values of  $A_I$  and  $A_P$  are also presented for comparison.

New Parameters		Previous Parameters		Damage
$A_I$	$A_P$	$A_I$	$A_P$	
1.296	0.233	2	0.4	20%
1.997	0.418	3	0.6	50%
3.344	0.595	4.8	0.8	80%

*Table 6.17. New Parameters for P-I equations*

The new  $A_I$  and  $A_P$  values are then used in conjunction with Eq. (6.2) to define the expressions for the new P-I curves. It is necessary to note that the values of  $C_P$ ,  $C_I$  and  $D$  in Eq. (6.2) stay the same (see Section 6.3.2.1). The resulting diagram is presented in Figure 6.59.



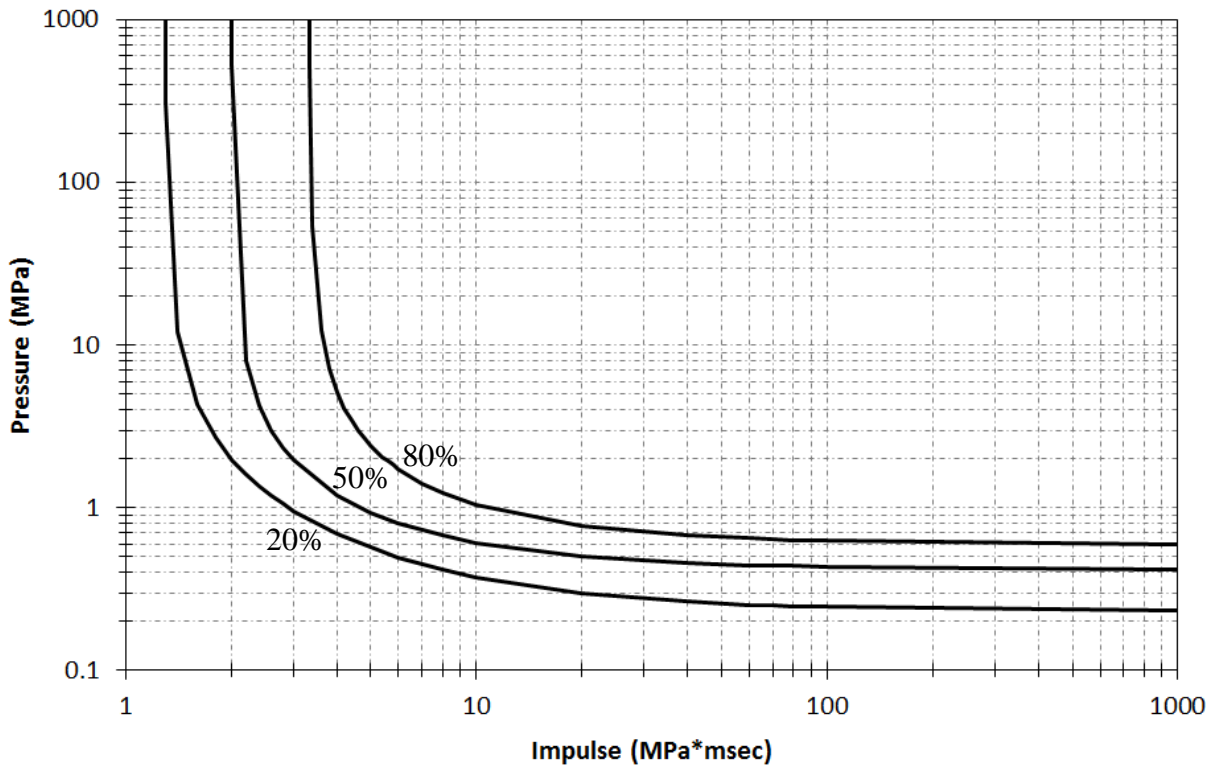


Figure 6.59. New P-I diagram derived for the axial force of 1229.1 kN

In order to verify the obtained P-I curves, three additional sets of data points were generated using FE analyses and the combined (Sets PI1n), pressure-controlled (Sets PI2n) and impulse-controlled (Sets PI3n) search algorithms. The results of the FE analyses are plotted alongside the new P-I curves in Figure 6.60. As can be seen, the three data sets fall, with some small divergence, into the boundaries defined by the P-I curves.

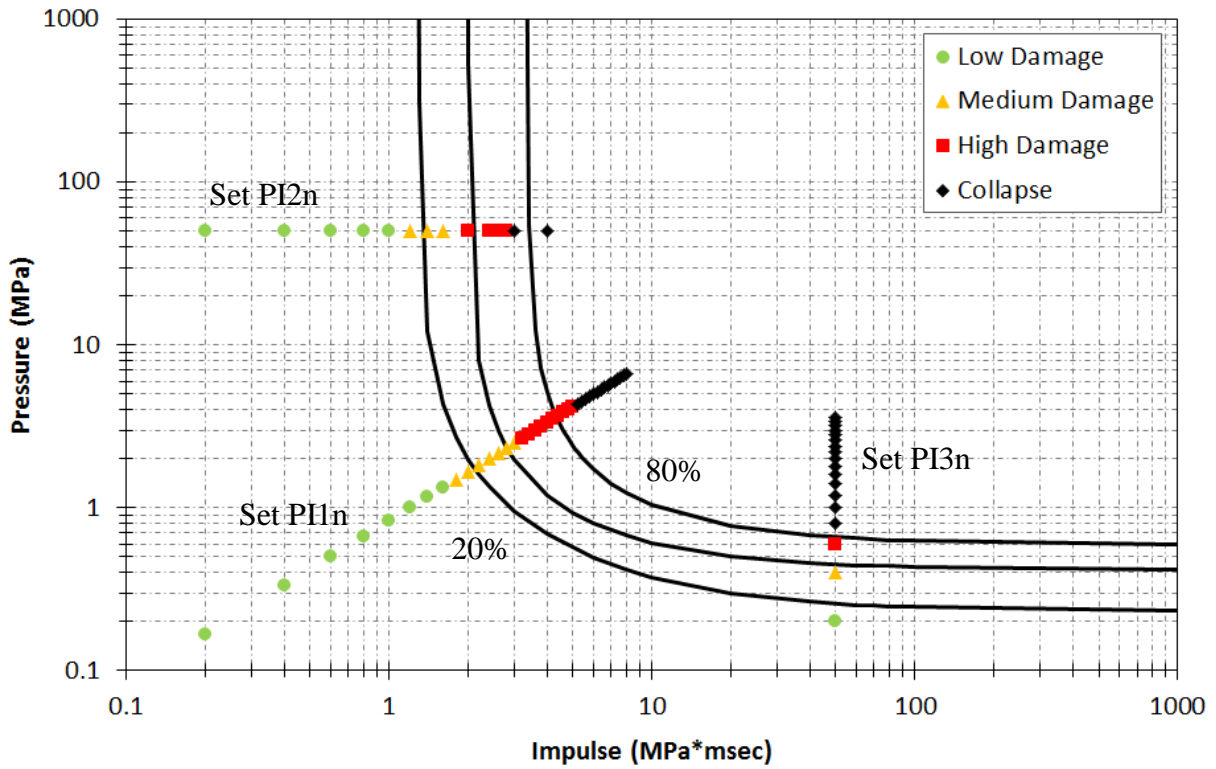


Figure 6.60. New PI curves and FE analyses results

The old and new P-I curves derived for the 80% damage level are overlaid in the diagram in Figure 6.61. It can be observed that the curve representing the axially unloaded column is the most remote from the coordinate axes. The application of the axial force shifts the curve towards the axes due to the additional damage induced by the present of the force. This observation matches the parametric investigation discussed in Chapter 6, Section 6.2.2 which showed an increase in damage levels in the column with the increase in the axial force.

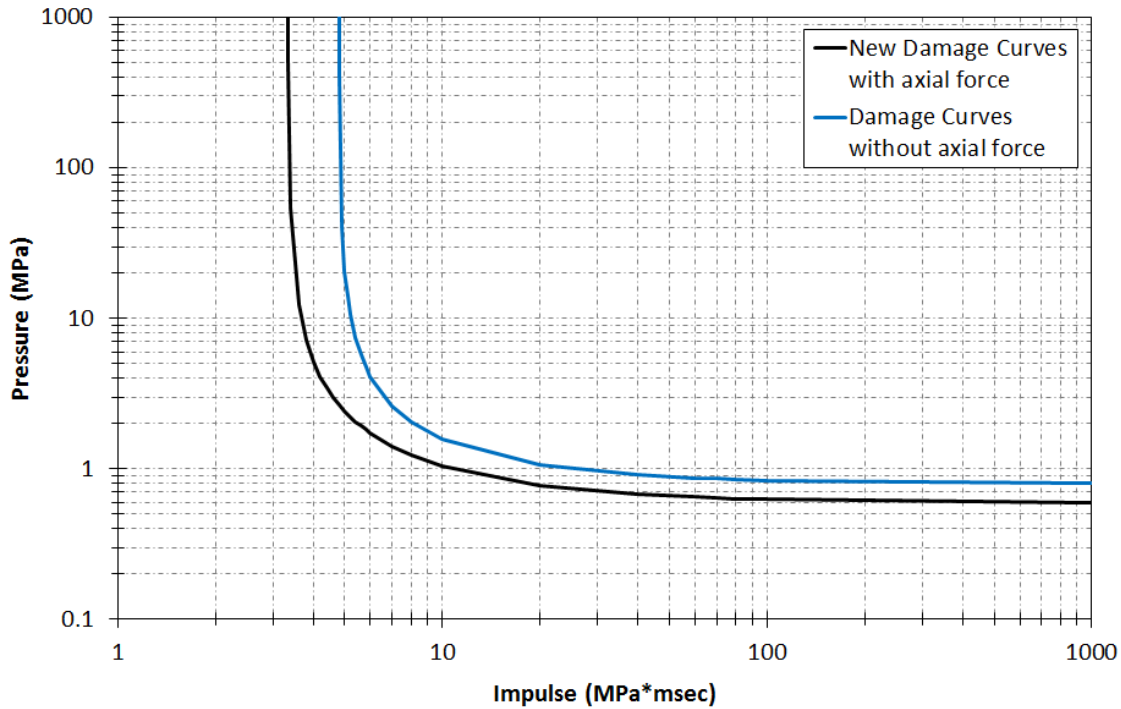


Figure 6.61. Comparison of P-I curves derived with and without axial force

### 6.3.5. Conclusions

This chapter focuses on derivation of P-I diagrams describing the response of a typical reinforced concrete column subjected to the blast load. Initially, the procedure for derivation of P-I curves is outlined. Next, the P-I diagrams are derived for an axially unloaded column developing 20%, 50% and 80% damage levels based on data sets generated by FE simulations. The analytical expression accurately describing the P-I curves is obtained by fitting the data sets. Special attention is then given to the influence of axial force that represents the sum of the ‘dead’ and ‘live’ loads carried by the column prior to blast application. To simplify the derivation of new P-I curves describing the post-blast state of the column subjected to different levels of axial force and developing different levels of damage, the graphical method, introduced in Chapter 4, is implemented. For this purpose, the complementary axial force-impulse (N-I) and axial force-pressure (N-P) diagrams, each including three curves for 20%, 50% and 80% damage levels, are built based on sets of data points obtained using FE simulations. Analytical expressions describing the N-I and N-P diagrams are derived based on fitting the data. A column subject to an axial force equal to 50% of its carrying capacity is then studied. The new P-I curves are then drawn for the column based on the complementary diagrams and validated using new sets of FE-generated data. The response mechanism of the column in different blast-induced loading regimes is

also studied and compared. It is shown that shearing off the columns supports is the dominant response mechanism in the impulsive loading regime; the flexural damage becomes more important in the quasi-static loading regime, while the dynamic loading regime is dominated by a combination of shear and bending.

## References

- [1] T. Rodríguez-Nikl, Experimental simulations of explosive loading on structural components reinforced concrete columns with advanced composite jackets. 2006.
- [2] A. K. Chopra, Dynamics of structures: theory and applications to earthquake engineering. Upper Saddle River, NJ: Prentice Hall, 2015.
- [3] fib, fib Model Code for Concrete Structures 2010: FIB MODEL CODE 2010 O-BK. Weinheim, Germany: Wiley-VCH Verlag GmbH & Co. KGaA, 2013.
- [4] ABAQUS (2014) ‘ABAQUS Documentation’, Dassault Systèmes, Providence, RI, USA.
- [5] Y. Shi, H. Hao, and Z.-X. Li, ‘Numerical derivation of pressure-impulse diagrams for prediction of RC column damage to blast loads’, *Int. J. Impact Eng.*, vol. 35, no. 11, pp. 1213–1227, 2008.
- [6] MATLAB (2010) R2010.a, The MathWorks Inc., Natick, MA, 2000.

## Chapter 7: Summary, Conclusions and Future Work

### 7.1 Summary and Conclusions

The research described in this Thesis is concerned with the numerical investigation of the structural response of reinforced concrete (RC) columns under blast loads, by means of dynamic nonlinear finite element (NLFE) analysis. This study aims at (i) providing an in depth understanding of the mechanics underlying RC structural response under blast loading and (ii) identifying (qualitatively and quantitatively) the effect of certain important design parameters (e.g. the amount and arrangement of the reinforcement, the geometry of the specimen, the boundary conditions imposed, the level of axial loading applied) on the exhibited behaviour. The numerical investigation was carried out through the use of a well-established commercial finite element package (Abaqus) and employed a numerical model capable of accounting for the brittle nature of concrete. The latter model forms an extension to the '*brittle crack*' model in Abaqus and was developed in order to overcome the shortcomings of the existing concrete model which assumes that material behaviour in compression is essentially linear elastic. The verification of the validity of the numerical predictions is based on a comparative study with relevant experimental data. The validated models are then employed to investigate the effect of various parameters associated on the exhibited response.

On the basis of the predictions obtained from the FE analysis a new graphical method is developed, based on building complementary diagrams, for the effective derivation of Pressure-Impulse (P-I) diagrams. This method aims to overcome the problems associated with their inherent sensitivity to any change in the state of the analysed structural system. Through the combined use of the validated FE model and the proposed graphical method, P-I diagrams and the associated complementary diagrams are presented and the efficiency and applicability of the methodology is demonstrated.

The main conclusions that can be drawn from each of the chapters are outlined below;

Chapter 2 provides an overview of blast loads and their effect on RC structural response. Typical engineering assumptions for the modelling of blast loads are presented. A detailed discussion on the effect of loading rate on the material behaviour of concrete is presented followed by an overview of the methods employed in research and practice for assessing RC

structural response under high loading rates and blast loads in particular. The main conclusions drawn from this part of the work are associated with the limitations of the different assessment methods used for studying RC structural response under blast loads. More specifically;

- Experimental data is limited due to military classification. Furthermore experimental studies are characterised by complexity of setup, high cost and safety related issues.
- Material failure is often hard to capture reliably in an experimental setup due to the extreme speed and intensity of the imposed load and the resulting disintegration of components. As a result, there is difficulty correlating the measured response to the actual physical state of the specimens as data obtained from experimental tests is usually characterised by considerable scatter which differs from test to test. In the case of blast loads post failure behaviour is important.
- Available experimental data show that steel reinforcement is crucial for the energy absorbing capacity of the structural concrete elements, and thereby the capacity to withstand blast and fragment loading and avoid structural collapse.
- Simple specialised design code procedures (as used in military codes), such as SDOF, rely on a number of simplifications/assumptions concerning both material behaviour and structural response which do not account for the brittle nature of concrete and its sensitivity to triaxial stress conditions or the localised response often exhibited.
- Detailed NLFE is a widely used efficient method for investigating RC structures under blast loads and is capable of providing more detailed insight on the mechanisms underlying RC structural response under blast loads.
- NLFE predictions are dependent on certain assumptions adopted by the FE package and on the assumptions it employs. NLFE analyses can be very complex and require an experienced analyst and high computational resources.

Chapter 3 presents the P-I diagram as an efficient tool widely used for preliminary assessment and prediction of damage (or survivability) of structures subjected to extreme load conditions, such as those exhibited by blast loads. A full and detailed analytical solution of an elastic beam based on the Euler-Bernoulli beam theory and subjected to a transverse load was presented. The beam was used to derive P-I diagrams under various pressure time histories. On the basis of this discussion it was shown that;

- P-I diagrams are sensitive to the form of the load time history and highly sensitive to the level of the axial force.

In Chapter 4 a new graphical method for the efficient derivation of P-I diagrams is developed. This method is based on building complementary *loading/structural parameter vs. impulse* and *loading/structural parameter vs. pressure* graphs. These complementary diagrams describe, respectively, the structural response in the impulsive and (quasi-)static regimes and define the position of each P-I diagram. The advantages and efficiency of the graphical method proposed in this chapter is demonstrated using an elastic beam-column subjected to an axial force and a transverse blast load.

- The effectiveness of the graphical method for the derivation of new P-I diagrams from an existing one is demonstrated.
- The proposed method forms a powerful tool for preliminary design as well as quick assessment of typical structural elements or structural elements exposed to extreme loads generated by explosions.

Chapter 5 presents the development of finite element RC models capable of providing accurate predictions concerning the structural response of beams and columns under blast and impact loads. An extension of the existing ‘*brittle crack*’ material model already available in Abaqus was developed by incorporating a user defined subroutine procedure. The predictions of the proposed material model were validated against experimental data describing high loading rates. The numerical predictions obtained reveal that;

- The extended brittle crack model overcomes the limitations of the existing model concerning the behaviour of concrete in compression.
- The ability to incorporate damage definition for the concrete elements and the possibility of removing damaged elements leads to a more stable solution procedure.
- Only a small number of material properties, which are simple to obtain, are required in the extended brittle crack model. Overall, the extended brittle crack model offers a robust reliable concrete model.
- The subject model revealed that for plain concrete specimens under high rate loading that the observed effects, both experimentally and numerically, are largely associated with structural effects such as cracking, wave propagation in nonlinear medium and inertia.



- The resulting FE model proved capable of providing valid predictions concerning the response of beam and column specimens under different loading regimes. The models were validated by comparing to experimental data. In all cases the extended brittle crack model provided satisfactory results.

Based on the work conducted in Chapter 5, Chapter 6 uses one of the validated models to investigate RC structural response of columns under blast loads.

The numerical investigation revealed changes to the structural response mechanism for different levels intensity of the imposed of blast and axial loads.

- Under increasing high intensity loads the mode of failure exhibited shifted from flexural to brittle cracking and from global behaviour localised failure close to supports.

Modelling strategy concerning the reinforcement, i.e. beam or truss elements, also had an effect on structural response mechanisms, largely on post failure behaviour.

- Prior to peak loading the type of elements used to model reinforcement doesn't contribute to any change in the structural reaction, however the effect of the reinforcement modelling is significant on the post failure behaviour. When modelled as beam elements the reinforcement contributed to energy dissipation via structural mechanisms such as catenary action which transfer loads to the supports after the specimen failed.

In the examination of different loading regimes with low pressure it was observed that the static structural response mirrored the applied load in the static case, the dynamic case lead to an amplification of the response and the impulsive case responded stiffly leading to less damage. This trend was observed again in the study of reaction times.

- In the dynamic region the response was amplified, however in this study the pressures were increased and durations reduced leading to pronounced damage which in turn allowed for energy dissipation leading to reduced structural reaction forces.

Chapter 6 also presents the derivation of P-I diagrams for a RC column using the finite element method with the extended brittle crack material model for concrete. Complementary diagrams were built for axial force and used to demonstrate the new graphical method. For the case study the axial force on the column is changed and new P-I curves drawn based on the complementary diagrams. The study was validated using new sets of FE-generated data.

The response mechanism of the column in different blast-induced loading regimes was also studied and compared.

- The shearing off of columns supports is the dominant response mechanism in the impulsive loading regime; the flexural damage becomes more important in the quasi-static loading regime, while the dynamic loading regime is dominated by a combination of shear and bending.

## **7.2 Future Work**

Suggestions for future work include;

- On the basis of the validated models developed in the subject thesis for predicting the behaviour of individual RC beam and column specimens it is possible to develop more intricate models representing more complex structural forms (e.g. RC frames) which consist of more than one component. This will provide insight on the influence of local damage sustained due to loads such as blast on the global behaviour of structures.
- The extent of detailed modelling of 3D structures under blasts will be investigated. The study will use simplified methods, such as P-I diagrams, to locate the onerous locations for the RC structural members. The frame will be modelled using the detailed 3D modelling previously studied for the members likely to be subjected to extensive damage moving into beam element representation further away from the blast zone. This study will attempt to quantify the safe distance for reverting into simplified structural models, therefore reducing computational costs.
- Both the latter models (simplified and advanced) can be employed to investigate the progressive collapse mechanisms exhibited by RC structures. This will combine the detailed modelling of RC structures with simplifications to allow for reduced calculation time to further examine mechanisms involved and predictions involved in disproportionate collapse.
- On the basis of the findings of the subject thesis advanced SDOF models can be developed. The proposed SDOF models will take into account the dependency of deformation shape on the loading rate. This will provide a practice tool, easy to employ that will account for the influence of local effects and therefore provide an accurate estimation of the behaviour of high rate loading on RC components.

- Extension of the P-I graphical method to include additional parameters. This will allow the change of various parameters simultaneously and give more design freedom and quicker damage estimation for users.

# Appendix A

## A.1. Introduction

Limited analytical work on the blast dynamics of axially preloaded beams can be found in the scientific literature. Although the numerical models, in particular the finite element analysis, are the main tool used for assessment of structures subjected to explosive loads (e.g. [1]–[6]), the analytical methods remain an essential tool that provides a comprehensive insight into the physical behaviour of a structural element. These methods offer fast and reliable solutions especially suitable for the preliminary design and post-blast loading assessment. In addition, they are often utilised as a sound benchmark for the verification of the numerical methods and for the development of new computational models.

Detailed analytical solutions for free lateral vibrations of elastic beams with axial preload and for forced lateral vibrations of elastic beams without axial loads are covered in multiple research papers [7]–[12] and textbooks [13]–[25]. At the same time, the solution for the combination of these two problems has attracted only limited attention. A notable analytical work on this topic was published by Virgin and Plaut [26], where the authors investigated the steady state linear response of elastic beams subjected to a quasi-static axial force and a distributed harmonically varying transverse load.

## A.2. Axially preloaded elastic beam subjected to blast loads

It is assumed that the axial force is quasi-static, while the transverse load could be either a distributed pressure load or a point force with a non-harmonic time history. The elastic beam-column of the length  $l$  is described using the Euler-Bernoulli (or classical) beam theory [13]–[25]. This theory assumes that the beam deflections are solely influenced by the bending moment, ignoring the effects of the rotation of the cross-section and shear deformation. As a result, it is more suitable for slender beams and tends to overestimate the natural frequencies [12] in the beams with higher thickness to span ratios. Notwithstanding, this theory provides a reasonable approximation for many engineering problems and is most commonly used. In many engineering applications it is important to be able to calculate the maximum response of a system, e.g., the maximum beam deflection. If light structural damping is assumed, the amount of energy it can dissipate in the short duration of motion is quite small. Thus, its effect on the maximum response of the beam to a single pulse excitation can be neglected [27].

The Euler-Bernoulli beam motion is governed by a partial differential equation of motion, an external forcing function, and boundary and initial conditions. In this research the obtained non-homogeneous initial and boundary value problem is solved using the method of decomposition into the modes of vibration (i.e., *eigenfunction* expansion). It is noted that the problems that can be solved with separation of variables are relatively limited; the equation must be linear as the solution is found as a sum of simple solutions.

The governing equation of motion reads (e.g., [16], [22], [23], [25])

$$EIu'''' + Fu'' + m\ddot{u} = P(x, t) \quad (\text{A1})$$

where  $u(x, t)$  is the beam deflection,  $u'$  represents a partial derivative with respect to the space variable  $x$  and  $\dot{u}$  with respect to time  $t$ ,  $EI$  is the flexural stiffness of the beam,  $F$  the axial force,  $m$  the mass per unit length of the beam and  $P(x, t)$  the transverse excitation force. Assume henceforth that  $EI$  and  $m$  are constant along the beam.

Eq. (A1) can be generalised using linear differential operators as

$$M(\ddot{u}) + L(u) = P(x, t) \quad (\text{A2})$$

where  $M$  and  $L$  have the form

$$\mathcal{L}(\xi) = a_0\xi + a_1\frac{\partial\xi}{\partial x} + a_2\frac{\partial^2\xi}{\partial x^2} + \dots$$

Using the method of separation of variables and the decomposition into the contributions of individual modes  $u(x, t)$  can be expressed as

$$u(x, t) = \sum_{i=1}^{\infty} \phi_i(x)q_i(t) \quad (\text{A3})$$

where  $\phi_i(x)$  is the  $i^{\text{th}}$  free vibration mode of the beam and  $q_i(t)$  is the function of time.  $q_i$  is decomposed into the particular and homogenous parts representing the solutions of Eq. (A1) in its particular and homogenous forms.

$$q_i = q_i^p + q_i^h \quad (\text{A4})$$

This formulation leads to the following decomposition of the beam deflection

$$u = \sum_{i=1}^{\infty} \phi_i(q_i^p + q_i^h) = \sum_{i=1}^{\infty} \phi_i q_i^p + \sum_{i=1}^{\infty} \phi_i q_i^h = u^p + u^h$$

Note that both  $u^p$  and  $u^h$  need to satisfy Eq. (A1)

We begin the solution of the present problem with formulating the expression for  $q_i^p$ . Premultiplying Eq. (A2) by  $\phi_j$  and integrating it along the column length yields

$$\sum_{i=1}^{\infty} \ddot{q}_i^p \int_0^l \phi_j M(\phi_i) dx + \sum_{i=1}^{\infty} q_i^p \int_0^l \phi_j L(\phi_i) dx = \int_0^l \phi_j P(x, t) dx \quad (\text{A5})$$

Applying the orthogonality properties of the free vibration modes (e.g. [14], [16], [22], [27]) Eq. (A5) becomes

$$m_{ii} \ddot{q}_i^p + k_{ii} q_i^p = Q_i \quad (\text{A6})$$

where  $m_{ii}$  and  $k_{ii}$  are the generalized mass and stiffness of the beam

$$m_{ii} = \int_0^l \phi_i M(\phi_i) dx = m \int_0^l \phi_i \phi_i dx \quad (\text{A7})$$

$$k_{ii} = \int_0^l \phi_i L(\phi_i) dx = EI \int_0^l \phi_i'' \phi_i'' dx - F \int_0^l \phi_i' \phi_i' dx \quad (\text{A8})$$

and  $Q_i$  is the generalised force

$$Q_i = \int_0^l \phi_i P(x, t) dx \quad (\text{A9})$$

Eq. (A8) is obtained using the integration by parts leading to two sets of additional terms that represent the boundary conditions

$$[\phi_i (EI \phi_i''' + F \phi_i')]_0^l = 0 \quad \text{and} \quad [\phi_i' (EI \phi_i'')]_0^l = 0 \quad (\text{A10})$$

The first set represents the conditions that either the deflection or the shear force at the ends of the beam is zero, while the second set represents the condition that either the rotation or the moment at the ends of the beam is zero.

It is convenient to separate the excitation in the form

$$P(x, t) = P_0 p(x) f(t) \quad (\text{A11})$$

where  $P_0$  is the maximum value and  $p(x)$  the spatial distribution of the load and  $f(t)$  the time history of the excitation. Eq. (A6) can then be rearranged into

$$\ddot{q}_i^p + \omega_i^2 q_i^p = P_0 \Gamma_i f(t) \quad (\text{A12})$$

where  $\omega_i$  is the natural frequency of the beam and

$$\Gamma_i = m_{ii}^{-1} \int_0^l \phi_i(x) p(x) dx \quad (\text{A13})$$

the modal participation factor [27]. Finally, the contribution of the  $i^{\text{th}}$  mode to  $p(x)$  is

$$p_i(x) = \Gamma_i p(x) \phi_i(x)$$

The solution of Eq. (A10) is [27]

$$q_i^p(t) = P_0 \Gamma_i D_i(t) \quad (\text{A14})$$

where  $D_i(t)$  is the deformation response of the  $i^{\text{th}}$  mode SDOF system. Consequently, Eq. (A3) becomes

$$u^p(x, t) = \sum_{i=1}^{\infty} P_0 \Gamma_i \phi_i(x) D_i(t) \quad (\text{A15})$$

To find  $\phi_i(x)$  and  $q_i^h(t)$  the differential equation (A1) is rearranged in the homogeneous form as

$$EIu'''' + Fu'' + m\ddot{u} = 0 \quad (\text{A16})$$

Using  $u^h(x, t) = \sum_{i=1}^{\infty} \phi_i(x) q_i^h(t)$  and thus  $u_i^h = \phi_i q_i^h$  the homogeneous partial differential equation (A16) can be divided into two linear differential equations corresponding to the  $i^{\text{th}}$  mode of vibration

$$EI\phi_i'''' + F\phi_i'' + m\omega_i^2\phi_i = 0 \quad (\text{A17})$$

$$\ddot{q}_i^h - \omega_i^2\ddot{q}_i^h = 0 \quad (\text{A18})$$

Assuming that

$$\phi(x) = C \exp(s_i x)$$

Eq. (A17) can be reduced to the following characteristic equation

$$EIs_i^4 + Fs_i^2 - m\omega_i^2 = 0 \quad (\text{A19})$$

with the quadratic roots

$$s_{i,1(2)}^2 = \frac{F}{2EI} \left[ -1 \pm \sqrt{1 + 4m\omega_i^2 EI / F^2} \right] \quad (\text{A20})$$

As a result,  $\phi_i(x)$  can be expressed as [16]

$$\phi_i(x) = C_1 \sinh a_i x + C_2 \cosh a_i x + C_3 \cos b_i x + C_4 \sin b_i x \quad (\text{A21})$$

where  $a_i^2 = s_{i,1}^2$ ,  $b_i^2 = -s_{i,2}^2$  and  $C_1$ - $C_4$  are the arbitrary constants found from the application of the boundary conditions (A10). Therefore, the final form of  $\phi_i(x)$  strongly depends on the beam boundary conditions.

The solution of the equation (A18) is

$$q_i^h(t) = C_5 \sin \omega_i t + C_6 \cos \omega_i t \quad (\text{A22})$$

where  $C_5$  and  $C_6$  are the arbitrary constants found from initial conditions (i.e., initial deflections and velocities). Assuming zero initial conditions (i.e.,  $q_i^h(0) = \dot{q}_i^h(0) = 0$ ) results in  $C_5 = C_6 = 0$ . Therefore,  $q_i^h = 0$  so  $q_i \equiv q_i^p$  which leads to  $u^h = 0$  and  $u \equiv u^p$ .

### A.2.1. Pinned-pinned supports

To study the typical behaviour of axially preloaded beams subjected to the blast loads, pinned-pinned supports are considered resulting in the following set of four boundary conditions

$$u(0, t) = u''(0, t) = u(l, t) = u''(l, t) = 0 \quad (\text{A23})$$

or equivalently

$$\phi_i(0) = \phi_i''(0) = \phi_i(l) = \phi_i''(l) = 0 \quad (\text{A24})$$

Application the boundary conditions yields the mode shapes,  $\phi_i$

$$\phi_i(x) = C_4 \sin b_i x \quad (\text{A25})$$

and the frequency equation as

$$\sin b_i l = 0 \quad (\text{A26})$$

with the solution  $b_i l = i\pi$  (where  $i = 1, 2, 3, \dots$ ). Finally,  $\phi_i(x)$  and  $\omega_i$  equal [16]

$$\phi_i(x) = A_i \sin \frac{i\pi x}{l} \quad \text{and} \quad \omega_i^2 = \left(\frac{i\pi}{l}\right)^4 \frac{EI}{m} - \left(\frac{i\pi}{l}\right)^2 \frac{F}{m} \quad (\text{A27})$$

Substituting the expression for  $\phi_i(x)$  from Eq. (A27) into Eq. (A7) and taking into account that  $m_{ii} = ml$  results in  $A_i = \sqrt{2}$ .

### A.2.2. Forced vibration phase: $t \leq t_0$

Taking into account Eqs. (A27) and carrying out some algebraic manipulations on Eq. (A8) leads to

$$k_{ii} = ml\omega_i^2 = \left(\frac{i\pi}{l}\right)^4 EI l - \left(\frac{i\pi}{l}\right)^2 Fl \quad (\text{A28})$$

The solution of Eq. (A12) can be obtained for the  $i^{\text{th}}$  mode of vibration using convolution integral as



$$q_i(t) = q_i^p(t) = P_0 \Gamma_i \frac{1}{\omega_i} \int_0^t f(\tau) \sin[\omega_i(t - \tau)] d\tau \quad (\text{A29})$$

Comparing Eqs. (A14) and (A29) and taking into account the expression for  $\Gamma_i$  in Eq. (A13) the  $i^{\text{th}}$  mode deformation response  $D_i(t)$  can be expressed as

$$D_i(t) = \frac{1}{\omega_i} \int_0^t f(\tau) \sin[\omega_i(t - \tau)] d\tau = \frac{1}{\omega_i} I_i(t) \quad (\text{A30})$$

Substituting  $\phi_i(x)$  from Eqs. (A27) into Eq. (A29) finally yields the displacements of the axially preloaded beam in the forced vibration phase

$$u_1(x, t) = \sum_{i=1}^{\infty} \sqrt{2} P_0 \Gamma_i \frac{1}{\omega_i} \sin \frac{i\pi x}{l} \int_0^t f(\tau) \sin[\omega_i(t - \tau)] d\tau \quad (\text{A31})$$

In engineering practice, the spatial and temporal distributions of different extreme loads are usually modelled using various simplifying assumptions. The shape of the spatial distribution of the transverse excitation load  $p(x)$  is represented in Eq. (A31) by  $\Gamma_i$ . Table A1 presents a number of typical  $p(x)$  and corresponding expressions for  $\Gamma_i$ .

Spatial distribution	$p(x)$	$\Gamma_i$
Concentrated load located at $\xi$	$\delta(x - \xi)$	$\sqrt{2} \frac{\sin(i\pi\xi/l)}{ml}$
Uniformly distributed load	1	$\sqrt{2} \frac{1 - \cos i\pi}{i\pi m}$
Triangularly distributed load	$\frac{x}{l}$	$(-1)^{i+1} \frac{\sqrt{2}}{i\pi m}$
	$1 - \frac{x}{l}$	$\frac{\sqrt{2}}{i\pi m}$
Sine-shaped distributed load	$\sin \frac{n\pi x}{l}$	$\begin{cases} (\sqrt{2}\pi m)^{-1} & i = n \\ 0 & i \neq n \end{cases}$
Exponentially shaped distributed load	$\exp \frac{n\pi x}{l}$	$\frac{\sqrt{2}i}{\pi m(i^2 + n^2)} (1 - e^{n\pi} \cos i\pi)$

Table A.1: Modal participation factors  $\Gamma_i$  for different spatial load distributions for pinned-pinned beams

### A.2.3. Free vibration phase: $t > t_0$

After the transverse blast load ends the system starts vibrating freely. Therefore, Eq. (A12) is reduced to a homogeneous form

$$\ddot{q}_i + \omega_i^2 q_i = 0 \quad (\text{A32})$$

The solution of this homogeneous equation (A32) is [16], [27]

$$u_2(x, t) = \sum_{i=1}^{\infty} (A_i \cos \omega_i t + B_i \sin \omega_i t) \sin \frac{i\pi x}{l} \quad (\text{A33})$$

where  $A_i$  and  $B_i$  are arbitrary constants. In order to assure the continuity in the motion of the beam at  $t = t_0$  the following conditions should be satisfied

$$u_1(x, t_0) = u_2(x, t_0) \quad \text{and} \quad \dot{u}_1(x, t_0) = \dot{u}_2(x, t_0) \quad (\text{A34})$$

These continuity conditions (A34) are used to determine the coefficients  $B_i$  and  $C_i$ . Then the motion of the axially preloaded beam in the free vibration phase is obtained as

$$u_2(x, t) = \sum_{i=1}^{\infty} \sqrt{2} P_0 \Gamma_i \frac{1}{\omega_i} \sin \frac{i\pi x}{l} \left[ I_i \cdot \cos[\omega_i(t - t_0)] + \frac{\dot{I}_i}{\omega_i} \cdot \sin[\omega_i(t - t_0)] \right] \quad (\text{A35})$$

where  $I_i$  is the part of the normalised impulse applied to the  $i^{\text{th}}$  mode of vibration and  $\dot{I}_i$  its time derivative defined as

$$I_i = \int_0^{t_0} f(\tau) \sin[\omega_i(t_0 - \tau)] d\tau \quad \text{and} \quad \dot{I}_i = \omega_i \int_0^{t_0} f(\tau) \cos[\omega_i(t_0 - \tau)] d\tau \quad (\text{A36})$$

Comparing Eqs. (A15) and (A35) leads to the SDOF response  $D_i(t)$  in the form

$$D_i(t) = \frac{1}{\omega_i} \left[ I_i \cdot \cos[\omega_i(t - t_0)] + \frac{\dot{I}_i}{\omega_i} \cdot \sin[\omega_i(t - t_0)] \right] \quad (\text{A37})$$

### A.2.4. Time of maximum deflection

The maximum response of the beam to the blast and impact loads is commonly characterised by the peak deflections and the time  $t_m$  when it takes place. However, in the present formulation, the time of total maximum deflection cannot be found directly and it has to be estimated from the maximum deflections (amplitudes) of the modal responses. The peak deflection of the free vibration phase  $t_{m,i}$  can be found as

$$t_{m,i} = t_0 + \frac{1}{\omega_i} \tan^{-1} \left[ \dot{I}_i / (\omega_i I_i) \right] \quad (\text{A38})$$

where  $I_i$  and  $\dot{I}_i$  are given by Eqs. (A36). The analytical solution for  $t_{m,i}$  in the force vibration phase can only be obtained for a limited number of load time histories:

$$t_{m,i} = \frac{\pi}{\omega_i} \quad \text{for the rectangular shape} \quad (\text{A39})$$

$$t_{m,i} = \frac{1}{\omega_i} \text{Arg } Z_i \quad \text{for the triangular shape} \quad (\text{A40})$$

where  $\text{Arg } Z_i$  is the principal value of the argument of the complex number

$$Z_i = \frac{2\omega_i t_0}{1+(\omega_i t_0)^2} + j \frac{1-(\omega_i t_0)^2}{1+(\omega_i t_0)^2} \quad (\text{41})$$

and  $j = \sqrt{-1}$ . Eqs. (A38, A39 and A40) can be used for the calculation of the upper limit of the beam deflection as the sum of the mode amplitudes. Assuming that the maximum deflection appears at the mid-span of the beam,  $x = l/2$ , the possible maximum deflection  $u_m$  becomes

$$u_m = EIP_0 \sum_{i=1}^{\infty} \Gamma_i \phi_{i,m}(l/2) D_{i,m} \quad (\text{A42})$$

where  $D_{i,m}$  is the maximum value of  $D_i$ . The upper limits for  $D_{i,m}$  can be found as

$$D_{i,m} = \frac{1}{\omega_i} I_i(t_{m,i}) \quad \text{for the forced vibration phase} \quad (\text{A43})$$

$$D_{i,m} = \frac{1}{\omega_i} \sqrt{I_i^2 + (\dot{I}_i/\omega_i)^2} \quad \text{for the free vibration phase} \quad (\text{A44})$$

where  $I_i(t_{m,i}) = \int_0^{t_{m,i}} f(\tau) \sin[\omega_i(t_{m,i} - \tau)] d\tau$ .

When transverse pressure loads with more complicated time histories (e.g., concave, exponential, sinusoidal, etc.) are acting on the beam-column, the time of the maximum deflection in the forced vibration phase can only be found using numerical analysis.

### A.2.5. Mode contribution

The maximum deflection of Eq. (A42) is given by an infinite series, which in practice needs to be truncated to obtain a numerical solution. The number of terms to be taken into account generally depends on a type of the applied load and the desired accuracy of the solution. The discussion on the effect of higher modes and its contribution to the dynamic response of beams can be found in [27], [28]. To assess the influence of each term in the solution (A42), the contribution of the  $i^{\text{th}}$  mode to the peak deflection  $u_m$  is expressed relatively to the contribution of the first mode  $u_{1,m}$  as

$$u_m = u_{1,m} (1 + \sum_{i=2}^{\infty} \mu_i) \quad (\text{A45})$$

where  $\mu_i$  is the relative modal contribution factor defined as

$$\mu_i = \frac{u_{i,m}}{u_{1,m}} = \sum_{j=1}^{\infty} \frac{\Gamma_j}{\Gamma_1} \cdot \frac{\phi_{j,m}}{\phi_{1,m}} \cdot \frac{D_{j,m}}{D_{1,m}} \quad (\text{A46})$$

The first ratio in Eq. (A46) depends on  $p(x)$ . The second ratio in Eq. (A46) can be readily found using Eqs. (A27) as

$$\frac{\phi_{i,m}}{\phi_{1,m}} = \frac{\phi_i(l/2)}{\phi_1(l/2)} = \sin \frac{i\pi}{2} \quad (\text{A47})$$

To find the ratio  $D_{i,m}/D_{1,m}$ ,  $\omega_i$  in the second Eq. (A27) is rearranged into

$$\omega_i = \left(\frac{i\pi}{l}\right)^2 \sqrt{\frac{EI}{m}} \sqrt{1 - \frac{F}{F_{bi}}} = \bar{\omega}_i \sqrt{1 - \frac{F}{F_{bi}}} \quad (\text{A48})$$

where  $\bar{\omega}_i = (i\pi/l)^2 \sqrt{EI/m}$  is the natural frequency of the pinned-pinned beam without the axial force (i.e.,  $F = 0$ ) and  $F_{bi} = (i\pi/l)^2 EI$  the  $i^{\text{th}}$  Euler buckling load of the beam. Taking into account Eqs. (A43) and (A44) the ratio  $D_{i,m}/D_{1,m}$  becomes

$$\frac{D_{i,m}}{D_{1,m}} = i^{-2} \frac{\sqrt{1-F/F_{b1}} I_i(t_m)}{\sqrt{1-F/F_{bi}} I_1(t_m)} \quad \text{for the forced vibration phase} \quad (\text{A49})$$

$$\frac{D_{i,m}}{D_{1,m}} = i^{-2} \frac{\sqrt{1-F/F_{b1}} \sqrt{I_i^2 + (i/\omega_i)^2}}{\sqrt{1-F/F_{bi}} \sqrt{I_1^2 + (i_1/\omega_1)^2}} \quad \text{for the free vibration phase} \quad (\text{A50})$$

Finally,  $\mu_i$  is obtained as

$$\mu_i = \sum_{i=3,5,7}^{\infty} i^{-2} \frac{\Gamma_i}{\Gamma_1} \sin \frac{i\pi}{2} \sqrt{\frac{1-F/F_{b1}}{1-F/F_{bi}}} \frac{I_i(t_m)}{I_1(t_m)} \quad \text{for the forced vibration phase} \quad (\text{A51})$$

$$\mu_i = \sum_{i=3,5,7}^{\infty} i^{-3} \frac{\Gamma_i}{\Gamma_1} \sin \frac{i\pi}{2} \sqrt{\frac{1-F/F_{b1}}{1-F/F_{bi}}} \frac{\sqrt{I_i^2 + (i/\omega_i)^2}}{\sqrt{I_1^2 + (i_1/\omega_1)^2}} \quad \text{for the free vibration phase} \quad (\text{A52})$$

It is necessary to point out that in real structures  $F$  is limited to the first Euler buckling force  $F_{b1}$ . Therefore, the ratio  $F/F_{bi}$  becomes negligible for  $i \geq 3$  and Eqs. (A51) and (A52) can be further simplified to

$$\mu_i \cong \sum_{i=3,5,7}^{\infty} i^{-2} \frac{\Gamma_i}{\Gamma_1} \sin \frac{i\pi}{2} \sqrt{1 - \frac{F}{F_{b1}}} \frac{I_i(t_m)}{I_1(t_m)} \quad \text{for the forced vibration phase} \quad (\text{A53})$$

$$\mu_i \cong \sum_{i=3,5,7}^{\infty} i^{-2} \frac{\Gamma_i}{\Gamma_1} \sin \frac{i\pi}{2} \sqrt{1 - \frac{F}{F_{b1}}} \frac{\sqrt{I_i^2 + (i/\omega_i)^2}}{\sqrt{I_1^2 + (i_1/\omega_1)^2}} \quad \text{for the free vibration phase} \quad (\text{A54})$$

Both  $I_i$  and  $i/\omega_i$  (see Eq. (A36)) and so  $\mu_i$  decrease with increasing  $i$ .

## References

- [1] S. Foo, A. G. Razaqpur, A. A. Nassr, M. Campidelli, and M. J. Tait, 'Dynamic Response of Steel Columns Subjected to Blast Loading', *J Struct Eng J. Struct. Eng.*, vol. 140, no. 7, 2014.
- [2] H. M. I. Thilakarathna, D. P. Thambiratnam, M. Dhanasekar, and N. Perera, 'Numerical simulation of axially loaded concrete columns under transverse impact and vulnerability assessment', *Int. J. Impact Eng.*, vol. 37, no. 11, pp. 1100–1112, Nov. 2010.
- [3] Y. Shi, H. Hao, and Z. Li, 'Numerical derivation of pressure–impulse diagrams for prediction of RC column damage to blast loads', *Int. J. Impact Eng.*, vol. 35, no. 11, pp. 1213–1227, 2008.
- [4] W. W. El-Dakhkhni, W. F. Mekky, and S. H. Changiz-Rezaei, 'Vulnerability Screening and Capacity Assessment of Reinforced Concrete Columns Subjected to Blast', *J. Perform. Constr. Facil.*, vol. 23, no. 5, pp. 353–365, Oct. 2009.
- [5] S. Astarlioglu, T. Krauthammer, D. Morency, and T. P. Tran, 'Behavior of reinforced concrete columns under combined effects of axial and blast-induced transverse loads', *Eng. Struct.*, vol. 55, pp. 26–34, Oct. 2013.
- [6] A. A. Nassr, A. G. Razaqpur, M. J. Tait, M. Campidelli, and S. Foo, 'Strength and stability of steel beam columns under blast load', *Int. J. Impact Eng.*, vol. 55, pp. 34–48, May 2013.
- [7] S. Timoshenko, 'On the correction for shear of the differential equation for transverse vibrations of bars of uniform cross-section', *Philos. Mag.*, p. 744, 1921.
- [8] S. Timoshenko, 'On the transverse vibrations of bars of uniform cross-section', *Philos. Mag.*, p. 125, 1922.
- [9] T. C. Huang, 'The Effect of Rotatory Inertia and of Shear Deformation on the Frequency and Normal Mode Equations of Uniform Beams With Simple End Conditions', *J. Appl. Mech.*, vol. 28, no. 4, p. 579, 1961.
- [10] H. Abramovich, 'Natural frequencies of Timoshenko beams under compressive axial loads', *J. Sound Vib.*, vol. 157, no. 1, pp. 183–189, Aug. 1992.

- [11] H. Matsunaga, 'Free Vibration and Stability of Thin Elastic Beams Subjected to Axial Forces', *J. Sound Vib.*, vol. 191, no. 5, pp. 917–933, Apr. 1996.
- [12] S. . Han and T. W. H. Benaroya, 'Dynamics of transversely vibrating beams using four engineering theories.', *Shock Vib. Dig.*, vol. 32, no. 5, 2000.
- [13] J. M. Biggs, *Introduction to structural dynamics*. New York: McGraw-Hill, 1964.
- [14] L. Meirovitch, *Analytical methods in vibrations*. New York: Macmillan, 1967.
- [15] H. McCallion, *Vibration of linear mechanical systems*. London: Longman, 1973.
- [16] F. S. Tse, I. E. Morse, and R. T. Hinkle, *Mechanical vibrations: theory and applications*. Boston: Allyn and Bacon, 1978.
- [17] S. Timoshenko, D. H. Young, and W. Weaver, *Vibration problems in engineering*. New York: Wiley, 1974.
- [18] W. T. Thomson, *Theory of vibration with applications*. Englewood Cliffs, N.J.: Prentice-Hall, 1981.
- [19] D. J. Inman, *Engineering vibration*. Upper Saddle River, N.J.: Prentice Hall, 2001.
- [20] S. S. Rao, *Mechanical vibrations*. Upper Saddle River, N.J.: Pearson Prentice Hall, 2004.
- [21] H. Benaroya, *Mechanical vibration: analysis, uncertainties, and control*. Upper Saddle River, N.J.: Prentice Hall, 1998.
- [22] S. S. Rao, *Vibration of continuous systems*. Hoboken, N.J.: Wiley, 2007.
- [23] L. N. Virgin, *Vibration of axially loaded structures*. New York, NY: Cambridge University Press, 2007.
- [24] A. W. Leissa and M. S. Qatu, *Vibrations of continuous systems*. New York: McGraw-Hill, 2011.
- [25] S. G. Kelly, *Mechanical vibrations: theory and applications*. Stamford, CT: Cengage Learning, 2012.

- [26] L. Virgin and R. Plaut, 'Effect Of Axial Load On Forced Vibrations Of Beams', *J. Sound Vib.*, vol. 168, no. 3, pp. 395–405, 1993.
- [27] A. K. Chopra, *Dynamics of structures: theory and applications to earthquake engineering*. Englewood Cliffs, N.J.: Prentice Hall, 1995.
- [28] W. Karthaus and J. W. Leussink, *Dynamic Loading: More Than Just a Dynamic Load Factor*. Ft. Belvoir: Defense Technical Information Center, 1983.

## Appendix B

### Brittle Crack Compression Subroutine

```
subroutine vusdfld(  
c Read only -  
* nblock, nstatev, nfieldv, nprops, ndir, nshr,  
* jElem, kIntPt, kLayer, kSecPt,  
* stepTime, totalTime, dt, cmname,  
* coordMp, direct, T, charLength, props,  
* stateOld,  
c Write only -  
* stateNew, field )  
c  
include 'vaba_param.inc'  
c  
dimension jElem(nblock), coordMp(nblock,*),  
* direct(nblock,3,3), T(nblock,3,3),  
* charLength(nblock), props(nprops),  
* stateOld(nblock,nstatev),  
* stateNew(nblock,nstatev),  
* field(nblock,nfieldv)  
character*80 cmname  
c  
c Local arrays from vgetvrm are dimensioned to  
c maximum block size (maxblk)  
c  
parameter( nrData=6 )  
character*3 cData(maxblk*nrData)  
dimension rData(maxblk*nrData), jData(maxblk*nrData)  
c  
jStatus = 1  
call vgetvrm( 'LE', rData, jData, cData, jStatus )
```



```

c
if( jStatus .ne. 0 ) then
  call xplb_abqerr(-2,'Utility routine VGETVRM '//
*   'failed to get variable.',0,zero,' )
  call xplb_exit
end if
c
call setField( nblock, nstatev, nfieldv, nrData,
*   rData, stateOld, stateNew, field)
c
return
end
subroutine setField( nblock, nstatev, nfieldv, nrData,
*   strain, stateOld, stateNew, field )
c
include 'vaba_param.inc'
c
dimension stateOld(nblock,nstatev),
*   stateNew(nblock,nstatev),
*   field(nblock,nfieldv), strain(nblock,nrData)
c
do k = 1, nblock
c
  field(k,2) = 1
c
  Values of current strain:
  eps1 = strain(k,1)
  eps2 = strain(k,2)
  eps3 = strain(k,3)
c
c
  Chose the minimum strain of the 3 directions
  eps = min(eps1, eps2, eps3)
c

```

```

c   Chose the maximum strain of the 3 directions
    eps_max = max(eps1, eps2, eps3)
c
c   Check if minimum is in compression
    if (eps < 0.d0) then
        epsab = abs(eps)
c       Minimum value of strain up to this point in time:
        epsmax = stateOld(k,1)
c       Use the minimum strain as a field variable
        field(k,1) = max( epsab, epsmax )
c       Store the minimum strain as a solution dependent state
        stateNew(k,1) = field(k,1)
c       Failure criterion
c       FailureStrain = -0.0035
        FailureStrain = -0.003
        if( eps < FailureStrain ) then
            field(k,2) = 0.0
        end if
    else
        stateNew(k,1) = stateOld(k,1)
    end if
c
c   Check erosion in tension
    if (eps_max > 0.d0) then
        FailureStrain_max = 0.1
        if (eps_max > FailureStrain_max) then
            field(k,2) = 0.0
        end if
    end if
c
stateNew(k,2) = field(k,2)
c

```

```
    end do  
c  
    return  
end
```